Model-independent measurement of the CKM angle γ in $B^{\pm} \to [h^+h^-\pi^+\pi^-]_D h'^{\pm}$ $(h = K, \pi)$ decays at LHCb and BESIII

Martin Duy Tat

St John's College

University of Oxford

A thesis submitted for the degree of

Doctor of Philosophy

Trinity 2024

Acknowledgements

I would first like to express my gratitude to Guy Wilkinson for his fantastic supervision during my four years in the Oxford LHCb group. His excellent guidance, invaluable feedback and constant encouragement has inspired me to become a better researcher. Additionally, the numerous research opportunities he has provided me have been crucial for my academic career growth. I am also thankful to Neville Harnew for his endless patience and support during my work with TORCH. Under his supervision, I had the chance to participate in hands-on testbeam work, which taught me many important skills that I hope to make use of in future detector work. I should also extend my thanks to Roger Forty for allowing me to make significant contributions towards the ARC detector project.

The analyses described in this thesis would not have been possible without the infinite wisdom and helpful suggestions from Sneha Malde. I am very grateful for all her valuable advice and everything she has taught me about the BPGGSZ method. Furthermore, I must thank Sneha for the privilege of doing tutorial teaching. In addition, I have been given several teaching opportunities by Malcolm John as well, and I will always be grateful to both Sneha and Malcolm for the experience, skills and knowledge that I acquired during my teaching duties.

Many thanks to all students and postdocs in Oxford LHCb, who have made this journey a much more pleasant experience. Thanks should also be awarded to Sue Geddes and Kim Proudfoot for their incredible effort in running the department. And many thanks to Aker Scholarship for providing me funding for four years, allowing me to eat excessive amounts of sandwiches and chicken.

I would also like to take this opportunity to acknowledge my undergraduate tutors Tony Weidberg and Georg Viehhauser, who first introduced me to particle physics. They have always supported me through my undergraduate studies, they helped me secure my funding for a PhD in Oxford and it is always lovely to regularly meet them for some coffee and cake.

A special thanks to my sister Martine. I will forever appreciate the constant interruptions with hilarious Kirby memes, which have caused a great amount of laughter.

Finally, words cannot describe my appreciation for my amazing fiancé Sophia, who has always been by my side for the last eight years. We have shared many of our happiest moments together during our time in Oxford, and I cannot wait to start a new chapter of our lives as postdoctoral researchers together.

Abstract

This thesis describes two complementary analyses related to the four-body $D^0 \to K^+K^-\pi^+\pi^-$ and $D^0 \to \pi^+\pi^-\pi^+\pi^-$ decays, where the ultimate objective is to study *CP* violation and measure the CKM angle γ. First, a model-independent determination of parameters describing the strong-phase difference between the D^0 and $\overline{D}^0 \to K^+K^-\pi^+\pi^-$ decays is performed. The analysis uses a sample of quantum-correlated $D\overline{D}$ pairs produced in e^+e^- collisions at the $\psi(3770)$ resonance. The data sample corresponds to an integrated luminosity of $16\,\text{fb}^{-1}$, recorded by the BESIII detector. The measurement is performed in bins of phase space, using a five-dimensional binning scheme optimised for sensitivity to γ.

In the second part, a sample of *pp* collisions collected by the LHCb detector, corresponding to $9\,\text{fb}^{-1}$ of integrated luminosity, is used to obtain a model-independent measurement of γ with the $B^\pm \to Dh^\pm$ decay, where $h = K$ or π. The neutral charm meson subsequently decays to the four-body $D \to K^+K^-\pi^+\pi^-$ or $\pi^+\pi^-\pi^+\pi^-$ modes. This is the first binned measurement of γ using these multi-body decays, utilising strong-phase parameters from BESIII as external inputs. Additionally, a study of the phase-space integrated *CP*-violating effects is also performed.

The result is $\gamma = (53.6^{+8.6}_{-6.7})^\circ$, which is a combination of both phase-space binned and phase-space integrated *CP*-violating observables. It is one of the most precise stand-alone measurements of the CKM angle γ. The uncertainties are currently statistically dominated.

Contents

1 Introduction

If the Standard Model of Particle Physics (SM) had been correct, the world as we know it could have been very different. In fact, all matter in the universe would perhaps not exist, since it would quickly annihilate with the anti-matter that is also present. The universe would end up as a large soup of energy, mostly in the form of photons. Particles such as electrons or quarks could enter in and out of existence through pair production, but never stay around long enough to form stable matter.

How can such a world be reconciled with the reality of a matter-dominated universe? The SM cannot answer this. Moreover, the SM has several other deficiencies. For instance, it cannot explain the nature of dark matter or dark energy, nor is it compatible with general relativity. Clearly, the Standard Model is incomplete!

An understanding of fundamental differences between particle and anti-particle interactions is a potential first step towards a complete theory of particle physics. Very precise measurements of key SM parameters can play a crucial role in revealing the mechanism that generates an asymmetry between matter and anti-matter.

Throughout the history of particle physics, many discoveries have been guided by existing precision measurements. In particular, precise measurements at low energies can be sensitive to new physics at higher energy scales through loop-level corrections. An example is the Glashow-Illiopoulos-Maiani mechanism [1], which predicted the existence of the charm quark, and was motivated by the suppression of

flavour-changing neutral currents, such as the $K^0 \to \mu^+\mu^-$ decay or K^0-$\overline{K}^0$ mixing. A related example is the top quark mass, which was constrained before its discovery by global fits [2] of electroweak observables and by B^0-$\overline{B}^0$ mixing parameters [3, 4].

The work presented in this thesis follows the same theme of precision measurements. Specifically, the Cabibbo-Kobayashi-Maskawa (CKM) quark-mixing matrix [5, 6] was proposed in 1973 by Makoto Kobayashi and Toshihide Maskawa, and it built on previous work by Nicola Cabibbo in 1963. It was developed as an explanation for *CP* violation, which is one of the ingredients for understanding matter and anti-matter asymmetry. The CKM matrix describes the quark flavours and how they couple together through charged-current weak interactions.

By over-constraining the CKM parameters with precise measurements, potential discrepancies may reveal hints to where new physics beyond the SM may lie. The central topic of interest for this thesis is the CKM angle γ, which is considered a "standard candle" measurement for the SM. Precision measurements of this SM reference, when compared with determinations that are sensitive to non-SM effects, may indirectly reveal physics beyond the SM.

This thesis studies the decay $B^\pm \to Dh^\pm$, where $h = K$ or π, and the neutral charm meson subsequently decays into $D \to K^+K^-\pi^+\pi^-$ or $\pi^+\pi^-\pi^+\pi^-$. The analysis is performed in bins of phase space, which requires external charm strong-phase inputs. The analysis therefore benefits greatly from the complementarity between hadron colliders and charm factories.

The thesis is structured as follows. Chapter 2 provides a general background to *CP* violation and the strategies for determining γ. In Chapter 3, the optimised phase-space binning is developed. The strong-phase inputs are measured with a data set taken in e^+e^- collisions at the $D\overline{D}$ threshold, corresponding to $16\,\text{fb}^{-1}$ of integrated luminosity. The data are collected by the BESIII detector, which is introduced in Chapter 4. The subsequent analysis is described in Chapters 5 and 6. The final part of the thesis concerns an analysis of a data set corresponding to $9\,\text{fb}^{-1}$ collected by the LHCb experiment, which is described in Chapter 7. In Chapters 8 and 9, one of the world's most precise stand-alone measurements of the CKM angle γ is presented.

2

Theoretical background

Contents

2.1 The Standard Model of Particle Physics

The Standard Model of Particle Physics (SM) is one of the most successful theories in fundamental science. To date, this theory of elementary particle interactions has not been falsified, and it has been experimentally verified to a precision of 10^{-12} [7]. In addition to its impressive agreement with precision measurements, the SM also predicted the existence of several elementary particles. These include

the $W^{\pm}$ and Z bosons, top and charm quarks, and the Higgs boson, which were all observed subsequently by experiment.

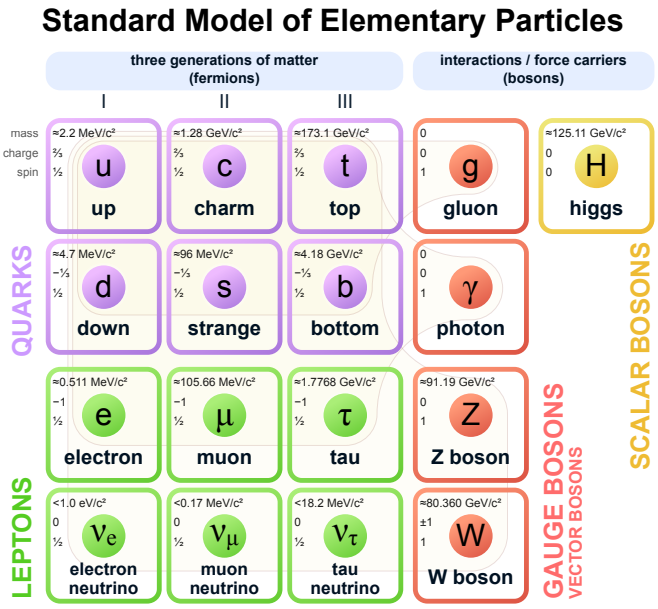

Figure 2.1: Elementary particles of the Standard Model. Illustration taken from Ref. [8].

The fundamental building blocks of the SM are presented in Fig. 2.1, and these elementary particles can in general be categorised as either fermions, which have half-integer spin, or bosons, which have integer spin. These particles interact with each other through the electromagnetic, weak and strong interactions[1]. There are two classes of fermions. The quarks, which form the top two rows of fermions in Fig. 2.1, participate in all three interactions. The last two rows of fermions are known as leptons. The charged leptons, which are the electron, muon and tau, interact through both the electromagnetic and weak interactions, while their neutral partners, known as neutrinos, only undergo weak interactions.

The gauge bosons, which are listed in the fourth column in Fig. 2.1, are known as exchange particles or force carriers. Particles interact by exchanging these gauge bosons, as illustrated in Fig. 2.2. Specifically, the diagram on the top left in Fig. 2.2 shows an electromagnetic interaction through the exchange of a photon γ. Therefore, photons are the force carriers of the electromagnetic interaction. Similarly, the top

[1]A fourth interaction, known as the gravitational interaction, is not described by the SM.

right diagram in Fig. 2.2 shows a strong interaction with a gluon exchange, while the bottom diagrams show weak interactions mediated by the $W^{\pm}$ and Z bosons.

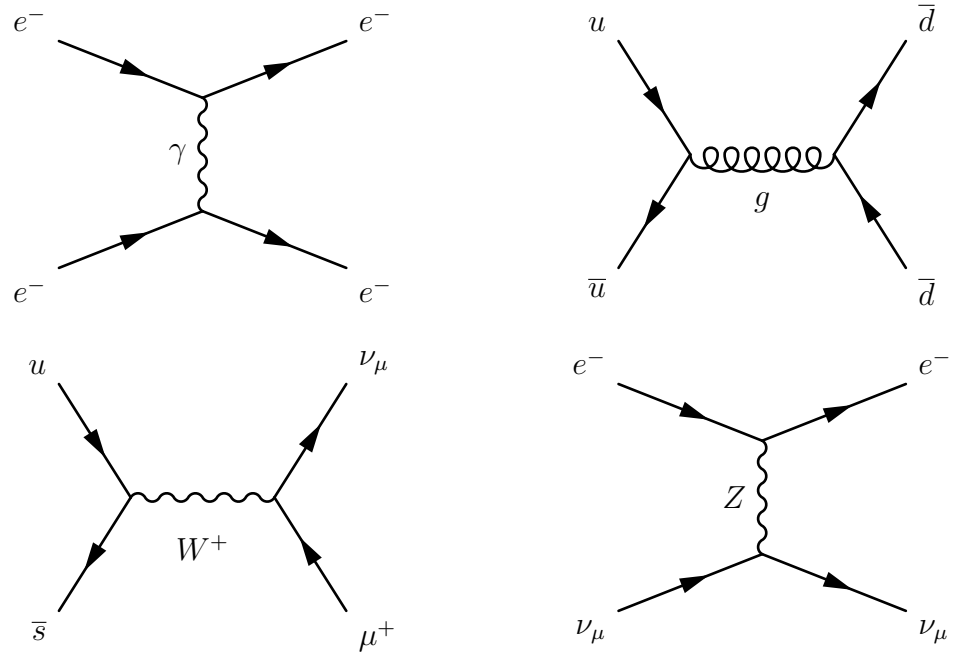

Figure 2.2: Feynman diagrams of (top left) electromagnetic, (top right) strong and (bottom) weak interactions

The first generation of fermions, which form the leftmost column in Fig. 2.1, make up almost all visible matter in the universe. The up and down quarks are usually tightly bound by the strong interaction to form protons and neutrons. Together with the electron, which is a first generation lepton, these make up all atoms in the visible universe. Additionally, the electron is accompanied by a corresponding neutral lepton, known as an electron neutrino, which only interacts through the weak interaction.

The second and third generations of fermions can be considered as heavier copies of the first generation of fermions. Apart from the heavier particle masses, these fermions have the same charge and spin, and their interactions are found experimentally to be identical to those of the first generation of fermions.

In technical terms, the SM is constructed as a gauge theory. Such theories are characterised by a set of N fermion quantum fields ψ, and under the SU(N) transformation $\psi \to V\psi$, where $V^\dagger V = I$, the action is left invariant. Furthermore,

if V is allowed to depend on the spacetime coordinates x_μ, it is necessary to introduce a massless gauge field A_μ, in order to keep the action invariant under the local gauge transformation.

For $N = 3$, the gauge field is identified as a gluon field, and the three components of ψ are the three colour charges of the strong interaction. Furthermore, the gauge theory with the symmetry $\mathrm{U}(1) \times \mathrm{SU}(2)$ is known as the electroweak interaction, with four accompanying massless gauge bosons. Through the Higgs mechanism, this symmetry is spontaneously broken into U(1), where one massless gauge field is identified as a photon field, while the remaining three become the W^+, W^- and Z bosons. Thus, the full SM is a gauge theory under the symmetry group $\mathrm{U}(1) \times \mathrm{SU}(2) \times \mathrm{SU}(3)$.

While the photon and gluons fields are massless, the $W^\pm$ and Z gauge bosons are observed to have mass. In order to preserve local gauge invariance, these gauge fields obtain their masses through their interaction via the Higgs field. The observation of the Higgs boson, which is an excitation of the Higgs field, was the final elementary particle of the SM that was discovered.

The existence of the Higgs boson also has significant implications for fermions, which obtain their masses through a coupling term in the SM Lagrangian of the form $\psi_i y_{ij} \psi_j \phi$, where ϕ is the Higgs field. The complex 3×3 matrix y_{ij} allows the mass eigenstates to differ from the flavour eigenstates, and this allows for many interesting phenomena that will be discussed further in Sections 2.2 and 2.3.

2.2 Symmetries in Particle Physics

Although gauge symmetries play a crucial role in the construction of the SM, as described in Section 2.1, symmetries also have a much more important role in physics. According to Noether's theorem [9], every continuous symmetry of the action of a system has a corresponding conservation law. Specifically, the invariance of the SM action under temporal and spatial translations leads to the conservation of energy and momentum, while gauge symmetries are responsible for the conservation of charge.

In addition, there are three discrete transformations that were originally thought to be fundamental symmetries:

1. Charge conjugation C changes the signs of all additive quantum numbers of a particle, which include electric charge, lepton number and quark flavours.

2. Parity P inverts the direction of all vectors, such that a particle with momentum $\vec{p}$ is transformed into a particle moving with momentum $-\vec{p}$.

3. Time reversal T transforms time t to $-t$.

Each of the operators C, P and T have eigenvalues ± 1, which are referred to as even and odd eigenvalues, respectively. Any Lorentz-invariant quantum field theory must be invariant under the combined CPT transformation [10]. The implications of this symmetry is that all particles in the universe have the same mass and lifetime as their corresponding anti-particles.

Experimentally, each of the C, P and T transformations are also found to be symmetries of the electromagnetic and strong interactions, meaning that those interaction terms in the SM Lagrangian are invariant under such transformations. However, this is not the case in weak decays. In 1956 an experiment, proposed by C. N. Yang and T. D. Lee [11] and conducted by C. S. Wu et al. [12], confirmed the violation of P symmetry. Furthermore, in the weak interaction it is found that both C and P are maximally broken. In the framework of the SM, the violation of C and P occur because the weak charged currents, which are mediated by the $W^{\pm}$ boson, exclusively couple left-handed fermions and right-handed anti-fermions.

Although both C and P are maximally violated, the combined operation CP was initially expected to be a fundamental symmetry. This transformation turns left-handed fermions into right-handed anti-fermions. In 1964, in an experiment by J. W. Cronin and V. L. Fitch [13] involving neutral kaons, it was established that CP was broken as well. This discovery also implies that T must be broken such that the combined CPT transformation is a symmetry. The violation of T symmetry has also been explicitly observed in the kaon system by the CPLEAR experiment [14].

The violation of *CP* has very important implications for baryogenesis, a process during the early universe that produced a small asymmetry in baryonic matter. Although this asymmetry was very small, around $\mathcal{O}(10^{-9})$, its consequence is that everything in the visible universe today consists of matter, and not anti-matter. The role of *CP* violation in baryogenesis can be summarised with Sakharov's three conditions for baryogenesis [15]:

1. Baryon number must be violated, such that more baryons than anti-baryons may be produced.

2. *C* and *CP* symmetries must be violated. If only baryon number is violated, for every process that produces excess baryons there is also a process that produces the same excess of anti-baryons.

3. Interactions must occur out of thermal equilibrium.

Although both *C* and *CP* violation are described by the SM, the observed size of *CP*-violation effects are currently many orders of magnitude smaller than that required to explain baryogenesis [16]. Therefore, it is essential to understand the mechanism that generates *CP* violation and properly understand the origin of *CP*-violation effects that is responsible for baryogenesis.

2.3 The CKM matrix and *CP* violation

In the SM, the origin of *CP* violation can be traced back to quark couplings with the $W^{\pm}$ boson. An example is shown in the diagram at the bottom left of Fig. 2.2, where the $W^{\pm}$ boson couples quarks across different generations. In contrast to this, the other diagrams in Fig. 2.2 show processes with photon, gluon and Z boson couplings, and these couple exclusively to quarks and leptons within the same generations.

This seemingly odd behaviour of $W^{\pm}$ couplings with quarks occurs because in general, the quark flavour eigenstates that couple to the $W^{\pm}$ boson are different from their mass eigenstates. The up-type quark mass eigenstates (u, c, t), in the conventional basis, are chosen to be identical to their flavour eigenstates

(u', c', t'). The down-type quark eigenstates are then related by the unitary CKM matrix V_{CKM} [5, 17]

$$\begin{pmatrix} d' \\ s' \\ b' \end{pmatrix} = V_{\text{CKM}} \begin{pmatrix} d \\ s \\ b \end{pmatrix} = \begin{pmatrix} V_{ud} & V_{us} & V_{ub} \\ V_{cd} & V_{cs} & V_{cb} \\ V_{td} & V_{ts} & V_{tb} \end{pmatrix} \begin{pmatrix} d \\ s \\ b \end{pmatrix},$$

which allows the $W^{\pm}$ boson to couple quarks between different generations. The CKM matrix is directly related to the complex matrix y_{ij} mentioned in Section 2.1.

The CKM matrix has 3×3 complex entries, or a total of $2 \times 9 = 18$ parameters. However, the unitarity condition imposes 9 constraints on the elements. Furthermore, since the six quark wavefunctions have five arbitrary phase differences, there are only $18 - 9 - 5 = 4$ free parameters.

In the parameterisation proposed in Ref. [18], the four free parameters are identified as three rotation angles θ_{12}, θ_{13}, θ_{23} and a complex phase δ_{CP},

$$V_{\text{CKM}} = \begin{pmatrix} 1 & 0 & 0 \\ 0 & c_{23} & s_{23} \\ 0 & -s_{23} & c_{23} \end{pmatrix} \begin{pmatrix} c_{13} & 0 & s_{13}e^{-i\delta_{CP}} \\ 0 & 1 & 0 \\ -s_{13}e^{-i\delta_{CP}} & 0 & c_{13} \end{pmatrix} \begin{pmatrix} c_{12} & s_{12} & 0 \\ -s_{12} & c_{12} & 0 \\ 0 & 0 & 1 \end{pmatrix},$$

where $c_{ij} \equiv \cos(\theta_{ij})$ and $s_{ij} \equiv \sin(\theta_{ij})$. The angle θ_{12} is identified as the Cabibbo angle θ_C [5].

The presence of a complex non-zero phase δ_{CP} in the CKM matrix has implications for *CP* violation, as this phase swaps sign under *CP* transformations. Such phases are referred to as weak phases and are to be compared with strong phases, which do not change sign under *CP*. Strong phases are usually introduced in processes that involve intermediate states due to QCD interactions.

In a process with strong phase ξ and weak-phase δ_{CP}, its amplitude $A = |A|e^{i(\xi+\delta_{CP})}$ transforms under *CP* into $\bar{A} = |A|e^{i(\xi-\delta_{CP})}$. Hence, when both the strong phase ξ and weak phase δ_{CP} are non-zero, the amplitude will have a different phase factor. In processes where there is another amplitude B for this to interfere with, the combined decay rate $\left||A|e^{i(\xi+\delta_{CP})} + B\right|^2$ differs from its *CP* conjugate, $\left||A|e^{i(\xi-\delta_{CP})} + B\right|^2$, which is a violation of *CP* symmetry. In fact, δ_{CP} is the only observed *CP*-violating phase in the SM.

The CKM matrix can be expressed using the Wolfenstein parameterisation [19] in order to emphasise the relative sizes and phases of the CKM matrix,

$$V_{\mathrm{CKM}} = \begin{pmatrix} 1-\lambda^2/2 & \lambda & A\lambda^3(\rho - i\eta) \\ -\lambda & 1-\lambda^2/2 & A\lambda^2 \\ A\lambda^3(1-\rho-i\eta) & -A\lambda^2 & 1 \end{pmatrix} + \mathcal{O}(\lambda^4), \qquad (2.1)$$

where $s_{12} = \lambda$, $s_{23} = A\lambda^2$ and $s_{13} = A\lambda^3(\rho + i\eta)$. In this parameterisation, it becomes apparent that to leading order, the non-zero imaginary elements are V_{ub} and V_{td}.

2.4 The Unitarity Triangle and the CKM angle γ

A convenient representation of the size of *CP* violation in the SM is found by using the nine unitarity conditions of V_{CKM}, which can be expressed as $\sum_i V_{ij}V_{ij}^* = \delta_{jk}$. V_{ij} are the components of the CKM matrix. The six conditions with $i \neq k$ can be visualised as closed triangles on the complex plane, all with the same area. It can be shown that the level of *CP* violation is proportional to the area of these triangles [20]. The triangle with $i = 1$ and $k = 3$ is particularly interesting from an experimental point of view,

$$1 + \frac{V_{ud}V_{ub}^*}{V_{cd}V_{cb}^*} + \frac{V_{td}V_{tb}^*}{V_{cd}V_{cb}^*}$$

as all three sides and angles of this triangle are of similar sizes. This particular triangle is known as the Unitarity Triangle (UT) and is shown in Fig. 2.3. Experimentally, by measuring the lengths of the sides and the size of the angles of the UT, one can test the unitarity of the CKM matrix by overconstraining the UT.

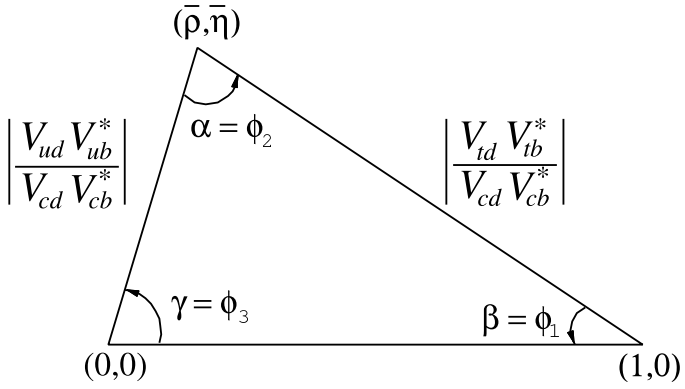

Figure 2.3: The Unitarity Triangle. Source: Particle Data Group [21].

The angle γ, which is also denoted ϕ_3, is the main topic of interest for this thesis. It is defined as

$$\gamma = -\arg\left(\frac{V_{ud}V_{ub}^*}{V_{cd}V_{cb}^*}\right), \tag{2.2}$$

and by comparing Eq. (2.1) and Fig. 2.3, the angle γ is identified as the phase δ_{CP} to order $\mathcal{O}(\lambda^4)$.

In addition to its importance in the understanding of *CP* violation in the SM, measurements of γ are also crucial for precision tests of the SM, which may reveal inconsistencies. In particular, γ is the only angle in the UT which can be measured in processes at tree level. Furthermore, direct measurements of γ do not require external inputs from theory, making it a clean observable with theoretical uncertainties smaller than $\mathcal{O}(10^{-7})$ [22]. Therefore, γ is an ideal standard candle for precision tests of the SM. Currently, the direct measurements have a world average of $\gamma = (65.9^{+3.3}_{-3.5})^\circ)$ [23].

The direct measurements can be compared with indirect measurements, which are obtained by constraining the other angles and sides of the UT. By assuming the unitarity of the CKM matrix, which implies that the UT is a closed triangle, the angle γ may be deduced. Several of these indirect measurements are performed on loop-level processes, which may be sensitive to physics beyond the SM. Thus, by comparing the indirect loop-level measurements of γ with the direct tree-level measurements, new physics effects where the CKM matrix is non-unitary may be revealed.

2.5 Indirect loop-level constraints on γ

Figure 2.4 shows loop-level measurements that are sensitive to γ from Ref. [23]. The most important physics observables are the measurements of the CKM angle β and the measurement of $|V_{td}V_{tb}^*/V_{cd}V_{cb}^*|$, which is the length of the side opposite of the CKM angle γ. It can also be seen in Fig. 2.4 that measurements of neutral kaon mixing-induced *CP*-violation, encoded in the parameter ϵ_K, can to some extent constrain γ at loop level.

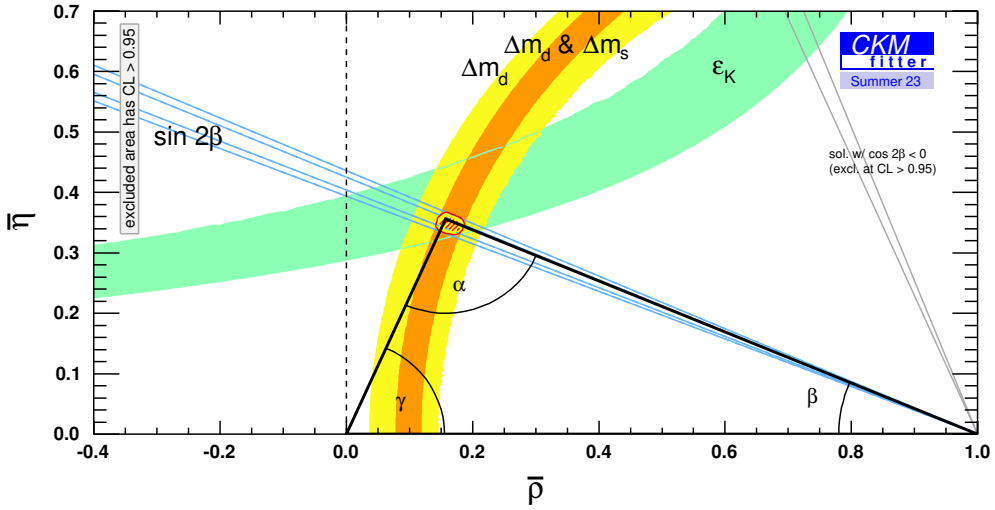

Figure 2.4: Loop level measurements of γ from CKMFitter [23].

Measurements of the angle β can be obtained through the study of time-dependent *CP* violation in neutral B^0 mesons. Recently, LHCb published a world-leading measurement [24] using decays of B^0 and $\overline{B}^0$ mesons to $J/\psi K^0_S$ and $\psi(2S)K^0_S$. Together with the HFLAV average [25], the result is $\beta = (22.5 \pm 0.4)°$, which is the most precisely known CKM angle.

The measurement of the length $|V_{td}V^*_{tb}/V_{cd}V^*_{cb}|$ can be obtained from analyses of B^0-$\bar{B}^0$ [26] and B^0_s-$\bar{B}^0_s$ [27] oscillations. However, while the mixing frequencies Δm_d and Δm_s are known to high precision, the interpretation of these observables in terms of the CKM side length $|V_{td}V^*_{tb}/V_{cd}V^*_{cb}|$ requires external inputs from lattice QCD that are dominated by theoretical uncertainties. Therefore, the combined indirect loop-level measurement of γ, which is $(66.3^{+0.7}_{-1.9})°$ [23], is dominated by theoretical lattice QCD uncertainties. Nevertheless, it is more precise than the direct measurements of γ.

2.6 Direct measurement of γ in $B^{\pm} \to DK^{\pm}$ decays

The golden channel for direct measurements of γ is $B^{\pm} \to DK^{\pm}$, where D can either be a D^0 or a $\overline{D}^0$ meson. The Feynman diagrams of these decays are shown in

Fig. 2.5, where the left diagram shows the favoured $B^- \to D^0 K^-$ decay. The right diagram shows $B^- \to \overline{D}^0 K^-$, which is colour suppressed and also CKM suppressed. The quark transitions of these diagrams are $b \to c\bar{u}s$ and $b \to u\bar{c}s$, respectively. According to Eq. (2.2), the weak-phase difference between these diagrams is exactly the angle γ. To observe interference effects between these diagrams, the D^0 and $\overline{D}^0$ mesons must decay to a common final state. Thus, the CKM angle γ can be measured directly from the interference effects in $B^\pm \to DK^\pm$ decays.

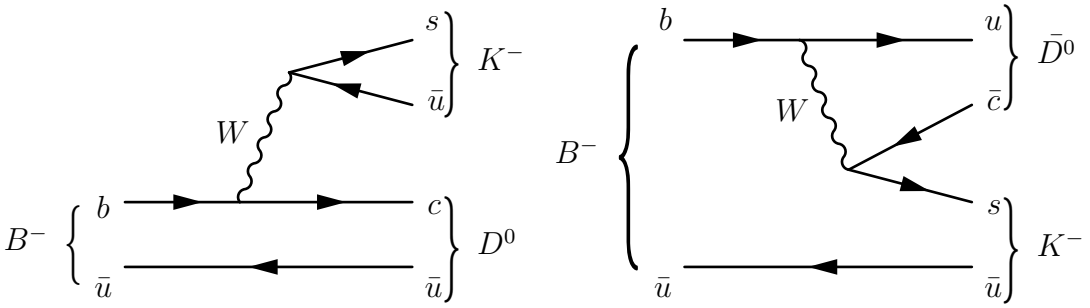

Figure 2.5: Feynman diagrams of $B^- \to DK^-$ decays at tree level.

Quantitatively, the decay amplitude of the B^- decay is a coherent sum of the two amplitudes represented by the diagrams in Fig. 2.5,

$$\mathcal{A}(B^- \to DK^-) = \mathcal{A}(B^- \to D^0 K^-)\Big[\mathcal{A}(D^0) + \mathcal{A}(\overline{D}^0) r_B^{DK} \exp\Big(i(\delta_B^{DK} - \gamma)\Big)\Big], \quad (2.3)$$

where r_B^{DK} is the magnitude of the ratio between the $B^- \to \overline{D}^0 K^-$ and $B^- \to D^0 K^-$ amplitudes and δ_B^{DK} is their strong-phase difference. Since γ is the weak-phase difference, under a *CP* transformation it changes sign, and the corresponding expression for B^+ decays is

$$\mathcal{A}(B^+ \to DK^+) = \mathcal{A}(B^+ \to \overline{D}^0 K^+)\Big[\mathcal{A}(\overline{D}^0) + \mathcal{A}(D^0) r_B^{DK} \exp\Big(i(\delta_B^{DK} + \gamma)\Big)\Big]. \quad (2.4)$$

The prefactors $\mathcal{A}(B^- \to D^0 K^-)$ and $\mathcal{A}(B^+ \to \overline{D}^0 K^+)$ in Eqs. (2.3) and (2.4) are the decay amplitudes when the charm meson decays to a flavour-specific final state, such as $D^0 \to K^- \mu^+ \nu_\mu$. Since these tree-level decays do not exhibit any interference effects, these prefactors must be equal, and effectively they normalise the decay rate. While normalisation factors are treated as free parameters, they are not parameters of interest and will be referred to as nuisance parameters in this thesis.

In Eqs. (2.3) and (2.4), the three unknown parameters are γ, δ_B^{DK} and r_B^{DK}. The angle γ is therefore measured together with the parameters δ_B^{DK} and r_B^{DK}, whose values are affected by unknown QCD effects. By treating these as nuisance parameters instead of using external inputs from theory, the measurement of γ becomes theoretically clean. From the CKM matrix elements, and the colour suppression factor of three, it can be estimated that $r_B^{DK} \approx 0.1$, which gives a measure of the size of *CP*-violation effects.

The diagrams of the decays $B^\pm \to D^0\pi^\pm$ and $B^\pm \to \overline{D}^0\pi^\pm$ are analogous to those in Fig. 2.5, but with the s quark replaced by a d quark. These decays have a branching fraction that is 13 times larger than that of the $B^\pm \to DK^\pm$ mode [21], and the identical decay topology make these decays convenient for measuring γ as well, with different nuisance parameters $\delta_B^{D\pi}$ and $r_B^{D\pi}$. However, from CKM matrix elements, it is estimated that $r_B^{D\pi} \approx 0.005$, making the *CP*-violating effects about 20 smaller than those in the $B^\pm \to DK^\pm$ decay. In addition, since the CKM matrix elements of these $B^\pm$ decays differ by a relative minus sign, the asymmetries in the $B^\pm \to D\pi^\pm$ mode are usually opposite in sign to those in $B^\pm \to DK^\pm$.

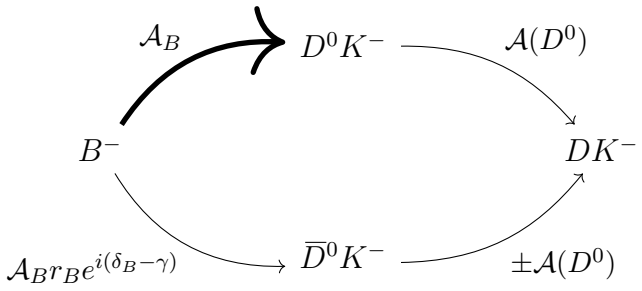

Figure 2.6: Visualisation of the two decay paths in a $B^- \to DK^-$ decay, with D decaying into a *CP*-eigenstate. The amplitude $\mathcal{A}_B$ is shorthand for the favoured $B^- \to D^0K^-$ decay.

The amplitudes of the charm meson decay, $\mathcal{A}(D^0)$ and $\mathcal{A}(\overline{D}^0)$, take different relative values depending on the type of D decay considered. In a strategy proposed in Refs. [28, 29], which will be referred to as the GLW method, D meson decays to *CP* eigenstates are considered. A visualisation of the two decay paths is shown in Fig. 2.6, where the relative thickness of the arrows indicate the relative sizes of each amplitude.

Important *CP*-even D decays are $D \to K^+K^-$ and $D \to \pi^+\pi^-$, while $D \to K^0_S\pi^0$ is an important *CP*-odd decay. The amplitudes in such decays are related by $\mathcal{A}(D^0) = \pm\mathcal{A}(\overline{D}^0)$, where the positive (negative) sign applies to *CP*-even (odd) eigenstates. With these simplifications, the $B^\pm$ decay rates can be calculated from Eqs. (2.3) and (2.4) to be

$$\Gamma(B^\mp \to DK^\mp) = h\Big[1 + \left(r_B^{DK}\right)^2 \pm 2r_B^{DK}\cos\left(\delta_B^{DK} \mp \gamma\right)\Big], \tag{2.5}$$

where the normalisation constant $h = \Gamma(B^- \to D^0K^-)\Gamma(D^0)$ is the decay rate of the favoured decay path. The third term, which represents the interference effects, is different between B^- and B^+ and is therefore responsible for *CP*-violation effects when both the strong- and weak-phase differences are non-zero.

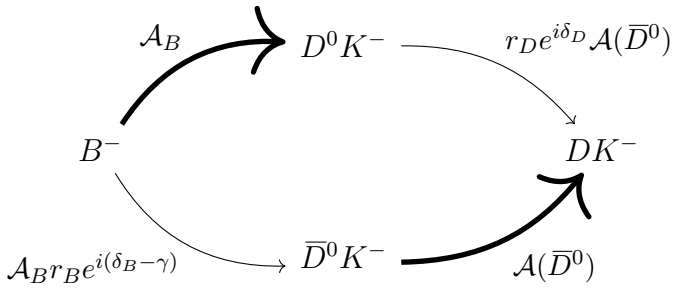

Figure 2.7: Visualisation of the two decay paths in a OS $B^- \to DK^-$ decay. The amplitude $\mathcal{A}_B$ is shorthand for the favoured $B^- \to D^0K^-$ decay.

In the second method for determining γ, which is known as the ADS method [30], D decays to final states with a net strangeness are studied. These final states, such as the Cabibbo-Favoured (CF) decay $D^0 \to K^-\pi^+$ are very powerful due to the existence of a corresponding Doubly Cabibbo-Suppressed (DCS) decay $D^0 \to K^+\pi^-$. By parameterising the suppression as $\mathcal{A}(D^0 \to K^+\pi^-) = r_D^{K\pi}e^{-i\delta_D^{K\pi}}\mathcal{A}(\overline{D}^0 \to K^+\pi^-)$, the decay rates of the $B^\pm$ decays are

$$\Gamma(B^\mp \to DK^\mp) = h\Big[\left(r_D^{K\pi}\right)^2 + \left(r_B^{DK}\right)^2 + 2r_B^{DK}r_D^{K\pi}\cos\left(\delta_B^{DK} + \delta_D^{K\pi} \mp \gamma\right)\Big]. \tag{2.6}$$

The parameter $\delta_D^{K\pi}$ is the strong-phase difference between the CF and DCS charm-decay amplitudes. Note that for these decays, the favoured $B^\pm$ decay is followed by a DCS D decay, while the suppressed $B^\pm$ decay has a subsequent CF D decay.

Thus, as illustrated in Fig. 2.7, the two decay paths are similar in magnitude, and the relative interference effects are expected to be large. These "ADS" decays are also known as Opposite Sign (OS) decays, as the kaon from the $B^{\pm}$ decay has the opposite sign to that of the D decay. This is different from Same Sign (SS) decays, where the favoured (suppressed) $B^{\pm}$ decay is further enhanced (suppressed) by a CF (DCS) charm decay. The interference effects are therefore very small,

$$\Gamma(B^{\mp} \to DK^{\mp}) = h\Big[1 + \left(r_B^{DK} r_D^{K\pi}\right)^2 + 2r_B^{DK} r_D^{K\pi} \cos\left(\delta_B^{DK} - \delta_D^{K\pi} \mp \gamma\right)\Big], \quad (2.7)$$

making such decays convenient for the normalisation of observed yields.

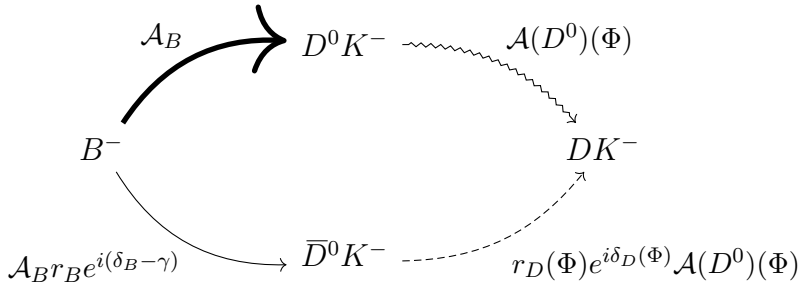

Figure 2.8: Visualisation of the two decay paths in a SCMB $B^- \to DK^-$ decay. The amplitude $\mathcal{A}_B$ is shorthand for the favoured $B^- \to D^0K^-$ decay.

A third class of charm decays that are powerful for determining γ are self-conjugate multi-body (SCMB) decays. Such decays can proceed through intermediate resonances, which are localised in a multi-dimensional phase space. Generally, the D^0 and $\overline{D}^0$ decay amplitudes to a phase-space location Φ will be different, as illustrated by the different arrow patterns in Fig. 2.8. The differential decay rate over some small region of phase space $\mathrm{d}\Phi$ is

$$\begin{aligned}\Gamma(B^{\mp} \to DK^{\mp})(\Phi) = h\Big[&|\mathcal{A}(D^0)(\Phi)|^2 + \left(r_B^{DK}\right)^2 |\mathcal{A}(\overline{D}^0)(\Phi)|^2 \\ &+2r_B^{DK}|\mathcal{A}(D^0)(\Phi)||\mathcal{A}(\overline{D}^0)(\Phi)| \cos\left(\delta_B^{DK} - \delta_D(\Phi) \mp \gamma\right)\Big],\end{aligned} \quad (2.8)$$

where the charm hadronic parameters r_D and δ_D are now functions of Φ. The total decay rate is found by integrating Eq. (2.8) over $\mathrm{d}\Phi$.

The parameter $\delta_D(\Phi)$ is the strong-phase difference between the decays of D^0 and $\overline{D}^0$ at the phase-space position Φ. Note in particular that external

knowledge of δ_D and its dependence on phase space Φ is desirable in order to achieve competitive sensitivity to γ. In Section 2.7, three different methods on how to treat r_D and δ_D will be discussed.

2.7 Methods for measuring γ in self-conjugate multi-body charm decays

In this thesis, the focus will be on measuring the CKM angle γ for the first time using the four-body SCMB decays $D^0 \to K^+K^-\pi^+\pi^-$ and $D^0 \to \pi^+\pi^-\pi^+\pi^-$, commonly denoted $D^0 \to h^+h^-\pi^+\pi^-$. Such a measurement, known as the BPGGSZ method [31–34], can be performed using an amplitude model to predict δ_D at every phase-space location, and this approach is described in Section 2.7.1. However, this thesis aims to achieve a model-independent measurement by directly measuring the strong-phase difference δ_D. Sections 2.7.2 and 2.7.3 outline the ideas and strategies for this model-independent determination. While the descriptions target the four-body $D^0 \to h^+h^-\pi^+\pi^-$ decays, the techniques listed are applicable to any SCMB decay.

2.7.1 Model-dependent determination of γ

In a model-dependent determination of γ, an amplitude model is used to predict $\mathcal{A}(D^0)$ at each phase-space point Φ. This allows for an unbinned likelihood function to be constructed from a data set of $B^\pm \to DK^\pm$ decays using Eq. (2.8). With an unbinned maximum likelihood fit, the best possible statistical sensitivity to γ is achieved.

An amplitude model is conventionally expressed using the isobar formalism, where the amplitudes of intermediate resonances are considered in a coherent sum,

$$\mathcal{A}(\Phi) = \sum_k a_k e^{i\phi_k} \mathcal{F}_k(\Phi), \tag{2.9}$$

with real parameters a_k and φ_k describing the magnitude and relative phase of each resonance. The functions $\mathcal{F}_k$ are lineshapes, such as Breit-Wigner functions,

describing the resonances. To determine the parameters a_k and φ_k, the model is fitted to a sample of flavour-tagged D^0 decays.

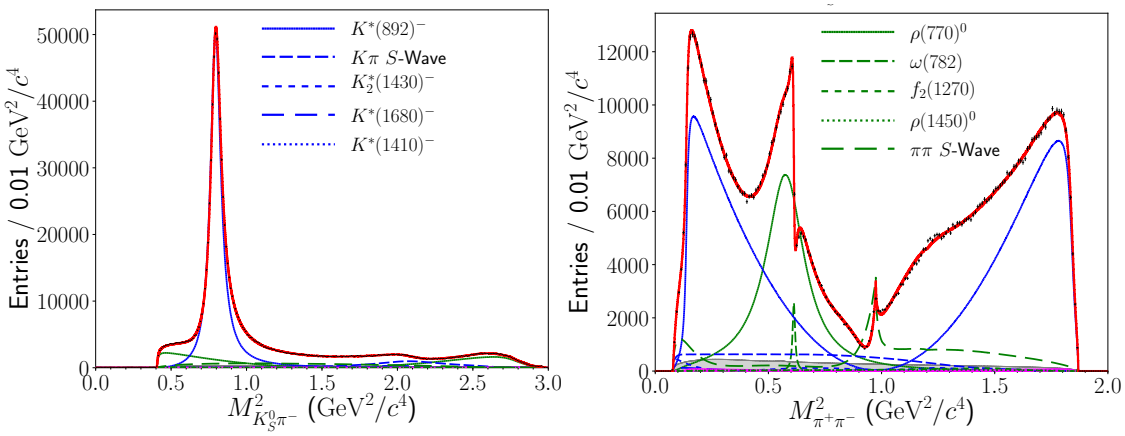

Figure 2.9: The (left) $K^0_S\pi^-$ and (right) $\pi^+\pi^-$ invariant-mass spectra of $D^0 \to K^0_S\pi^+\pi^-$, with the projections of different components from the Belle 2018 amplitude model [35] shown in coloured curves. The data are shown as black data points.

Isobar models, constructed using Eq. (2.9), in general provide an accurate prediction of the phase-space distributions. This is shown for the $D^0 \to K^0_S\pi^+\pi^-$ decay in Fig. 2.9, where a clear $K^{*-} \to K^0_S\pi^-$ resonance is seen on the left, but on the right several other resonances are also well described, such as the $\rho^0 \to \pi^+\pi^-$ and $\omega \to \pi^+\pi^-$ resonances.

However, it should be emphasised that isobar models are only effective at predicting invariant-mass distributions, which depend on the modulus squared of Eq. (2.9), but the amplitude model has no direct information about the strong-phase difference. For this reason, it is extremely challenging to evaluate a reliable systematic uncertainty due to the model dependence, and the wrong choice of model can potentially bias the measurement of γ. Thus, while the model-dependent method for determining γ using Eq. (2.8) directly in an unbinned fit results in the maximal sensitivity, such a method is not reliable as it can have systematic biases that are impossible to assess.

2.7.2 Phase-space binned analysis of four-body charm decays

A strategy for obtaining a model-independent measurement of γ, with minimal degradation of the statistical sensitivity, is to extract information about the strong-phase difference in the charm system using charm-threshold data. These data are readily available from e^+e^- charm factories and the information can be used as external inputs in the study of $B^\pm \to DK^\pm$ data. The procedure for performing these strong-phase measurements will be outlined in Section 2.8.

Unfortunately, without a model, the functional form of $\delta_D(\Phi)$ is unknown, and it would require a very large sample of charm-threshold data to determine the value of δ_D at every single phase-space location. A more practical approach is to divide the phase space Φ into $\mathcal{N}$ discrete regions, which are labelled with bin indices $i = 1, 2, ..., \mathcal{N}$, and the average strong-phase differences are determined separately for each bin.

In addition, since *CP* violation in the charm system is known to be much smaller than that in the $B^\pm \to DK^\pm$ decay, it may be assumed that *CP* is conserved in the D decay. In Ref. [36], a potential bias of $(-2.7 \pm 3.2)^\circ$ in γ was determined, due to *CP*-violation effects in the $D^0 \to K^0_S\pi^+\pi^-$ decay. The study used measurements of *CP* violation in this mode from the CDF collaboration [37]. However, the three-body decay $D^0 \to K^0_S\pi^+\pi^-$ is dominated by CF amplitudes, which are less affected by direct *CP* violation. Any presence of *CP*-violation effects are therefore expected to have a larger effect on γ measurements in four-body $D^0 \to h^+h^-\pi^+\pi^-$ decays, which are Singly-Cabibbo Suppressed (SCS) decays. Nevertheless, the constraints on *CP*-violation parameters have been measured with much greater precision by the LHCb collaboration [38], and these effects on γ are considered to be outside the scope of this thesis.

Under *CP* conservation, for every D^0 decay at Φ with strong-phase difference δ_D, there must exist a corresponding *CP*-conjugated decay at the phase-space conjugated location $\bar{\Phi}$ with strong-phase difference $-\delta_D$. Kinematically, $\bar{\Phi}$ is obtained from Φ by swapping particle charges and reversing their momenta.

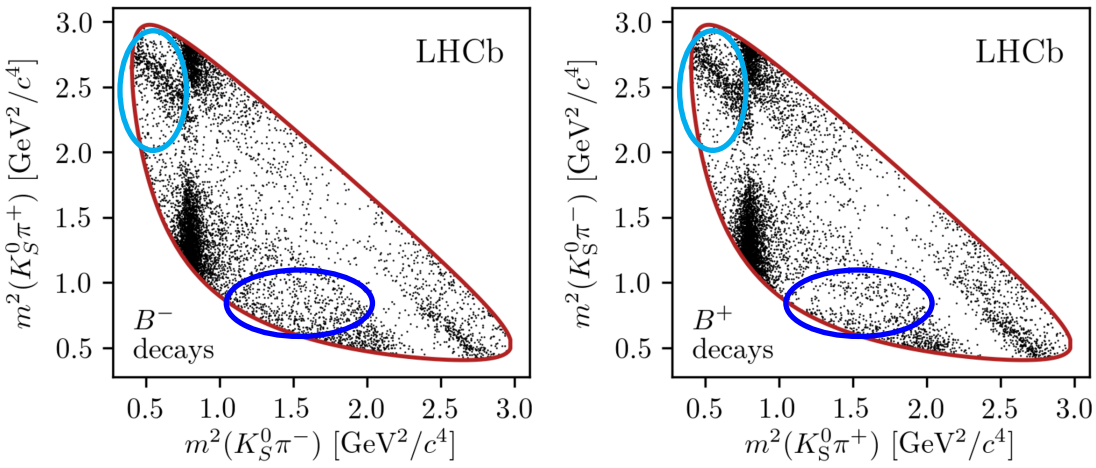

Figure 2.10: The Dalitz space of $B^\pm \to DK^\pm$, with $D \to K^0_S\pi^+\pi^-$. The B^- decays are shown on the left and B^+ decays are on the right. The figure is taken from Ref. [39].

Effectively, *CP* symmetry constrains the strong-phase difference in one half of phase space to its *CP* conjugate. This can be exploited by splitting bin i into two bins $\pm i$ which are related by a *CP* transformation, making a total of $2\mathcal{N}$ bins labelled $i = \pm 1, \pm 2, ..., \pm\mathcal{N}$. The exact choice of an optimised binning scheme for the $D^0 \to K^+K^-\pi^+\pi^-$ decay is discussed in Chapter 3, while that of the decay $D^0 \to \pi^+\pi^-\pi^+\pi^-$ is obtained from Ref. [40].

The strength of this binned method is that *CP*-violation effects may be large in local phase-space regions, but when averaged over all phase space these effects are diluted. This is caused by the integration of Eq. (2.8) over phase space, and large variations in $\delta_D(\Phi)$ will dilute the size of this interference term. This is illustrated in Fig. 2.10, which shows the Dalitz plots of $D^0 \to K^0_S\pi^+\pi^-$ for the $B^\pm \to DK^\pm$ decays from the analysis presented in Ref. [39]. The prominent resonance along the vertical is a $K^{*-} \to K^0_S\pi^-$ resonance, while that along the diagonal is a $\rho^0 \to \pi^+\pi^-$ resonance.

The blue and cyan ellipses in Fig. 2.10 highlight areas with large asymmetries between B^+ and B^- decays. It is also important to note that there are more B^- decays than B^+ decays in the blue ellipse, while for the cyan ellipse there are more B^+ decays. The difference in *CP* asymmetries is driven by the difference in the strong-phase difference. Therefore, by carefully picking a binning scheme, large

local *CP*-violation effects may be isolated and thus reduce the dilution effects. More importantly, if a sub-optimal binning scheme is used, only the statistical sensitivity is degraded, but no systematic biases are introduced to the measurement.

The phases of the interference term in Eq. (2.8) can be simplified to

$$\begin{aligned} r_B^{DK}\cos\Big(\delta_B^{DK} - \delta_D(\Phi) \mp \gamma\Big) =& r_B^{DK}\cos\Big(\delta_B^{DK} \mp \gamma\Big)\cos\Big(\delta_D(\Phi)\Big) \\ &+ r_B^{DK}\sin\Big(\delta_B^{DK} \mp \gamma\Big)\sin\Big(\delta_D(\Phi)\Big) \\ =& x_\mp^{DK}\cos\Big(\delta_D(\Phi)\Big) + y_\mp^{DK}\sin\Big(\delta_D(\Phi)\Big), \end{aligned}$$

where the last line defines the Cartesian *CP*-violating observables

$$x_\pm^{DK} \equiv r_B^{DK}\cos\Big(\delta_B^{DK} \pm \gamma\Big), \quad y_\pm^{DK} \equiv r_B^{DK}\sin\Big(\delta_B^{DK} \pm \gamma\Big), \tag{2.10}$$

which contain all information about the physics parameters γ, δ_B^{DK} and r_B^{DK}. The parameterisation in terms of the *CP*-violating observables avoids trigonometric relations and therefore possesses better behaved statistical properties. A geometric illustration of this parameterisation is shown in Fig. 2.11. The wedge angle between the points (x_+, y_+) and (x_-, y_-) is interpreted as 2γ, while the angle between the bisector of this wedge and the horizontal is δ_B.

For the binned measurement, Eq. (2.8) is integrated over each phase-space bin i, which results in a relationship between the bin yield $N_i^\mp$ of $B^\mp$ decays in bin i, and the physics parameters γ, δ_B^{DK} and r_B^{DK},

$$N_i^\mp = h_{DK}^\mp\Big[K_i + \Big(\Big(x_\mp^{DK}\Big)^2 + \Big(y_\mp^{DK}\Big)^2\Big)K_{-i} + 2\sqrt{K_i K_{-i}}\Big(x_\mp^{DK}c_i + y_\mp^{DK}s_i\Big)\Big]. \tag{2.11}$$

The parameter c_i is the amplitude-averaged cosine of the strong-phase differences between D^0 and $\overline{D}^0$ decays in bin i, defined as

$$c_i = \frac{\int_i \mathrm{d}\Phi |\mathcal{A}(D^0)||\mathcal{A}(\overline{D}^0)| \cos\Big(\delta_D(\Phi)\Big)}{\sqrt{\int_i \mathrm{d}\Phi |\mathcal{A}(D^0)|^2 \int_i \mathrm{d}\Phi |\mathcal{A}(\overline{D}^0)|^2}} \tag{2.12}$$

and the expression for sine of the strong-phase difference, s_i, is analogous. The parameters K_i are the fractional yields of D^0 decays in i, in the absence of interference, defined as

$$K_i = \frac{\int_i \mathrm{d}\Phi |\mathcal{A}(D^0)|^2}{\int \mathrm{d}\Phi |\mathcal{A}(D^0)|^2}, \tag{2.13}$$

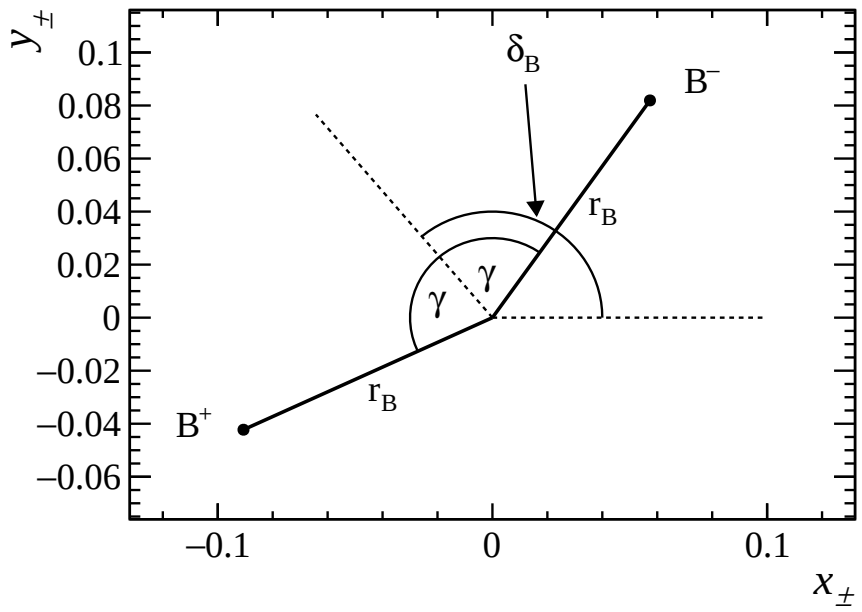

Figure 2.11: A geometric visualisation of the Cartesian parameterisation $x_\pm$ and $y_\pm$, in terms of the physics parameters γ, δ_B and r_B.

which by definition is normalised such that $\sum_i K_i = 1$. The corresponding fractional $\overline{D}^0$ bin yields, denoted by $\bar{K}_i$, are defined analogously, but by *CP* conservation they satisfy the relations $\bar{K}_i = K_{-i}$. Similarly, the strong-phase parameters can be shown to obey $c_i = c_{-i}$ and $s_i = -s_{-i}$ by *CP* conservation.

While Eq. (2.11) in its current form can in theory be used for determining γ from a sample of $B^\pm \to DK^\pm$ decays, there are several experimental considerations that alter its form. First, it should be noted that the normalisation constants $h^\pm_{DK}$ are now split by charge, unlike Eqs. (2.5)-(2.7), where it is necessary to have a common normalisation in order to measure a difference in the global B^- and B^+ decay rate. The separation of $h^\pm_{DK}$ by charge has the effect of removing any dependence on detection asymmetries between positively and negatively charged particles. The production asymmetry between B^- and B^+ mesons may also be absorbed into the separate $h^\pm_{DK}$ parameters. Additionally, any dependence on the global *CP*-violation effects is removed, and the measurement is therefore only sensitive to relative *CP*-violation effects in local regions.

The detection asymmetries arise because the nuclear-interaction cross sections

differ between positively and negatively charged hadrons. This is particularly significant for kaons, since s and $\overline{s}$ quarks interact differently with the detector material. The size of this effect is around 1% for kaons [41]. The detection asymmetry is expected to be smaller, but non-zero, for pions.

Although the LHC is a pp collider that produces an equal number of b and $\overline{b}$ quarks through the strong interaction, the subsequent hadronisation is different between B^- and B^+ mesons [42]. This phenomenon is understood by studying the hadronisation process in the presence of other quarks, which at the LHC are the valence quarks that do not participate in the hard pp interaction. Thus, since the valence quarks influence the hadronisation of b and $\overline{b}$ quarks differently, a non-negligible production asymmetry between B^- and B^+ is induced.

The second experimental consideration is the treatment of the fractional bin yields K_i, which must be corrected for the non-uniform detector acceptance across phase space. A modified set of fractional bin yields F_i can be defined as

$$F_i = \frac{\int_i \mathrm{d}\Phi \eta(\Phi)|\mathcal{A}(D^0)|^2}{\int \mathrm{d}\Phi |\mathcal{A}(D^0)|^2}, \tag{2.14}$$

where $\eta(\Phi)$ is the phase-space acceptance due to detector effects. Equation. (2.11) must therefore be modified into

$$N_i^{\mp} = h_{DK}^{\mp}\Big[F_i + \Big(\big(x_{\mp}^{DK}\big)^2 + \big(y_{\mp}^{DK}\big)^2\Big)F_{-i} + 2\sqrt{F_i F_{-i}}\big(x_{\mp}^{DK}c_i + y_{\mp}^{DK}s_i\big)\Big]. \tag{2.15}$$

By allowing the F_i to be free parameters, the detector effects may therefore be absorbed into these parameters, which eliminates the need for any efficiency corrections to observed bin yields. The necessity of this correction is demonstrated by Fig. 2.12, which shows a comparison between LHCb simulation samples of $B^{\pm} \to DK^{\pm}$ decays with $D \to K^+K^-\pi^+\pi^-$, and the corresponding simulation generated in AmpGen without detector effects. Several of the reconstructed invariant-mass distributions are sculpted by detector effects, which has a direct impact on the F_i values. Furthermore, small effects such as D^0-$\overline{D}^0$ mixing and bin migration can also be absorbed into the F_i parameters to first order. In total there

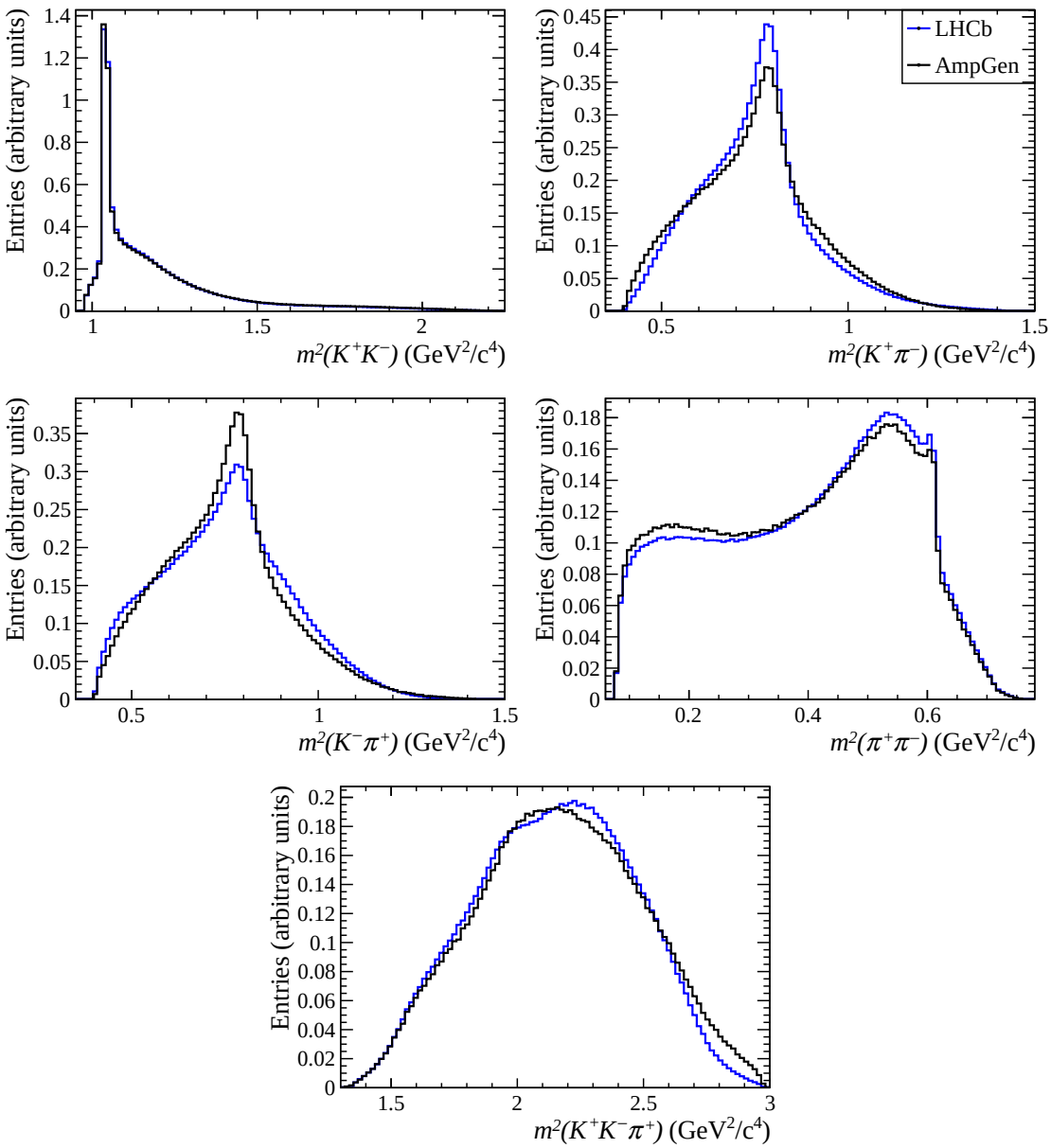

Figure 2.12: A comparison of five independent invariant-mass distributions of the $D^0 \to K^+K^-\pi^+\pi^-$ decay between the LHCb simulation samples and samples generated in AmpGen without detector effects.

are $2\mathcal{N}$ such parameters that must be determined, but the constraint $\sum_i F_i = 1$ reduces this to $2\mathcal{N} - 1$ independent parameters.

Third, for the mode $B^\pm \to D\pi^\pm$, the bin yields will obey an equation almost identical to Eq. (2.11), but with all DK superscripts replaced by $D\pi$. Since these decay modes have an identical topology with a common D decay, any phase-space acceptance or other detector effects $\eta(\Phi)$ are expected to be similar between these

modes. This is demonstrated in Fig. 2.13, where a comparison of five independent invariant-mass distributions of the $D^0 \to K^+K^-\pi^+\pi^-$ decay from LHCb simulation is shown, and it is found that these distributions are nearly identical between $B^\pm \to DK^\pm$ and $B^\pm \to D\pi^\pm$.

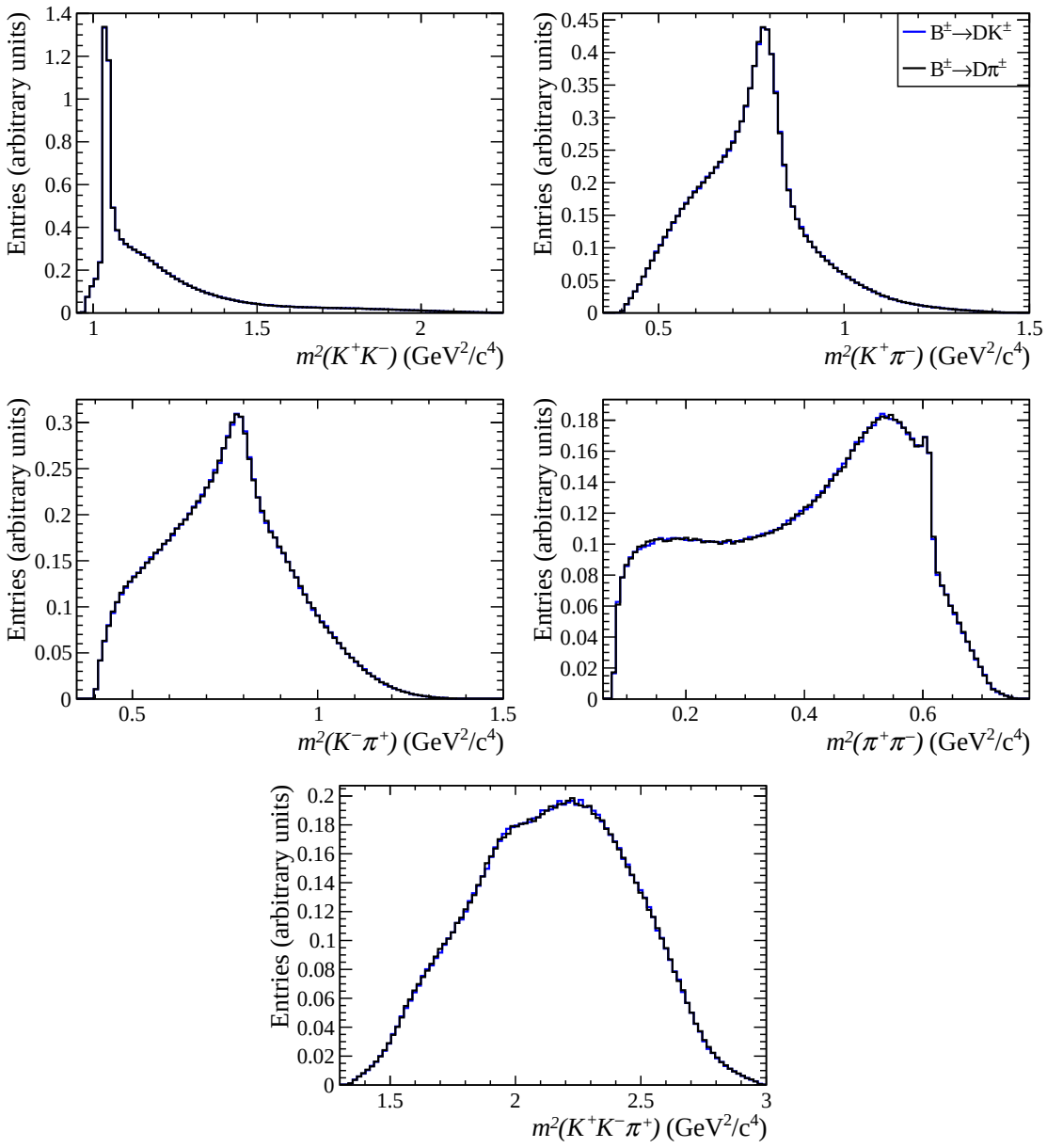

Figure 2.13: A comparison of five independent invariant-mass distributions of the $D^0 \to K^+K^-\pi^+\pi^-$ decay between $B^\pm \to DK^\pm$ and $B^\pm \to D\pi^\pm$, obtained from LHCb simulation samples.

The similarity in the kinematics of these decays therefore allows them to share the same D hadronic parameters F_i, c_i and s_i in Eq. (2.11). This is crucial for

the measurements of F_i, which are mostly constrained by $B^\pm \to D\pi^\pm$ since its branching fraction is 13 times larger than that of $B^\pm \to DK^\pm$ [21]. The sensitivity to c_i and s_i from $B^\pm \to Dh^\pm$ decays is limited, and therefore these are almost entirely constrained by charm-threshold inputs.

Unfortunately, as there are eight *CP*-violating observables $x_\pm^{DK}$, $y_\pm^{DK}$, $x_\pm^{D\pi}$ and $y_\pm^{D\pi}$, but only five physics parameters γ, δ_B^{DK}, r_B^{DK}, $\delta_B^{D\pi}$ and $r_B^{D\pi}$, such a parameterisation can lead to highly unstable fits. To reduce the degeneracy in the Cartesian *CP*-violating observables, alternative *CP*-violating observables for the $B^\pm \to D\pi^\pm$ decay are defined as

$$x_\xi^{D\pi} \equiv \Re(\xi^{D\pi}), \quad y_\xi^{D\pi} \equiv \Im(\xi^{D\pi}), \quad \xi^{D\pi} \equiv \frac{r_B^{D\pi}}{r_B^{DK}} \exp\left[i(\delta_B^{D\pi} - \delta_B^{DK})\right], \tag{2.16}$$

which can be expressed in terms of $x_\pm^{D\pi}$ and $y_\pm^{D\pi}$ using

$$\begin{aligned} x_\pm^{D\pi} =& x_\xi^{D\pi} x_\pm^{DK} - y_\xi^{D\pi} y_\pm^{DK}, \\ y_\pm^{D\pi} =& x_\xi^{D\pi} y_\pm^{DK} - y_\xi^{D\pi} x_\pm^{DK}. \end{aligned}$$

This parameterisation reduces the number of *CP*-violating observables to six independent parameters $x_\pm^{DK}$, $y_\pm^{DK}$, $x_\xi^{D\pi}$ and $y_\xi^{D\pi}$. The $x_\xi^{D\pi}$ and $y_\xi^{D\pi}$ observables also do not have a direct dependence on γ, which is advantageous since the $B^\pm \to D\pi^\pm$ decay has limited sensitivity to γ.

In summary, Eq. (2.15) is the key relationship between the observed $B^\pm \to DK^\pm$ yields in phase-space bins, and the *CP*-violating observables $x_\pm^{DK}$ and $y_\pm^{DK}$, the fractional bin yields F_i, the normalisations $h_{DK}^\pm$ and the strong-phase parameters c_i and s_i. Additionally, the $B^\pm \to D\pi$ decay will also have a set of equations, with the DK labels replaced with $D\pi$ and the *CP*-violating observables expressed in terms of $x_\xi^{D\pi}$ and $y_\xi^{D\pi}$.

In total, Eq. (2.15) provides each phase-space bin with four independent equations, making a total of $8\mathcal{N}$ independent equations. These equations are used to determine the six *CP*-violating observables, $2\mathcal{N}-1$ fractional bin yields and four normalisation parameters, which form a set of $2\mathcal{N}+9$ unknown parameters. For a unique solution, it is required that $8\mathcal{N} \geq 2\mathcal{N}+9$, which is true if $\mathcal{N} \geq 2$.

2.7.3 Phase-space integrated analysis of four-body charm decays

In Section 2.7.2, the normalisation constants $h_{DK}^{\pm}$ are kept independent between B^- and B^+ decays, which ensures that the binned BPGGSZ measurement is unaffected by production and detector asymmetries. However, in fully charged four-body charm decays, model-independent strong-phase studies have shown that these decays are predominantly *CP*-even [43, 44], and useful constraints on γ may be extracted from the global *CP*-violating effects. Such a measurement will be referred to as a phase-space integrated measurement, as the analysis considers the total $B^{\pm} \to Dh^{\pm}$ yield over the whole phase space. When Eq. (2.11) is summed over all bins, the integrated yield becomes

$$N^{\mp} = h\Big[1 + \left(r_B^{DK}\right)^2 + 2(2F_+ - 1)\cos\left(\delta_B^{DK} \mp \gamma\right)\Big], \tag{2.17}$$

where

$$2F_+ - 1 \equiv \sum_i \sqrt{K_i K_{-i}}\, c_i$$

can be considered to be the cosine of the strong-phase difference, amplitude-averaged over all of phase space. The parameter F_+ is to be identified as the *CP*-even fraction. Equation (2.17) is to be compared with Eq. (2.5), and the two expressions are found to be identical in the case of a *CP*-even (*CP*-odd) decay, where $F_+ = 1$ ($F_+ = 0$). The phase-space integrated method is therefore also known as the quasi-GLW method [45].

In general, as the multi-body decay can proceed via both *CP*-even and *CP*-odd intermediate states, its *CP* content will be a mixture that dilutes the sensitivity to γ, with $2F_+ - 1$ as the dilution factor. This was initially appreciated by Ref. [45], where the channel $D^0 \to \pi^+\pi^-\pi^0$ was identified as a promising decay mode for improving the precision on γ. The *CP*-even fraction of this decay has been measured to be $F_+ = 0.973 \pm 0.017$ [46], showing that this is an almost pure *CP*-even decay.

Experimentally, from the four phase-space integrated yields $N^{\pm}$ of $B^{\pm} \to DK^{\pm}$ and $B^{\pm} \to D\pi^{\pm}$, the *CP* asymmetry is determined,

$$\mathcal{A}_h \equiv \frac{\Gamma(B^- \to Dh^-) - \Gamma(B^+ \to Dh^+)}{\Gamma(B^- \to Dh^-) + \Gamma(B^+ \to Dh^+)}, \tag{2.18}$$

for $h = \pi$ or K, and also the double ratio between the $B^{\pm} \to DK^{\pm}$ and $B^{\pm} \to D\pi^{\pm}$ yield,

$$\mathcal{R}_{CP} \equiv \frac{\mathcal{R}_{hh\pi\pi}}{\mathcal{R}_{K\pi\pi\pi}}, \quad \mathcal{R}_f \equiv \frac{\Gamma(B^- \to [f]_D K^-) + \Gamma(B^+ \to [f]_D K^+)}{\Gamma(B^- \to [f]_D \pi^-) + \Gamma(B^+ \to [f]_D \pi^+)}. \tag{2.19}$$

The double ratio $\mathcal{R}_{\mathcal{CP}}$ is normalised by the corresponding ratio of the SS four-body decay $D^0 \to K^-\pi^+\pi^-\pi^+$, which is obtained from Ref. [47]. By construction, the three *CP*-violating observables $\mathcal{A}_K$, $\mathcal{A}_\pi$ and $\mathcal{R}_{CP}$ are independent of efficiency corrections.

From Eq. (2.17), it can be shown that the relationship between the *CP*-violating observables and the physics parameters is

$$A_h = \frac{2r_B^{Dh}(2F_+ - 1)\sin(\delta_B^{Dh})\sin(\gamma)}{1 + (r_B^{Dh})^2 + 2r_B^{Dh}(2F_+ - 1)\cos(\delta_B^{Dh})\cos(\gamma)}, \tag{2.20}$$

$$\mathcal{R}_{CP} = 1 + (r_B^{DK})^2 + 2r_B^{DK}(2F_+ - 1)\cos(\delta_B^{DK})\cos(\gamma), \tag{2.21}$$

where terms containing $r_B^{D\pi}$ have been left out in the expression for $\mathcal{R}_{CP}$, and corrections from D^0-$\overline{D}^0$ mixing are also omitted from both equations. However, such effects are readily included, using the formalism developed in Ref. [48].

Equations (2.20) and (2.21) have a four-fold degeneracy due to the invariance under the transformations $(\gamma, \delta_B) \to (\delta_B, \gamma)$ and $(\gamma, \delta_B) \to (\pi - \gamma, \pi - \delta_B)$, and the GLW method can therefore not provide a unique solution for γ. Nevertheless, it can provide interesting constraints that can be combined with the phase-space binned measurement.

2.8 Quantum-correlated $D\bar{D}$ pairs

The model-independent measurement strategy described in Section 2.7.2 and 2.7.3 requires the knowledge of the strong-phase parameters c_i and s_i. Although these can in principle be determined using $B^{\pm} \to Dh^{\pm}$ decays, in order to obtain a precise determination of γ, it is desirable to measure these parameters directly at a charm factory. Section 2.8.1 describes the theoretical description of quantum-correlated $D\overline{D}$ pairs, and in Section 2.8.2 these ideas are applied to three categories of decay modes to determine c_i and s_i in a model-independent manner.

2.8.1 Double-tag analysis in phase-space bins

At charm factories, the $\psi(3770)$ charmonium state is produced at threshold in e^+e^- collisions. The $\psi(3770)$ meson, which has a charge-conjugation eigenvalue $C = -1$, decays into a $D\overline{D}$ pair in a strong interaction that conserves the C quantum number. Since no additional particles are produced at threshold, the $D\overline{D}$ pair is in an entangled state, with charge-conjugation eigenvalue $C = -1$. Its wavefunction is therefore antisymmetric,

$$|\psi\rangle = \frac{1}{\sqrt{2}}\Big(|D^0\rangle|\overline{D}^0\rangle - |\overline{D}^0\rangle|D^0\rangle\Big),$$

and in the subsequent decays, there is a direct correlation between the two D mesons. Such a $D\overline{D}$ pair is for this reason referred to as a quantum-correlated $D\overline{D}$ pair.

Experimentally, quantum-correlation effects can be observed as a suppression or enhancement of decay rates, and these effects depend on the CP content of the D-decay final states. The left plot in Fig. 2.14 shows an example of such a correlation effect, where the branching fraction of $D \to K^-\pi^+$ is enhanced when it is reconstructed together with a CP-even final state, but it is suppressed when the other D decay is CP-odd. In the right plot, a similar effect is seen in the $D \to K^+K^-\pi^+\pi^-$ decay, but here it is the events tagged with CP-odd decays that are enhanced.

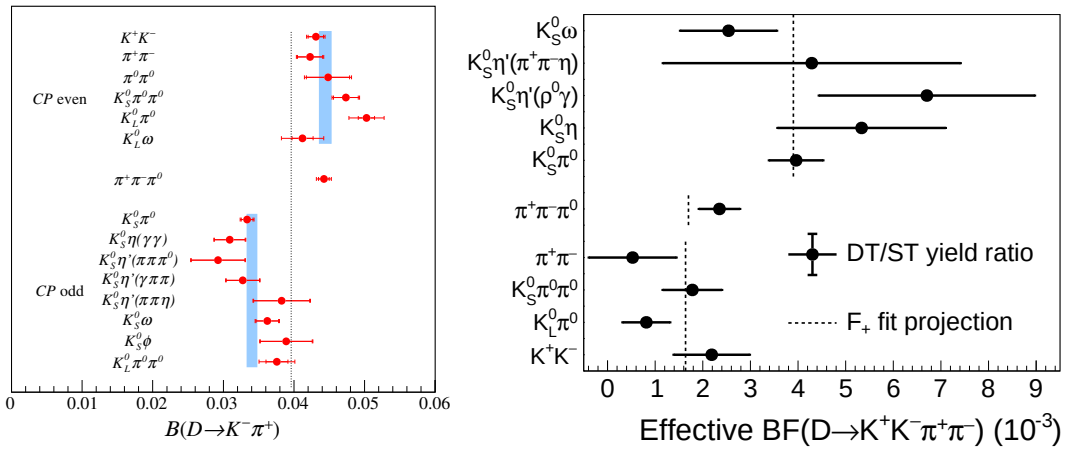

Figure 2.14: An example of quantum correlation effects in the (left) $D \to K^-\pi^+$ [49] and (right) $D \to K^+K^-\pi^+\pi^-$ [43] decays. The horizontal axis shows the branching fraction, which can be suppressed or enhanced when tagged with CP-even and CP-odd decays.

The D-decay modes are not necessarily limited to pure CP-even or CP-odd decay modes, although the asymmetry effects in such decays are easiest to compare and visualise. In principle any decay with known strong-phase information provides useful constraints on strong-phase parameters. Furthermore, the analysis shown on the right in Fig. 2.14 is integrated over phase space, so the asymmetry effects may be diluted. Generally, both D decays can be considered in phase-space bins, which enhances the local asymmetry effects.

Therefore, to set up a generalised formalism for the analysis of strong-phase parameters, the amplitude of both D decays need to be considered. If the first D meson decays into a final state f, in the phase space bin labelled by i, while the second D meson decays into g in a phase space bin j, then the combined decay amplitude is

$$\mathcal{A}(f,g) = \frac{1}{\sqrt{2}}\Big(\mathcal{A}(D^0 \to f)\mathcal{A}(\overline{D}^0 \to g) - \mathcal{A}(\overline{D}^0 \to f)\mathcal{A}(D^0 \to g)\Big),$$

where $\mathcal{A}(D^0 \to f)$ is the amplitude of the $D^0 \to f$ decay, and similarly for $D^0 \to g$. The combined amplitude of the D and $\overline{D}$ meson decays is denoted by $\mathcal{A}(f,g)$ and it is normalised to unity. The amplitude squared becomes

$$\begin{aligned}|\mathcal{A}(f,g)|^2 = \frac{1}{2}\Big[&|\mathcal{A}(D^0 \to f)|^2|\mathcal{A}(\overline{D}^0 \to g)|^2 \\ &+|\mathcal{A}(\overline{D}^0 \to f)|^2|\mathcal{A}(D^0 \to g)|^2 \\ &-2\Re\Big(\mathcal{A}(D^0 \to f)\mathcal{A}^*(\overline{D}^0 \to f)\mathcal{A}(\overline{D}^0 \to g)\mathcal{A}^*(D^0 \to g)\Big)\Big].\end{aligned}$$

Analogously to the approach described in Section 2.7.2, the total yield of events where the first D meson decays into bin i and the second D meson decays into bin j is found through integrating over the phase-space bins, resulting in

$$\begin{aligned}M_{ij}(f,g) =& 2\frac{N_{D\bar{D}}}{2}\mathrm{BF}(D^0 \to f)\mathrm{BF}(D^0 \to g) \\ &\times\Big[K_i^f \bar{K}_j^g + \bar{K}_i^f K_j^g - 2\sqrt{K_i^f \bar{K}_i^f K_j^g \bar{K}_j^g}\Big(c_i^f c_j^g + s_i^f s_j^g\Big)\Big].\end{aligned} \tag{2.22}$$

where $M_{ij}(f,g)$ is the double-tag yield of $D \to f$ and $D \to g$ in bins i and j, respectively, the normalisation constant $\mathrm{BF}(D^0 \to f)$ is identified as the branching fraction of $D^0 \to f$ and $N_{D\bar{D}}$ is the number of $D\overline{D}$ pairs produced. The additional

factor of 2 in front is due to combinatorics, since there are two ways for one D meson to decay to f and the other decay to g.

If CP is assumed to be conserved in the charm system, Eq. (2.22) is invariant under the transformation $i \to -i$ and $j \to -j$. Therefore, the bin number of the tag side can be restricted to be strictly positive, $j > 0$, since an event reconstructed in bin $(i, -j)$ will be equivalent to an event in bin $(-i, +j)$. This eliminates the factor 1/2, resulting in the expression

$$\begin{aligned} M_{ij}(f,g) =& 2N_{D\bar{D}}\mathrm{BF}(D^0 \to f)\mathrm{BF}(D^0 \to g) \\ & \times \Big[K_i^f \bar{K}_j^g + \bar{K}_i^f K_j^g - 2\sqrt{K_i^f \bar{K}_i^f K_j^g \bar{K}_j^g}\Big(c_i^f c_j^g + s_i^f s_j^g\Big)\Big]. \end{aligned} \tag{2.23}$$

In this thesis, a strong-phase study is performed using Eq. (2.23), and such an analysis is referred to as a double-tag analysis. Each D-meson decay is known as a tag, or tag mode. In the double-tag analysis, several different tag modes are combined into double-tag events, which are $e^+e^- \to \psi(3770) \to D\overline{D}$ processes where both D mesons are reconstructed. An example is illustrated in Fig. 2.15, which shows an e^+e^- interaction that produces a $\psi(3770)$ that decays into a $D\overline{D}$ pair. The dashed lines connecting the two D mesons indicate that they are quantum correlated. The left meson is reconstructed as a $D \to K^0_S\pi^+\pi^-$ decay, while the remaining four tracks are found to originate from a $D \to K^+K^-\pi^+\pi^-$ decay.

The analysis performed in this thesis will be restricted to double-tag events where one of the D mesons is always reconstructed in a specific final state, such as $D \to h^+h^-\pi^+\pi^-$, and this tag is referred to as the signal mode. The other D decay is referred to as the tag mode, and different categories of tag modes exhibits different types of quantum-correlation effects with the signal mode $D \to h^+h^-\pi^+\pi^-$.

An important advantage of double-tag analyses is that systematic uncertainties due to efficiencies and unknown branching fractions can be eliminated by normalising Eq. (2.23) by its single-tag yield. The single-tag yield of the decay $D \to g$ is defined as the number of events where one of the D mesons is reconstructed in the $D \to g$ final state, while no requirements are imposed on the other D decay.

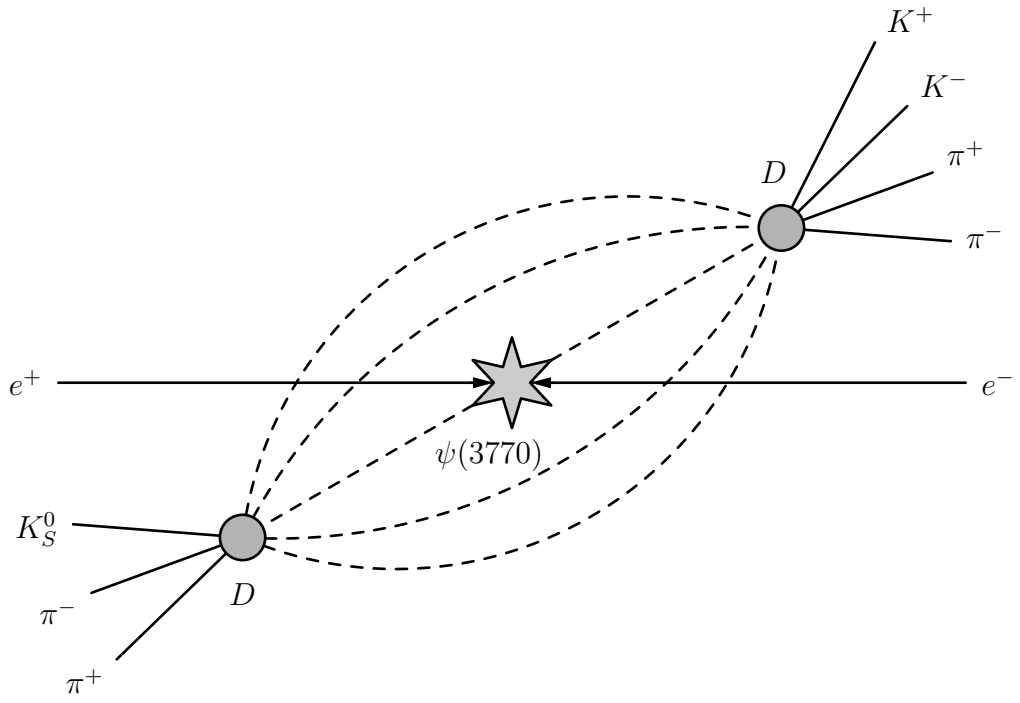

Figure 2.15: An illustration of a double-tag event in a e^+e^- collider, with the dashed lines indicating a quantum-correlated $D\overline{D}$ pair that originate from the $\psi(3770)$ state in the middle. The D-meson on the left decays into the final state $D \to K^0_S\pi^+\pi^-$, while the D-meson on the right decays into $D \to K^+K^-\pi^+\pi^-$.

Specifically, the branching fraction $D^0 \to g$ in Eq. (2.23) is cancelled in the ratio of double- and single-tag yields.

To obtain an expression for the single-tag yield from Eq. (2.23), one sums over all phase space bins of i and j, which results in

$$M(f,g) = 2N_{D\bar{D}}\mathrm{BF}(D^0 \to f)\mathrm{BF}(D^0 \to g)\Big(1 - (2F_+^f - 1)(2F_+^g - 1)\Big).$$

Here, the fact that the sum of all K_i is unity has been exploited, while the terms containing s_i vanish because in the sum over i, s_i and s_{-i} will cancel. The parameters F_+^f and F_+^g are the *CP*-even fractions of the decay $D \to f$ and $D \to g$, respectively.

If *CP* violation is neglected in the D^0 system, D^0 will have an equal probability of decaying into a *CP*-even and *CP*-odd state. Thus, if one considers $D^0 \to f$ for all possible final states f, the sum of $2F_+^f - 1$ over f will vanish. One is left with

$$M(g) = 2N_{D\bar{D}}\mathrm{BF}(D^0 \to g), \tag{2.24}$$

which is, by definition, the single-tag yield of $D^0 \to g$. Note that in deriving this expression, D-$\bar{D}$ mixing has been neglected. In Ref. [40], it is shown that Eq. (2.24) has to be modified to

$$M(g) = 2N_{D\bar{D}}\mathrm{BF}(D^0 \to g)\Big(1 - (2F_+^g - 1)y\Big), \tag{2.25}$$

where $y = (\Gamma_1 - \Gamma_2)/2\Gamma_D$ is a mixing parameter [21].

Together with the single-tag yields, the double-tag yields, Eq. (2.23) can be conveniently expressed as

$$\frac{M_{ij}(hh\pi\pi, g)}{M(g)} = \mathrm{BF}(D^0 \to hh\pi\pi)\Big[K_i\bar{K_j^g} + \bar{K_i}K_j^g - 2\sqrt{K_i\bar{K_i}K_j^g\bar{K_j^g}}\Big(c_ic_j^g + s_is_j^g\Big)\Big], \tag{2.26}$$

where the decay $f = h^+h^-\pi^+\pi^-$ is the signal mode. Similarly, $D \to g$ is denoted as the the tag mode. The superscripts of K_i, c_i and s_i have also been dropped, and unless stated explicitly this will always refer to the decay $D^0 \to h^+h^-\pi^+\pi^-$. In addition, the mixing correction in Eq. (2.25) has also been dropped, but in Eq. (2.26) and all subsequent expressions it is implied that the single-tag yield $M(g)$ is corrected for mixing effects.

2.8.2 Extraction of D^0-$\overline{D}^0$ strong-phase parameters

The tag modes g can in general be split into three categories. In the first category, g is a flavour tag, which is not binned on the tag side. Pure flavour tags, such as $D^0 \to K^-e^+\nu_e$, provide unambiguous information about the flavour of the signal $D \to h^+h^-\pi^+\pi^-$ decay. In this case, $c_j^g = s_j^g = 0$ because $\mathcal{A}(D^0 \to g)$ and $\mathcal{A}(\overline{D}^0 \to g)$ are never non-zero simultaneously. If the $D \to h^+h^-\pi^+\pi^-$ decay is reconstructed in bin i, with a $D \to K^-e^+\nu_e$ on the tag side, then $K_j^g = 1$ and $\bar{K_j}^g = 0$ since the flavour has been tagged as D^0. Eq. (2.23) simplifies to

$$\frac{M_i(hh\pi\pi, g)}{M(g)} = \mathrm{BF}(D^0 \to hh\pi\pi)\bar{K_i}. \tag{2.27}$$

However, there are decays such as $D \to K^-\pi^+$, which are quasi-flavour tags. They are dominated by CF amplitudes, but also contain contamination from the corresponding DCS amplitudes. In this case, the fractional bin yields are $K_j^g = 1$ and

$\bar{K_j^g} = \left(r_D^{K\pi}\right)^2$, while the strong-phase parameters simplify to $c_j^g = R^{K\pi}\cos\left(\delta_D^{K\pi}\right)$ and $s_j^g = R^{K\pi}\sin\left(\delta_D^{K\pi}\right)$. The parameters $r_D^{K\pi}$ and $\delta_D^{K\pi}$ are identical to those used in the ADS method to measure γ. The double-tag yield of flavour tags generalises to

$$\begin{aligned}\frac{M_i(hh\pi\pi, g)}{M(g)} =& \mathrm{BF}(D^0 \to hh\pi\pi) \\ &\times\Big[\bar{K_i} + \left(r_D^{K\pi}\right)^2 K_i - 2r_D^{K\pi}R^{K\pi}\sqrt{K_i\bar{K_i}}\Big(c_i\cos\left(\delta_D^{K\pi}\right) + s_i\sin\left(\delta_D^{K\pi}\right)\Big)\Big].\end{aligned} \tag{2.28}$$

The parameter $R^{K\pi}$, known as the coherence factor, describes the dilution of the strong phase difference across the phase space of the flavour tag decay. For the two-body decay $D \to K^-\pi^+$, $R^{K\pi}$ is equal to unity, but for multi-body decays, such as $D \to K^-\pi^+\pi^0$ and $D \to K^-\pi^+\pi^-\pi^+$, the coherence factors have been measured to be $R^{K\pi\pi^0} = 0.78 \pm 0.04$ and $R^{K\pi\pi\pi} = 0.52^{+0.12}_{-0.10}$ [50].

In the second category, the tag mode is a *CP* eigenstate, or a SCMB state with a known F_+ value. The yield in bin i, after summing Eq. (2.26) over all j, is

$$\frac{M_i(hh\pi\pi, g)}{M(g)} = \mathrm{BF}(D^0 \to hh\pi\pi)\Big[K_i + \bar{K_i} - 2\sqrt{K_i\bar{K_i}}c_i(2F_+^g - 1)\Big], \tag{2.29}$$

which does not have a dependence on s_i.

In the third category of tag modes, one has a SCMB decay that is also binned in phase space, and this is described by Eq. (2.26). SCMB tags therefore provide sensitivity to both c_i and s_i.

In summary, in a strong phase analysis of $D^0 \to h^+h^-\pi^+\pi^-$, Eqs. (2.23),(2.28) and (2.29) describe the relationship between the ratio of the double tag and single tag-yields, and the charm strong-phase parameters c_i, s_i and K_i. The flavour tags are generally CF decays with higher branching fractions and mostly constrain the fractional bin yields K_i. The interference effects in flavour tags are suppressed by $r_D \sim \tan^2(\theta_c)$, and therefore the sensitivity to the strong-phase parameters c_i and s_i is limited. From Eq. (2.29), the *CP* tags are expected to provide important information on the c_i parameters. Similarly, SCMB tags are sensitive to both c_i and s_i, described by Eq. (2.23).

Additionally, since all measured observables are expressed as a ratio of double tag and single-tag yields, the measurement of c_i, s_i and K_i will be independent of efficiencies and branching fractions, to first order. Any systematic uncertainties due to uncertainties in the efficiency from MC or unknown branching fractions are fully contained in the measured branching fraction BF($D^0 \to hh\pi\pi$).

3

Optimised binning scheme for $D^0 \to K^+K^-\pi^+\pi^-$

Contents

The measurement strategy outline in Section 2.7.2 assumed the existence of a binning scheme optimised for sensitivity to the CKM angle γ. In this chapter, the design of such a binning scheme is discussed. Its performance is quantitatively assessed using the maximum-likelihood method, which is a common data analysis technique for estimating model parameters from measurements. The key principles of maximum likelihood fits, which will be used repeatedly throughout this thesis, are explained in Appendix A.

3.1 From amplitude model to binning scheme

3.1.1 An amplitude analysis of $D^0 \to K^+K^-\pi^+\pi^-$

The crucial tool in the construction of a binning scheme for the $D^0 \to K^+K^-\pi^+\pi^-$ decay is a recent amplitude model of this decay, developed by the LHCb collaboration [38]. The amplitude analysis was performed on a sample of b-hadron decays into $D^0\mu^-X$ collected in 2011 and 2012. The charge of the $\mu^\pm$ tags the flavour of the D^0 decay. In total, the sample contained 1.6×10^5 $D^0 \to K^+K^-\pi^+\pi^-$ candidates. This section contains a brief summary of this analysis, while a more detailed description can be found in Ref. [38].

To describe the decay, the isobar model was used, as described in Section 2.7.1. Two main decay topologies are considered. In the first, the D^0 meson can decay to a pair of unstable intermediate states, such as $D^0 \to \phi(1020)\rho$, shown in Fig. 3.1a, which subsequently decay into a pair of charged kaons and pions, respectively. In the second, the D^0 meson can undergo a cascade of excited kaon decays, as shown in Fig. 3.1b where it first decays to $D^0 \to K_1(1400)^+K^-$, with $K_1(1400)^+ \to K^{*0}\pi^+$ and $K^{*0} \to K^+\pi^-$.

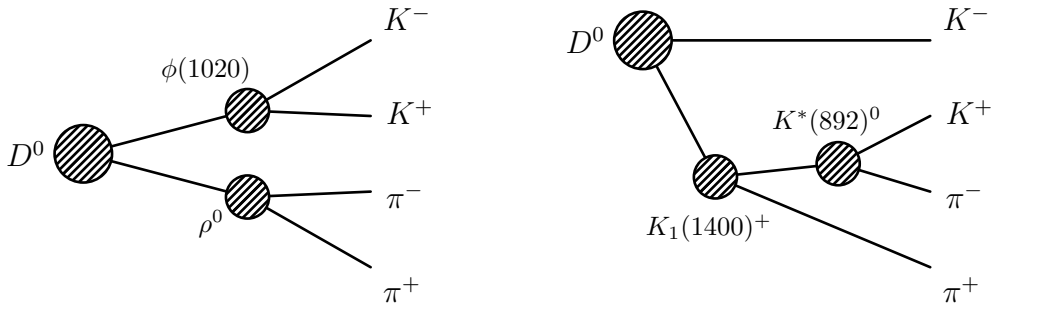

(a) $\phi(1020)(\to K^+K^-)\rho^0(\to \pi^+\pi^-)$ **(b)** $K_1(1400)^+(\to K^*(892)^0(\to K^+\pi^-))K^-$

Figure 3.1: The two decay topologies considered in the amplitude analysis of $D^0 \to K^+K^-\pi^+\pi^-$.

In Table 3.1, the different resonances that are considered and their associated quantum numbers are listed. Most resonances are described by a Relativistic Breit-Wigner lineshape, but resonances that are broad or near a threshold have more complex descriptions. In addition, when resonances have large overlaps the K-matrix formalism is used [51]. This applies to the KK, $\pi\pi$ and $K\pi$ S-wave contributions.

Table 3.1: Resonances considered in the amplitude analysis of $D^0 \to K^+K^-\pi^+\pi^-$ [38].

	KK	$\pi\pi$	$K\pi$	$KK\pi$	$K\pi\pi$
$J^P = 0^+$	$a_0(980)$ $f_0(980)$ $f_0(1370)$	$f_0(980)$ $f_0(1370)$	$K_0^*(1430)$		
$J^P = 1^+$				$a_1(1260)$	$K_1(1270)$ $K_1(1400)$
$J^P = 1^-$	$\phi(1020)$	$\rho(770)$ $\omega(782)$ $\rho(1450)$	$K^*(892)$ $K^*(1680)$		$K^*(1410)$ $K^*(1680)$
$J^P = 2^+$	$f_2(1270)$ $a_2(1320)$	$f_2(1270)$	$K_2^*(1430)$		$K_2^*(1430)$

To build the amplitude model, an iterative procedure is used. In each iteration, an unbinned likelihood function $\mathcal{L}$ is constructed following the procedure described in Section A.1, and minimised with respect to the magnitude a_k and phase φ_k of each component. The resonance that produces the largest decrease in $\mathcal{L}$ is then added. This is repeated until the total fit fraction starts diverging, which is caused by many overlapping resonances. The four largest components and their parameters a_k and φ_k are listed in Table 3.2, while the full model with 26 components can be found in Ref. [38].

To implement and fit the the amplitude model of $D^0 \to K^+K^-\pi^+\pi^-$, the AmpGen framework [52] was used. It is a library for fitting and generating multi-body decays, designed specifically for models with very complex amplitudes containing many combinations of propagators and spin matrix elements. AmpGen achieves a fast amplitude evaluation by generating efficient low-level source, which is compiled and dynamically linked to the executable. This also allows for flexibility in constructing the amplitude model, and the generated source code can be used directly without the need to rely on a specific software framework. For the analysis presented in this thesis, the generated source code for the $D^0 \to K^+K^-\pi^+\pi^-$ model can be found in Ref. [53].

Table 3.2: The dominant components in the amplitude analysis of $D^0 \to K^+K^-\pi^+\pi^-$ [38]. The uncertainties are statistical and systematic, respectively.

Amplitude	a_k	φ_k (rad)
$D^0 \to [\phi(1020)(\rho-\omega)^0]_{L=0}$	1 (fixed)	0 (fixed)
$D^0 \to K_1(1400)^+K^-$	$0.614 \pm 0.011 \pm 0.031$	$1.05 \pm 0.02 \pm 0.05$
$D^0 \to [K^-\pi^+]_{L=0}[K^+\pi^-]_{L=0}$	$0.282 \pm 0.004 \pm 0.008$	$-0.60 \pm 0.02 \pm 0.10$
$D^0 \to K_1(1270)^+K^-$	$0.452 \pm 0.011 \pm 0.017$	$2.02 \pm 0.03 \pm 0.05$

3.1.2 The five-dimensional phase-space of $D^0 \to K^+K^-\pi^+\pi^-$

The method for measuring the CKM angle γ described in Section 2.7.2 requires a set of instructions for assigning $B^\pm \to Dh^\pm$ candidates to different phase-space bins. This is referred to as a binning scheme, and it must be optimised for the best possible precision on γ. In order to develop such a phase-space binning, a mathematical description of phase space itself is required, as well as an understanding of its dimensionality.

For an N-body decay, where all decay products are spinless particles, each final-state particle is described by its four-momentum. This makes a total of $4N$ parameters. Furthermore, the N-body decay must obey the following constraints:

- The total energy and momentum must be conserved, which is a set of four constraints;
- Each particle must be on shell, $E^2 - |\vec{p}|^2c^2 = m^2c^4$, resulting in N constraints in total;
- The arbitrary choice of reference frame requires two rotations and a boost that provide three constraints.

In total, there are $3N-7$ degrees of freedom in an N-body decay. In particular, for a three-body decay there are two degrees of freedom, and the corresponding two-dimensional phase space is commonly referred to as a Dalitz plot.

In the three-body decays $D \to K^0_S h^+h^-$, the strong-phase parameters c_i and s_i were measured, using two-dimensional binning schemes, by CLEO [54] and more precise measurements were subsequently provided by BESIII [55–57]. The

binning schemes are visualised in Fig. 3.2 on a Dalitz plot described by the variables $\Phi = (m^2_+, m^2_-)$, which are the squared invariant masses of the $K^0_S\pi^\pm$ pairs. Under *CP* transformations, $m^2_\pm$ is transformed into $m^2_\mp$. To ensure that each bin has a corresponding *CP*-conjugated bin, the binning scheme is defined symmetrically about the line $m^2_+ = m^2_-$, with $m^2_+ > m^2_-$ ($m^2_+ < m^2_-$) defined as positive (negative) bins.

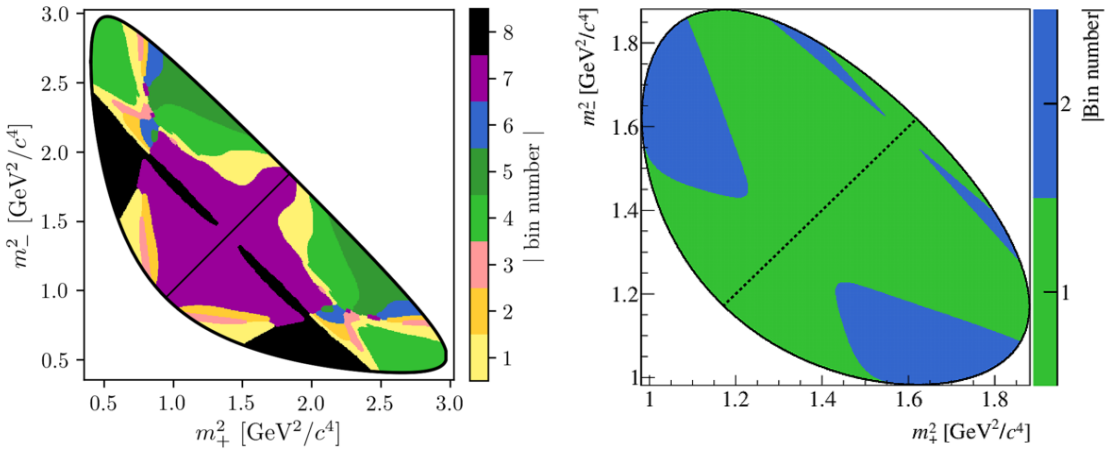

$K^0_S\pi^+\pi^-$ $K^0_SK^+K^-$

Figure 3.2: Left: The "equal δ" binning scheme for $D^0 \to K^0_S\pi^+\pi^-$. Right: The 2×2 binning scheme for $D^0 \to K^0_SK^+K^-$. The figures are from Ref. [39].

In four-body decays, which have an additional three degrees of freedom, the five-dimensional phase-space cannot be easily visualised. Nevertheless, a binning scheme may be defined analogously, with the help of an amplitude model. A possible strategy, similar to that in Ref. [54] for the $D \to K^0_S\pi^+\pi^-$ decays, is to use five arbitrary parameters that describe the phase-space location Φ and provide the decay amplitude and bin number as lookup tables.

However, in five dimensions, a fine-grained lookup table is highly inefficient, and previous analyses of four-body decays have sought more convenient binning schemes. In an analysis of the decay $D \to K^0_S\pi^+\pi^-\pi^0$, described in Ref. [58], no amplitude model currently exists, and so the known resonances were separated into different bins. For the decay $D \to \pi^+\pi^-\pi^+\pi^-$, described in Ref. [40], an efficient lookup table using an optimised binary tree was developed. Finally, for the CF and DCS decays

$D \to K^{\pm}\pi^{\mp}\pi^{+}\pi^{-}$, described in Ref. [59], the binning scheme was solely based on the model-predicted strong-phase difference between the CF and DCS decays.

The strategy developed for the decay $D \to K^{+}K^{-}\pi^{+}\pi^{-}$ in this thesis uses a combination of the approaches developed for $D \to \pi^{+}\pi^{-}\pi^{+}\pi^{-}$ and $D \to K^{\pm}\pi^{\mp}\pi^{+}\pi^{-}$. First, for each D decay candidate, which has its kinematics described by the four-momenta of the four final-state particles, the model-predicted amplitudes $\mathcal{A}(D^0)$ and $\mathcal{A}(\overline{D}^0)$ are obtained using the amplitude model described in Section 3.1.1. The ratio of these amplitudes can be defined as

$$\frac{\mathcal{A}(D^0)(\Phi)}{\mathcal{A}(\overline{D}^0)(\Phi)} = r_D(\Phi)e^{i\delta_D(\Phi)},$$

where δ_D is interpreted as the strong-phase difference between the D^0 and $\overline{D}^0 \to K^{+}K^{-}\pi^{+}\pi^{-}$ decays at the phase-space location Φ. Similarly, r_D is the magnitude of the ratio of these amplitudes. Effectively, this choice of variables projects the five-dimensional phase-space Φ onto a two-dimensional plane described by the parameters δ_D and r_D. Note that this projection uses the model predictions of δ_D and r_D, and not their actual values, which are unknown.

3.1.3 Binning scheme using model-predicted hadronic parameters

In the design of an optimised binning scheme, Eq. (2.11),

$$N_i^{\mp} = h_{DK}^{\mp}\Big[K_i + \Big(\big(x_{\mp}^{DK}\big)^2 + \big(y_{\mp}^{DK}\big)^2\Big)K_{-i} + 2\sqrt{K_iK_{-i}}\Big(x_{\mp}^{DK}c_i + y_{\mp}^{DK}s_i\Big)\Big], \quad (2.11)$$

must be considered carefully. Since this relationship between the bin yields and γ depends on the relative size of the interference term, the strategy must be to maximise the size of this term. This can be achieved in two ways. First, the magnitude of c_i and s_i must be maximised. Second, the values of K_i must be chosen to favour the interference term relative to the other two terms.

To maximise the magnitude of the strong-phase parameters c_i and s_i, the integral in Eq. (2.12) must be performed over a region which maximises the total integral. If $\delta_D(\Phi)$ changes significantly within a bin, the sinusoidal oscillations

will average to zero, and the sensitivity to γ will be diluted. Thus, the integral must be performed over a region where $\delta_D(\Phi)$ has minimal variation in order to maximise the magnitude of c_i and s_i.

A naive procedure for ensuring minimal variation in $\delta_D(\Phi)$ is to divide the model-prediction of $\delta_D(\Phi)$ into $\mathcal{N}$ equally spaced bins,

$$-\pi + \frac{2\pi}{\mathcal{N}}(i-1) < \delta_D(\Phi) < -\pi + \frac{2\pi}{\mathcal{N}}i,$$

such that candidates near $\delta_D(\Phi) = -\pi$ are assigned bin $i = 1$, while candidates near $\delta_D(\Phi) = +\pi$ are put into bin $\mathcal{N}$.

To obtain values of K_i that favour the interference term of Eq. (2.11), each bin i should be split into a pair of conjugate bins $+i$ and $-i$ such that the difference in the magnitude of K_i and K_{-i} is maximised. This can be achieved by noting that under a *CP* transformation, $(\delta_D, r_D) \to (-\delta_D, 1/r_D)$. Therefore, bin i should be split at the boundary $r_D = 1$, or equivalently $\ln(r_D) = 0$. Furthermore, because of the sign swap of δ_D, the order of the bins need to be reversed in the conjugated bins. In summary, the assignment of bins $\pm i$ is

$$-\pi + \frac{2\pi}{\mathcal{N}}(i-1) < \delta_D < -\pi + \frac{2\pi}{\mathcal{N}}i, \quad i < 0, \tag{3.1}$$

$$\pi - \frac{2\pi}{\mathcal{N}}(-i-1) < \delta_D < \pi - \frac{2\pi}{\mathcal{N}}(-i), \quad i > 0. \tag{3.2}$$

The number of bins $\mathcal{N}$ is chosen to ensure a sufficient number of D candidates in each bin in the charm-threshold data. For the analysis presented in this thesis, a binning scheme with $\mathcal{N} = 4$ is used, but a binning scheme with $\mathcal{N} = 8$ is also determined for future analyses.

The binning schemes are visualised in two dimensions described by the parameters δ_D and $\ln(r_D)$ in Fig. 3.3. In summary, a $D \to K^+K^-\pi^+\pi^-$ decay is assigned a bin by calculating δ_D and r_D using the amplitude model, and Fig. 3.3 is used to assign a bin number.

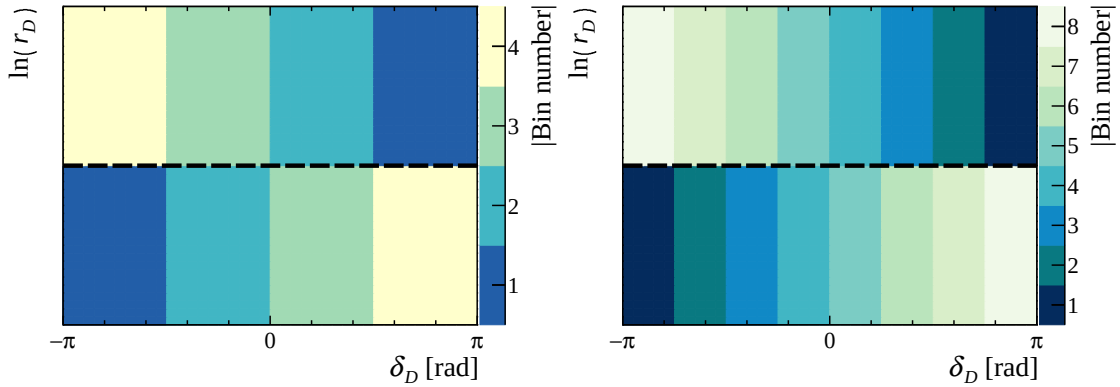

(a) 2×4 bins. **(b)** 2×8 bins.

Figure 3.3: A two-dimensional visualisation of the simple binning schemes for the $D \to K^+K^-\pi^+\pi^-$ decay.

3.1.4 Optimisation of the five-dimensional binning scheme

The choice of binning scheme described in Section 3.1.3 successfully assigns phase-space regions with similar strong-phase content to the same bins, and by construction it is expected that the large difference between K_i and K_{-i} will enhance the interference effects used to measure γ. However, since the choice of bin boundaries in δ_D is arbitrary, the simple binning schemes presented in Fig. 3.3 may not necessarily provide optimal sensitivity to γ.

In Ref. [43], where a phase-space integrated strong-phase measurement is performed, it is found that the $D \to K^+K^-\pi^+\pi^-$ decay is predominantly *CP*-even. It is therefore expected that the regions near $\delta_D = 0$ have more dominant resonances and a finer binning in this region will thus provide higher sensitivity to γ, while regions near $\delta_D = \pm\pi$ can have a more coarse binning without degrading the sensitivity to γ significantly.

A metric for describing the sensitivity to γ is the Q-value [60]. It is defined as the ratio of the γ precision in an unbinned fit, which has maximal statistical sensitivity, relative to that of a binned fit. To derive an analytical form of Q, it may be assumed that the measured bin yields $N_i^{\pm}$ of $B^{\pm} \to DK^{\pm}$ decays are Poisson distributed and independent. With Eq. (2.11), a likelihood function is constructed using the method described in Sections A.1 and A.2, with $x_{\pm}$ and $y_{\pm}$

as model parameters. If these are assumed to be Gaussian distributed, it can be shown that their uncertainties $\sigma(x_\pm)$ are given by

$$\frac{1}{\sigma^2(x_\pm)} = \sum_i \left(\frac{1}{\sqrt{N_i^\pm}} \frac{\mathrm{d}N_i^\pm}{\mathrm{d}x_\pm} \right)^2, \tag{3.3}$$

and similarly for $\sigma(y_\pm)$. In the derivation of Eq. (3.3), it has been assumed that $x_\pm, y_\pm \ll 1$, and therefore only leading order terms in $x_\pm$ and $y_\pm$ are kept.

Equation 3.3 predicts the $x_\pm$ and $y_\pm$ uncertainties from a binned fit. The predicted uncertainty in an unbinned fit of a sample of $B^\pm \to DK^\pm$ decays is analogously derived from Eq. (2.8), resulting in

$$\frac{1}{\sigma^2(x_\pm)} = \int \mathrm{d}\Phi \left(\frac{1}{\sqrt{\Gamma(B^\pm)}} \frac{\mathrm{d}\Gamma(B\pm)}{\mathrm{d}x_\pm} \right)^2. \tag{3.4}$$

From these measurements of $x_\pm$ and $y_\pm$, which are assumed to be uncorrelated, a new likelihood function is constructed, using Eq. (2.10) with γ, δ_B and r_B as model parameters. Again, assuming that γ is Gaussian distributed, it follows that its uncertainty due to the measurement of $B^\pm$ bin yields is

$$\frac{1}{\sigma^2(\gamma)} = \frac{r_B^2}{\sigma^2(x_-)} + \frac{r_B^2}{\sigma^2(y_-)}. \tag{3.5}$$

Hence, from combining Eqs. (3.3)-(3.5), the analytical expression for the Q-value of the $B^\pm$ decay is

$$Q_\pm^2 = \frac{\sum_i \left[\left(\frac{1}{\sqrt{N_i^\pm}} \frac{\mathrm{d}N_i^\pm}{\mathrm{d}x_\pm} \right)^2 + \left(\frac{1}{\sqrt{N_i^\pm}} \frac{\mathrm{d}N_i^\pm}{\mathrm{d}y_\pm} \right)^2 \right]}{\int \mathrm{d}\Phi \left[\left(\frac{1}{\sqrt{\Gamma(B^\pm)}} \frac{\mathrm{d}\Gamma(B^\pm)}{\mathrm{d}x_\pm} \right)^2 + \left(\frac{1}{\sqrt{\Gamma(B^\pm)}} \frac{\mathrm{d}\Gamma(B^\pm)}{\mathrm{d}y_\pm} \right)^2 \right]}. \tag{3.6}$$

The average Q-value from B^- and B^+ decays, $Q^2 = (Q_-^2 + Q_+^2)/2$, is used as the metric of the binning scheme performance. From Eqs. (2.8) and (2.11), Eq. (3.6) can be written in terms of c_i, s_i and K_i as

$$Q_\pm^2 = 1 - \sum_i \frac{K_i K_{-i} \left(1 - c_i^2 - s_i^2\right)}{N_i^\pm}. \tag{3.7}$$

Here $N_i^\pm$ are calculated using Eq. (2.11) with h set to unity. The calculation of the parameters c_i, s_i and K_i, which depend on the choice of binning scheme, is

described in Section 3.3. Note that the value of $N_i^{\pm}$ depends on γ, δ_B and r_B, but since the magnitude of r_B is small, the dependence is very weak. In the binning scheme optimisation, the values $\gamma = 75°$, $\delta_B = 130°$ and $r_B = 0.1$ are used.

A simplified form of Eq. (3.6) is obtained in the limit $x_\pm, y_\pm \to 0$,

$$Q_\pm^2 = \sum_i K_i (c_i^2 + s_i^2).$$

The Q-value can therefore be interpreted as a coherence factor, averaged over all phase-space bins with K_i as a weight. With an infinite number of bins, $c_i^2 + s_i^2 \to 1$ in the absence of any dilution. On the other hand, a poor binning scheme will have a low coherence and $c_i^2 + s_i^2 \ll 1$, resulting in a low Q-value.

An optimal binning scheme for a measurement of γ is obtained by adjusting the bin boundaries in δ_D, while keeping the division line at $\ln(r_B) = 0$ fixed. Furthermore, since the region with strong-phase difference δ_D is related to that at $-\delta_D$ by a *CP*-conjugation, the bin boundaries are adjusted symmetrically in pairs around $\delta_D = 0$. The bin boundaries at $\delta_D = 0$ and $\delta_D = \pm\pi$ are kept fixed during the optimisation.

In summary, to optimise the binning scheme with $\mathcal{N} = 4$, shown in Fig. 3.3a, a single pair of bin boundaries is varied until the value of Q is maximised. The optimal bin boundary position is found to be at $\delta_D = 1.209\,\text{rad}$, resulting in $Q = 0.85$. Similarly, the binning scheme in Fig. 3.3b with $\mathcal{N} = 8$ is optimised by allowing three pairs of bin boundaries to vary, and its performance is found to be $Q = 0.90$, with bin boundaries at $\delta_D = 0.458, 1.155$ and $2.096\,\text{rad}$.

The optimal binning schemes are visualised in Fig. 3.4. In comparison with those in Fig. 3.3, the binning schemes in Fig. 3.4 have finer bins near $\delta_D = 0$ and more coarse bins near $\Delta\delta_D = \pm\pi$, as expected for a decay that is predominantly *CP*-even.

3.2 An unbinned benchmark for γ

In the past, there have been several analyses that have studied the feasibility of measuring γ using the $B^\pm \to DK^\pm$ decay with the subsequent four-body decay $D \to K^+K^-\pi^+\pi^-$. This four-body decay was first proposed in Ref. [61] using a

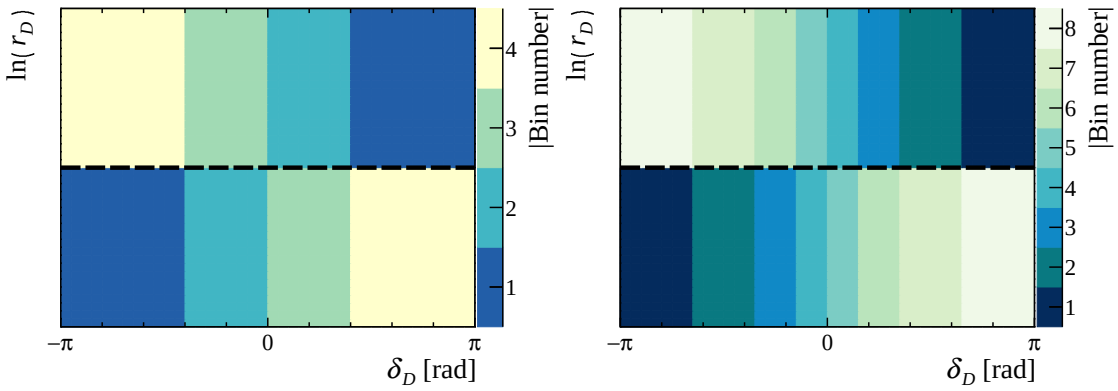

2×4 bins. 2×8 bins.

Figure 3.4: A two-dimensional visualisation of the optimised binning schemes for the $D \to K^+K^-\pi^+\pi^-$ decay.

model-dependent unbinned maximum likelihood fit, and it was predicted that a sample of 1000 $B^\pm \to DK^\pm$ decays can achieve a precision of 14°. These studies were based on an amplitude model by the FOCUS collaboration [62]. In addition, a more recent amplitude analysis by the CLEO collaboration [63] predicted a precision of 11° on γ with a sample of 2000 $B^\pm \to DK^\pm$ decays.

It is desirable to perform the same study using the most recent amplitude model by LHCb [38] described in Section 3.1.1. To simulate a $B^\pm \to DK^\pm$ decay from the amplitude model of $D \to K^+K^-\pi^+\pi^-$, the amplitudes of the D^0 and $\overline{D}^0$ decays are combined in AmpGen according to Eqs. (2.3) and (2.4), which is equivalent to Eq. (2.8). For these studies, the parameters $\gamma = 75°$, $\delta_B = 130°$ and $r_B = 0.1$ are used to generate pseudo-experiments in AmpGen, each containing 2000 $B^\pm \to DK^\pm$ decays, with an equal number of B^+ and B^- decays.

The AmpGen framework is also used to perform a maximum likelihood fit of each pseudo-experiment, with γ, δ_B and r_B as free parameters. The LHCb amplitude model is used to construct an unbinned likelihood function and the uncertainties are assessed using the procedure outlined in Sections A.1-A.3. An example of the confidence regions obtained from a fit is shown in Fig. 3.5, where the 68.27% and 95.45% confidence level regions are plotted. The black crosses indicate the input parameters used to generate the data set.

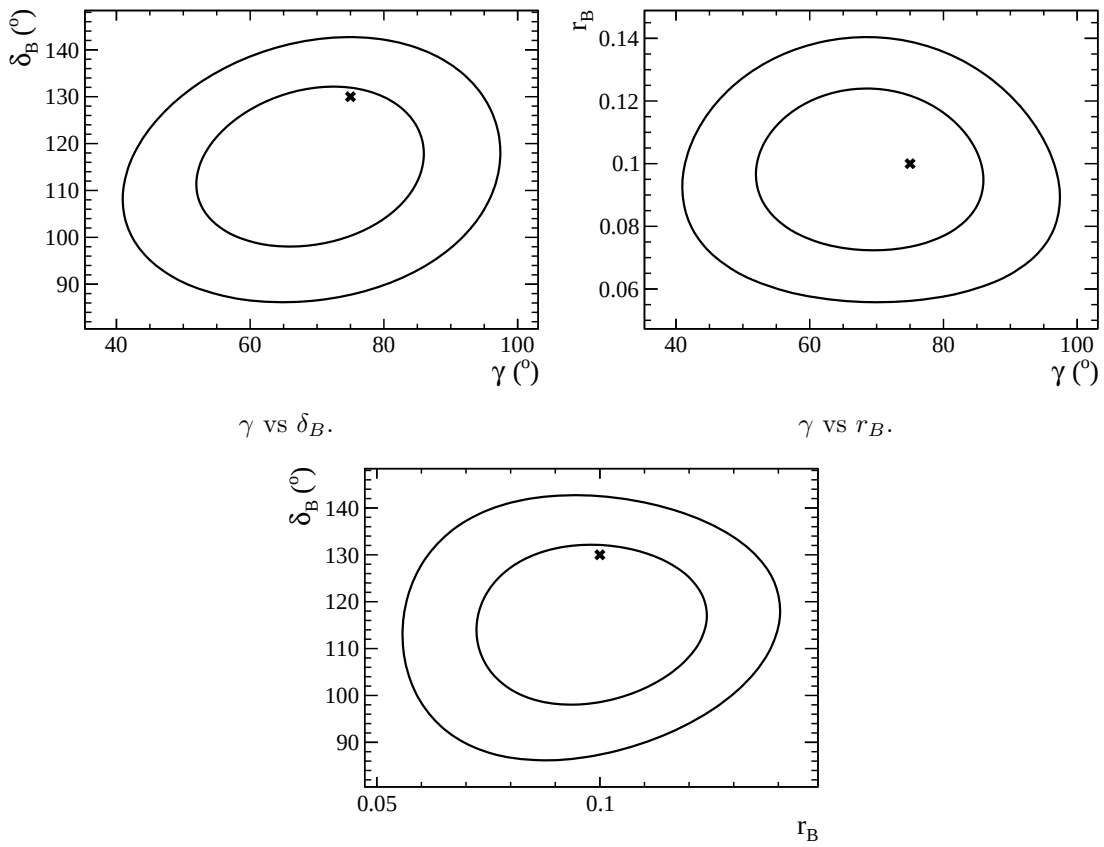

γ vs δ_B. γ vs r_B.

r_B vs δ_B.

Figure 3.5: Results from an unbinned fit of a sample of 2000 generated decays of $B^{\pm} \to DK^{\pm}$. The plots show the $\Delta\chi^2 = 2.30$ and 6.18 contours, which correspond to a 68.27% and 95.45% confidence level, respectively. The crosses indicate the parameters used to generate the data set.

In total, 1000 pseudo-experiments are generated and fitted. On the left in Fig. 3.6, the distribution of fitted values of γ is shown. By fitting a Gaussian function, with its mean, standard deviation and normalisation as free parameters, it is found that this distribution has a mean of $(75.1 \pm 0.3)^\circ$ and a standard deviation of $(10.51 \pm 0.26)^\circ$. Thus, with a sample of 2000 $B^{\pm} \to DK^{\pm}$ candidates, the unbinned maximum likelihood fit benchmark is around 10.5° and the maximum likelihood estimators are found to be unbiased. The standard deviation of the left plot in Fig. 3.6 is consistent with the fitted γ uncertainties shown on the right in Fig. 3.6.

A well-known property of maximum likelihood estimators is that their distributions are asymptotically Gaussian distributed [64]. It is therefore expected that

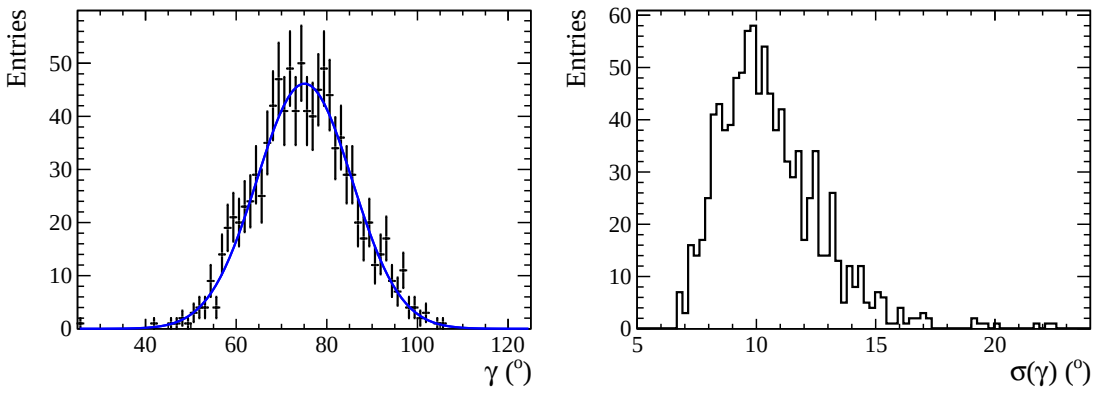

Figure 3.6: On the left are the fitted values of γ and on the right are its associated uncertainties $\sigma(\gamma)$, obtained from a set of 1000 fits to pseudo-experiments.

if the data set is sufficiently large, the pull, defined as

$$\frac{\mu^{\text{fit}} - \mu^{\text{gen}}}{\sigma(\mu)}, \tag{3.8}$$

obeys a normal Gaussian distribution, which has a zero mean and unit standard deviation. In Eq. (3.8), $\mu^{\text{fit}} \pm \sigma(\mu)$ is the fitted value of μ and its uncertainty. The parameter μ^{gen} is the input used to generate the data set. Thus, it is useful to quantify the statistical properties of γ, δ_B and r_B by studying the extent in which their pull distributions differ from a normal Gaussian distribution.

The pulls of γ, δ_B and r_B are shown in Fig. 3.7. Each distribution is fitted with a Gaussian function and the fitted mean and standard deviations are listed in Table 3.3. No biases are seen in the parameters γ and δ_B, and their standard deviations are found to be consistent with unity. For that reason, the uncertainties on γ and δ_B are expected to be well behaved, with the correct 68.27% coverage probability.

Table 3.3: Mean and standard deviation of the pull distributions obtained from unbinned fits to pseudo-experiments.

Variable	Pull mean	Pull standard deviation
γ	-0.03 ± 0.04	1.043 ± 0.030
δ_B	$+0.01 \pm 0.03$	1.013 ± 0.029
r_B	$+0.25 \pm 0.03$	0.955 ± 0.026

In contrast, the parameter r_B is found to have a clear bias, and its pull distribution has a standard deviation slightly smaller than unity. Such behaviour

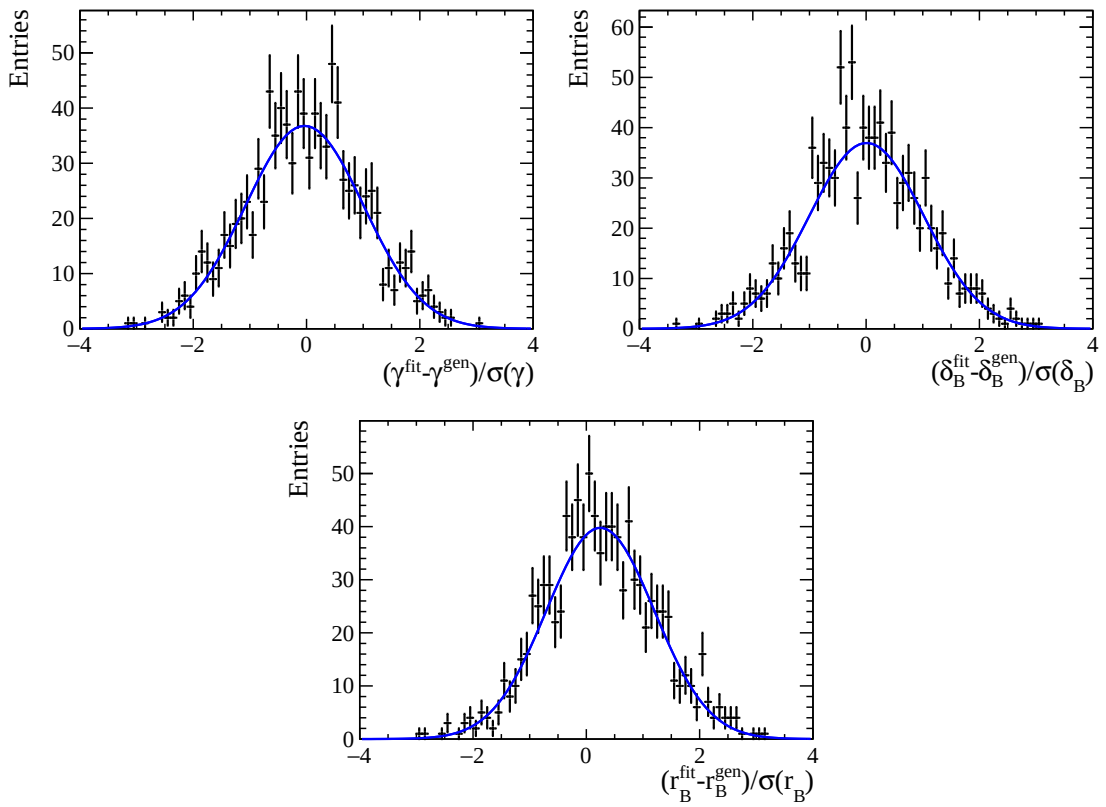

Figure 3.7: Pull distributions obtained from unbinned fits of 1000 pseudo-experiments performed in AmpGen.

was also observed in similar analyses [39]. As outlined in Ref. [64], the convergence of a maximum likelihood estimator distribution to a Gaussian distribution depends on the size of the third derivative, or skewness, of the likelihood function. Intuitively, the convergence is slower if the likelihood function differs significantly from a parabola near its minimum.

It is understood that the physical requirement $r_B > 0$ introduces a non-negligible skewness to the profile likelihood of r_B, therefore leading to a slower convergence to a Gaussian distribution. Nevertheless, with larger sample sizes the pull distribution of r_B showed a reduced bias and its standard deviation approached unity. This shows that despite the presence of the physical boundary, the distribution r_B is asymptotically Gaussian.

3.3 Model-predicted strong-phase parameters

To perform a fit analogous to that described in Section 3.2 in bins of phase space, Eq. (2.8) must be replaced with (2.11). However, such a fit does not use knowledge of the amplitude $\mathcal{A}(D^0)$, but instead information about the four-body charm decay is encoded in the parameters K_i, c_i and s_i. Although it is desirable to constrain these parameters in a model-independent manner, for this feasibility study they can be obtained from the amplitude model using Eqs. (2.12) and (2.13).

In three-body decays, where the phase space Φ is two-dimensional, the integrals in Eqs. (2.12) and (2.13) can be determined numerically to arbitrary precision, using methods such as the trapezoid rule, over the two-dimensional Dalitz plane within the kinematic boundary. For four-body decays, the trapezoid rule is significantly more challenging because the five dimensions of Φ makes it computationally expensive. Additionally, it is impossible to find a parameterisation $\vec{x}$ of phase space where Φ is a flat space. Mathematically, this means that the measure $\mathrm{d}\Phi = R(\vec{x})\mathrm{d}^5\vec{x}$ will always have a non-trivial phase-space density $R(\vec{x}) \neq 1$.

A more convenient approach is to perform a Monte-Carlo (MC) integration, which effectively replaces the integral with a sum over points that are uniformly sampled over the region that is integrated over. For instance, Eq. (2.13) can be approximated as

$$K_i = \frac{\sum_{\vec{x}\in\Phi_i}|\mathcal{A}(D^0)(\vec{x})|^2}{\sum_{\vec{x}\in\Phi}|\mathcal{A}(D^0)(\vec{x})|^2}, \tag{3.9}$$

where in the numerator, there is a sum over a sample of uniformly sampled points $\vec{x}$ that are in the region Φ_i, corresponding to bin i. Similarly, the denominator has a sum over the whole phase space. The expression for c_i and s_i is analogous.

For three-body decays, such as $D^0 \to K^0_S h^+h^-$, the phase space is visualised in Fig. 3.2, and an important property is that using the parameterisation $\vec{x} = (m^2_+, m^2_-)$, the phase space is flat. Thus, points that are uniformly distributed in Φ are also uniformly distributed in the Dalitz plane shown in Fig. 3.2. The sums in Eq. (3.9) can therefore be interpreted as a sum over points that are uniformly sampled in the regions shown in Fig. 3.2.

This method of MC integration can be generalised for the $D \to K^+K^-\pi^+\pi^-$ decay. Instead of using uniformly sampled data points, a sample of non-resonant $D \to K^+K^-\pi^+\pi^-$ decays are generated using an algorithm by Raubold and Lynch [65]. The sums in Eq. (3.9) are performed over the phase-space points of these non-resonant decays, and this ensures that regions of phase space that have a higher or lower phase-space density will be weighted appropriately. In addition to being computationally efficient, in five dimensions or higher this method also converges faster than the trapezoid rule.

Table 3.4: Model prediction of c_i, s_i, K_i, A_i for the optimised 2×4 binning scheme.

Bin number	c_i	s_i	K_i	K_{-i}	V_i	V_{-i}
1	−0.3621	−0.6589	0.0312	0.1031	0.1148	0.1148
2	0.8082	−0.3263	0.1010	0.2554	0.1450	0.1450
3	0.8360	0.3370	0.1259	0.2718	0.1457	0.1457
4	−0.3804	0.6297	0.0253	0.0864	0.0945	0.0945

Table 3.5: Model prediction of c_i, s_i, K_i, A_i for the optimised 2×8 binning scheme.

Bin number	c_i	s_i	K_i	K_{-i}	A_i	V_{-i}
1	−0.7309	−0.4352	0.0149	0.0471	0.0558	0.0559
2	−0.0080	−0.8527	0.0176	0.0611	0.0635	0.0635
3	0.6426	−0.6028	0.0290	0.1004	0.0746	0.0746
4	0.9159	−0.1722	0.0707	0.1499	0.0658	0.0658
5	0.9253	0.1886	0.0842	0.1694	0.0750	0.0750
6	0.6869	0.6017	0.0405	0.0987	0.0672	0.0671
7	−0.0001	0.8492	0.0139	0.0474	0.0505	0.0506
8	−0.7366	0.4040	0.0125	0.0427	0.0475	0.0475

Using this method of MC integration, the parameters c_i, s_i and K_i are calculated for the 2×4 and 2×8 binning schemes, and the numerical values are given in Tables 3.4 and 3.5. The fractional bin volume V_i, defined as the fraction of non-resonant decays in bin i, has also been calculated. The calculation uses a sample of 5×10^7 non-resonant $D \to K^+K^-\pi^+\pi^-$ decays. As a cross check, the calculation is performed using a second independent sample of 5×10^7 non-resonant decays, and the differences are found to be of order $\mathcal{O}(10^{-4})$.

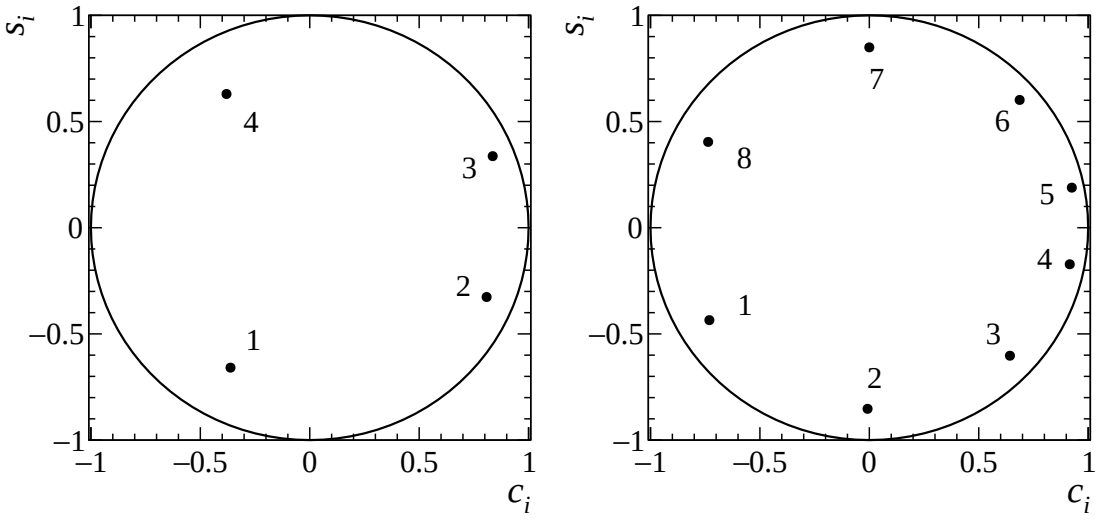

(a) 2×4 bins. **(b)** 2×8 bins.

Figure 3.8: Model prediction of c_i vs s_i for the optimised binning schemes.

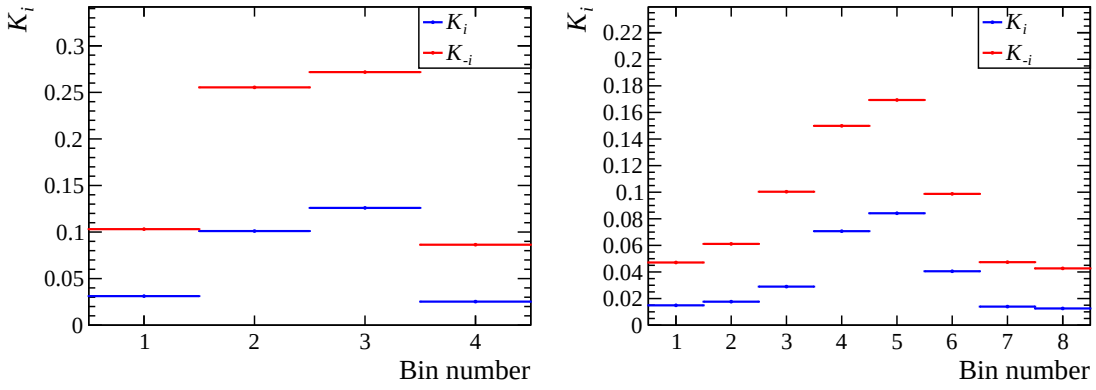

(a) 2×4 bins **(b)** 2×8 bins

Figure 3.9: Model prediction of F_i for the optimised binning schemes.

The c_i and s_i parameters are also plotted in Fig. 3.8, and their values are consistent with Fig. 3.4. The points near $(c_i, s_i) = (1, 0)$ are found to be closer to the unit circle since these bins cover a smaller range in δ_D, as seen in Fig. 3.4. In general, the (c_i, s_i) points are well separated from the centre, as expected from the high Q-value.

In Fig. 3.9, the model-predicted K_i values are plotted, with $i > 0$ in blue and $i < 0$ in red. By design, the $i > 0$ bins have D-decays with $\ln(r_D) < 0$, so these bins are expected to be suppressed, relative to the $i < 0$ bins. In fact, these suppressed bins behave similar to the ADS decays described by Eq. (2.6), and the asymmetry

between B^+ and B^- is therefore expected to be relatively large in these bins.

3.4 Performance of binned fit of γ

The performance of the optimised binning schemes described in Section 3.1.4 can be predicted from the combination of the calculated Q-value from Section 3.1.4 and the unbinned benchmark obtained from Section 3.2. Based on Q-values of $Q = 0.85$ and $Q = 0.90$ for the 2×4 and 2×8 binning schemes, the unbinned benchmark of $(10.51 \pm 0.26)^\circ$ results in a predicted sensitivity of $(12.36 \pm 0.31)^\circ$ and $(11.68 \pm 0.29)^\circ$ for the two binning schemes.

The performance can also be tested directly by performing a binned maximum likelihood fit of the same pseudo-experiments as those used in the unbinned fit described in Section 3.2. To construct a binned likelihood function from Eq. (2.11), the D decays in all pseudo-experiments are binned according to Fig. 3.4. The bin yields, $N_i^{\pm} \pm \sqrt{N_i^{\pm}}$, are assumed to be Gaussian distributed and independent, so the likelihood function takes the form of Eq. (A.2).

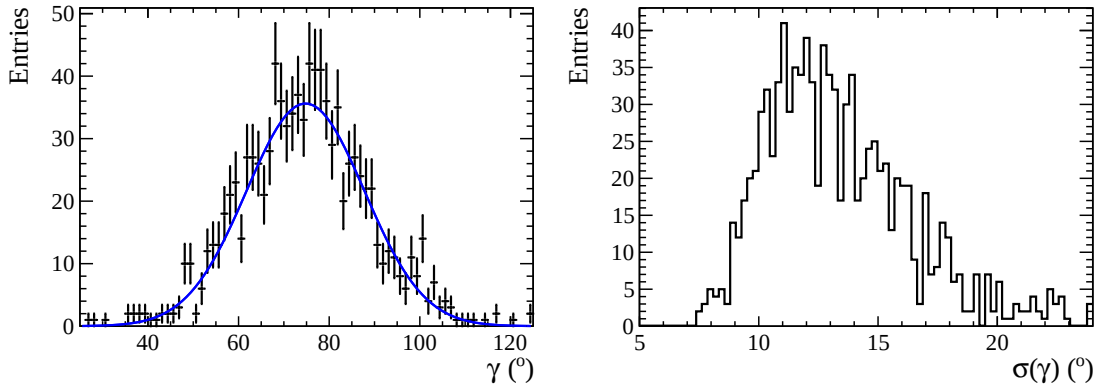

Figure 3.10: On the left are the fitted values of γ and on the right are its associated uncertainties $\sigma(\gamma)$, obtained from a set of 1000 binned fits to pseudo-experiments using the optimised 2×4 binning scheme.

The fitted values of γ for the 2×4 and 2×8 binning schemes are shown on the right of Figs. 3.10 and 3.11, respectively. The blue curve, which shows the fitted Gaussian function, indicates a γ precision of $(13.0 \pm 0.4)^\circ$ and $(12.2 \pm 0.4)^\circ$ for the two binning schemes, and this is consistent with the uncertainty distributions

plotted on the right in Figs. 3.10 and 3.11. These values are also consistent with the sensitivity expected based on the Q-values.

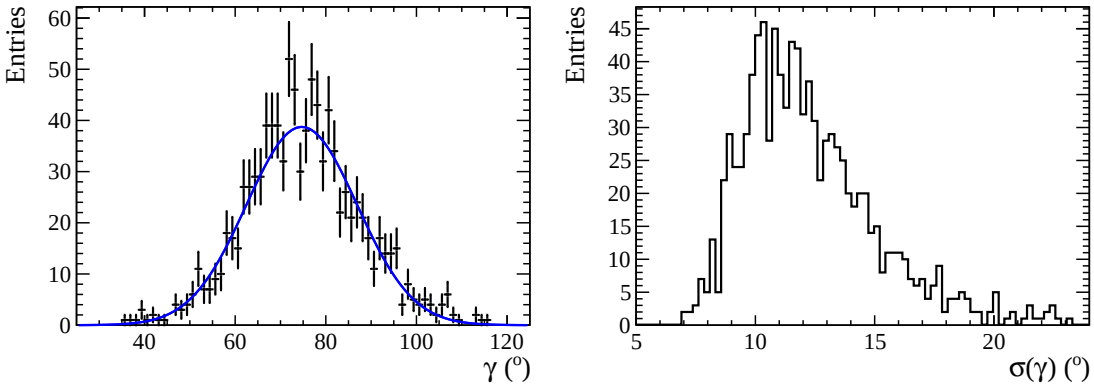

Figure 3.11: On the left are the fitted values of γ and on the right are its associated uncertainties $\sigma(\gamma)$, obtained from a set of 1000 binned fits to pseudo-experiments using the optimised 2×8 binning scheme.

The pull distributions of γ, δ_B and r_B are also studied in order to make sure that the fits are unbiased with uncertainties that have the correct coverage probability. The distributions for the 2×4 binning scheme are shown in Fig. 3.12, and those for the 2×8 binning scheme are similar. The mean and standard deviation of the fits with a Gaussian function are listed in Tables 3.6 and 3.7, and the behaviour of γ, δ_B and r_B is very similar to that of the unbinned fit. The bias in r_B is worse in the 2×4 binning scheme due to the poorer statistical sensitivity.

Table 3.6: Mean and standard deviation of the pull distributions obtained from binned fits to pseudo-experiments using the 2×4 binning scheme.

Variable	Pull mean	Pull standard deviation
γ	-0.02 ± 0.03	0.984 ± 0.029
δ_B	-0.04 ± 0.04	1.063 ± 0.032
r_B	-0.23 ± 0.03	0.950 ± 0.024
x_+	-0.02 ± 0.03	0.951 ± 0.024
y_+	-0.04 ± 0.03	1.010 ± 0.026
x_-	-0.05 ± 0.03	0.984 ± 0.025
y_-	-0.02 ± 0.03	0.948 ± 0.024

Ultimately, the binned fit of $B^\pm \to DK^\pm$ decays will be performed using the parameters $x_\pm$ and $y_\pm$ instead of γ, δ_B and r_B. Therefore, the binned maximum

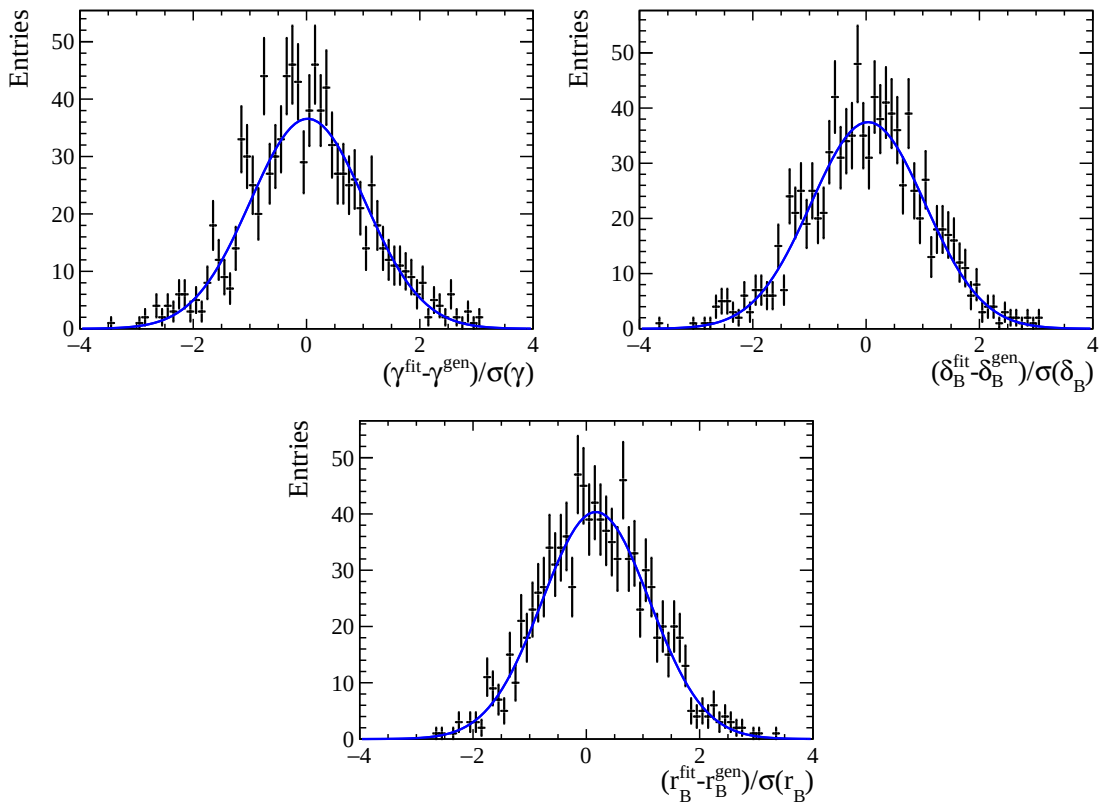

Figure 3.12: Pull distributions obtained from binned fits of 1000 pseudo-experiments using the optimised 2×4 binning scheme.

Table 3.7: Mean and standard deviation of the pull distributions obtained from binned fits to pseudo-experiments using the 2×8 binning scheme.

Variable	Pull mean	Pull standard deviation
γ	$+0.02 \pm 0.03$	1.011 ± 0.030
δ_B	$+0.03 \pm 0.03$	1.006 ± 0.027
r_B	$+0.17 \pm 0.03$	0.951 ± 0.025
x_+	$+0.05 \pm 0.03$	0.975 ± 0.026
y_+	$+0.02 \pm 0.03$	1.002 ± 0.028
x_-	-0.01 ± 0.03	0.966 ± 0.025
y_-	-0.01 ± 0.03	0.936 ± 0.025

likelihood fits are also performed using this Cartesian parameterisation, and the pull distributions are shown in Fig. 3.13. The numerical fit results are also listed in Figs. 3.6 and 3.7. Since this parameterisation does not suffer from the physical boundary at $r_B = 0$, all the $x_\pm$ and $y_\pm$ pull distributions are found to agree much better with a normal Gaussian function. Some of the standard deviations of the pull

distributions are smaller than unity, which imply over-estimated uncertainties, but the effect is minor.

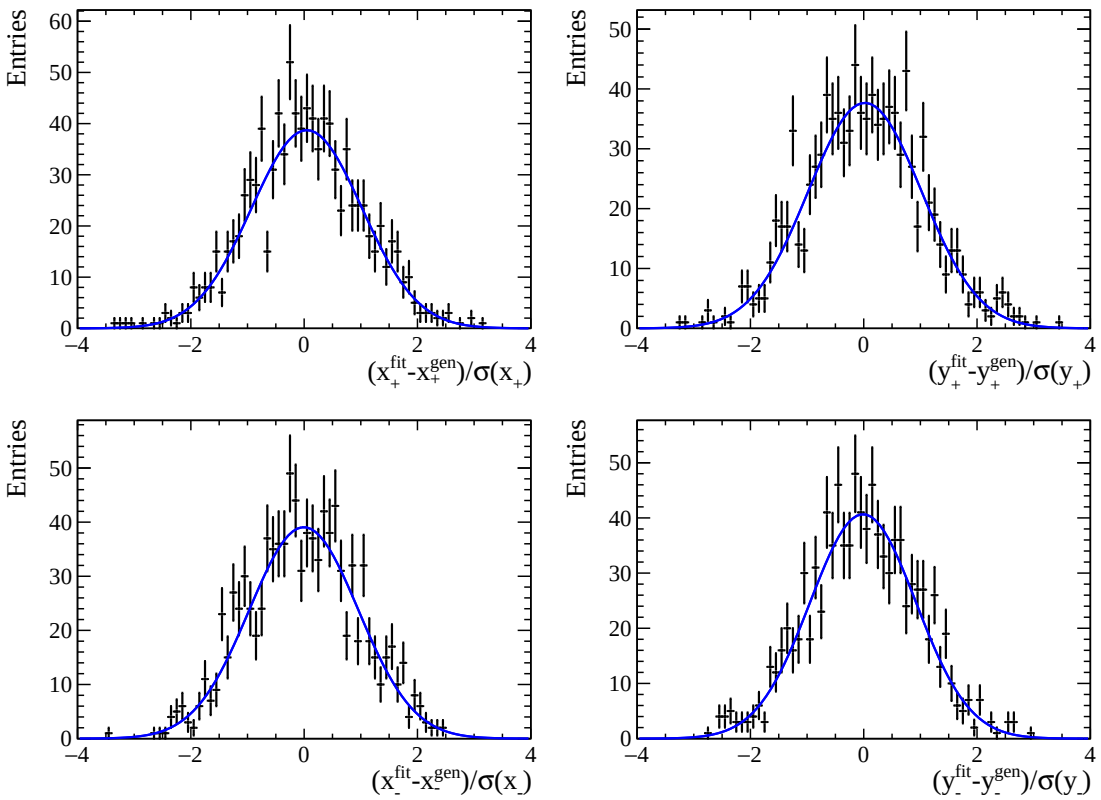

Figure 3.13: Pull distributions obtained from binned fits of 1000 pseudo-experiments using the optimised 2×4 binning scheme.

In conclusion, the binning schemes presented in Section 3.1.4 have been found to perform within expectations, without introducing any biases. Some uncertainties are found to over-estimate the coverage probability, but these effects are very small. The expected precisions on γ in a binned fit of 2000 $B^\pm \to [K^+K^-\pi^+\pi^-]_D K^\pm$ candidates are 12.4° and 11.7° for the 2×4 and 2×8 binning schemes, respectively.

4
The BESIII detector

Contents

The Beijing Spectrometer III [66] (BESIII) detector enables studies of e^+e^- collisions to be conducted in a low track-multiplicity environment. The electron and positron beams are provided by the Beijing electron-positron collider II [67] (BEPCII), which is multi-bunch storage ring with a 237.5 m circumference, located at the Institute of High Energy Physics (IHEP) in China. The e^+ and e^- beams, which circulate in separate rings, are provided by a 202 m long linear accelerator that can accelerate each beam to 1.89 GeV.

BEPCII is designed to operate with a centre-of-mass energy range from $\sqrt{s} =$ 2.00 GeV to 4.95 GeV. Under normal operation, each ring can store 93 bunches with a bunch spacing of 8 ns. At the interaction point, the beams collide with a horizontal crossing angle of 11 mrad. The BEPCII peak instantaneous design luminosity is $1 \times 10^{33}\,\mathrm{cm}^{-2}\,\mathrm{s}^{-1}$, which is achieved at $\sqrt{s} = 3.773\,\mathrm{GeV}$ with a beam current of 910 mA.

During collisions, the beam current will decrease as the electron and positron beams are depleted, until the collision rate is too low for efficient data taking. To maximise the integrated luminosity, a top-up injection scheme is adopted, which avoids the need to dump the remaining beams. Instead, newly accelerated electrons and positrons are directly injected into the storage rings, which reduces the detector dead-time significantly.

A schematic overview of the detector is shown in Fig. 4.1. The main subdetectors that are discussed in this chapter are the multi-wire drift chamber, the time-of-flight system, the electromagnetic calorimeter and the muon identifier.

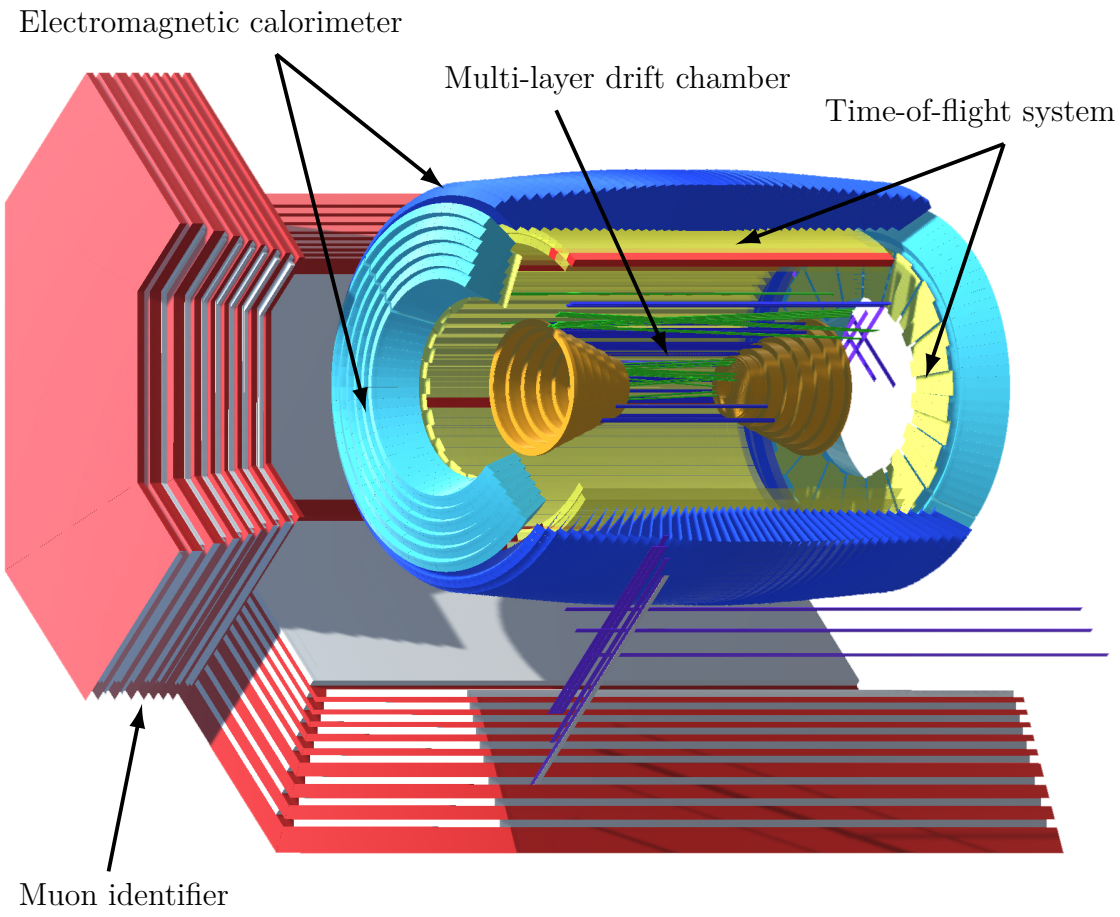

Figure 4.1: A visualisation of the BESIII detector, taken from Ref. [68]. Between the calorimeter and the muon identifier, shown in blue and red respectively, there is also a superconducting solenoidal magnet, which is not shown.

The physics programme of BESIII covers a wide range of topics, such as the study of light hadrons and exotic states, charmonium physics, QCD and τ physics, and

charm physics. In the charm analysis presented in this thesis, the samples collected at the $D\overline{D}$ threshold, $\sqrt{s} = 3.773\,\text{GeV}$, are considered. Data at this energy, also known as the $\psi(3770)$ threshold, were collected during two different data-taking periods.

Initially, when data taking started in 2009, an instantaneous luminosity of $0.32 \times 10^{33}\,\text{cm}^{-2}\,\text{s}^{-1}$ [66] was achieved, which allowed for a data set of $(2.932 \pm 0.014)\,\text{fb}^{-1}$ [69, 70] to be collected at $\sqrt{s} = 3.773\,\text{GeV}$ between 2010 and 2011. In 2016, the BESIII detector reached a milestone, when it reached its peak instantaneous design luminosity. Recently, during the data-taking period 2021 to 2024, a new data set corresponding to $(17.34 \pm 0.04)\,\text{fb}^{-1}$ at the $D\overline{D}$ threshold was collected, bringing the total integrated luminosity to $(20.28 \pm 0.04)\,\text{fb}^{-1}$.

At the present time, data collected in 2024 are currently not available for analysis. Therefore, only data collected between 2010-2011 and 2021-2023 are analysed, which corresponds to $(16.08 \pm 0.04)\,\text{fb}^{-1}$.

4.1 Multi-layer drift chamber

The tracking system consists of a cylindrical multi-layer drift chamber (MDC), illustrated by the green and blue wires in Fig. 4.1. The outer radius is 0.81 m, while the inner radius is 59 mm, which is only 2 mm from the beam pipe.

The MDC volume consists of a cylindrical outer chamber, which has a length of 2.6 m and covers a polar angle range of $|\cos(\theta)| < 0.83$, where θ is the angle relative to the beam axis, or z-axis. The inner chamber, which covers $|\cos(\theta)| < 0.93$, has conical end caps to accommodate the intrusion of the focusing magnets on either side of the interaction point. Both chambers share a common gas volume, which consists of 60% helium and 40% propane. This mixture ensures an optimal efficiency while minimising multiple scattering, which limits the momentum resolution.

The drift chamber is divided into small square drift cells, each consisting of a sense wire (anode) at the centre and eight field wires (cathode) surrounding it. The sense wires are 25 µm in diameter, made from gold-plated tungsten with 3% rhenium, while the field wires consist of gold-plated aluminium with a diameter

of 110 µm. The inner chamber cells have a width of approximately 12 mm, while the outer chamber size is 16 mm.

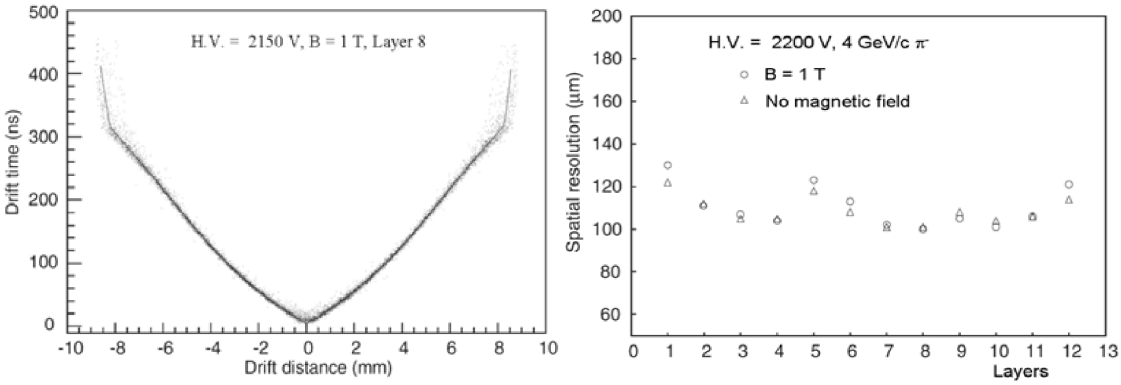

Figure 4.2: Left: Relationship between the radial position r and the measured time t of a particle detected by a wire in the MDC. Right: Average position resolution of each MDC layer. Figures are taken from Ref. [66].

When a charged particle passes through a cell, the gas mixture is ionised along the track. The positively charged ions and negatively charged electrons drift toward the cathode and anode, respectively. On the left of Fig. 4.2, a relationship between the the drift time of ionised electrons and the radial distance of the charged particle from the sense wire is shown. By using this relationship, together with timing measurements of the ionised electrons at the anode, the radial distance of the charged particle is determined. When measurements from multiple sense wires are combined, a two-dimensional trajectory of the charged particle is reconstructed.

A prototype MDC consisting of twelve layers was tested and the single-wire resolution was determined in each layer, shown on the right of Fig. 4.2. A resolution of 100 µm is achieved in several layers, and the average position resolution is 112 µm.

In order to reconstruct the third dimension, which is along the z-axis, the cells are arranged in 43 separate layers, where layers 9-20 and 37-43 are parallel to the beam axis. The remaining layers, 1-8 and 21-36, are oriented with a small stereo angle, such that the charged-track position along the z-axis can be measured with a resolution of 3-4 mm.

The momenta of charged particles are determined by the MDC with the help of a 1 T magnetic field provided by a superconducting solenoidal magnet. The

magnet is not shown in Fig. 4.1, but it occupies the volume between the muon identifier and the calorimeter, which are shown in red and blue, respectively. The expected momentum resolution is 0.5% at 1 GeV/c.

In addition to tracking, the energy deposits of charged particles in the MDC also provide valuable information for Particle Identification (PID). Specifically, the energy loss per unit length, $\mathrm{d}E/\mathrm{d}x$, is given by the Bethe-Block equation [21], demonstrated on the left of Fig. 4.3 for different particle species. This energy-loss information, which is determined by the pulse height of MDC hits, is particularly important for pion-kaon separation at momentum below 0.6 GeV/c and electron-pion separation above 0.4 GeV/c.

4.2 Time-of-flight system

The PID capabilities provided by the MDC are greatly enhanced by a dedicated Time-of-flight (TOF) system that surrounds the MDC. In Fig. 4.1 the TOF system indicated in light yellow and is made up of plastic scintillation counters. The barrel has two staggered layers of scintillators with 88 scintillation counters each. This covers the radial region $[0.81, 0.93]$ m and has a total length of 2.3 m. Each scintillator is 50 mm thick and the scintillation light is detected by Photon-Multiplier Tubes (PMTs).

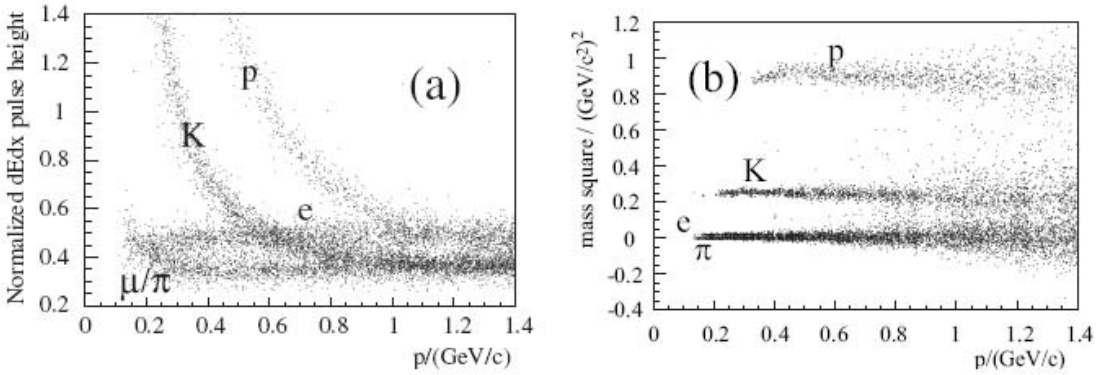

Figure 4.3: Left: Normalised pulse heights from each charged particle species in the MDC, as a function of momentum p. Right: Reconstructed invariant-mass squared as a function of momentum, using information from the TOF system. The figure is taken from Ref. [71].

On the right, Fig. 4.3 shows typical distributions of reconstructed particle mass squared for different momenta, and these are determined using the flight path, momentum and timing information from the TOF system. The time resolution from the two barrel layers is 78 ps [72], which is dominated by the rise-time of the scintillation light, fluctuations in the photon arrival time at the PMT and the photoelectron transition-time spread of the PMT.

In the end-cap region, the TOF system initially consisted of a layer of scintillation counters similar to those in the barrel. The time resolution, 110 ps, is worse than the barrel since there is only a single layer of scintillators. In 2015, the end-cap system was replaced by a multi-gap resistive plate chamber [73–75] (RPC) that has 36 modules in each end cap, split into two staggered layers. Each module has twelve readout strips to ensure a high granularity, read out from both ends to improve the timing resolution. The new upgraded end cap achieves a resolution of 60 ps, which benefits 82% of the data set analysed in this thesis.

4.3 Electromagnetic calorimeter

The purpose of the electromagnetic calorimeter (EMC) is to provide accurate measurements of photon energies from the decays of π^0, η and heavier hadrons. Furthermore, a finely segmented calorimeter allows for an accurate determination of shower positions, which is necessary for reconstructing photon-momentum directions. The EMC can also provide PID power to separate charged pions from electrons, as the latter deposits a large fraction of its energy in the EMC.

In the BESIII detector, the EMC consists of Thallium-doped Cesium-Iodide scintillator crystals, or CsI(Th). The crystals are suitable for detecting low-energy photons, which is crucial for studying radiative decays, and the light yield is high. The light is read out by silicon photodiodes. In total, there are over 6000 crystals, arranged into 56 rings in the barrel and six rings in each end cap. This ensures that each crystal covers about 3° in both polar and azimuthal directions. The crystals have a depth of 28 cm, which covers 15.1 radiation lengths.

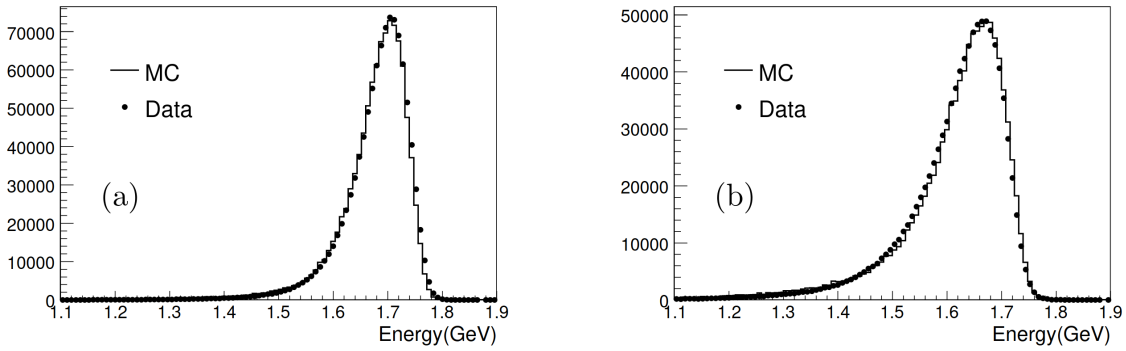

Figure 4.4: Energy of reconstructed Bhabha events in the EMC barrel on the left and end cap on the right. The figure is taken from Ref. [76].

The photon energy resolution is 2.5% (5%) for 1 GeV/c photons in the barrel (end-cap) region, which is determined by the shower-energy leakage, non-uniformity in the scintillator-light production and dead areas between crystals. This is demonstrated in Fig. 4.4, which shows a comparison of the shower energy reconstructed in data, shown as points, and simulation, shown by the histogram. Good agreement is found between data and simulation, however the resolution is worse in the end cap (right), compared to the barrel (left). This is because there is more dead material in front of the end cap. Both the barrel and end-cap showers show a significant tail on the lower side of the energy distribution due to these effects.

4.4 Muon chamber

The muon chamber (MUC), shown in red in Fig. 4.1, consists of RPCs inserted into the steel plates of the magnet return yoke. The MUC system has an octagonal shape, with nine layers of RPCs in each octant of the barrel. The end caps consist of eight RPC layers in each quadrant. The layers alternate between readout strips in the polar and azimuthal directions. To reconstruct a muon, hits in both orientations are combined and matched with a track reconstructed by the MDC. Since the position resolution in the MUC suffers from multiple scattering by the EMC, magnet coil and steel layers, the momenta of identified muons is determined by the MDC.

4.5 The trigger system

The trigger system is a crucial part of the BESIII detector, and it ensures that only interesting physics events are retained. The e^+e^- collision rate at the BESIII interaction point is 125 MHz, and it is expected that beam-related backgrounds, mostly due to loss of electrons and positrons, could result in up to 13 MHz of rate. In comparison, the maximum rate of physics events, which occurs at the J/ψ resonance, is only 2 kHz. This is to be compared with the BESIII data acquisition system, which can record events up to 4 kHz.

The trigger system consists of a hardware trigger and a software trigger. After each e^+e^- collision, signals from each subdetector are passed through the hardware-trigger stage, which uses information such as tracks in the MDC, signals in the TOF scintillators, clusters in the EMC and hits in the MUC to make a global trigger decision.

Events accepted by the hardware trigger are transmitted to an online computer farm that performs full event building. An event filter is applied, which is designed to reduce the background rate by a factor two. The event filter also classifies events into different categories, such as e^+e^-, $\mu^+\mu^-$, hadronic and cosmic rays. By design, the total trigger efficiency is close to 100% [77] for events with two or more tracks.

4.6 Simulation of BESIII

Simulated data samples are produced with a GEANT4-based [78] Monte Carlo package, which includes the geometric description of the BESIII detector and the detector response. The simulation models the beam-energy spread and initial-state radiation in e^+e^- annihilations with the generator KKMC [79].

Inclusive simulation samples are centrally produced, and they include the production of $D\overline{D}$ pairs, non-$D\overline{D}$ decays of the $\psi(3770)$, production of the J/ψ and $\psi(2S)$ states with initial-state radiation, and the continuum processes incorporated in KKMC [79]. The purpose of these samples is to identify possible background contributions in each reconstructed decay mode. Furthermore, large dedicated

simulation samples are produced to accurately determine detection efficiencies and background retentions.

All particle decays are modelled with EVTGEN [80, 81] using branching fractions either taken from the Particle Data Group [21] when available, or otherwise estimated with LUNDCHARM [82, 83]. Final-state radiation (FSR) from charged final-state particles is incorporated using the PHOTOS package [84].

5

Selection of single- and double-tag events

Contents

This chapter describes the selection of charged particles and photons from collisions recorded by the BESIII detector. Furthermore, the strategy for combining these particles into a decay tree of neutral D mesons is presented. The selected samples of $e^+e^- \to D\overline{D}$ events are required for an analysis of strong-phase parameters of the $D^0 \to K^+K^-\pi^+\pi^-$ decay.

5.1 Tag modes

The D-decay modes, or tags, which are of interest for measuring strong-phase parameters, can be classified as flavour tags, *CP* tags and self-conjugate multi-body (SCMB) tags. The list of tags considered for this measurement are listed in Table 5.1, and these are commonly referred to as tag modes. In addition, the signal mode $D \to K^+K^-\pi^+\pi^-$ is also listed in Table 5.1, and it is marked with a double dagger ‡ to distinguish it from the tag modes with known strong-phase information.

Although the tag mode $D \to \pi^+\pi^-\pi^0$ is a decay of mixed *CP* content, it is listed as a *CP*-even decay in Table 5.1. Its *CP*-even fraction has been measured to be 0.973 ± 0.017 [46], making it predominantly *CP* even. Similarly, the *CP*-even fraction of $D \to K^0_S\pi^+\pi^-\pi^0$ has been measured by BESIII to be $0.235 \pm 0.010 \pm 0.002$ [85], and since this decay is predominantly *CP*-odd, it is grouped with the *CP*-odd tags.

Table 5.1: Tag modes used in this analysis. The flavour tags refer to D^0 decays, and charge conjugation is implied. The signal mode has also been listed with a ‡ superscript. The modes with a † superscript are considered with a partial reconstruction of the signal mode $D \to K^+K^-\pi^+\pi^-$, in addition to the full reconstruction.

Tag mode type	Tag modes
Flavour	$K^-\pi^+$, $K^-\pi^+\pi^0$, $K^-\pi^+\pi^-\pi^+$, $K^-e^+\nu_e$
CP-even	$K^+K^{-\dagger}$, $\pi^+\pi^-$, $K^0_S\pi^0\pi^0$, $\pi^+\pi^-\pi^0$, $K^0_L\pi^0$
CP-odd	$K^0_S\pi^{0\dagger}$, $K^0_S\eta_{\gamma\gamma}$, $K^0_S\eta'_{\pi\pi\eta}$, $K^0_S\eta'_{\pi\pi\gamma}$, $K^0_S\pi^+\pi^-\pi^0$
SCMB	$K^0_S\pi^+\pi^{-\dagger}$, $K^0_L\pi^+\pi^-$, $K^+K^-\pi^+\pi^{-\ddagger}$

The decay $D \to K^0_S\eta'$ is listed twice in Table 5.1 with different subscripts, since the η' meson is reconstructed in two different decay channels, $\eta' \to \pi^+\pi^-\eta$ and $\eta' \to \pi^+\pi^-\gamma$, and each of these have separate selections. The decay $D \to K^0_S\eta$ is also shown with the subscript $\gamma\gamma$, indicating that it is reconstructed in the $\eta \to \gamma\gamma$ decay channel. There exists another interesting decay channel of the η meson, $\eta \to \pi^+\pi^-\pi^0$, which is considered as a part of the $D \to K^0_S\pi^+\pi^-\pi^0$ tag mode.

The D-decay modes in Table 5.1 are reconstructed by first considering all reconstructed tracks and showers. The selections of these are described in Section 5.2 and 5.3, respectively. In each event, all possible combinations that result in D-decay candidates consistent with those listed in Table 5.1 are kept for further analysis.

Experimentally, the tag modes in Table 5.1 can be categorised as fully or partially reconstructed tags. In fully reconstructed tags, which include all tags in Table 5.1 without a $K^0_{\rm L}$ meson or an electron-neutrino ν_e, all particles in the final state are reconstructed in the detector. The reconstruction of fully reconstructed tags is described in Section 5.4.

In contrast, tags that are partially reconstructed contain a missing particle, such as a $K^0_{\rm L}$ meson or an electron-neutrino ν_e, the presence of which is inferred from the missing four-momentum. Furthermore, a novel reconstruction method where the signal mode $D \to K^+K^-\pi^+\pi^-$ is partially reconstructed is also considered in this measurement, and the tag modes where such a reconstruction is attempted are labelled with a dagger † in Table 5.1. Section 5.5 describes all partially reconstructed tags.

The signal mode $D \to K^+K^-\pi^+\pi^-$ is considered in bins of phase space, using the 2×4 binning scheme described in Chapter 3. The $D \to K^0_{S,L}\pi^+\pi^-$ tag modes in Table 5.5 are the only tag modes that are phase-space binned. These three-body decays are binned according to the "equal δ" binning scheme [54–56] with 2×8 bins. The values of c_i, s_i and K_i for the $K^0_{\rm S}\pi^+\pi^-$ tag mode that are used in the analysis are the combined BESIII and CLEO results from Appendix A in Ref. [56]. The numbers for the $K^0_{\rm L}\pi^+\pi^-$ tag mode are obtained from the same table, but the sign of all c_i and s_i parameters are swapped since they are defined with an additional π strong-phase difference in Ref. [54–56].

5.2 Charged particle reconstruction

Charged particles that emerge from the e^+e^- collisions are detected in the MDC as a series of hits, which are analysed using the algorithm described in Ref. [86] to reconstruct helical trajectories. Each trajectory is identified as a charged particle, and these trajectories are referred to as tracks. Each track is required to be within the MDC acceptance, which is $\cos(\theta) \leq 0.93$. The polar angle θ is defined with respect to the z-axis, which is the symmetry axis of the MDC.

The D^0 meson, which has a lifetime of 4.103×10^{-13} s [21], is expected to have a mean decay length of less than 20 µm at the $\psi(3770)$ threshold. This is smaller than the position resolution of the MDC, and therefore direct daughters of the D meson will have tracks that originate from the IP. Furthermore, most of these tracks will either be from charged pions or kaons, which must be distinguished using PID information from $\mathrm{d}E/\mathrm{d}x$ in the MDC and timing measurements by the TOF detector system.

Thus, to reconstruct tracks that directly originate from a D meson, the transverse impact parameter V_{xy} and the impact parameter V_{z} along the beam direction are required to be within 1 cm and 10 cm, respectively, to ensure that the charged particles originate from the IP. Additionally, several PID requirements, listed in Table 5.2, are also imposed to ensure that charged pions, kaons and electrons are correctly identified. The probabilities P_π, P_K and P_e are determined from the likelihood of each mass hypothesis, which is interpreted as a χ^2 variable. The tracks that satisfy these impact parameter and PID requirements are denoted as good tracks, while those that do not satisfy these selection criteria are simply referred to as tracks.

Table 5.2: The PID requirements on the reconstructed $K^\pm$, $\pi^\pm$ and $e^\pm$. The probability of a particle being a charged pion, kaon or electron is denoted by P_π, P_K, P_e, respectively.

$\pi^\pm$	$K\pm$	$e^\pm$
$P_\pi \geq 0$	$P_K \geq 0$	$P_e \geq 0$
$P_\pi \geq P_K$	$P_K \geq P_\pi$	$P_e > P_\pi$
		$P_e > P_K$

The selection of electrons is also improved further by following the strategy in Ref. [87]. For a track to be identified as an electron, it must deposit sufficient energy in the EMC and information about the shape of the electromagnetic shower is also used, in addition to the PID requirements listed in Table 5.2. The energy E measured by the EMC, divided by the momentum p reconstructed from the MDC track, must be above a threshold that is dependent on $|\cos(\theta)|$, where θ is the polar angle.

The momenta of good tracks that are identified as electrons must also be corrected for FSR by searching for showers within 5° of the electron momentum direction. The momenta of these showers are added to the electron momentum. Additionally, any event containing showers with energy greater than 300 MeV which are not used in the D meson reconstruction are rejected. This suppresses background events with additional photons that are not from FSR, such as $D \to K^-\pi^+\pi^0$.

5.3 Neutral particle reconstruction

5.3.1 Reconstruction of single photons

In this analysis, the only neutral particle that can be detected directly by the BESIII detector are photons, which are identified using showers in the EMC. The deposited energy of each shower must be more than 25 MeV in the barrel region, which corresponds to $|\cos(\theta)| < 0.8$. In the end-cap region, $0.86 < |\cos(\theta)| < 0.92$, the minimum shower energy is 50 MeV.

To suppress electronic noise and showers that are unrelated to the event, the difference between the EMC time and the start of the event must be within $[0, 700]$ns. Charged tracks that go through the EMC can also fake the signal of a photon by leaving a shower, and therefore showers are required to be separated by more than 10° from the position of any charged track in the EMC, as measured from the IP.

5.3.2 Short-lived neutral particles

The remaining neutral particles used in this analysis, which are the short-lived K^0_S, π^0, η and η' mesons, are reconstructed by adding the four-momenta of their daughter particles, which is some combination of photons and charged particles. The specific decay channels of these particles are listed in Table 5.3. The invariant mass of the daughter particles are required to be within the ranges listed in the second column in Table 5.3. These regions roughly correspond to a $3\,\sigma$ window around the mass peak.

Although the K^0_S meson is short-lived, its lifetime is sufficiently long that the separation between the D-decay and K^0_S-decay vertices is measurable in the MDC. Thus, the pion daughter tracks are not subject to the requirements of good tracks,

which are only appropriate for tracks originating from the IP. Instead, the only IP requirement is that $V_z < 20\,\text{cm}$. Furthermore, no PID requirements are necessary as the K^0_S decays have negligible background involving particles other than pions.

Table 5.3: Invariant mass and χ^2 requirements in the selection of short-lived neutral particles.

Particle	Decay final state	Invariant mass window	χ^2 requirement
K^0_S	$\pi^+\pi^-$	$[487, 511]\,\text{MeV}/c^2$	100
π^0	$\gamma\gamma$	$[115, 150]\,\text{MeV}/c^2$	20
η	$\gamma\gamma$	$[505, 575]\,\text{MeV}/c^2$	20
η'	$\pi^+\pi^-\eta$	$[940, 976]\,\text{MeV}/c^2$	-
η'	$\pi^+\pi^-\gamma$	$[940, 970]\,\text{MeV}/c^2$	-

However, in the absence of IP requirements on the K^0_S-decay daughters, the $\pi^+\pi^-$ invariant-mass resolution is poorer, compared to decays formed by good tracks. This can be improved by constraining the charged pion tracks to originate from a common vertex, which is allowed to be physically separated from the IP. Such a vertex fit uses information from the hits in the MDC, but it also recalculates the four-momenta while taking the vertex constraint into account. To ensure that the two charged pion tracks are consistent with a common decay vertex, the χ^2 of the vertex fit is required to be less than 100.

Similarly, since the width of the $\gamma\gamma$ invariant-mass distribution of π^0 and η candidates is dominated by experimental resolution, the four-momentum resolution of the π^0 and η mesons in the two-photon decay channel can be improved by constraining the $\gamma\gamma$ invariant mass to the π^0 or η masses. The resulting χ^2 of this kinematic fit is required to be less than 20.

The χ^2 requirements for the K^0_S vertex fit and the π^0 and η kinematic fits are also listed in Table 5.3. Since the number of degrees of freedom in these fits is not readily available, a statistical interpretation of these requirements is not straightforward to determine. Nonetheless, the criteria are sufficiently loose that it is nearly 100% efficient on correctly reconstructed signal candidates. The refitted four-momenta are used in the subsequent analysis.

The invariant-mass distributions from the reconstruction of BESIII simulation samples are shown in Fig. 5.1. For the K^0_S invariant mass, a comparison of the distribution before and after the vertex fit is also shown. For η' decays, no fits are performed.

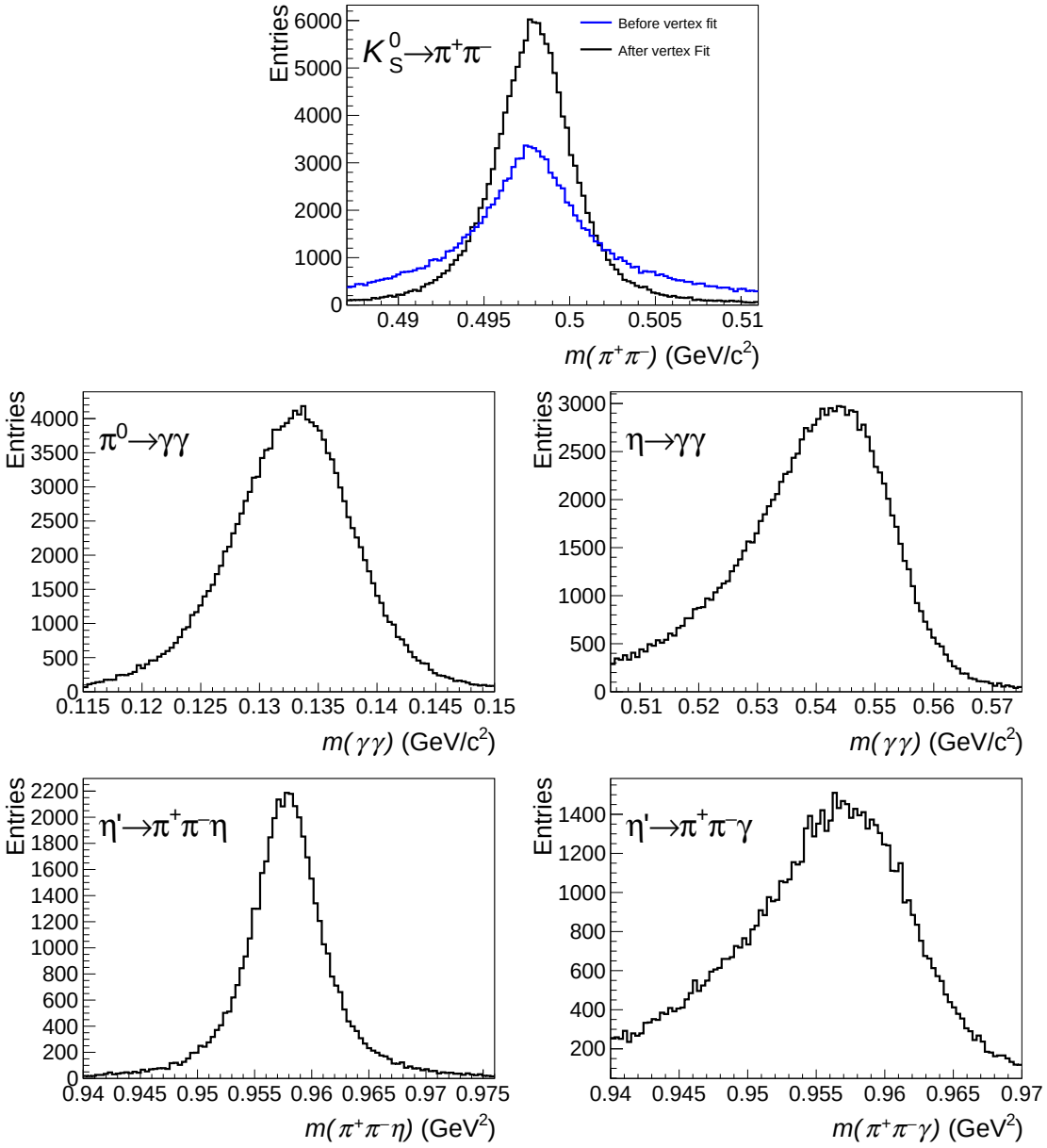

Figure 5.1: BESIII simulation of the reconstructed invariant masses of the π^0, η, K^0_S and η' mesons. The top plot also shows a comparison between the K^0_S invariant-mass distribution before and after a vertex fit.

In tag modes containing a K^0_S meson, there is potentially a background where two oppositely charged pions originating directly from the D meson can fake a

K^0_S candidate when the $\pi^+\pi^-$ invariant mass is similar to the K^0_S mass. Since they originate from a real D decay, this background peaks in the D invariant-mass spectrum. Its invariant-mass shape is very similar to that of D decays with a K^0_S meson, which could bias the signal yield.

To separate D decays with real K^0_S candidates from those without an intermediate K^0_S meson, the K^0_S decay vertex is required to be separated from the primary vertex. This is quantified by the K^0_S flight significance, defined as the flight distance of the K^0_S before it decays, divided by the flight-distance uncertainty. The flight distance and its uncertainty is calculated in a fit that combines the result of the K^0_S vertex fit with the primary vertex position. In this analysis, all K^0_S candidates are required to have a flight significance greater than two.

5.3.3 Rejection of $K^0_S \to \pi^+\pi^-$ contamination

At the end of Section 5.3.2, the suppression of peaking backgrounds from $\pi^+\pi^-$ decays that fake a K^0_S candidate is described. Conversely, a D decay with a $\pi^+\pi^-$ pair could also be a K^0_S decay in disguise. The tag modes that are particularly vulnerable to this peaking background are the $D \to \pi^+\pi^-\pi^0$, $K^-\pi^+\pi^-\pi^+$ and $K^+K^-\pi^+\pi^-$ tag modes, which are contaminated by $D \to K^0_S\pi^0$, $K^0_S K^-\pi^+$ and $K^0_S K^+K^-$, respectively. To reduce this background, the flight significance of all pairs of oppositely charged pions in these tag modes is required to be less than two.

In the $D \to K^+K^-\pi^+\pi^-$ selection, the flight-significance requirement is insufficient to suppress the K^0_S contamination, due to the larger branching fraction of the $D \to K^0_S K^+K^-$ decay. Therefore, $D \to K^+K^-\pi^+\pi^-$ events where the $\pi^+\pi^-$ pair has an invariant mass lying close to the K^0_S mass are also removed from the analysis. Using a simulated sample of $D \to K^0_S K^+K^-$ decays, reconstructed as $K^+K^-\pi^+\pi^-$, it is found that a rejection of candidates in the asymmetric region $m(\pi^+\pi^-) \in [477, 507]\,\mathrm{MeV}/c^2$ is an optimal selection. The bias in the reconstructed K^0_S mass is due to the good track requirements on the charged pions, as well as the flight significance requirement. Both these selections are more likely to reject

$\pi^+\pi^-$ pairs with higher invariant mass, since these pions have a higher momentum and can fly further before they decay.

Table 5.4: Efficiency, or the fraction of $D \to K^0_S K^+ K^-$ decays removed by the flight significance and mass-window requirements, in the $K^+K^-\pi^+\pi^-$ mode.

K^0_S requirement	Efficiency (10^{-2})
No requirement	0
Flight significance	74.56
Invariant mass	92.18
Flight significance and invariant mass	95.42

Table 5.4 shows the efficiency, defined as the fraction of $D \to K^0_S K^+ K^-$ events that are removed by the flight significance and asymmetric mass window requirements, in the $K^+K^-\pi^+\pi^-$ selection. The numbers are obtained from the simulation.

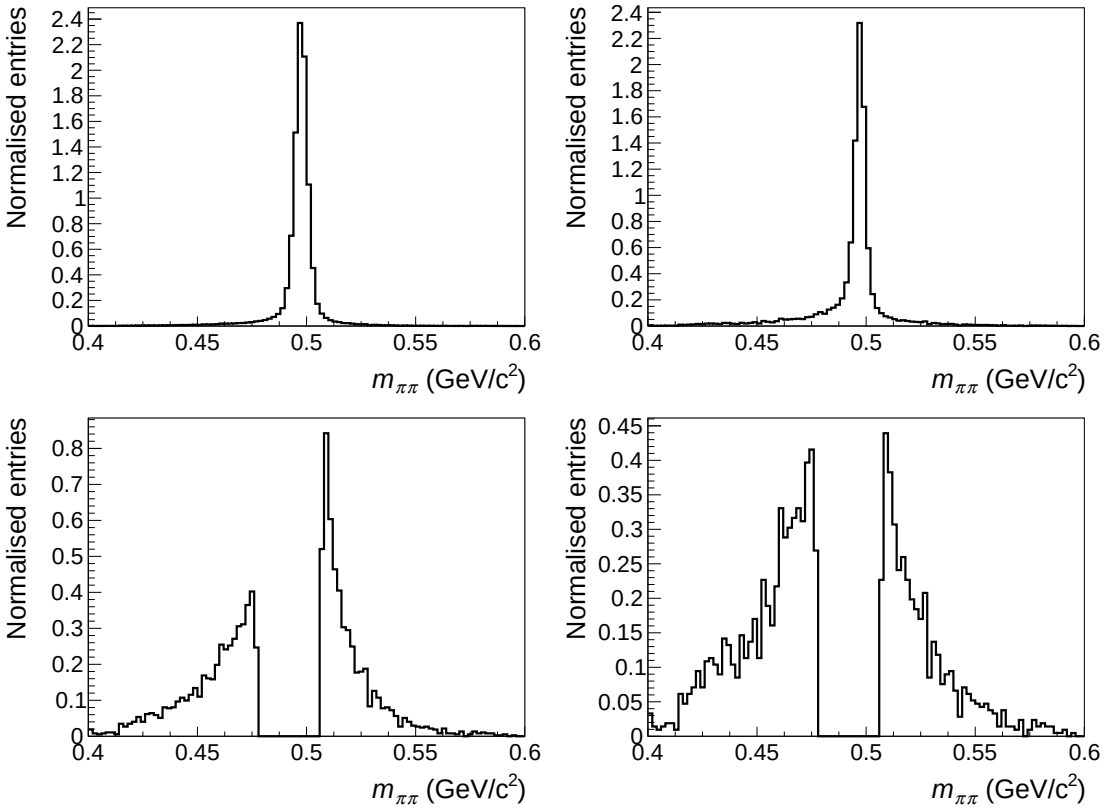

Figure 5.2: The $m_{\pi^+\pi^-}$ invariant mass of a $D \to K^0_S K^+ K^-$ simulation sample, reconstructed as $K^+K^-\pi^+\pi^-$. Top left: No K^0_S rejection requirements applied. Top right: Flight-significance requirement applied. Bottom left: Invariant-mass window requirement applied. Bottom right: Both requirements applied.

Fig. 5.2 shows the corresponding $\pi^+\pi^-$ invariant masses with the different requirements. The asymmetric mass window is found to be effective when combined with the flight-significance requirement. This is particularly clear in the bottom left histogram in Fig. 5.2, where the absence of a requirement on the flight significance results in a smaller bias in the reconstructed K^0_S mass. In summary, the two requirements remove over 95% of the $K^0_S K^+ K^-$ background.

5.4 Fully reconstructed decay modes

5.4.1 Four-momentum constraints for fully reconstructed decays

In fully reconstructed tag modes, two types of selection are performed. In the first selection, one D meson is reconstructed in the $D \to K^+K^-\pi^+\pi^-$ signal mode, while the other D meson is reconstructed as the tag mode. The data set of double-tag events is analysed to determine the double-tag yields, but they must be normalised by the corresponding single-tag yields, as mentioned in Section 2.8.1. Thus, in the second selection, which is the single-tag selection, the tag mode is selected without reconstructing the other D meson in the event.

To reconstruct a D meson, its invariant mass is determined from the four-momenta of its daughter particles. However, since the D meson originates from a $\psi(3770)$ decay at the threshold of $D\overline{D}$ production, no additional particles are produced in the event. Therefore, by energy conservation, the D-meson energy is equal to the beam energy $E_{\rm beam}$. With this constraint, the D invariant mass is

$$M_{\rm BC} = \sqrt{E^2_{\rm beam} - \left|\sum_i \vec{p}_i\right|^2}, \tag{5.1}$$

which is referred to as the beam-constrained mass. The sum runs over all daughters of the D meson, and $\vec{p}_i$ are their three-momenta.

In addition, since the D energy must equal the beam energy, it is useful to study the difference between the reconstructed D energy and the beam energy, defined as

$$\Delta E \equiv \sum_i E_i - E_{\rm beam}, \tag{5.2}$$

where the E_i are the reconstructed energies of each daughter particle. For a perfectly reconstructed event, $\Delta E = 0$, but the finite detector resolution smears this into a wider peak. By imposing appropriate selection requirements around $\Delta E = 0$, the level of background can be significantly reduced. This is mostly important for combinatorial background, where random tracks combine to form fake D candidates, and also misidentification background, which is from real D decays with daughter particles that have been assigned the wrong mass hypothesis.

Since the resolution of ΔE depends on the final-state particles, the ΔE requirements are determined separately for each tag mode by considering the single-tag ΔE distribution. Furthermore, detector resolution is generally underestimated by the simulation, so the requirements need to be different between data and simulation. The optimisation of the ΔE signal windows are described in Section 5.4.2.

In many events, in particular those with a large number of tracks, it is possible to build multiple D-decay candidates that pass the selection described in Sections 5.1, 5.2 and 5.3. These are known as multiple candidates, and in the single-tag selection the candidate with the ΔE value closest to zero is retained, while the rest are discarded. For the double-tag selection, the beam-constrained mass on both the signal and tag side, $M_{\rm BC}^{\rm signal}$ and $M_{\rm BC}^{\rm tag}$, respectively, are calculated and the combination with the average $M_{\rm BC}$ closest to the D^0 mass is chosen.

To distinguish signal and background decays, both $M_{\rm BC}^{\rm signal}$ and $M_{\rm BC}^{\rm tag}$ can be used as discriminating variables, where correctly reconstructed signal events have a distribution with a signal peak at the D mass in both $M_{\rm BC}^{\rm signal}$ and $M_{\rm BC}^{\rm tag}$ simultaneously. However, in this analysis, which has a limited sample size of double-tag events, only the $M_{\rm BC}^{\rm signal}$ variable is used to discriminate signal and background decays, and it is simply denoted as $M_{\rm BC}$.

5.4.2 Optimisation of ΔE selection

To determine the appropriate ΔE selection requirements, a maximum likelihood fit is performed on the ΔE distribution, and a $3\,\sigma$ window is selected around the

signal peak. The signal is modelled as two independent Gaussian functions, while a Chebychev polynomial is used for the background.

In tag modes with fewer events, a second-order polynomial is found to describe the background well. In tag modes with larger branching fractions, higher reconstruction efficiencies and significant background levels, higher order polynomials are used to ensure a good agreement between the fit and the model. This, however, opens up the possibility of overfitting, where models with a superfluous number of parameters can fit to random fluctuations in the data.

Nevertheless, it is found to be necessary in some tag modes. In particular, in the selection of decays with neutral particles, polynomials up to order five are required in the fit to data to describe small systematic effects in the background distribution, such as partially reconstructed or misidentified decays. In simulation, polynomials up to order eight are used.

In Fig. 5.3, the ΔE distributions of the K^+K^- and $K^-\pi^+$ tag modes are shown, and the fit model is superposed. The $D \to K^+K^-$ mode, which is a SCS decay, shows a smaller signal-to-background ratio, while the CF $D \to K^-\pi^+$ decay has a much higher purity due to its larger branching fraction.

The fit model, which describes the signal as two Gaussian functions with mean μ_1 and μ_2, and standard deviation σ_1 and σ_2, has an average mean of

$$\mu = f\mu_1 + (1-f)\mu_2,$$

and a combined standard deviation of

$$\sigma^2 = f\sigma_1^2 + (1-f)\sigma_2^2 + f(1-f)(\mu_1 - \mu_2)^2.$$

The $3\,\sigma$ signal regions, which are calculated using $\mu \pm 3\sigma$, are indicated in Fig. 5.3 by the vertical dashed lines. Events within this region are retained for the strong-phase analysis. The same ΔE selection requirements are also applied to the double-tag selection, where the ΔE requirements for $D \to K^+K^-\pi^+\pi^-$ are applied to the signal mode as well.

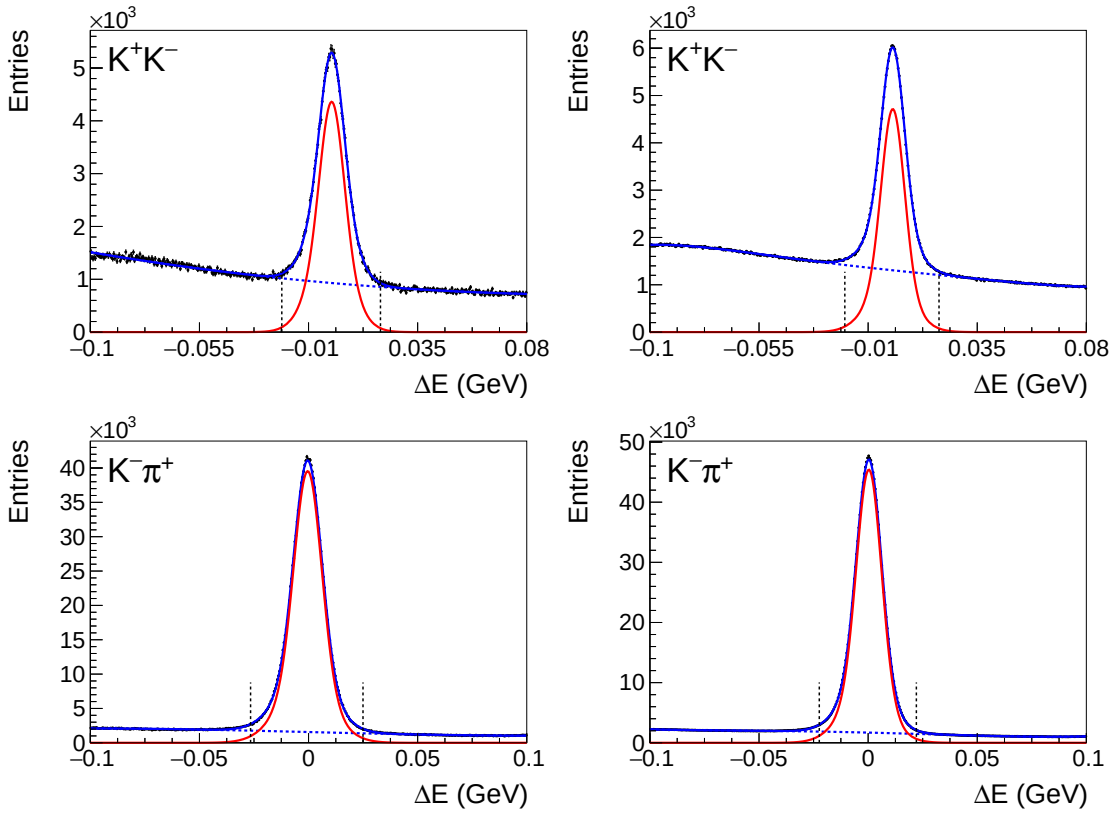

Figure 5.3: The ΔE distribution from (left) data and (right) simulation. The data points are shown in black with uncertainties, while the fit model is the solid blue line. The signal and background components are also plotted as a solid red curve and dotted blue curve, respectively. The vertical dashed lines indicate the $3\,\sigma$ region that is selected.

In tag modes that require photon reconstruction, the resolution is worse compared to fully charged final states. It is therefore expected that the ΔE signal window will be wider, and this is shown for the $K^0_S\pi^0$ tag mode on top of Fig. 5.4. In addition, the ΔE distribution has an asymmetric tail on the left because of material effects where the photon energy can be deposited in the material in front of the EMC, such as the TOF system [88].

In two- and three-body D decays, the combinatorial background is well described by a smooth polynomial function. In four-body decays, it is found from simulation that the presence of multiple candidates can alter the shape of the ΔE distribution. Specifically, since the BESIII processing software by default picks the candidate with the ΔE value closest to zero, events with a large number of tracks are more likely to retain a combination with ΔE near zero. This effect is seen clearly in

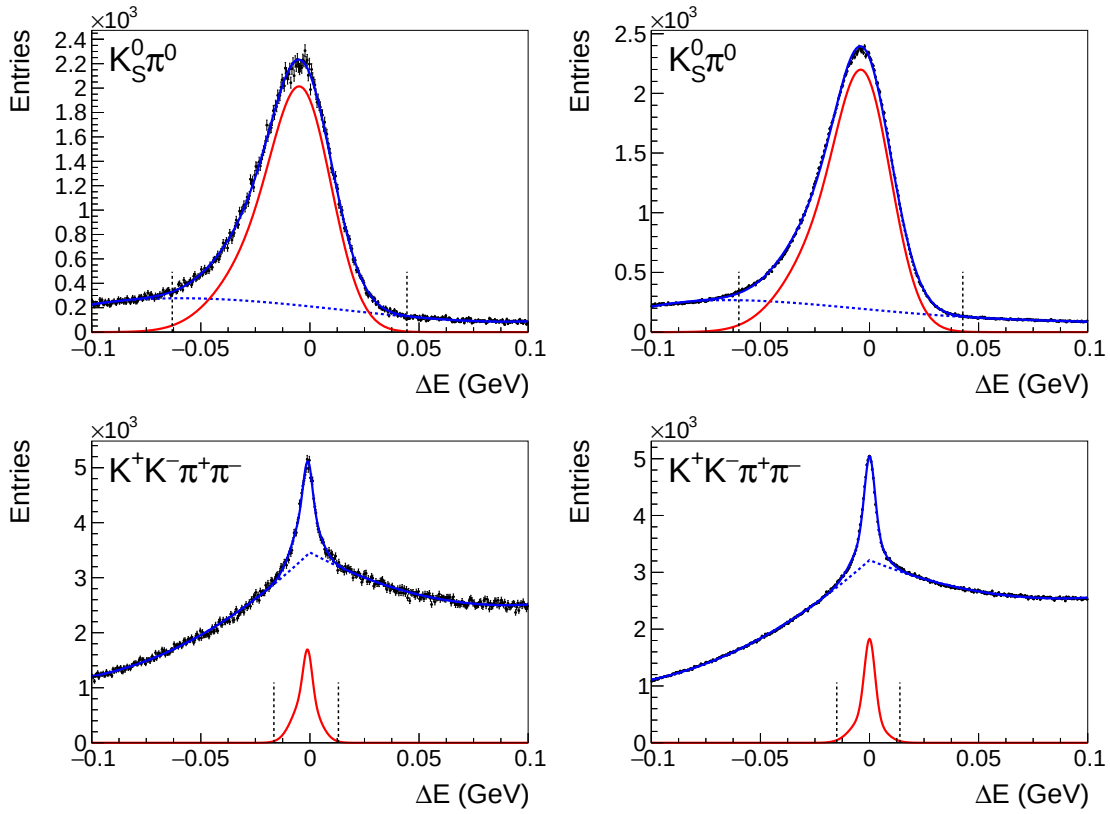

Figure 5.4: The ΔE distribution from (left) data and (right) simulation. The data points are shown in black with uncertainties, while the fit model is the solid blue line. The signal and background components are also plotted as a solid red curve and dotted blue curve, respectively. The vertical dashed lines indicate the $3\,\sigma$ region that is selected.

the lower plots of Fig. 5.4, which show the $K^+K^-\pi^+\pi^-$ signal mode. This decay is a SCS decay with many multiple candidates, and therefore the background is found to have a sharp feature at $\Delta E = 0$.

There are several alternative strategies for picking between multiple candidates that do not introduce peaking structures in the ΔE distribution. An example is to choose a candidate at random. However, it is inevitable that adopting such a strategy will reduce the reconstruction efficiency. Furthermore, the ΔE and $M_{\rm BC}$ variables are found to be uncorrelated, and thus, the determination of yields described in Section 6.1 is not biased by picking a candidate based on its ΔE value. Any alternative strategy is therefore unlikely to improve the analysis.

Instead, the solution is to directly model this effect by allowing the polynomial background to float independently on either side of $\Delta E = 0$, while constraining the

polynomials to be continuous at $\Delta E = 0$. This is found to fit the combinatorial background well, and in fits to simulation samples it is found to reproduce the correct signal shape. This piece-wise continuous polynomial function is used in the $K^-\pi^+\pi^-\pi^+$ and $K^0_S\pi^+\pi^-\pi^0$ tag modes as well, but since these are CF decays, the relative impact of this effect is smaller in these modes.

A summary of the ΔE signal regions in data and simulation is shown in Table 5.5. The regions determined in data are consistently wider that those in simulation.

Table 5.5: ΔE signal regions for fully reconstructed tag modes.

Tag mode	Data (MeV)	Simulation (MeV)
$K^+K^-\pi^+\pi^-$	$[-16.5, 13.1]$	$[-15.0, 13.9]$
$K^0_S\pi^+\pi^-$	$[-25.6, 23.1]$	$[-18.7, 18.8]$
$K^-\pi^+$	$[-26.6, 25.0]$	$[-22.4, 22.1]$
$K^-\pi^+\pi^0$	$[-42.0, 31.9]$	$[-36.6, 28.7]$
$K^-\pi^+\pi^-\pi^+$	$[-22.2, 18.5]$	$[-17.7, 16.4]$
K^+K^-	$[-21.0, 19.7]$	$[-19.6, 19.2]$
$\pi^+\pi^-$	$[-28.5, 27.2]$	$[-23.9, 24.0]$
$K^0_S\pi^0$	$[-63.1, 44.5]$	$[-59.9, 42.8]$
$K^0_S\pi^0\pi^0$	$[-71.9, 53.0]$	$[-59.6, 43.8]$
$K^0_S\eta$	$[-40.9, 38.7]$	$[-39.5, 38.3]$
$K^0_S\eta'_{\pi\pi\eta}$	$[-29.1, 26.7]$	$[-26.9, 25.9]$
$K^0_S\eta'_{\rho\gamma}$	$[-43.9, 34.3]$	$[-35.8, 28.3]$
$\pi^+\pi^-\pi^0$	$[-49.6, 40.7]$	$[-47.0, 37.9]$
$K^0_S\pi^+\pi^-\pi^0$	$[-38.6, 31.2]$	$[-32.8, 26.6]$

5.5 Partially reconstructed decay modes

In the selection of fully reconstructed D decays described in Section 5.4, each D meson is reconstructed separately, which allows for both a single- and a double-tag selection. This is beneficial for the normalisation of double-tag yields, as mentioned in Section 2.8.1, and the selection is also much cleaner since the total energy of each D meson is constrained by the beam energy.

It is also possible to perform a partial-event reconstruction, where one particle in the final state is not reconstructed. The selection starts with a fully reconstructed single-tag selection of one of the D mesons, including the requirements on ΔE.

From the remaining tracks and showers, the other D meson is reconstructed, but with a missing particle. The four-momentum of the missing particle, p_{miss}, is inferred from the reconstructed momenta of the other tracks and showers, and from four-momentum conservation of the e^+e^- interaction.

Since information about the missing energy is required in order to calculate the missing four-momentum, it is not possible to perform a single-tag selection on partially reconstructed decay modes. Furthermore, the variable ΔE does not exist for partially reconstructed D mesons. Therefore, double-tag selections with partially reconstructed decays have a lower signal purity, but provide access to decay modes that are otherwise inaccessible.

5.5.1 Decay with invisible neutrino

The tag mode $D^0 \to K^-e^+\nu_e$ is partially reconstructed with a missing neutrino ν_e, which does not leave any signature in the BESIII detector. Since the tag mode is partially reconstructed, the fully reconstructed D meson is the signal mode $K^+K^-\pi^+\pi^-$. To remove combinatorial background, only events where the beam-constrained mass of the signal mode satisfies $M_{\text{BC}} \in [1.855, 1.875]\,\text{GeV}/c^2$ are considered. From the remaining tracks and showers, only events with a good charged track identified as a kaon and a good charged track identified as an electron are kept for further analysis. Events with additional tracks are rejected.

The discriminating variable for the $K^-e^+\nu_e$ tag mode is

$$U_{\text{miss}} = E_{\text{miss}} - |\vec{p}_{\text{miss}}|, \tag{5.3}$$

where E_{miss} and $\vec{p}_{\text{miss}}$ are the missing energy and momentum, respectively. For a missing neutrino, U_{miss} has a signal peak at zero. A demonstration of such a reconstruction performed using a BESIII simulation sample is shown on top in Fig. 5.5. A small tail on the right of the signal peak is seen due to FSR from the e^+ lepton.

5.5.2 Tag modes with missing K_L^0 meson

There are several important D-decay modes that involve a $K_{\rm L}^0$ meson, which due to its long lifetime travels through the whole BESIII tracking volume. It is possible to detect its presence by looking for showers in the EMC, which are in fact hadronic interactions of the $K_{\rm L}^0$ meson with the detector material. However, it has been found that treating it as an invisible particle provides a better selection efficiency and a higher signal purity.

In this thesis, the only tag modes containing a $K_{\rm L}^0$ meson are the $D \to K_{\rm L}^0\pi^0$ and $K_{\rm L}^0\pi^+\pi^-$ decays. The single-tag selection of the signal mode $K^+K^-\pi^+\pi^-$ proceeds in an identical manner to that described for the missing ν_e in Section 5.5.1, including the requirements on $M_{\rm BC}$ and ΔE. From the other D decay, a single π^0 candidate is reconstructed in the $K_{\rm L}^0\pi^0$ tag, and any events containing additional π^0 and η candidates are rejected. Furthermore, events with additional tracks are also removed from the sample, and this requirement is effective at removing decays with $K_{\rm S}^0 \to \pi^+\pi^-$ candidates where the charged pions do not obey the good track requirements. The procedure for reconstructing the $D \to K_{\rm L}^0\pi^+\pi^-$ decay is analogous to that of $K_{\rm L}^0\pi^0$.

The variable that discriminates signal and background decays is the missing-mass squared,

$$M^2_{\rm miss} = E^2_{\rm miss} - |\vec{p}_{\rm miss}|^2, \tag{5.4}$$

which has a peaking distribution centred at the $K_{\rm L}^0$ mass. A reconstruction of $D \to K_{\rm L}^0\pi^0$ performed on BESIII simulation is shown on the left in Fig. 5.5. The distribution has a large tail on the right due to imperfect reconstruction of photon energies, and it is the same effect that causes the asymmetric distributions of ΔE in Fig. 5.4.

5.5.3 Partial reconstruction of the $D^0 \to K^+K^-\pi^+\pi^-$ decay

The analysis in Ref. [87] performed a study of tracking efficiencies of charged pions and kaons in momentum bins. It was found that for pion momenta greater than

0.1 GeV/c, which is the momentum range of interest to this analysis, the tracking efficiency of pions is over 90%. Kaons, on the other hand, have a tracking efficiency of under 75% at 0.3 GeV/c, which drops to 20% for kaons around 0.1 GeV/c.

The poor tracking efficiency of kaons has a particularly large impact on the decay $D \to K^+K^-\pi^+\pi^-$. The similar decays $D \to K^-\pi^+\pi^-\pi^+$ [89] and $D \to \pi^+\pi^-\pi^+\pi^-$ [44] have selection efficiencies that are almost two and three times greater, respectively. The reason is that the momentum spectrum of the kaons from $D \to K^+K^-\pi^+\pi^-$ is much lower than that of the other charged four-body D-decay modes.

To mitigate the low tracking efficiencies of kaons, a statistically independent selection is performed where one of the charged kaons of $D \to K^+K^-\pi^+\pi^-$ is not reconstructed. Since this selection has a partially reconstructed signal mode, the fully reconstructed single-tag selection is performed on the tag mode. Only the tag modes K^+K^-, $K^0_S\pi^0$ and $K^0_S\pi^+\pi^-$ are considered together with a partially reconstructed signal mode, because the poorer purity makes this analysis unfeasible for other tag modes with lower yields.

For the K^+K^- tag, the single-tag selection of two charged kaons is performed first. From the remaining tracks and showers, events with two good pion tracks of opposite charge and a single kaon track of any charge are retained, but no requirement is imposed on the number of tracks that do not satisfy the good track requirements.

The discriminating variable for the partial reconstruction of $K^+K^-\pi^+\pi^-$ is also M^2_{miss}, as defined in Eq. (5.4). An example of a reconstruction of a BESIII simulation sample is shown on the right in Fig. 5.5. A clean and symmetric distribution is seen, with a good mass resolution, since this final state only involves charged-particle tracks in the reconstruction.

The dominant background in this $K^+K^-\pi^+\pi^-$ selection are $D \to K^-\pi^+\pi^-\pi^+\pi^0$ decays, where a π^+ is misidentified as a K^+ and the π^0 is not reconstructed. This background is mostly removed by the ΔE requirements in the full reconstruction, but for the partial reconstruction it is a challenging background to distinguish from signal decays. The purity is found to improve by rejecting any events with π^0 candidates, or events where the kaons from $K^+K^-\pi^+\pi^-$ have an energy greater than

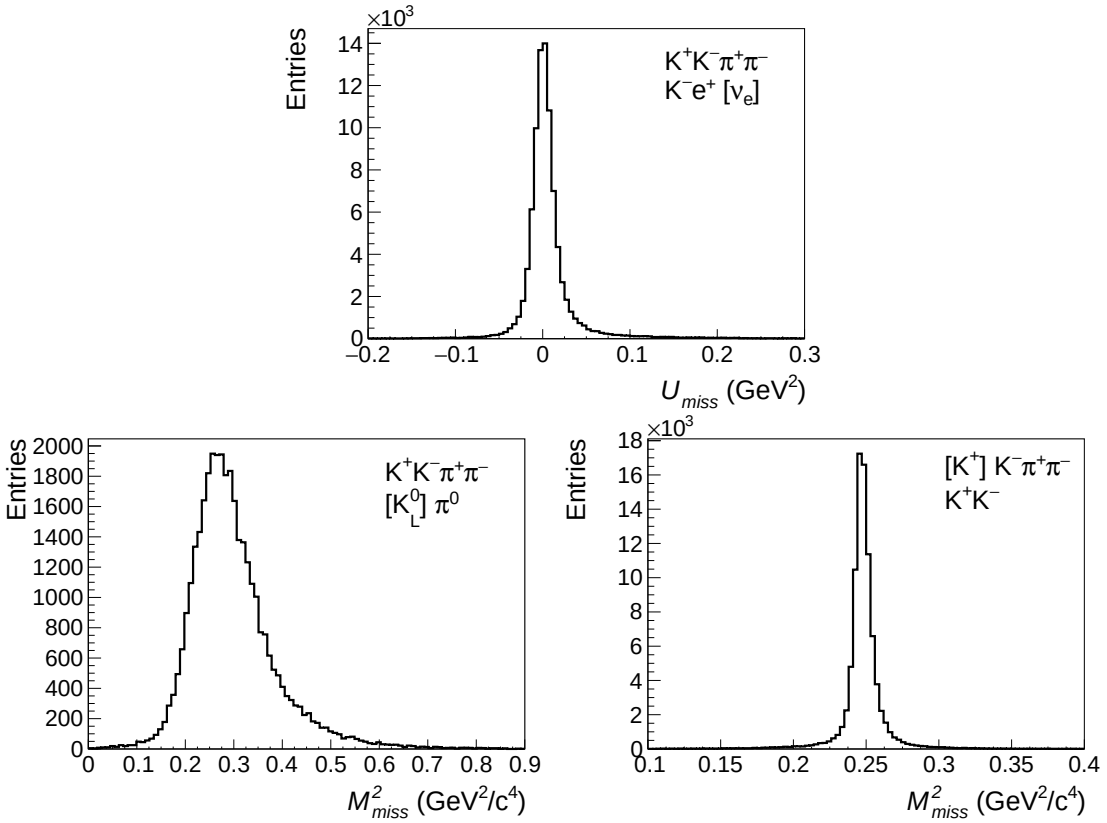

Figure 5.5: BESIII simulation of the $U_{\rm miss}$ and $M^2_{\rm miss}$ distributions of partially reconstructed $D \to K^0_{\rm L}\pi^0$, $K^-e^+\nu_e$ and $K^+K^-\pi^+\pi^-$. The label in the top right corner indicates the signal mode on the top and tag mode at the bottom, with the missing particle in square parentheses.

0.7 GeV. Additionally, by requiring $M^{\rm tag}_{\rm BC} \in [1.86, 1.87]\,{\rm GeV}/c^2$, the combinatorial background level is also reduced.

The samples of fully and partially reconstructed $D \to K^+K^-\pi^+\pi^-$ are selected in a mutually exclusive manner by requiring that the partially reconstructed mode has exactly three good charged tracks. In the fully reconstructed mode, all four D daughters are reconstructed from good charged tracks.

5.6 Kalman kinematic fit

In decay modes that are phase-space binned, it is crucial to minimise the level of bin-migration effects, which happen when a D decay is reconstructed in the wrong bin due to the finite momentum resolution of the D daughters. To improve the momentum resolution, a Kalman kinematic fit [90] is performed on the charged

D-daughter tracks. The fit recalculates the track momenta, under the constraint that the reconstructed D-meson invariant mass is equal to its PDG value [21].

The improvement in the momentum resolution in the x-direction of the $D \to K^+K^-\pi^+\pi^-$ decay is shown in Fig. 5.6 for each D daughter, and the other momentum components show a similar behaviour. It is found that the charged kaons initially have much worse momentum resolution than the charged pions, but after the kinematic fit the difference is resolution is reduced.

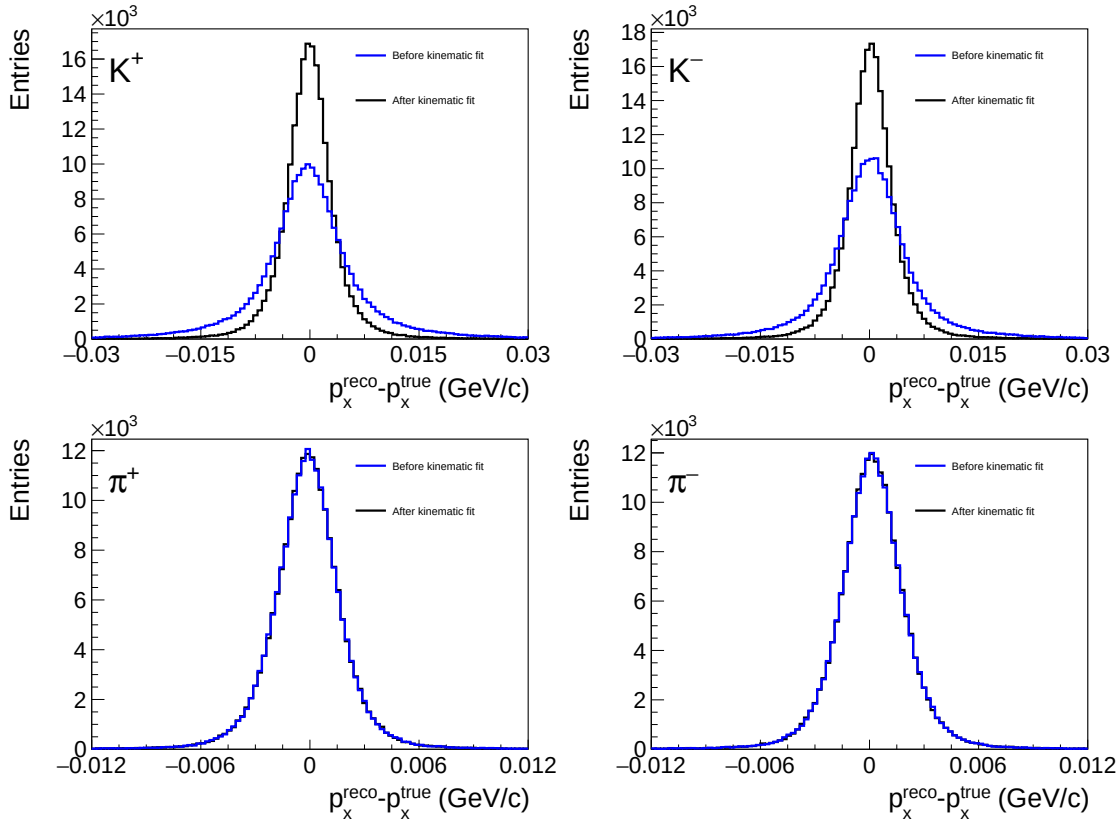

Figure 5.6: A comparison of the charged kaon and pion momenta before and after a Kalman kinematic fit, using a sample of BESIII simulation of $D^0 \to K^+K^-\pi^+\pi^-$.

In fully reconstructed decay modes, each D meson is kinematically refitted separately, since each D meson can be reconstructed independently of the other D decay. However, in partially reconstructed events, the full $D\overline{D}$ event is refitted together, since there is insufficient information from the partially reconstructed D meson alone to perform the fit. After the fit, the recalculated D daughter momenta are used in the phase-space bin determination.

If the χ^2 of the kinematic fit is greater than 200, the fit quality is poor and the result is not used in the subsequent analysis. Instead, the non-fitted D daughter momenta are used to determine the phase-space bin. In the BESIII simulation, the occurrence of fit failures is negligible, but in the presence of background decays this can occur.

5.7 Reweighting of phase-space distributions

One of the important uses of the BESIII simulation of $D^0 \to K^+K^-\pi^+\pi^-$ decays in this measurement is the determination of selection efficiencies in each bin and the level of bin-migration effects. However, these effects are highly sensitive to the phase-space distributions of the D decay. Specifically, the tracking efficiencies of kaons and pions are momentum dependent, and thus dependent on the resonant structure of the decay.

The BESIII simulation is generated using the model from Ref. [38]. The invariant-mass distributions of five independent combinations of D daughters from a sample of generated events in the BESIII simulation sample, before detector reconstruction, are shown in blue in Fig. 5.7. For comparison, the same model is used to generate a sample of D decays in AmpGen, which is shown in black. As expected, a perfect agreement is found.

The distributions in Fig. 5.7 describe the decay of a pure D^0 decay. However, in a double-tag event, the *CP* content of the tag mode can alter these phase-space distributions. In particular, if the tag mode is *CP*-odd, the signal decay $D \to K^+K^-\pi^+\pi^-$ will be that of a *CP*-even decay. Effectively, any *CP*-odd amplitude of this decay will be suppressed, and this can indirectly affect efficiency and bin-migration calculations.

To account for these effects, the BESIII simulation samples are reweighted such that the phase-space distributions match those of the *CP*-even D decay. This is performed using a Boosted Decision Tree (BDT) [91] implemented in the hep_ml framework [92]. The results are shown in blue in Fig. 5.8, with the AmpGen *CP*-even model shown in black for comparison. A good agreement is found.

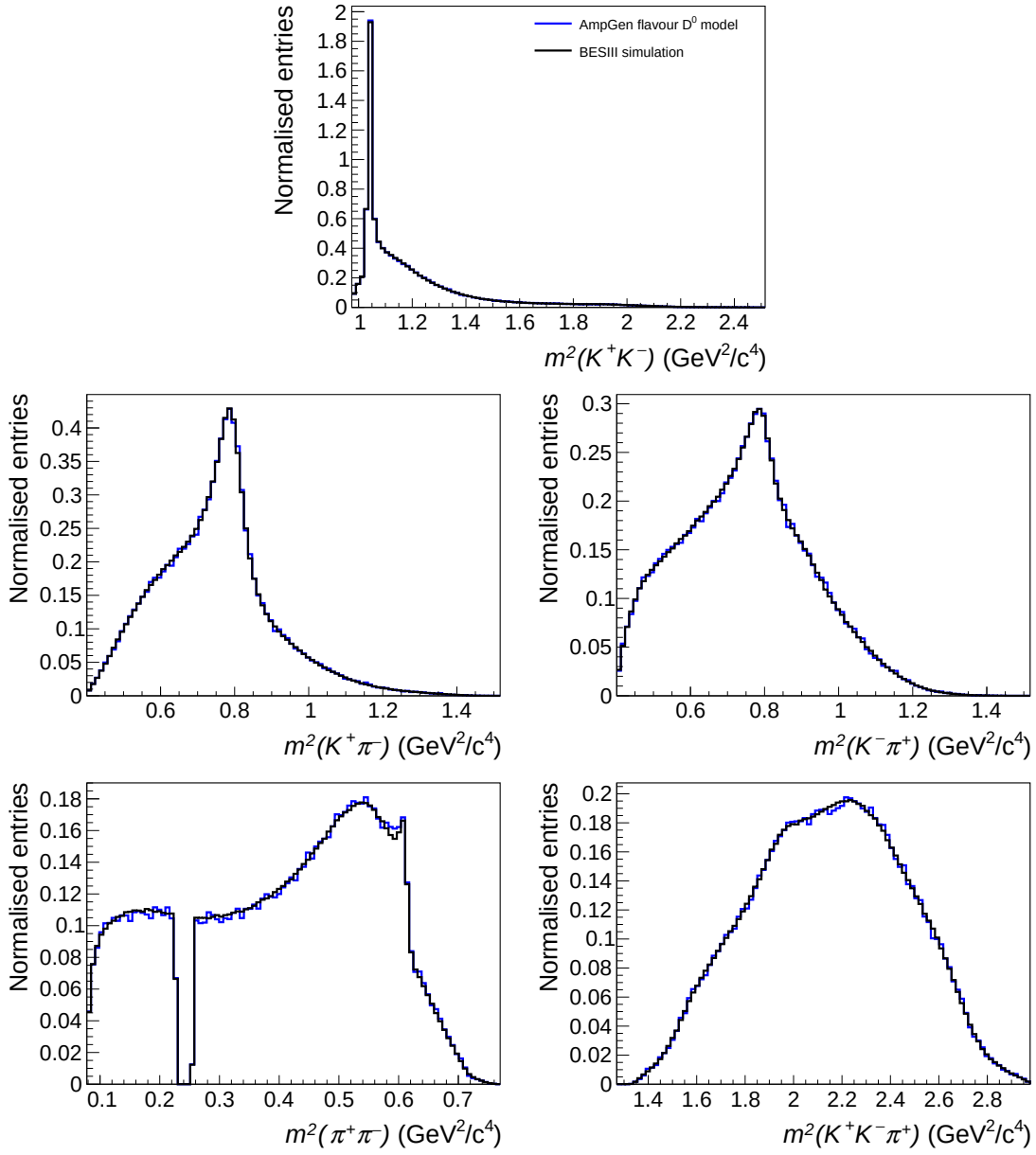

Figure 5.7: A comparison of five independent invariant-mass distributions between a sample of $D^0 \to K^+K^-\pi^+\pi^-$ decays generated in AmpGen, shown in blue, and a BESIII simulation sample before detector reconstruction, shown in black. Both generators use the model from Ref. [38].

An identical approach is also performed when the tag mode is *CP*-even, which projects out the *CP*-odd amplitudes of the $D \to K^+K^-\pi^+\pi^-$ decay. The results are shown in Fig. 5.9. An important difference between Fig. 5.8 and Fig. 5.9 is the $\pi^+\pi^-$ invariant-mass distribution, which is shown on the left at the bottom. In the *CP*-even $D \to K^+K^-\pi^+\pi^-$ model in Fig. 5.8, a prominent ρ^0 resonance

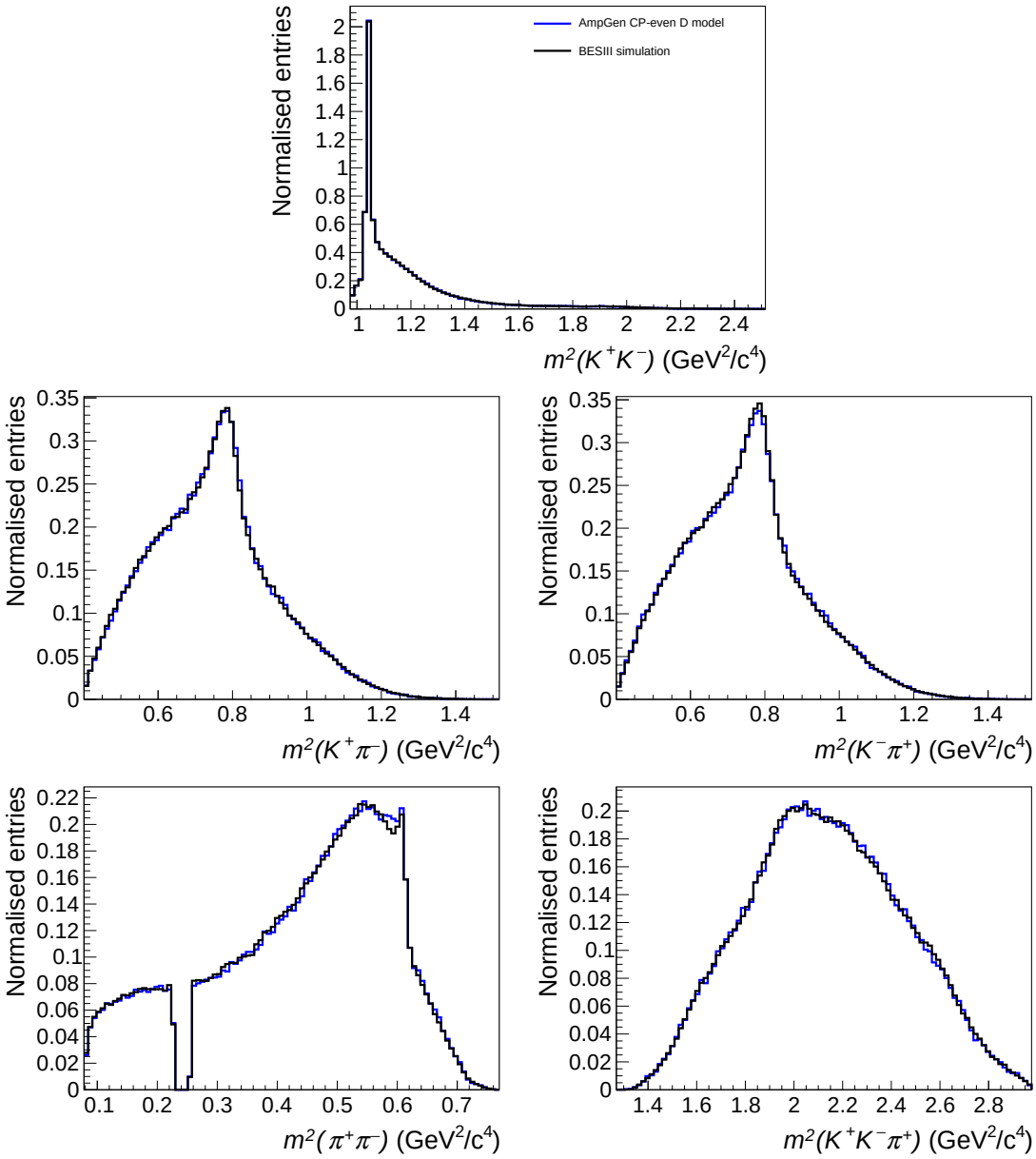

Figure 5.8: A comparison of five independent invariant-mass distributions between a sample of *CP*-even $D \to K^+K^-\pi^+\pi^-$ decays generated in AmpGen, shown in blue, and a BESIII simulation sample before detector reconstruction, shown in black. Both generators use the model from Ref. [38] and the BESIII simulation is reweighted to match the distributions of a *CP*-even D decay.

is seen, but it is mostly absent in Fig. 5.9.

This has a direct impact on the reconstruction efficiency, since the $\pi^+\pi^-$ distribution of *CP*-odd $D \to K^+K^-\pi^+\pi^-$ decay is mostly concentrated towards lower values of $m^2(\pi^+\pi^-)$, or equivalently higher $K^\pm$ momenta. As discussed in Section 5.5.3, the charged kaon tracking efficiency drops quickly at low momenta, and

thus the *CP*-odd $D \to K^+K^-\pi^+\pi^-$ decay is expected to have a higher reconstruction efficiency than that of the *CP*-even decay.

In simulation, it is found that *CP*-odd $D \to K^+K^-\pi^+\pi^-$ decays are reconstructed with an efficiency that is approximately 10% higher than corresponding *CP*-even decays.

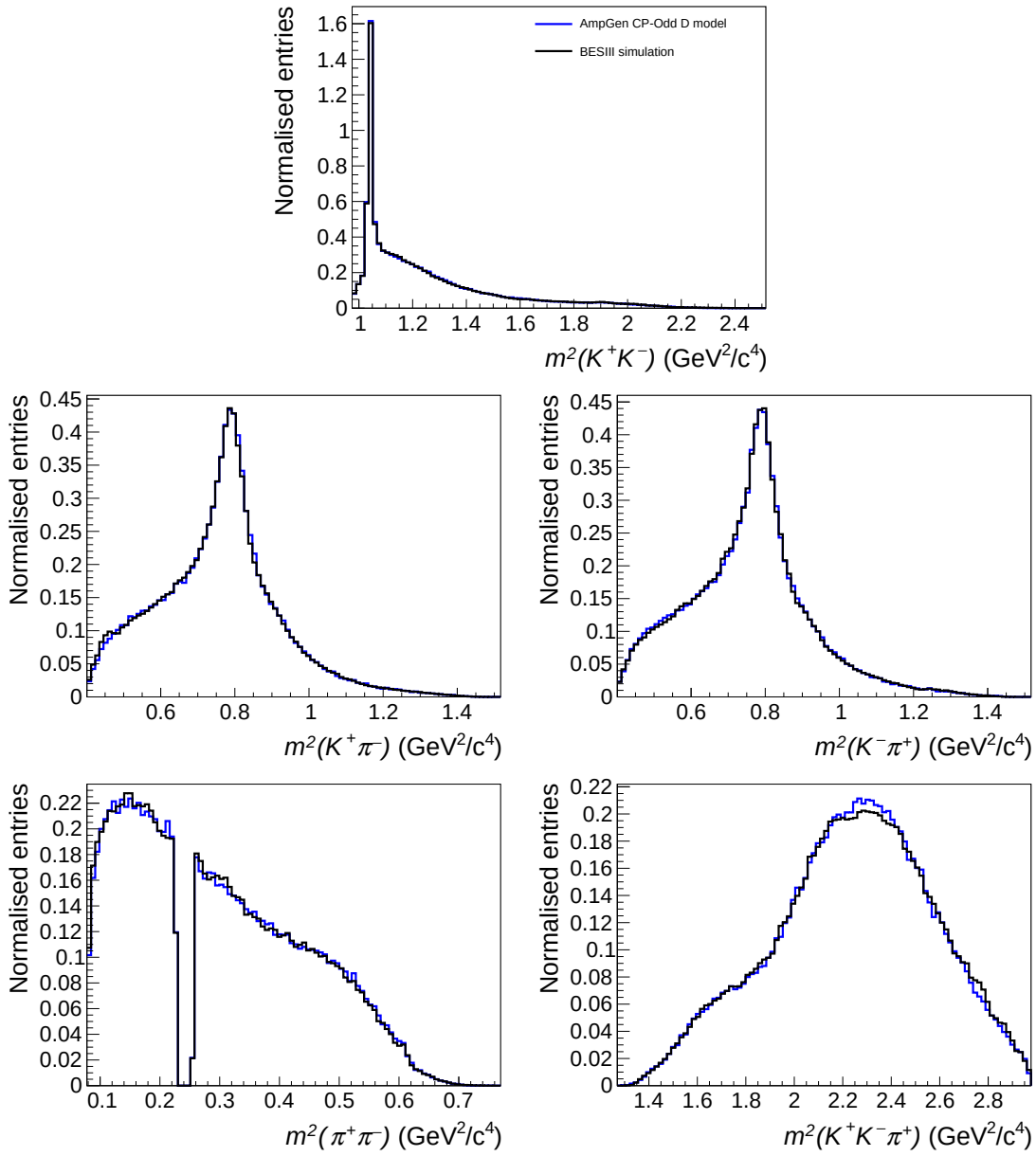

Figure 5.9: A comparison of five independent invariant-mass distributions between a sample of *CP*-odd $D \to K^+K^-\pi^+\pi^-$ decays generated in AmpGen, shown in blue, and a BESIII simulation sample before detector reconstruction, shown in black. Both generators use the model from Ref. [38] and the BESIII simulation is reweighted to match the distributions of a *CP*-odd D decay.

6

Measurement of strong-phase differences

Contents

This chapter uses the selection of single- and double-tag events described in Chapter 5 to determine the strong-phase parameters of $D^0 \to K^+K^-\pi^+\pi^-$, using the formalism from Section 2.8. The analysis can be split into two parts. First, the

single- and double-tag yields are determined for each tag mode. In the second part, these yields are interpreted in terms of the strong-phase difference and other nuisance parameters.

6.1 Maximum likelihood fit of single- and double-tag yields

6.1.1 Invariant mass fit model

The single-tag yield of each tag mode is determined using a maximum likelihood fit of the beam-constrained mass $M_{\rm BC}$. The Probability Density Function (PDF) that describes the $M_{\rm BC}$ distribution, which is referred to as the fit model, is used to construct a binned likelihood function from the data set of single-tag events, according to Eq. (A.4).

The fit model consists of three components. First, the PDF of signal decays is obtained directly from a BESIII simulation sample, which is different for each tag mode, using Kernel Density Estimation (KDE) [93]. The PDF obtained from KDE is convolved with a resolution function to account for differences in the resolution between data and simulation. An example of fit models using KDE is shown in Fig. 6.1, with the model shown in blue. A good agreement is found between the model and the data points, which is the simulation sample used to construct the model. Additionally, the $K^0_S\pi^0$ tag mode on the right is seen to have a worse mass resolution due to the π^0 reconstruction, compared to the fully charged $K^+K^-\pi^+\pi^-$ mode on the left.

In single-tag yield fits with a large number of events, which are the $K^-\pi^+$, $K^-\pi^+\pi^0$, $K^-\pi^+\pi^-\pi^+$ and $K^0_S\pi^+\pi^-$ tag modes, the resolution function is a double Gaussian function. In the other tag modes, a single Gaussian function is found to provide an adequate description of the resolution differences. In the fit, the mean and standard deviation of the Gaussian resolution functions are free parameters.

The second PDF component is a combinatorial background without any peaking structures. It is modelled with an Argus function [94], which is a smooth distribution with a kinematic end point at $M_{\rm BC} = 1.8865\,{\rm GeV}/c^2$ due to the fixed beam-energy

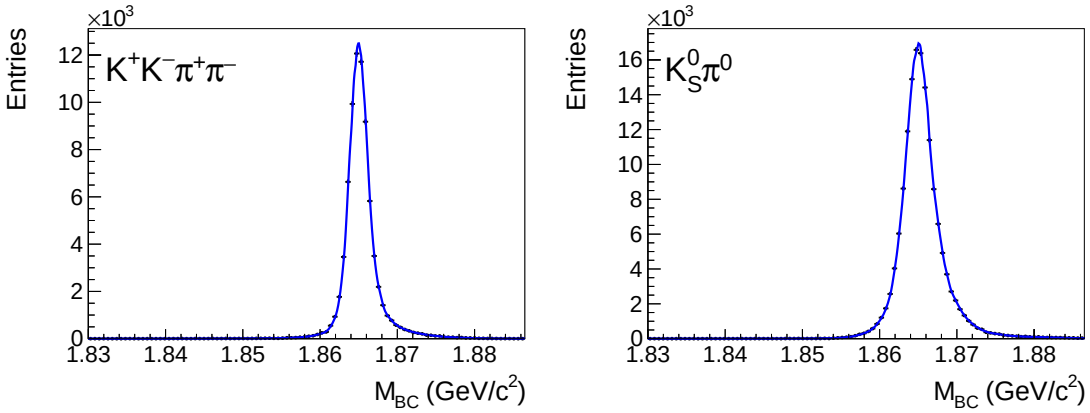

Figure 6.1: Examples of a fit model derived from BESIII simulation using KDE, with the $D^0 \to K^+K^-\pi^+\pi^-$ decay on the left and $D^0 \to K^0_S\pi^0$ decay on the right. The model is shown as a solid blue line, while the black data points show the simulation sample used to construct the model.

constraint. The Argus distribution has a single parameter that describes its shape, and in the fit this parameter is allowed to vary.

The third component of the fit model is referred to as the peaking background, which has peaking structures that cannot be described by a flat distribution, such as the Argus function. Each tag mode also has a different set of peaking backgrounds, each with different peaking shapes that need to be modelled. The determination of these PDFs is described in Section 6.1.3, and their shapes are kept fixed in the fit.

In order to normalise the fit model PDF, the likelihood function is extended to include Poisson-likelihood terms, analogous to Eq. (A.4), which describe the yield of each component. The yield of signal and combinatorial background are free parameters in the fit, while those of the peaking backgrounds are fixed to the values determined in Section 6.1.3. All yields are restricted to be strictly non-negative.

To determine the double-tag yield of fully reconstructed tag modes, an analogous fit is performed to the beam-constrained mass $M_{\rm BC}$ of the signal mode. The resolution function is a single Gaussian distribution for all double-tag modes. The data set of double-tag events is much smaller than that of single-tag events, and therefore an unbinned likelihood function is constructed, using Eq. (A.1). Similar to the single-tag selection, the combinatorial background is also modelled with an Argus function.

In partially reconstructed modes, the fit setup is similar, with $U_{\rm miss}$ or $M^2_{\rm miss}$ being the discriminating variable. The absence of a beam-energy constraint results in a combinatorial-background distribution which does not have a kinematic end point. Therefore, a first-order polynomial function is used to model this background, where both the slope and constant y-offset are allowed to vary in the fit.

The binning scheme of the $D^0 \to K^+K^-\pi^+\pi^-$ decay is that described in Chapter 3, which has $2 \times 4 = 8$ bins. Therefore, for each flavour tag, eight bin yields are determined. In *CP*-tags, Eq. (2.29) is invariant under the transformation $i \to -i$, and therefore bins i and $-i$ can be merged, which results in only four bin yields. Similarly, for SCMB tags, described by Eq. (2.23), the tag side bin can be restricted to $j > 0$ due to the equivalence of bin $(i, j) \to (-i, -j)$, and the total number of bin combinations is $2 \times 4 \times 8 = 64$.

6.1.2 Calculation of efficiency and bin-migration effects

The single- and double-tag yields must be corrected for reconstruction efficiencies in order to be interpreted. For single-tag yields, the efficiency $\epsilon^{\rm ST}$ is simply determined using large samples of BESIII simulation for each tag mode. The efficiency is calculated by taking the number of events that pass the full selection, divided by the number of generated events. The uncertainty is assumed to follow a binomial distribution.

For the double-tag yields, the bin efficiencies are calculated analogously, but the effects of bin migration must also be accounted for. These are both contained in the efficiency matrix, which is defined as

$$\epsilon^{\rm DT}_{ij} \equiv \frac{\text{Events reconstructed in bin } i}{\text{Events generated in bin } j}.$$

The diagonal elements of the efficiency matrix, which are interpreted as bin efficiencies, may differ by 1%-2% between phase-space bins due to differences in decay kinematics. The off-diagonal elements describe bin migration and are all less than 15%.

6.1.3 Peaking background estimation from simulation

In the fit of yields, peaking backgrounds must be carefully accounted for in order to avoid biases in the signal yield. However, due to the similarity in the PDF shape between signal decays and peaking backgrounds, these components are fixed in the fit. The impact of the assumptions made in fixing these parameters is assessed as a systematic uncertainty in Section 6.3.

The D-decay modes that contribute to the peaking backgrounds in each tag mode are identified using the inclusive BESIII simulation sample, which contains all known D decays. The tool TopoAna [95] is used to sort different decay topologies and systematically categorise different peaking backgrounds. For decays that have a non-negligible contribution, larger dedicated simulation samples are generated for the accurate determination of the yield and PDF shape.

Table 6.1: Background-to-signal ratio and the shape of peaking backgrounds in the single-tag yield fit.

Decay mode	Background decay	Ratio (10^{-2})	Shape parameterisation
$K^+K^-\pi^+\pi^-$	$K^0_S K^+K^-$	1.41 ± 0.12	Double Gaussian
$K^-\pi^+\pi^-\pi^+$	$K^0_S K^+\pi^-$	0.95 ± 0.10	Double Crystal Ball
$\pi^+\pi^-\pi^0$	$K^0_S\pi^0$	5.1 ± 0.9	Double Crystal Ball
$K^0_S\pi^0\pi^0$	$\pi^+\pi^-\pi^0\pi^0$	0.44 ± 0.07	Double Gaussian
$K^0_S\pi^0\pi^0$	$K^0_S K^0_S$	0.48 ± 0.06	Double Crystal Ball
$K^0_S\pi^0\pi^0$	$K^0_S\pi^0\gamma$	0.042 ± 0.006	Double Crystal Ball
$K^0_S\pi^0$	$\pi^+\pi^-\pi^0$	0.26 ± 0.05	Double Gaussian
$K^0_S\eta$	$\pi^+\pi^-\eta$	0.0271 ± 0.0032	Double Gaussian
$K^0_S\eta'(\pi^+\pi^-\gamma)$	$K^0_S\pi^+\pi^-\pi^0$	3.1 ± 0.5	Crystal Ball
$K^0_S\pi^+\pi^-$	$\pi^+\pi^-\pi^+\pi^-$	0.235 ± 0.018	Double Crystal Ball

To minimise any systematic dependence on the normalisation of peaking backgrounds, the yield of each peaking-background contribution is fixed as a ratio relative to the signal yield. This background-to-signal ratio is calculated as

$$\frac{\epsilon(\text{background})}{\epsilon(\text{signal})} \times \frac{\text{BF}(\text{background})}{\text{BF}(\text{signal})}$$

where BF is the branching fraction taken from the PDG [21] and ϵ(signal) is the signal efficiency, which is calculated using the approach described in Section 6.1.2. The background retention ϵ(background) is calculated analogously to the signal efficiency, using a simulation sample of background decays that undergo the same selection as that of signal.

Table 6.1 shows the resulting background-to-signal ratios. Most contributions are smaller than 1.5% of the signal yield, with the exception of the $K^0_S\pi^0$ and $K^0_S\pi^+\pi^-\pi^0$ contaminations in the $\pi^+\pi^-\pi^0$ and $K^0_S\eta'(\pi^+\pi^-\gamma)$ tag modes. These particular backgrounds are CF decays with large branching fractions.

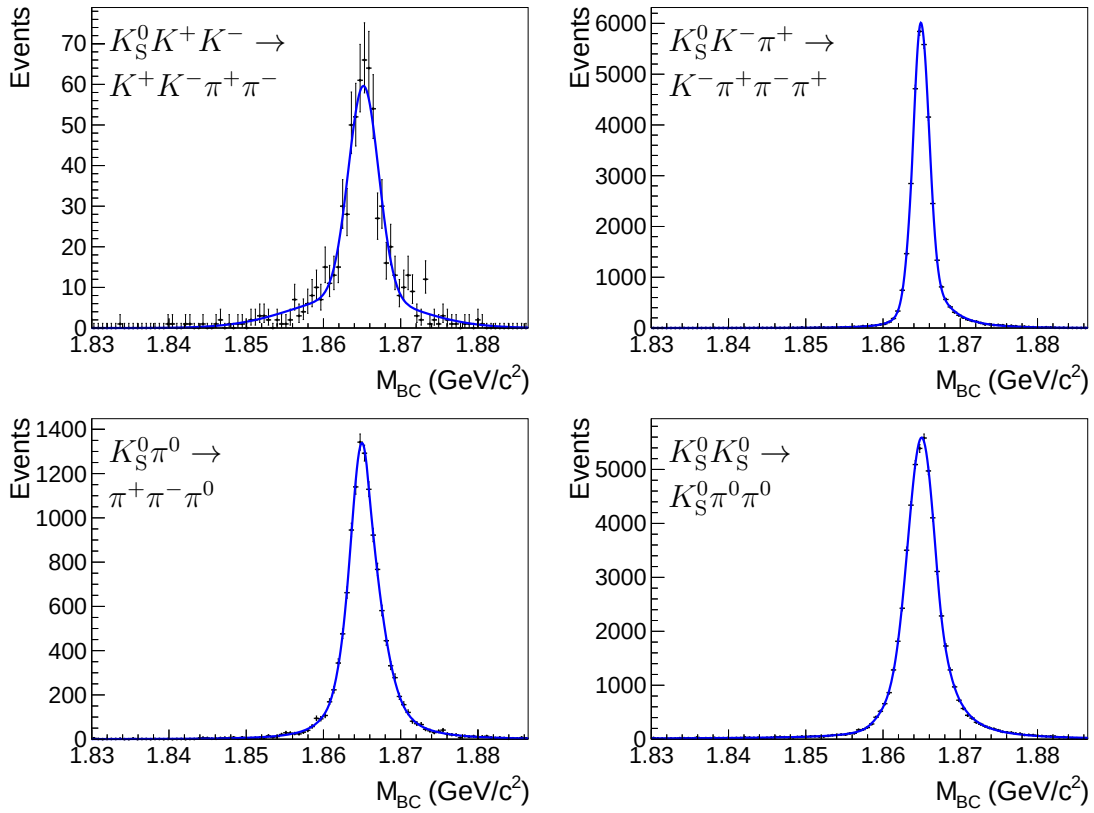

Figure 6.2: Examples of Gaussian and Crystal Ball functions fitted to simulated background-decay $M_{\rm BC}$ distributions. The top left corner indicates the background decay mode on top and the reconstructed tag mode below.

To model the $M_{\rm BC}$ distribution of peaking backgrounds, a combination of Crystal Ball functions, which are Gaussian functions with a power law tail, or Gaussian functions, are fitted to the distributions obtained from the simulation samples. The choice of model is empirical and the fit quality of each shape is checked to ensure a

good agreement between the simulation sample and the model. The model used for each peaking background is listed in the last column of Table 6.1. Figure 6.2 shows four examples of peaking backgrounds that are fitted with an empirical model. In the top left plot, the $K^0_S K^+ K^-$ background in the $K^+K^-\pi^+\pi^-$ signal mode has been fitted with a double Gaussian function, while the other three plots show similar fits to other background modes with a double Crystal Ball function. After the PDFs of these backgrounds have been determined, the parameters describing their PDFs are fixed in the maximum likelihood fit of the single-tag yields.

In the determination of double-tag yields, the peaking backgrounds are treated in an identical manner, but the background-to-signal ratios are determined in each bin. Since peaking backgrounds are small, bin-migration effects are neglected. Furthermore, peaking backgrounds can occur on either the signal mode or the tag mode. It is assumed that peaking background contributions in the signal mode and the tag mode are factorisable, and these are therefore treated independently. Background contributions from both signal and tag modes simultaneously are neglected.

6.1.4 Corrections to quantum correlation effects

The calculation of background-to-signal ratios in Section 6.1.3 uses branching fractions of D^0 decays that are originally in a flavour eigenstate. In $D\overline{D}$ events at the charm threshold, it is not always the case that the D mesons decay into a flavour-specific decay, and in general the decay rate of a particular D-meson decay mode can either be enhanced or suppressed, depending on the CP content of the other D meson decay. These effects are not accounted for by the BESIII simulation used in this analysis.

Thus, the yield of peaking-background contributions of double-tag events that are calculated in Section 6.1.3 must be corrected for such quantum-correlation effects. The correction factors can be determined from Eqs. (2.23),(2.28) and (2.29), using the same formalism that describes the quantum-correlation effects of the signal mode $D^0 \to K^+K^-\pi^+\pi^-$. The calculation requires knowledge of the strong-phase parameters c_i, s_i and K_i, which are the parameters that this analysis is attempting

to determine. To circumvent this circular dependence, initially the model predictions from Table 3.4 are used. After preliminary results of c_i and s_i are obtained, the calculations are updated using the model-independent measurement. Since the peaking backgrounds are in general very small, any imperfections associated with this iterative procedure have negligible impact on the measurement.

Table 6.2: Quantum-correlation correction factors for the peaking backgrounds on the tag side in *CP* tags in bins 2 and 3.

Bin number →		2	3
Tag mode	Background		
$\pi^+\pi^-\pi^0$	$K^0_S\pi^0$	5.2 ± 1.0	7.6 ± 2.0
$K^0_S\pi^0\pi^0$	$\pi^+\pi^-\pi^0\pi^0$	3.4 ± 2.5	5 ± 4
$K^0_S\pi^0\pi^0$	$K^0_S\pi^0\gamma$	3.4 ± 2.5	5 ± 4
$K^0_L\pi^0$	$K^0_L\pi^0\pi^0$	5.8 ± 1.2	9.3 ± 2.8
$K^0_L\pi^0$	$K^0_S\pi^0$	5.8 ± 1.2	9.3 ± 2.8
$K^0_S\pi^0$	$\pi^+\pi^-\pi^0$	0.19 ± 0.04	0.13 ± 0.04
$K^0_S\eta$	$\pi^+\pi^-\eta$	0.6 ± 0.4	0.6 ± 0.4
$K^0_S\eta'_{\pi^+\pi^-\gamma}$	$K^0_S\pi^+\pi^-\pi^0$	0.805 ± 0.012	0.790 ± 0.012

Analogous to the background-to-signal ratios calculated in Section 6.1.3, the quantum-correlation corrections are also calculated as ratios of yield enhancement or suppression between the background and signal yields. To obtain the correct background-to-signal ratio, the numbers from Section 6.1.3 must be multiplied by these corrections, which by definition are equal to unity in the absence of quantum-correlation effects.

To illustrate some extreme cases of such effects, the quantum-correlation correction factors for the peaking backgrounds in the *CP* tags are shown in Table 6.2 for bins 2 and 3. The *CP* content of pure *CP*-eigenstate decays are taken from Ref. [21], while for the $\pi^+\pi^-\pi^0$ and $K^0_S\pi^+\pi^-\pi^0$ decays, their *CP*-even fractions are obtained from Ref. [46] and [85], respectively. In decays of unknown *CP* content, such as $D^0 \to \pi^+\pi^-\pi^0\pi^0$ or $D^0 \to K^0_S\pi^0\gamma$, it is assumed that $F_+ = 0.5 \pm 0.5$.

Many of the corrections in Table 6.2 are very large, such as the $K^0_L\pi^0\pi^0$ background in the $K^0_L\pi^0$ tag, which are two decays of opposite *CP* eigenvalue. The $D^0 \to K^+K^-\pi^+\pi^-$ amplitude model [38] predicts that bins 2 and 3 are mostly

CP-even, and therefore the signal yield of *CP*-even tag modes are heavily suppressed, while *CP*-odd backgrounds in these bins are enhanced. Similarly, the corrections for the $\pi^+\pi^-\pi^0$ background in the $K^0_S\pi^0$ tag are very small, as this background is heavily suppressed by quantum correlations.

The quantum-correlation corrections of flavour tags are calculated in an analogous manner. The $D^0 \to K^-\pi^+\pi^-\pi^+$ decay is the only flavour tag where quantum-correlation effects must be accounted for due to the $D^0 \to K^0_S K^-\pi^+$ background. The non-trivial *CP* content of this background is taken from Ref. [96].

For the SCMB $K^0_S\pi^+\pi^-$ and $K^0_L\pi^+\pi^-$ tag modes, the dominant peaking backgrounds are $D^0 \to \pi^+\pi^-\pi^+\pi^-$ and $D^0 \to K^0_S\pi^+\pi^-$, respectively. In the latter case, the decay $K^0_S \to \pi^0\pi^0$ is not reconstructed, thus faking the behaviour of a missing K^0_L meson. Quantum-correlation corrections of these backgrounds are calculated using strong-phase information from Refs. [46, 56].

Since single-tag events are not affected by quantum-correlation effects, it is not necessary to perform corrections to peaking backgrounds in single-tag fits.

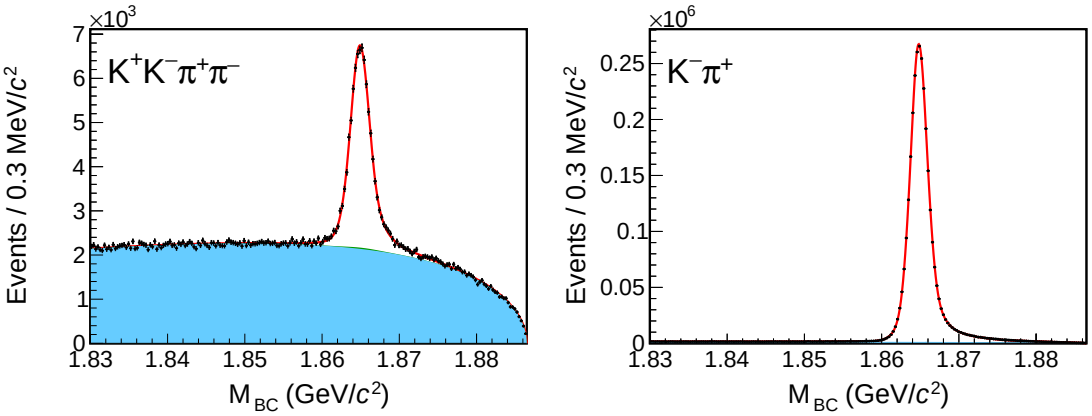

Figure 6.3: Single tag $M_{\rm BC}$ fits of (left) $D^0 \to K^+K^-\pi^+\pi^-$ and (right) $D^0 \to K^-\pi^+$. The red line shows the fit model, and the solid blue and green shapes are the flat- and peaking-background components, respectively. In fully reconstructed decays, the peaking-background contribution is very small.

6.1.5 Single-tag yields

The single-tag yields of all fully reconstructed tag modes, which are determined using the fit described in Section 6.1.1, are listed in Table 6.3, along with the

single-tag efficiencies. The uncertainties on the single-tag yields are statistical uncertainties, while the uncertainties on the efficiencies reflect the finite BESIII simulation sample sizes.

Examples of single-tag yield fits are shown in Fig. 6.3, where the red line shows the fit model and the solid blue shape is the combinatorial background. Peaking backgrounds are shown as solid green shapes, but these are very small in fully reconstructed tag modes. The $K^+K^-\pi^+\pi^-$ decay, which is shown on the left, has a low branching fraction and poor reconstruction efficiency, and since it is a four-body decay there is also a large amount of combinatorial background present. The plot on the right shows the single-tag fit of $D^0 \to K^-\pi^+$, which is a CF decay with a large branching fraction. Additionally, since this decay only has two charged particles in the final state, the level of combinatorial background is much lower.

Table 6.3: Single-tag yields in data and corresponding efficiencies as determined from simulation.

Tag mode	Single-tag yield	Efficiency (10^{-2})
$K^+K^-\pi^+\pi^-$	59057 ± 380	18.75 ± 0.04
$K^-\pi^+$	3020110 ± 1820	68.56 ± 0.05
$K^-\pi^+\pi^0$	5757990 ± 6240	36.92 ± 0.05
$K^-\pi^+\pi^-\pi^+$	3840200 ± 2490	41.18 ± 0.06
$K^-e^+\nu_e$	2396000 ± 33800	58.22 ± 0.19
K^+K^-	307164 ± 805	63.12 ± 0.05
$\pi^+\pi^-$	113074 ± 423	66.69 ± 0.05
$\pi^+\pi^-\pi^0$	601480 ± 1330	36.30 ± 0.05
$K^0_S\pi^0\pi^0$	123796 ± 542	14.48 ± 0.04
$K^0_L\pi^0$	346900 ± 12400	31.18 ± 0.13
$K^0_S\pi^0$	371507 ± 654	37.47 ± 0.05
$K^0_S\eta$	50548 ± 267	31.37 ± 0.05
$K^0_S\eta'_{\pi\pi\eta}$	18672 ± 149	11.82 ± 0.04
$K^0_S\eta'_{\pi^+\pi^-\gamma}$	46264 ± 273	18.09 ± 0.04
$K^0_S\pi^+\pi^-\pi^0$	734250 ± 2200	14.74 ± 0.04
$K^0_S\pi^+\pi^-$	916760 ± 1940	34.95 ± 0.05
$K^0_L\pi^+\pi^-$	1459500 ± 40600	39.59 ± 0.10

For the partially reconstructed tags, which are $K^-e^+\nu_e$, $K^0_L\pi^0$ and $K^0_L\pi^+\pi^-$, an effective single-tag efficiency is calculated from $\epsilon_{\rm DT}/\epsilon_{\rm ST}(KK\pi\pi)$. To determine the

single-tag yield, external inputs for the branching fractions, $e^+e^- \to D^0\overline{D}^0$ cross section [97, 98] and integrated luminosity [99] are required. The $K^-e^+\nu_e$ branching fraction is taken from the PDG [21], while the $K^0_L\pi^0$ branching fraction is obtained from Ref. [49]. The $K^0_L\pi^+\pi^-$ branching fraction is obtained from an internal BESIII analysis, but since this result is currently not published, this number is not used in the determination of c_i and s_i.

6.1.6 Double-tag yields

After the determination of single-tag yields of fully reconstructed tag modes in Section 6.1.5, an analogous maximum likelihood fit is performed on the the double-tag selection of these modes. Ideally, a two-dimensional fit would be performed on both the signal and tag side beam-constrained masses. However, due to the limited sample size of double-tag selections, the fit in this analysis is restricted to a one-dimensional fit of the beam-constrained mass $M_{\rm BC}$ of the signal side. In the analysis described by Ref. [43], it is demonstrated that the double-tag yields obtained from a one-dimensional fit of $M_{\rm BC}$ are consistent with those obtained from the full two-dimensional fit.

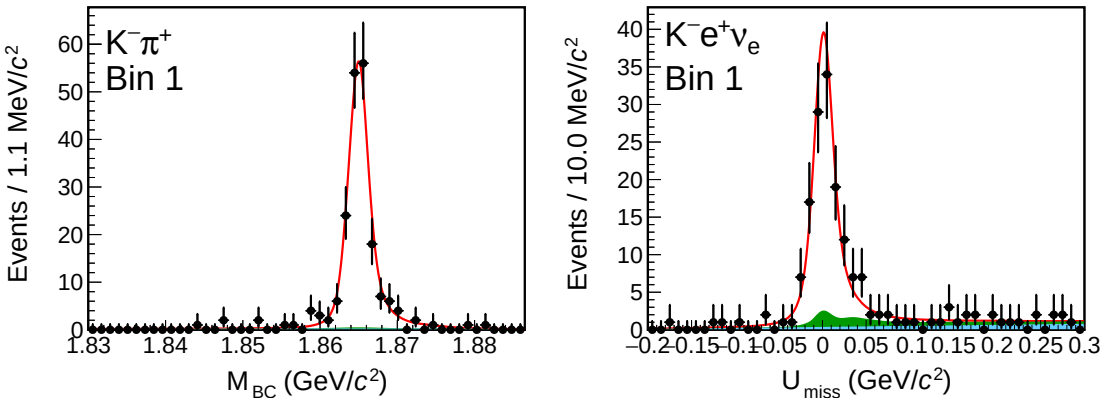

Figure 6.4: Double tag $M_{\rm BC}$ fits in bin +1 of the $K^-\pi^+$ tag on the left and $K^-e^+\nu_e$ tag on the right. The red line shows the fit model, and the solid blue and green shapes are the flat and peaking background components, respectively.

In addition to the fully reconstructed tag modes, a fit is also performed on the partially reconstructed double-tag samples involving $D^0 \to K^-e^+\nu_e$, $K^0_L\pi^0$ and $K^0_L\pi^+\pi^-$ tags. The $D^0 \to K^0_S\pi^+\pi^-$, K^+K^- and $K^0_S\pi^0$ tag modes are also

considered in a selection where the signal mode $D^0 \to K^+K^-\pi^+\pi^-$ is partially reconstructed with a missing kaon. These six selections of partially reconstructed decays provide valuable and complementary information on the $D^0 \to K^+K^-\pi^+\pi^-$ strong-phase parameters.

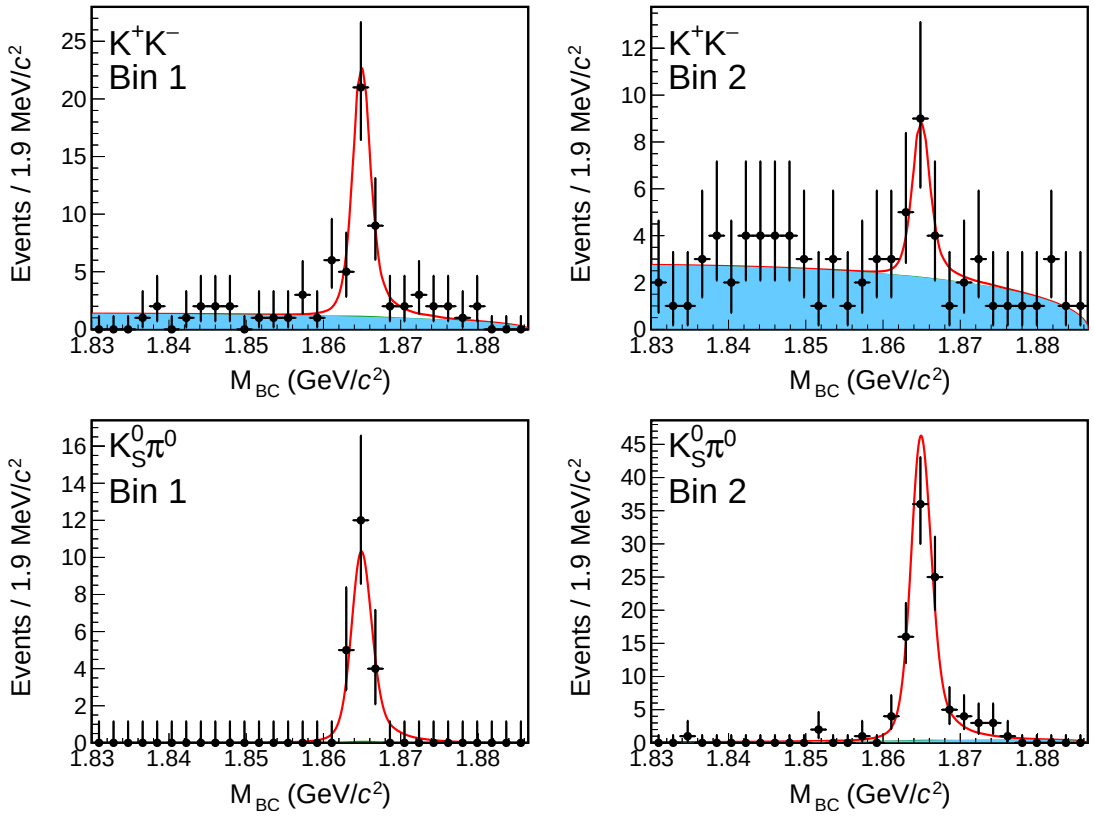

Figure 6.5: Double tag $M_{\rm BC}$ fits of the K^+K^- tag on top and the $K^0_S\pi^0$ tag at the bottom in bins 1 and 2. The red line shows the fit model, and the solid blue and green shapes are the flat and peaking background components, respectively.

The maximum likelihood fit of the double-tag selections uses a fit model analogous to that of single-tag selections. While $M_{\rm BC}$ is the discriminating variable in fully reconstructed decays, the $K^-e^+\nu_e$ tag uses $U_{\rm miss}$ and the remaining partially reconstructed modes use $M^2_{\rm miss}$ as fit variables. For each tag, all phase-space bins are fitted simultaneously. The parameters describing the resolution function and the combinatorial background shape are shared between all bins, while the yields are independently varied in each bin.

Examples of double-tag fits are shown in Fig. 6.4. The fully reconstructed two-body tag mode $D^0 \to K^-\pi^+$, shown on the left, is found to have a very low

background level, while the partially reconstructed $K^-e^+\nu_e$ tag on the right has a worse purity. The peaking backgrounds are mainly dominated by $K^-\pi^0e^+\nu_e$, $K^-\mu^+\nu_\mu$ and $K^-\pi^+\pi^0$ decays.

Figure 6.5 shows a comparison in bins 1 and 2 between the $D^0 \to K^+K^-$ and $K^0_S\pi^0$ tags, which are tags of opposite *CP* content. On the top, the K^+K^- tag is seen to have suppressed double-tag yields in bin 2, relative to bin 1. At the bottom, the $K^0_S\pi^0$ tag shows the opposite behaviour, where bin 1 is suppressed relative to bin 2. Since the overall DD wavefunction is *CP*-odd, Fig. 6.5 indicates that the phase-space bin 1 of the $D^0 \to K^+K^-\pi^+\pi^-$ decay is predominantly *CP*-odd, while bin 2 is dominated by *CP*-even amplitudes. These qualitative findings are consistent with the quantitative results discussed in Section 6.2.

Table 6.4: Double-tag yields of CP tags. The uncertainties are statistical only.

Bin number → Tag mode ↓	1	2	3	4
K^+K^-	$39.0^{+7.4}_{-6.4}$	$11.9^{+5.0}_{-4.1}$	$15.5^{+4.5}_{-4.5}$	$35.0^{+6.9}_{-6.3}$
$K^+K^{-\dagger}$	$34.9^{+8.1}_{-7.3}$	$27.2^{+8.1}_{-7.3}$	$24.0^{+9.4}_{-8.6}$	$27.0^{+6.8}_{-6.1}$
$\pi^+\pi^-$	$8.4^{+4.9}_{-4.1}$	$1.9^{+4.4}_{-1.9}$	$4.8^{+5.0}_{-4.3}$	$8.3^{+4.6}_{-3.8}$
$\pi^+\pi^-\pi^0$	$58.5^{+11.4}_{-10.8}$	$49.6^{+10.0}_{-9.4}$	$54.5^{+10.4}_{-10.0}$	$61.6^{+11.4}_{-10.8}$
$K^0_S\pi^0\pi^0$	$10.6^{+3.9}_{-3.3}$	$3.6^{+2.6}_{-1.9}$	$12.6^{+4.5}_{-3.8}$	$10.7^{+3.9}_{-3.2}$
$K^0_L\pi^0$	$30.9^{+7.9}_{-7.0}$	$18.1^{+4.7}_{-4.7}$	$11.5^{+3.8}_{-3.7}$	$19.8^{+6.8}_{-6.1}$
$K^0_S\pi^0$	$20.5^{+4.8}_{-4.2}$	$92.0^{+10.6}_{-9.8}$	$124.8^{+11.7}_{-11.0}$	$27.5^{+5.5}_{-5.0}$
$K^0_S\pi^{0\dagger}$	$6.7^{+5.6}_{-4.8}$	$92.1^{+12.3}_{-11.6}$	$113.2^{+13.2}_{-12.4}$	$12.2^{+5.7}_{-5.0}$
$K^0_S\eta$	$5.7^{+2.7}_{-2.1}$	$21.7^{+5.3}_{-4.6}$	$15.0^{+4.2}_{-3.6}$	$2.3^{+2.4}_{-1.6}$
$K^0_S\eta'_{\pi\pi\eta}$	$0.0^{+0.5}_{-0.0}$	$9.0^{+3.3}_{-2.7}$	$5.6^{+3.0}_{-2.2}$	$2.9^{+2.0}_{-1.4}$
$K^0_S\eta'_{\pi^+\pi^-\gamma}$	$3.8^{+2.2}_{-1.6}$	$12.0^{+4.1}_{-3.4}$	$15.0^{+4.3}_{-3.6}$	$1.9^{+1.7}_{-1.1}$
$K^0_S\pi^+\pi^-\pi^0$	$53.8^{+8.6}_{-7.9}$	$154.9^{+13.8}_{-13.1}$	$209.2^{+15.9}_{-15.2}$	$43.4^{+7.6}_{-6.9}$

The double-tag yields of each *CP* tag are listed in Table 6.4. The top six tag modes are *CP*-even, while the bottom six are *CP*-odd. All tag modes show the

same enhancement and suppression effects as those seen in Fig. 6.5. Generally, bins 1 and 4 show a *CP*-odd behaviour, while bins 2 and 3 are *CP*-even like.

Since many double-tag yields are very small, symmetric uncertainties that follow a Gaussian distribution are found to provide an inaccurate statistical coverage. Instead, for flavour- and *CP*-tag modes, Wilks' theorem is used, as described in Section A.3. For each yield, the profile likelihood function of the invariant-mass fit is scanned around the minimum to find $\Delta\mathcal{L} = 1$, from which asymmetric uncertainties are assigned. In SCMB tags, however, Wilks' theorem is found to be invalid due to very small bin yields. Therefore, instead of obtaining numerical values of bin yields, the profiled likelihood from the invariant-mass fit is used directly in the strong-phase determination described in Section 6.2.

It must be noted that $\mathcal{L}$ is in fact the logarithm of the likelihood function, multiplied by a factor -2. As explained in Appendix A, taking the logarithm has several practical advantages in maximum likelihood fits. The scaling by -2 allows for a direct identification of $\mathcal{L}$ as a χ^2 distribution, by Wilks' theorem. Henceforth, in this thesis the function $\mathcal{L}$ will be referred to as the "likelihood function".

6.2 Determination of strong-phase differences

6.2.1 Strong-phase fit strategy

The single- and double-tag yields obtained in Sections 6.1.6 and 6.1.5 are subsequently input to a maximum likelihood fit to determine the strong-phase parameters of the $D^0 \to K^+K^-\pi^+\pi^-$ decay mode. This fit, which will be referred to as the "strong-phase fit", uses Eqs. (2.23),(2.28) and (2.29). These equations are shown

again below for the $D^0 \to K^+K^-\pi^+\pi^-$ decay, with efficiencies shown explicitly,

$$\frac{M_{ij}(KK\pi\pi, g)}{M(g)} = \mathrm{BF}(D^0 \to KK\pi\pi)\frac{\epsilon^{\mathrm{DT}}_{ijab}}{\epsilon^{\mathrm{ST}}} \times\Big[K_a\bar{K}^g_b + \bar{K}_aK^g_b - 2\sqrt{K_a\bar{K}_aK^g_b\bar{K}^g_b}\Big(c_ac^g_b + s_as^g_b\Big)\Big], \quad (6.1)$$

$$\frac{M_i(KK\pi\pi, g)}{M(g)} = \mathrm{BF}(D^0 \to KK\pi\pi)\frac{\epsilon^{\mathrm{DT}}_{ij}}{\epsilon^{\mathrm{ST}}} \times\Big[\bar{K}_j + \Big(r_D^{K\pi}\Big)^2K_j - 2r_D^{K\pi}R^{K\pi}\sqrt{K_j\bar{K}_j}\Big(c_j\cos\Big(\delta_D^{K\pi}\Big) + s_j\sin\Big(\delta_D^{K\pi}\Big)\Big)\Big], \quad (6.2)$$

$$\frac{M_i(KK\pi\pi, g)}{M(g)} = \mathrm{BF}(D^0 \to KK\pi\pi)\frac{\epsilon^{\mathrm{DT}}_{ij}}{\epsilon^{\mathrm{ST}}}\Big[K_j + \bar{K}_j - 2\sqrt{K_j\bar{K}_j}c_j(2F^g_+ - 1)\Big]. \quad (6.3)$$

As mentioned at the end of Section 6.1.1, each SCMB tag, described by Eq. 6.1, has 64 bin yields. This makes a total of $3 \times 64 = 192$ bin yields, where the $K^0_{\mathrm{S}}\pi^+\pi^-$ tag with a partially reconstructed $K^+K^-\pi^+\pi^-$ signal mode is considered to be a separate tag mode, independent of the $K^0_{\mathrm{S}}\pi^+\pi^-$ and $K^0_{\mathrm{L}}\pi^+\pi^-$ tags with a full reconstruction of the signal mode. Similarly, there are four flavour tags with $4 \times 8 = 32$ bin yields and twelve *CP* tags with $12 \times 4 = 48$ bin yields. In total, the strong-phase fit uses 272 bin yields as input.

The strong-phase parameters that must be determined by the strong-phase fit are the four c_i parameters and four s_i parameters. In addition, there are eight K_i parameters, but since these are, by definition, normalised to unity, only seven K_i are independent.

An important motivation for normalising Eqs. (6.1)-(6.3) with the corresponding single-tag yield is because there are systematic differences between the reconstructed efficiencies obtained from the simulation and the actual efficiencies in data. The form of Eqs. (6.1)-(6.3), where all yields and efficiencies appear in a ratio between single- and double-tag selections, ensures that any systematic discrepancies in the reconstruction efficiencies of the tag mode is cancelled between single- and double-tag yields.

The only parameter affected by discrepancies in the signal mode is the branching fraction $\mathrm{BF}(D^0 \to KK\pi\pi)$, which takes the role as a normalisation constant.

By allowing this to be a free parameter, the strong-phase parameters become independent of these systematic biases. Additionally, since there currently exists no published value for the branching fraction of $D^0 \to K^0_{\rm L}\pi^+\pi^-$, its single-tag yield is calculated, in Section 6.1.5, using that of the $D^0 \to K^0_{\rm S}\pi^+\pi^-$ decay. However, to remove any systematic bias due to this choice of branching fraction, the branching fraction BF($D^0 \to KK\pi\pi$) is varied independently for this particular tag mode.

The values of the hadronic parameters r_D, R and δ_D of the flavour tags $D^0 \to K^-\pi^+\pi^0$ and $D^0 \to K^-\pi^+\pi^-\pi^+$, which appear in Eq. (6.2), are taken from the combination of BESIII, CLEO-c and LHCb results reported in Ref. [50]. In the case of $D^0 \to K^-\pi^+$, for which $R = 1$, the strong-phase fit has the potential to provide interesting information about $\delta_D^{K\pi}$, with negligible degradation in the sensitivity to the $D^0 \to K^+K^-\pi^+\pi^-$ strong-phase parameters. Therefore, the strategy is to let $r_D^{K\pi}\cos(\delta_D^{K\pi})$ and $r_D^{K\pi}\sin(\delta_D^{K\pi})$ be free parameters in the strong-phase fit. These parameters are Gaussian constrained to the results of SCMB decays from Ref. [49].

Table 6.5: Summary of free parameters in the fit.

Fit parameter	Number of parameters
c_i	4
s_i	4
K_i	7
$r_D^{K\pi}\cos(\delta_D^{K\pi})$	1
$r_D^{K\pi}\sin(\delta_D^{K\pi})$	1
BF($D^0 \to KK\pi\pi$)	1
BF($D^0 \to KK\pi\pi$) (for $K^0_{\rm L}\pi^+\pi^-$)	1
Total	19

In total, there are 19 free fit parameters in the strong-phase fit, and these are summarised in Table 6.5.

The efficiencies and efficiency matrices in Eqs. (6.1)-(6.3), which are determined from simulation, are fixed in the strong-phase fit. Similarly, external strong-phase information, such as the c_i, s_i and K_i parameters of the $K^0_{S,L}\pi\pi^-$ tag modes, and the single-tag yields $M(g)$, are also kept fixed in the strong-phase fit.

6.2.2 Fractional bin-yield parameterisation

In theory, it is possible to perform the strong-phase fit with the first seven K_i parameters as free parameters, while the final parameter is set to $K_4 = 1 - \sum_{i\neq 4} K_i$. However, such a parameterisation introduces large correlations between the individual coefficients, resulting in an unstable fit. It is beneficial to reparameterise the K_i to a more convenient form that automatically accounts for this constraint. The new parameterisation, known as the recursive fractions R_i, is defined as

$$R_i = \begin{cases} K_i, & i = -4 \\ K_i / \sum_{j\geq i} K_j, & -4 < i \leq +4, \end{cases}$$

which automatically constraints the final recursive coefficient to $R_4 = 1$. Therefore, this parameterisation automatically removes the redundant degree of freedom. The inverse transformation is

$$K_i = \begin{cases} R_i, & i = -N \\ R_i \prod_{j<i}(1 - R_j), & -N < i < +N \\ \prod_{j<i}(1 - R_j), & i = +N. \end{cases}$$

In the remainder of this thesis, all fit results will be provided in terms of R_i. This form is more convenient because it reflects the correct number of degrees of freedom in the fit, and it makes it easier for future strong-phase analyses to use c_i, s_i and K_i as an external inputs with a full covariance matrix.

6.2.3 Construction of likelihood function

To construct a likelihood function that accommodates the fit strategy described in Section 6.2.1, a multi-dimensional Gaussian likelihood function, Eq. (A.3), is used as a starting point. The set of bin yields, which are denoted x_0, x_1, ..., with a covariance matrix V_{ij}, are combined into the likelihood function

$$\mathcal{L} = \sum_i \sum_j (V^{-1})_{ij} \Big(x_i - \hat{x}_i(p_\alpha)\Big)\Big(x_j - \hat{x}_j(p_\alpha)\Big),$$

where $\hat{x}_i(p_\alpha)$ are predictions of x_i obtained from Eqs. (6.1)-(6.3). These predictions are functions of the free parameters p_1, p_2, ..., which are listed in Table 6.5.

For a likelihood function describing a set of Gaussian distributed measurements, the covariance matrix takes the form $V_{ij} = \rho_{ij}\sigma_i\sigma_j$, where σ_i are the symmetric bin-yield uncertainties and ρ_{ij} are the correlation coefficients. Unfortunately, as shown in Table 6.4, many of the bin yields have highly asymmetric uncertainties that cannot be described by a Gaussian distribution. Neither can they be described by a Poisson distribution, since many of these tag modes have non-negligible peaking and combinatorial backgrounds.

In Ref. [100], an alternative form of the covariance matrix was proposed, which provides an approximate description of the likelihood function for measurements with non-Gaussian distributions. It can be considered as a linear extrapolation of the covariance matrix from the asymmetric uncertainties,

$$\begin{aligned} V_{ij} =& \rho_{ij}\sigma_i(x_i - \hat{x}_i)\sigma_j(x_j - \hat{x}_j), \\ \sigma_i(x_i - \hat{x}_i) =& \sqrt{\sigma_+\sigma_- + (x_i - \hat{x}_i)(\sigma_- - \sigma_+)}, \end{aligned} \tag{6.4}$$

and in Ref. [100] it was shown that Poisson-like measurements are well described by such an approximation. However, Eq. (6.4) is limited to cases where $\sqrt{\sigma_+\sigma_-} \gg |\sigma_- - \sigma_+|$, such that the term linear in $x_i - \hat{x}_i$ is small. Thus, the double-tag yields listed in Table 6.4, as well as the yields of flavour tags, are suitable measurements where Eq. (6.4) is applicable. In the limit where $\sigma_- = \sigma_+$, Eq. (6.4) reduces to a conventional covariance matrix.

In SCMB tag modes, where many bin yields are close to zero, Eq. (6.4) is found to result in unstable strong-phase fits because $\sigma_- \approx 0$. For these tags, the unbinned profiled likelihood obtained from the invariant-mass fit provides the best possible description of these bin yields, but at the expense of computationally intensive fits.

6.2.4 Strong-phase fit bias study

To assess the stability of the strong-phase fit, as well as potential biases in the central values or uncertainties of the fit parameters, a set of fits to pseudo-experiments are performed. Due to the non-Gaussian nature of the bin yields, especially in the SCMB tags, it is found that drawing random numbers from a

Poisson or Gaussian distribution provides an inadequate description of the bin yield distributions. Therefore, for each double-tag mode, 1000 pseudo-experiments are generated using the invariant-mass fit model.

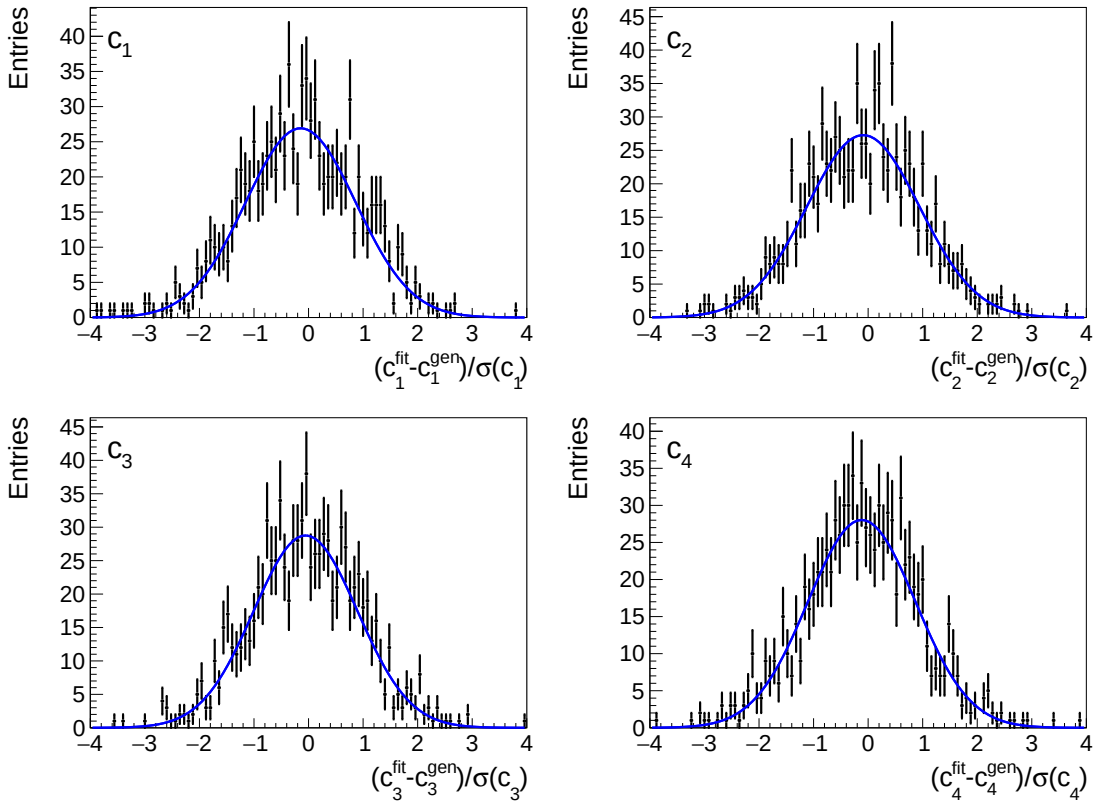

Figure 6.6: Pull distributions of s_i obtained from strong-phase fits of 1000 pseudo-experiments, shown as black data points. The blue curve is the Gaussian function fitted to this distribution.

In order to generate pseudo-experiments with similar properties as those of data, the bin yields are set using Eqs. (6.1)-(6.3), with the $D^0 \to K^+K^-\pi^+\pi^-$ strong-phase parameters set to those obtained in a fit to data. Similarly, the parameters describing the invariant-mass shapes are also taken from the fit to data.

In an identical manner to what is done with data in Section 6.1.6, each of the 1000 pseudo-experiments in each tag mode is fitted to determine the double-tag yields. The double-tag yields of all tag modes are used as inputs to the strong-phase fits, and the pulls of the fitted values of c_i and s_i are plotted in Figs. 6.6 and 6.7, respectively. The pull distributions of other parameters in the fit show similar behaviour. In total, 93.4% of the pseudo-experiment fits converge with a full covariance matrix.

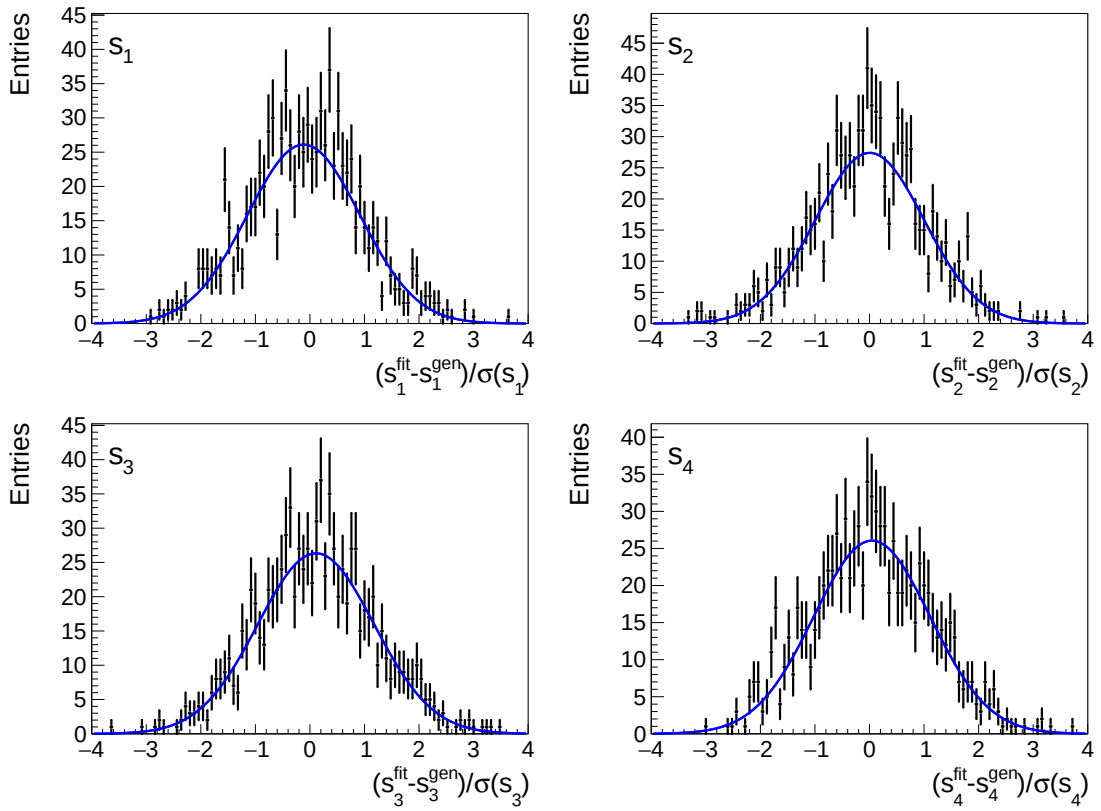

Figure 6.7: Pull distributions of s_i obtained from strong-phase fits of 1000 pseudo-experiments, shown as black data points. The blue curve is the Gaussian function fitted to this distribution.

The pull distributions are fitted with a Gaussian function, which is the blue curve in Figs. 6.6 and 6.7. The mean and widths of these functions are listed in Table 6.6, and it is found that all the pull distributions have widths that are consistent with unity. This indicates that the modified likelihood function, Eq. (6.4), provides a good description of the asymmetric uncertainties.

However, some of the pull distributions show biases in the central value that is up to 14% of the statistical uncertainty. Although the mean of the pull distributions from Table 6.6 can be used directly to correct for the biases in the fit to data, the assumptions behind the calculation of these corrections must be considered. Specifically, in the generation of pseudo-experiments it is implicitly assumed that the fit model described in Section 6.1.1 is the correct model. This includes the choice of nuisance parameters in the model, such as the size of peaking- and combinatorial-background components.

The accuracy of the bias corrections therefore depend on whether or not the corrections are sensitive to the exact values of nuisance parameters, which are taken directly from the fit to data. Fortunately, even though the fits described in Section 6.1 contain several backgrounds, the majority of these contributions are very small and it may be assumed that the exact sizes of these backgrounds have a negligible impact on the bias corrections.

Furthermore, it is also found that generating pseudo-experiments using model-predicted values of c_i and s_i, instead of those obtained from the fit to data, results in bias corrections that are consistent with those in Table 6.6. Hence, despite the limitations in the method used to determine the bias corrections in Table 6.6, it is deemed that a direct correction to the fit results in data using these values is appropriate.

Table 6.6: Mean and standard deviation of the pull distributions obtained from strong-phase fits of pseudo-experiments.

Variable	Pull mean	Pull standard deviation
c_1	-0.14 ± 0.04	1.01 ± 0.03
c_2	-0.09 ± 0.04	1.03 ± 0.03
c_3	-0.05 ± 0.03	0.95 ± 0.03
c_4	-0.12 ± 0.03	0.99 ± 0.03
s_1	-0.12 ± 0.04	1.03 ± 0.04
s_2	0.00 ± 0.04	1.00 ± 0.03
s_3	0.11 ± 0.04	1.07 ± 0.03
s_4	0.04 ± 0.04	1.07 ± 0.03

6.2.5 Strong-phase fit results

The data are fitted with the procedure outlined in Sections 6.2.1-6.2.3. The results presented in this section are also corrected for biases in their central values. The resulting c_i and s_i parameters are listed in Table 6.7, and they are also visualised in Fig. 6.8. In general, the (c_i, s_i) points lie close to the unit circle, meaning that the dilution of the strong-phase differences due to binning is minimal. Furthermore, the model-independent measurements agree well with the model predictions.

Table 6.7: Results of c_i and s_i from the strong-phase fit, after bias corrections. The uncertainties are statistical only.

Parameter	Fit result	Parameter	Fit result
c_1	-0.28 ± 0.09	s_1	-0.68 ± 0.24
c_2	0.83 ± 0.04	s_2	-0.18 ± 0.19
c_3	0.83 ± 0.03	s_3	0.27 ± 0.17
c_4	-0.28 ± 0.10	s_3	0.54 ± 0.28

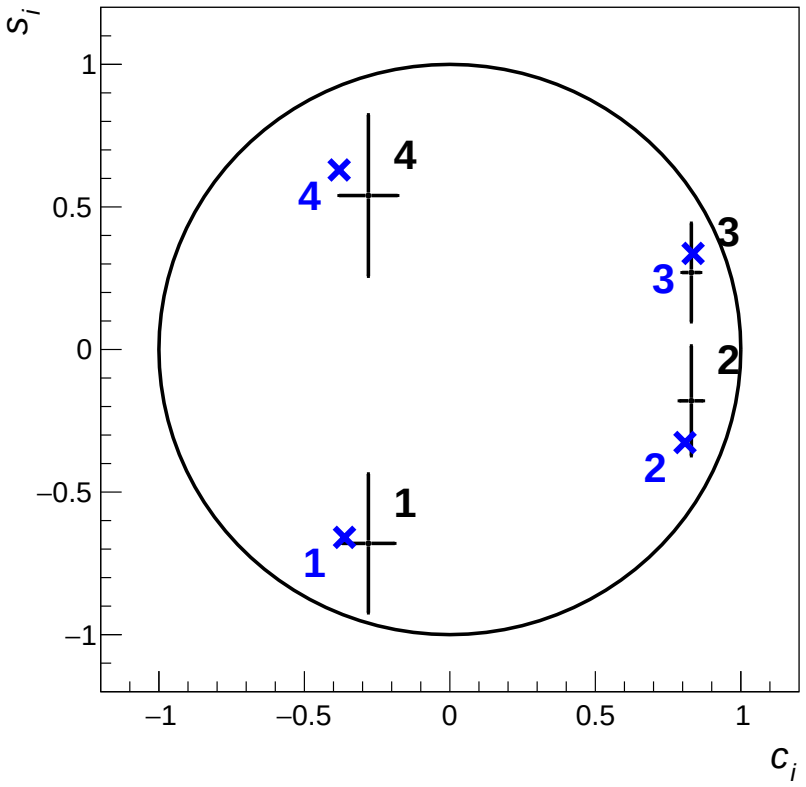

Figure 6.8: Fitted values of c_i vs s_i, which are shown as black data points. The blue crosses mark the corresponding model predictions.

It is also interesting to study the other free parameters of the strong-phase fit. Although several of these are considered to be nuisance parameters, they can still provide interesting information and also serve as useful cross checks of the fit. In particular, Table 6.8 shows a comparison of the external inputs of $r_D^{K\pi}\cos(\delta_D^{K\pi})$ and $r_D^{K\pi}\sin(\delta_D^{K\pi})$ from Ref. [49] and the fitted values, which are Gaussian constrained to the external inputs. On the left of Fig. 6.9, an alternative strong-phase fit

is performed where the Gaussian constraint on $r_D^{K\pi}\cos(\delta_D^{K\pi})$ and $r_D^{K\pi}\sin(\delta_D^{K\pi})$ is relaxed, and the resulting contours are shown. They are in agreement with the current world average from HFLAV [25].

While the improvements are minor, this analysis is the first study of quantum-correlated $D\overline{D}$ pairs to simultaneously measure $\delta_D^{K\pi}$ together with c_i and s_i. The results of Table 6.8 demonstrates the possibility of a high-precision measurement of $\delta_D^{K\pi}$ in an analogous strong-phase analysis of three-body decays such as $D^0 \to K^0_S\pi^+\pi^-$ and $K^0_L\pi^+\pi^-$.

Table 6.8: A comparison of the $r_D^{K\pi}\cos(\delta_D^{K\pi})$ and $r_D^{K\pi}\sin(\delta_D^{K\pi})$ parameters before and after the strong-phase fit, where these are constrained to the measurements from Ref. [49]. The uncertainties are statistical only.

Parameter	Before fit [49]	After constrained fit
$r_D^{K\pi}\cos(\delta_D^{K\pi})$	-0.0562 ± 0.0096	-0.0548 ± 0.0086
$r_D^{K\pi}\sin(\delta_D^{K\pi})$	-0.0110 ± 0.0140	-0.0121 ± 0.0137

On the right of Fig. 6.9, the fitted recursive fractions R_i are shown as black data points. The model predictions of R_i are shown in blue, and a good agreement with the fitted parameters is found. This agreement indicates that the efficiency and bin migration corrections are sufficiently accurate for this strong-phase measurement.

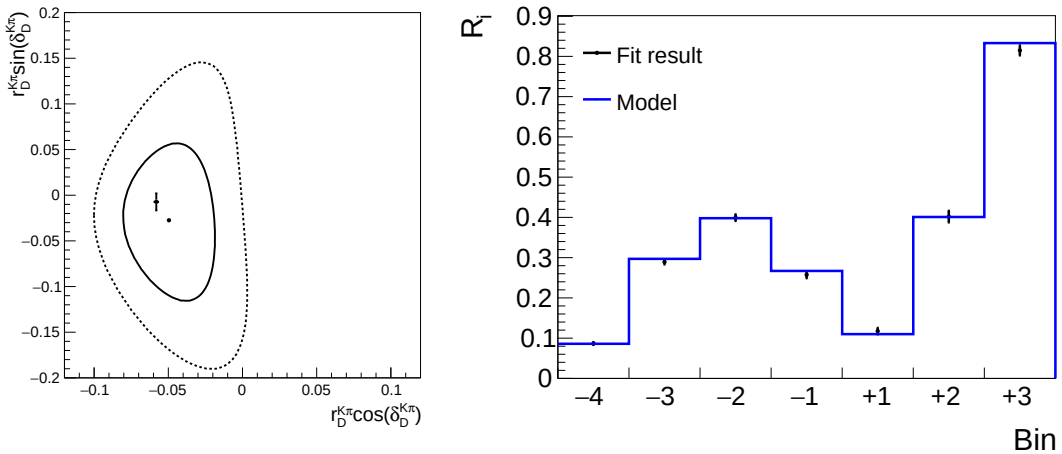

Figure 6.9: Left: The contours of $r_D^{K\pi}\cos(\delta_D^{K\pi})$ vs $r_D^{K\pi}\sin(\delta_D^{K\pi})$ obtained from the strong-phase fit. The solid and dashed contours correspond to $\Delta\chi^2 = 2.30$ and 6.18, respectively, with the black dot indicating the central value. The data point with uncertainties is the world average from HFLAV [25]. Right: A comparison of the fitted R_i values, shown as black data points, and their model predictions, which is the solid blue line.

Finally, it is interesting to compare the fitted branching fraction of $D^0 \to K^+K^-\pi^+\pi^-$, which is $\mathrm{BF}(KK\pi\pi) = (2.842 \pm 0.031) \times 10^{-3}$, to the PDG value $(2.47 \pm 0.11) \times 10^{-3}$ [21]. Although the fitted value is around $3\,\sigma$ higher than the value reported by the PDG, it is significantly more precise. Furthermore, this branching fraction determination is an absolute measurement, in contrast to previous studies where it was determined relative to that of other decays. Thus, it motivates a promotion of this nuisance parameter to a parameter of interest.

6.3 Systematic uncertainties of strong-phase parameters

There are several sources of systematic bias, which are split into three categories. For each contribution, a covariance matrix of all 19 free parameters is calculated. In this thesis only the numerical results of parameters related to the strong-phases of $D^0 \to K^+K^-\pi^+\pi^-$, as well as the branching fraction, are reported.

6.3.1 Uncertainties of fixed parameters

In the first category of systematic uncertainties, which contains the majority of contributions to the strong-phase systematic uncertainties, the uncertainties of fixed parameters in the strong-phase fit are propagated to the final result. For each contribution, the strategy is to repeat the strong-phase fit, each time smearing the parameters according to their covariance matrices. The resulting distribution of the 19 free parameters are used to build a sample covariance matrix.

The first contribution is the uncertainties on the single-tag yields, which are listed in Table 6.3. For fully reconstructed tag modes, these are statistical in origin and obtained directly from the single-tag fit. For partially reconstructed tags, where an effective single-tag yield is used, the uncertainties originate from the knowledge of branching fractions, $e^+e^- \to D^0\overline{D}^0$ cross section and the integrated luminosity. Therefore, the relative uncertainties of the $K^0_{\mathrm{L}}\pi^0$ and $K^-e^+\nu_e$ single-tag yields are significantly larger than those of fully reconstructed modes.

The next contribution of uncertainties are in the $D^0 \to K^0_{S,L}\pi^+\pi^-$, $\pi^+\pi^-\pi^0$ and $K^0_S\pi^+\pi^-\pi^0$ tag modes, where the uncertainties on the associated strong-phase parameters are taken from Refs. [46, 56, 85], respectively.

Similarly, there are uncertainties associated with the efficiencies and efficiency matrices obtained from simulation due to the finite sample sizes. For each tag, the uncertainty on the single-tag efficiency is assumed to follow a binomial distribution, using the fraction of events that is reconstructed. For the efficiency matrices in double-tag yields, each matrix element is assumed to follow a binomial distribution.

In the fit of single- and double-tag yields, there are uncertainties associated with the size of the peaking backgrounds. These uncertainties arise from the knowledge of the branching fractions and from the finite sample sizes of the simulation used to obtain the relative efficiencies. In the double-tag fits, there is also an additional uncertainty from the quantum-correlation corrections, which are propagated from the strong-phase measurements used to determine these corrections. To propagate these uncertainties to the strong-phase measurement, the fits in Sections 6.1.5 and 6.1.6 are repeated many times. In each iteration, the peaking backgrounds are smeared according to their covariance matrices and the strong-phase fit is repeated. The resulting spread and correlation between strong-phase parameters is used to build the covariance matrix of systematic uncertainties from peaking backgrounds.

6.3.2 Systematic bias due to the exclusion of $K^0_S K^+ K^-$ candidates

The second category of systematic bias has a single contribution, which is the bias in strong-phase parameters introduced by selection of $D^0 \to K^+K^-\pi^+\pi^-$. Specifically, as described in Section 5.3.3, an asymmetric mass-window rejection is imposed on the $\pi^+\pi^-$ invariant-mass spectrum in order to suppress contamination from $D^0 \to K^0_S K^+ K^-$.

The region of phase space that is excluded is relatively small, so its impact is assessed by calculating the model-predicted strong-phase parameters, using the

method described in Section 3.3, with and without the exclusion. The difference between the results is assigned as the systematic uncertainty.

6.3.3 Systematic uncertainties from tracking and PID efficiencies

Finally, the last category of systematic uncertainties are contributions that affect the branching fraction BF($KK\pi\pi$), but they do not impact on the strong-phase parameters c_i, s_i or R_i. These arise because of systematic discrepancies between the tracking and PID efficiencies determined from simulation, compared to the true efficiencies in data. This is assessed in momentum bins with a data-driven method using a calibration sample of double-tag events where both D meson decay into CF final states. The tables of efficiency differences between data and simulation are available as internal BESIII results [101]

To apply the results from the calibration sample to the $D^0 \to K^+K^-\pi^+\pi^-$ decay, a weighted sum over momentum bins is evaluated, using the momentum distribution of the charged kaons and pions from a BESIII simulation of this mode. For each pion track, the tracking and PID efficiency systematic uncertainties are determined to be 0.5% and 0.1%, respectively [101]. It is assumed each of these uncertainties are fully correlated between both pions of this decay, so the combined systematic uncertainties are 1.0% and 0.2%. However, since tracking and PID efficiencies are independent, these must be summed in quadrature, resulting in 1.0%.

Similarly, for each kaon track, both the tracking and PID uncertainties are 0.4%, or a combined systematic uncertainty of 1.1%. Since the selected calibration samples are different for kaons and pions, these may be assumed to be independent. Thus, the tracking and PID efficiencies of kaons and pions may be added in quadrature, and a systematic uncertainty of 1.5% is assigned to BF($KK\pi\pi$).

6.3.4 Summary of systematic uncertainties of strong-phase parameters

The uncertainties of c_i, s_i and BF($KK\pi\pi$) are summarised in Tables 6.9 and 6.10, where the total systematic uncertainty is obtained by adding the individual

Table 6.9: Summary of systematic uncertainties on BF, with each entry multiplied by 10^5. The abbreviations ST and DT mean single and double tag.

	BF($KK\pi\pi$)
ST yield	0.2
$K^0_L\pi^0$ ST yield	0.1
$K^-e^+\nu_e$ ST yield	0.6
External strong phases	0.2
Finite simulation size	0.4
ST and DT fit	0.4
K^0_S veto	0.0
Tracking and PID efficiencies	4.2
Total systematic	4.3
Statistical	3.1

covariance matrices. In the case of the strong-phase parameters in Table 6.10, the total systematic uncertainties are all much smaller than the statistical uncertainties, which are also shown for comparison. The leading systematic uncertainty is that from external strong-phase inputs. This is expected to reduce in the future, since more precise measurements from BESIII are expected with the full 20 fb^{-1} data set.

Table 6.10: Summary of systematic uncertainties on c_i, s_i. Each entry is multiplied by 10^3. The ordering is identical to that in Table 6.9

c_1	c_2	c_3	c_4	s_1	s_2	s_3	s_4
0.9	0.4	0.3	0.8	0.5	0.5	0.1	0.1
3.8	2.4	2.6	3.5	0.4	0.1	0.0	0.3
0.5	0.3	0.2	0.5	0.0	0.2	0.0	0.1
4.8	7.6	5.7	4.4	36.4	32.7	28.9	43.2
3.4	1.7	1.3	3.6	6.3	5.4	4.9	7.7
3.6	5.2	4.5	3.7	1.3	1.6	2.4	1.8
0.2	4.3	1.9	5.8	0.4	6.2	1.7	2.8
0.0	0.0	0.0	0.0	0.0	0.0	0.0	0.0
7.9	10.5	8.1	9.6	36.9	33.8	29.5	44.0
87.0	43.3	33.7	96.6	240.2	185.7	169.6	276.1

6.4 Summary of strong-phase analysis

Table 6.11 summarises the parameters c_i and s_i, which describe the strong-phase difference of the $D^0 \to K^+K^-\pi^+\pi^-$ decay. The first uncertainty is statistical and it is found to be much larger than the second uncertainty, which is due to systematic uncertainties. These parameters are used as external inputs in a model-independent measurement of the CKM angle γ, which is the topic of Chapter 9.

Also shown in Table 6.11 is the branching fraction of $D^0 \to K^+K^-\pi^+\pi^-$, which is fitted as a normalisation constant, but its uncertainty is less than half that of the current world average [21]. This determination is currently dominated by tracking and PID systematic uncertainties.

Table 6.11: Results from the strong-phase fit, after bias corrections. The first uncertainty is statistical and the second systematic.

Variable	Fit result
c_1	$-0.28 \pm 0.09 \pm 0.01$
c_2	$0.83 \pm 0.04 \pm 0.01$
c_3	$0.83 \pm 0.03 \pm 0.01$
c_4	$-0.28 \pm 0.10 \pm 0.01$
s_1	$-0.68 \pm 0.24 \pm 0.04$
s_2	$-0.18 \pm 0.19 \pm 0.03$
s_3	$0.27 \pm 0.17 \pm 0.03$
s_4	$0.54 \pm 0.28 \pm 0.04$
BF($KK\pi\pi$)	$(2.842 \pm 0.031 \pm 0.043) \times 10^{-3}$

7
The LHCb detector

Contents

The LHCb detector [102, 103] is one of four main experiments at the Large Hadron Collider (LHC), which is located at the European Organization for Nuclear Research (CERN). The LHC is a 27 km synchrotron designed to collide protons and heavy ions, and is built 100 m underground in the same tunnels as its predecessor, the Large Electron Positron (LEP) collider.

The protons are provided by a long chain of accelerators, starting with the Linear accelerator 2 (Linac 2), Proton Synchrotron Booster (PS Booster), Proton Synchrotron (PS) and the Super Proton Synchrotron (SPS). Two beams of 450 GeV

protons from the SPS are injected into separate beam pipes inside the LHC, where they circulate in opposite directions.

To keep the particles in circular orbits, there are 1232 superconducting dipole magnets placed around the ring. The two beam pipes share the same magnets, but the vertical magnetic fields are oriented in opposite directions inside the two beam pipes. The magnets are designed to provide a magnetic field of around 8 T, which allows each beam to reach an energy of 7 TeV, or a centre-of-mass energy of 14 TeV. The protons are accelerated with superconducting radiofrequency cavities.

When the protons have been accelerated, they undergo collisions at four crossing points where the beams intersect. At these locations, the four large LHC experiments are situated: ATLAS, CMS, ALICE and LHCb. Of these, the LHCb experiment is the only detector that is a single-arm forward spectrometer. It covers the forward region, corresponding to a pseudo-rapidity range $2 < \eta < 5$, where a large number of hadrons containing b or c quarks are produced. The LHCb detector covers an angular range of ± 250 mrad in the vertical direction and ± 300 mrad in the horizontal direction.

An overview of the detector layout is shown in Fig. 7.1. Near the interaction point, which is on the left, the Vertex Locator (VELO) forms the first part of the tracking system. Further downstream, the tracking system contains the Tracker Turicencis (TT) in front of a dipole magnet, followed by three tracking stations T1-T3 downstream of the dipole magnet.

The two Ring-Imaging Cherenkov (RICH) detectors, which are referred to as RICH1 and RICH2, provide the detector with unique particle identification capabilities. Finally, behind RICH2 are the electromagnetic and hadron calorimeters (ECAL and HCAL) and the five muon stations M1-M5.

Originally, the LHCb experiment was designed to study mixing, *CP* violation and rare decays in beauty and charm decays, but its physics programme has later evolved to include electroweak physics, QCD, spectroscopy, semi-leptonic decays, heavy ions and fixed-target physics.

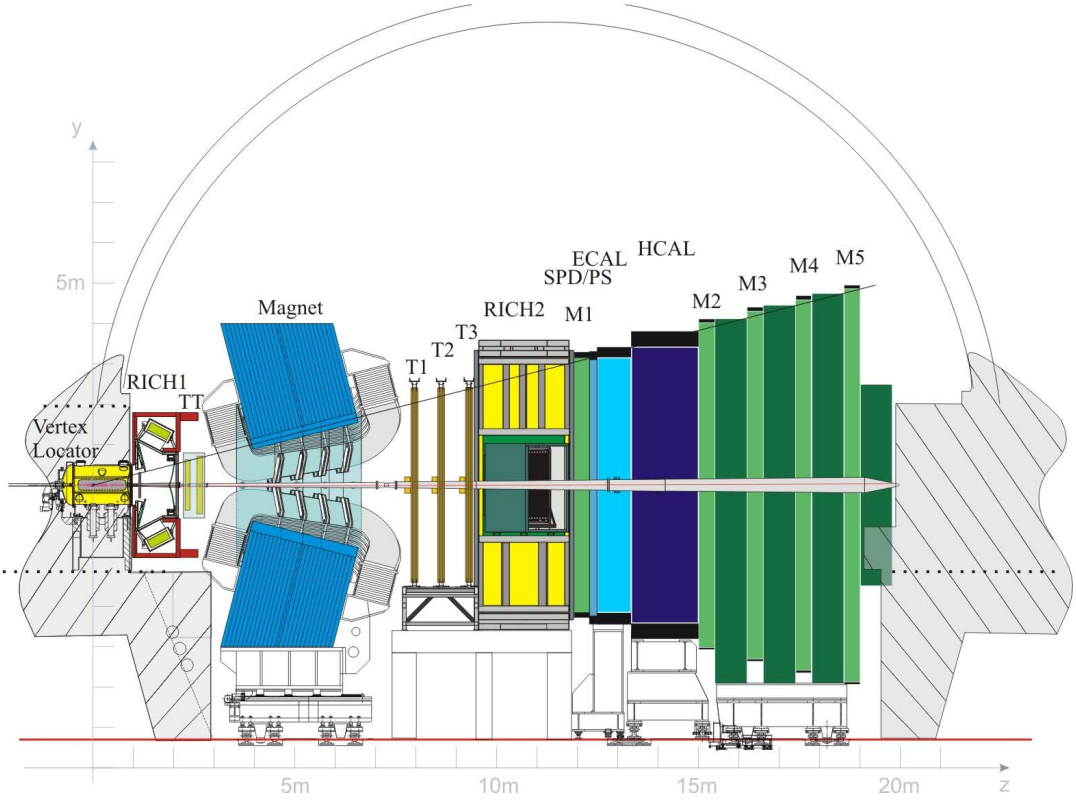

Figure 7.1: A visualisation of the LHCb detector, taken from Ref. [102].

The detector started data taking at the end of 2010, and the analysis described in the following chapters uses the data sets collected during Run 1, which ran between 2011 and 2012, and Run 2, from 2015 to 2018. The two runs recorded pp collisions corresponding to integrated luminosities of $3\,\text{fb}^{-1}$ and $6\,\text{fb}^{-1}$, respectively.

7.1 The tracking system

The tracking system at LHCb is excellent at reconstructing the trajectory of charged particles, which are commonly referred to as tracks. The different tracks considered in the reconstruction are illustrated in Fig. 7.2, of which the long tracks are the only tracks of interest for this thesis. In addition, downstream tracks are also important in other CP-violation analyses that consider K^0_S-meson decays to two charged pions, since this often occurs downstream of the VELO.

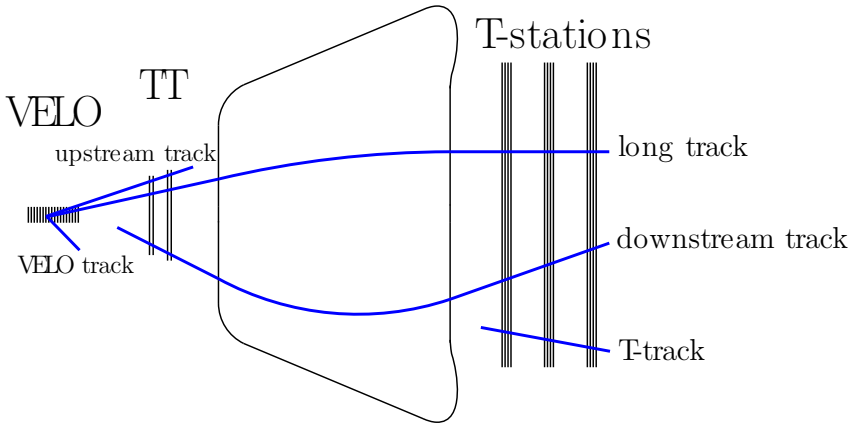

Figure 7.2: A diagram of track types that are reconstructed with the LHCb tracking system, taken from Ref. [104].

7.1.1 Vertex Locator

The VELO is a silicon-strip subdetector that surrounds the interaction point. It is essential for resolving the large number of tracks originating from the *pp* collision and precisely determines the positions of primary and secondary vertices. The sensors therefore sit only 7 mm from the beams, and to protect the silicon sensors the two halves of the VELO are free to move. During the injection and acceleration of the LHC beams, the VELO is retracted, due to the larger beam-aperture size required. Once the beams have reached their collision energy, with a stable beam condition, the VELO closes.

On the left of Fig. 7.3, one of the VELO halves is shown. It has a semi-circular shape, with an indentation in the middle where the beam enters. The silicon-strip pitch varies from 40 to 100 µm, and each half contains 21 standard modules used in physics analyses. Although tracks in the forward direction are the most important, the VELO also detects particles moving in the backward direction, which improves the primary vertex reconstruction (the *pp* collision point).

There are two possible orientations of the silicon-strip modules. A module can either be an R module, where the strips are oriented azimuthally, and this allows a measurement of the radial hit position. Similarly, a Φ module has strips

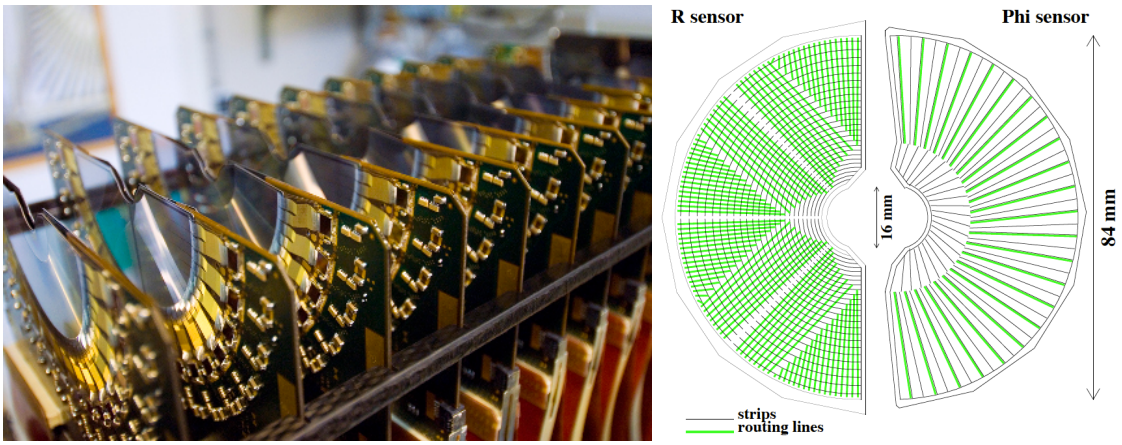

Figure 7.3: Left: A photograph of one half of the VELO during assembly. Right: An illustration of the R and Φ sensors of a VELO module. The figures are obtained from Ref. [105].

oriented radially, such that the azimuthal hit coordinate can be identified. The two module types are shown on the right in Fig. 7.3.

7.1.2 Tracking stations

Downstream of the VELO, there are four tracking stations. First, there is the TT, which is in front of the dipole magnet and it consists of silicon-strip sensors. Behind the magnet there are three additional tracking stations T1-T3. Each of these downstream tracking stations is split into an Inner Tracker (IT), which is a small cross-shaped region near the beam pipe, and an Outer Tracker (OT), which covers the remainder of the spectrometer acceptance.

The IT has a similar layout of silicon-strip sensors to the TT. The four silicon-strip tracking stations have four layers each in a x-u-v-x configuration, where the x layers have vertical strips and the u and v layers have stereo angles of $-5°$ and $5°$, respectively. The strips have a pitch of 183 µm in the TT and 198 µm in the IT. In total, the TT has an active area of $8\,\mathrm{m}^2$, while the three IT stations cover $4\,\mathrm{m}^2$ in total.

To cover the larger area, the OT consists of a drift-tube gas detector, where each gas-tight straw-tube has a diameter of 4.9 mm. The straws contain a mixture of 70% Argon, 28.5% CO_2 and 1.5% O_2. Each module has two staggered layers, and

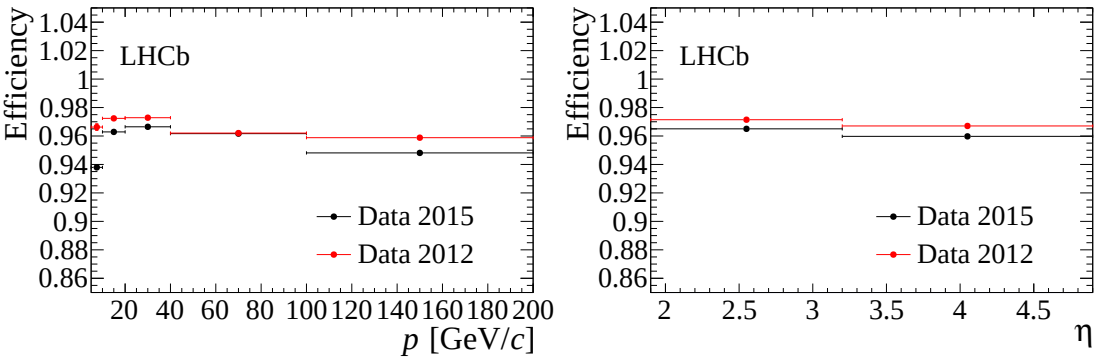

Figure 7.4: Track reconstruction efficiency from the data-taking periods 2012 and 2015, as a function of (left) momentum and (right) pseudo-rapidity. The figures are taken from Ref. [104].

each tracking station has four layers of modules in the same x-u-v-x configuration as the TT and IT. The working principles of these tubes is the same as that described in Section 4.1, and the achieved spatial resolution is 200 µm in the plane perpendicular to the wire.

The performance of the tracking system is demonstrated in Fig. 7.4, where the track reconstruction efficiencies from the 2012 and 2015 data-taking periods are shown as a function of momentum on the left and pseudo-rapidity on the right. In general, the efficiency is greater than 95%, determined using a tag-and-probe method with $J/\psi \to \mu^+\mu^-$ decays.

The tracking performance can also be quantified by studying how well the tracking system can identify primary vertices and measure impact parameters. The performance is shown in Fig. 7.5 along the x-direction, and the results along the y-direction are very similar. On the left, the resolution of the primary vertex position is shown as a function of the number of tracks. Naturally, with more tracks, the vertex position can be determined more accurately, and this results in a falling distribution. On the right, the impact parameter resolution is shown as a function of $1/p_T$. The linear increase is due to multiple-scattering effects at low momentum. At high momentum, an impact-parameter resolution of 12 µm is obtained.

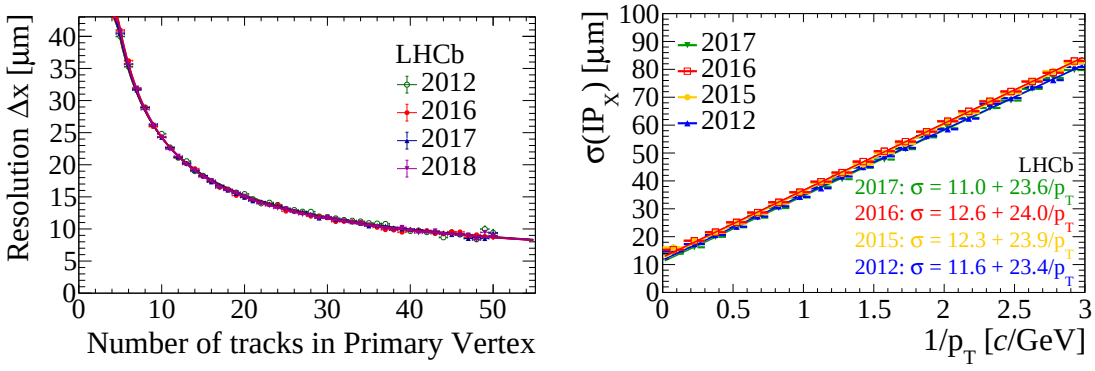

Figure 7.5: Left: Primary vertex resolution along x, as a function of track multiplicity. Right: Impact parameter resolution along x, as a function of the inverse transverse momentum. The different colours show different data-taking years. The plots are from Ref. [104].

7.1.3 The dipole magnet

The momenta of charged particles are determined from their deflection by the magnetic field between the TT and the three downstream tracking stations T1-T3. In Fig. 7.1, the particle trajectories bend in the horizontal direction, and the angular acceptance in this plane, $\pm 300\,\text{mrad}$, is therefore larger than that in the non-bending vertical plane, where it is $\pm 250\,\text{mrad}$. Although the original Technical Proposal suggested a superconducting dipole magnet, for cost-reduction reasons it was decided that a warm-magnet design was preferable.

The dipole magnet, which possesses some non-uniformity, has a bending power of $4\,\text{T}\,\text{m}$, defined as the field integral over the distance $z = 0$ to $z = 10\,\text{m}$ along the beam direction. As particles of different charge are deflected in opposite directions, the magnetic field is regularly interchanged between pointing upwards and downwards in order to cancel detection asymmetries. Together, the dipole magnet and the tracking stations achieve a 0.5% momentum resolution at low momentum, and at $200\,\text{GeV}/c$ the resolution has decreased to 1.0%.

7.2 Particle identification of hadrons

Particle identification (PID) capability is provided by four subdetectors in the LHCb experiment. The calorimeters, which are discussed in Section 7.3, can

recognise the presence of electrons and photons, and hence neutral pions. Similarly, charged tracks that reach the muon system, described in Section 7.4, are likely to be muons. Moreover, in the analysis of hadronic $B^{\pm}$ decays, it is crucial to distinguish between different species of hadrons. A Ring-Imaging Cherenkov (RICH) detector is highly suitable for this task; the LHCb detector has two such detectors, labelled RICH1 and RICH2. RICH1 is located upstream of the dipole magnet, while RICH2 is behind the tracking system.

The RICH working principles are based on the emission of Cherenkov radiation by charged particles traversing a medium with index of refraction n. The Cherenkov photons are emitted at an angle given by $\cos(\theta) = c/nv$ relative to the particle-momentum direction, where v is the particle speed. The photons are uniformly distributed in the azimuthal direction.

The key component of each RICH subdetector is a spherical mirror that images the cone of Cherenkov photons into a ring, which are then detected by a photon detector. Neglecting chromatic aberrations, photons emitted at the same Cherenkov angle are mapped into a circle of the same radius. Therefore, from a measurement of the photon hit position, combined with knowledge of the particle track, the Cherenkov angle can be reconstructed. The formalism for doing so is discussed in Ref. [106].

Figure 7.6 shows the different components of the RICH subdetectors, with RICH1 (RICH2) on the left (right). A charged particle entering the system from the left emits Cherenkov photons, which are reflected by spherical mirrors. Additionally, there are also plane mirrors that direct the photons away from the path of incoming particles. The advantage of this design is that the photon detectors may be placed outside the LHCb angular acceptance.

The photon detectors are hybrid photon detectors (HPDs), which consists of a photocathode deposited on the inside surface of a quartz window, which is sealed into a vacuum tube. When a photon hits the photocathode, a photoelectron is produced and accelerated towards a silicon sensor, which registers a hit.

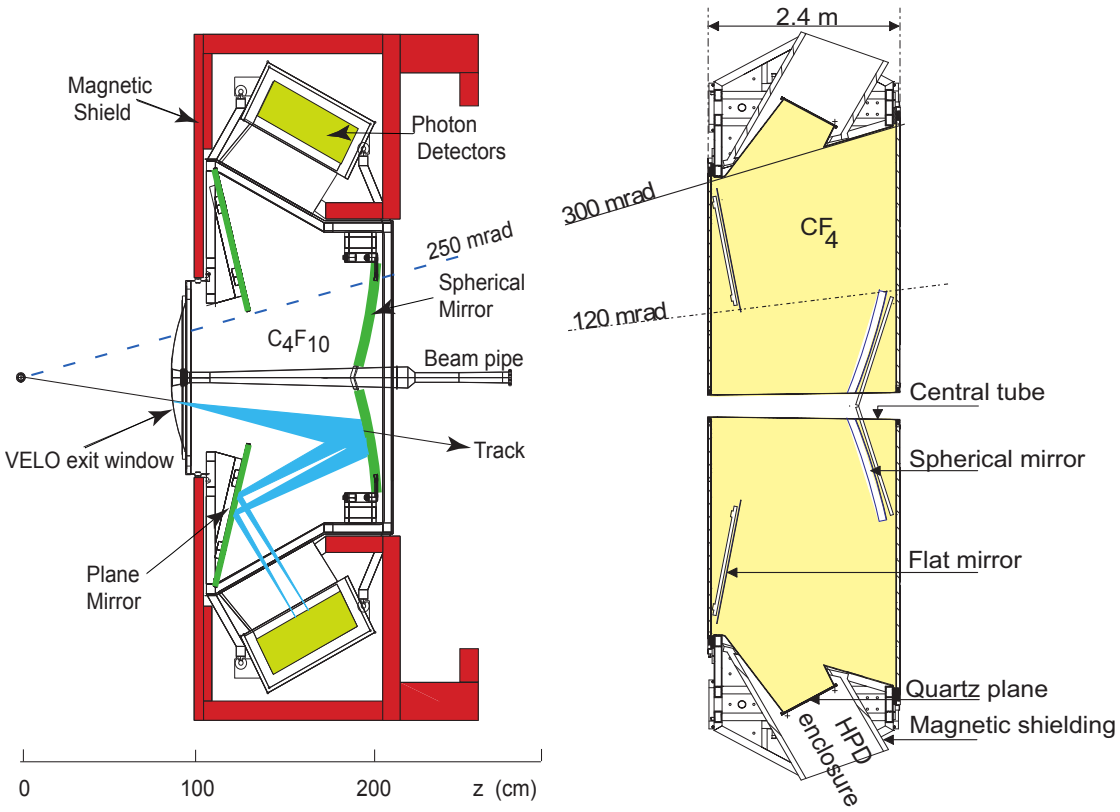

Figure 7.6: An overview of the RICH system, with RICH1 on the left and RICH2 on the right. Note the difference is scale. The diagrams are taken from Ref. [107].

The main difference between RICH1 and RICH2 is the radiator medium. In RICH1, a C_4F_{10} gas with an index of refraction $n_1 = 1.0014$ is used, which is suitable for particles at low momentum, up to approximately 60 GeV/c. In contrast, RICH2 uses a CF_4 gas with index of refraction $n_2 = 1.0005$, which can extend the momentum range up to about 150 GeV/c.

During Run 1, RICH1 also had an aerogel layer behind the entrance window, which is a suitable RICH radiator at particle momenta below 10 GeV/c. However, it was found during data taking that more photons than expected were scattered by this material, reducing the overall performance. It was therefore removed during the shutdown between Run 1 and 2.

The main factors affecting the PID separation power of RICH systems are the emission-point uncertainty, chromatic aberration and HPD pixel size. The first uncertainty is a consequence of using spherical mirrors which are slightly tilted with respect to the interaction region, instead of pointing mirrors with a parabolic shape.

This means that photons emitted from different positions along a particle track are focused onto circles with slightly different radii. Shrinking the radiator thickness can reduce this uncertainty, but this will also reduce the photon yield.

The second effect, chromatic aberration, is due to the variation of the index of refraction with photon energy, which the HPD cannot measure without precise timing capabilities. Finally, the HPD pixel size limits the precision of the photon hit position measured by the HPDs, and this uncertainty propagates into an uncertainty in the reconstructed Cherenkov angle.

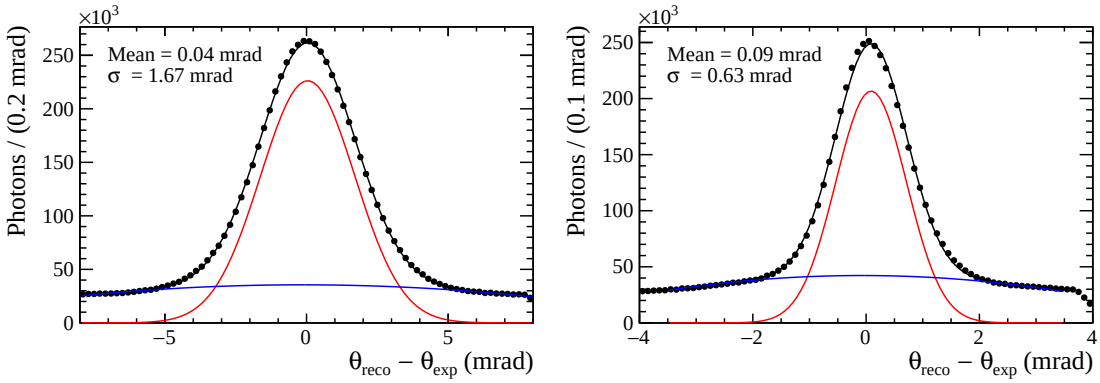

Figure 7.7: Left: An analysis of the Cherenkov angle resolution in (left) RICH1 and (right) RICH2. The figures are taken from Ref. [107].

To measure the single-photon Cherenkov angle resolution, a sample of high momentum tracks are considered, as these essentially travel at the speed of light. The Cherenkov angle has therefore saturated at a value given by $\cos(\theta) = 1/n$. In Fig. 7.7, a data-driven study of RICH1 on the left and RICH2 on the right is shown, and the resolutions are found to be 1.67 mrad and 0.63 mrad, respectively. For comparison, the pion-kaon Cherenkov-angle difference at a momentum of 30 GeV/c is 2.4 mrad in RICH1, and a more generic comparison between several particle species is shown on the left in Fig. 7.8. In RICH2, the separation is 0.56 mrad for pions and kaons at 80 GeV/c, while at 150 GeV/c, the separation reduces to 0.16 mrad.

In each pp event, there can be up to several hundred particles produced. Each of these particles, if above the Cherenkov-radiation threshold, could be associated with 20-30 photons. In such an intense environment, it is therefore unfeasible to consider each track in isolation. Instead, a global pattern-recognition algorithm [106]

is employed, which computes a likelihood of all tracks simultaneously. Initially, all particles are assigned a pion mass hypothesis, and an iterative procedure is performed. In each iteration, the likelihood is recalculated by changing the mass hypothesis of a single track, leaving the other tracks unchanged. The hypothesis that results in the greatest likelihood is retained.

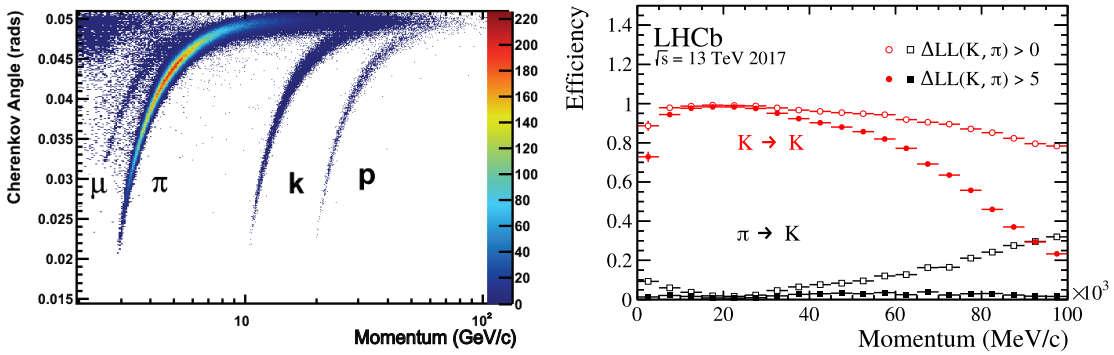

Figure 7.8: Left: A scatter plot of Cherenkov angles from different particle species in RICH1, as a function of momentum. Right: The pion-kaon PID performance, which is determined from calibration samples of $D^{*+} \to D^0\pi^+$, with $D^0 \to K^-\pi^+$. The figures are taken from Refs. [107, 108].

Using large calibration samples of $D^{*+} \to D^0\pi^+$ decays, where $D^0 \to K^-\pi^+$, the performance of the kaon-pion PID separation power can be assessed. The charge of the pion from the D^{*+} decay tags the flavour of the neutral D^0 meson, and it is therefore possible to unambiguously identify the pion and kaon products of the D^0 decay, without information from the RICH system. The results are shown on the left in Fig. 7.8, and a good separation is found up a momentum of 100 GeV/c.

7.3 Calorimeters

In the LHCb detector there are four calorimeter systems. From front to back, these are the Scintillator Pad Detector (SPD), Preshower (PS), Electromagnetic Calorimeter (ECAL) and Hadronic Calorimeter (HCAL). A lead plate, with a 15 mm thickness, is placed between the SPD and PS.

Figure 7.9 shows each component of the complete calorimeter structure. The calorimeters are segmented in the direction perpendicular to the beam, and cells

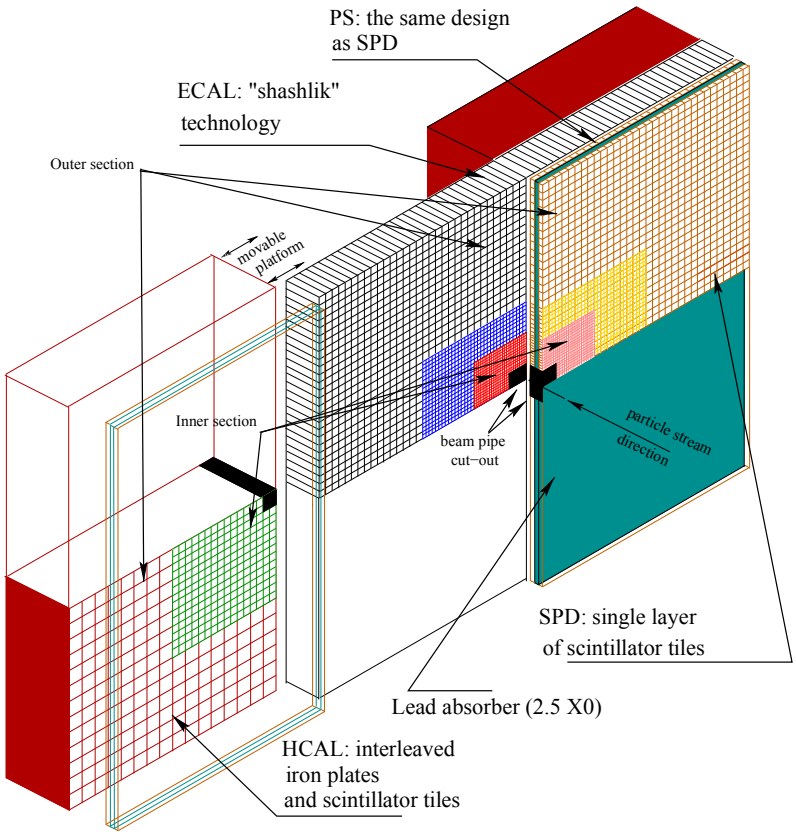

Figure 7.9: An overview of the LHCb calorimeter system, obtained from Ref. [109].

close to the beam pipe are smaller in size due to the larger number of particles in this region.

The four subdetectors operate on the same principle of alternating layers of absorber material and scintillator plates. Light is emitted when particles pass through the scintillators, and optical fibres guide the light to photomultiplier tubes, where the signal is converted into an energy measurement. The SPD, PS and ECAL employ lead as the absorber material, while the HCAL uses iron.

The purpose of the SPD is separating electrons from photons. Since there is no radiating material in front of the SPD, only charged particles such as electrons will generate a signal, unlike neutral photons. Charged pions and electrons can be separated by the PS, as only the latter will interact significantly with the lead plate between the SPD and PS.

For accurate energy measurements, electromagnetic showers from electrons and photons are fully contained inside the ECAL, which has a 25 radiation-length thickness. Due to space constraints, the HCAL only as a 5.6 nuclear interaction-length thickness. Thus, the HCAL is not used for accurate energy measurements, but it absorbs a sufficient amount of hadron energies to be used in the trigger system, which is discussed in Section 7.5.

7.4 Muon system

The muon system has five stations, labelled M1-M5, with a total area of 435 m^2. Stations M2-M5, located behind the calorimeters, contain multi-wire proportional chambers (MWPCs) interleaved with 80 cm thick iron absorbers. The MWPCs contain gold-plated tungsten wires with a diameter of 30 µm and a wire spacing of 2 mm. Inside each chamber there is a mixture of 40% Argon, 55% CO_2 and 5% CF_4 gas, which is ionised by muons passing through the MWPC. Since the anode is at high voltage, electrons from the ionisation drift towards the anode, creating a current. The iron absorbers ensure that only muons generate signals in the MWPC, neglecting a small amount of hadronic punch-through.

The inner part of M1 consists of gas electron multipliers, due to the large number of tracks near the beam pipe. The outer part of M1 contains MWPC chambers, similar to the other four stations.

On the left in Fig. 7.10, the locations of the muon stations and the absorber material are shown. The first station, M1, is located in front of the calorimeter in order to achieve a better transverse momentum measurement. This is used in the hardware trigger described in Section 7.5

In the plane transverse to the beam, the chambers are subdivided into four regions, as illustrated on the right of Fig 7.10. Each region is segmented into pads, where all pads within the same region have the same size. The segmentation of the pads has a finer granularity near the beam pipe, and specifically, the ratio between the linear size of pads in regions R1, R2, R3, R4 is 1:2:4:8. Furthermore,

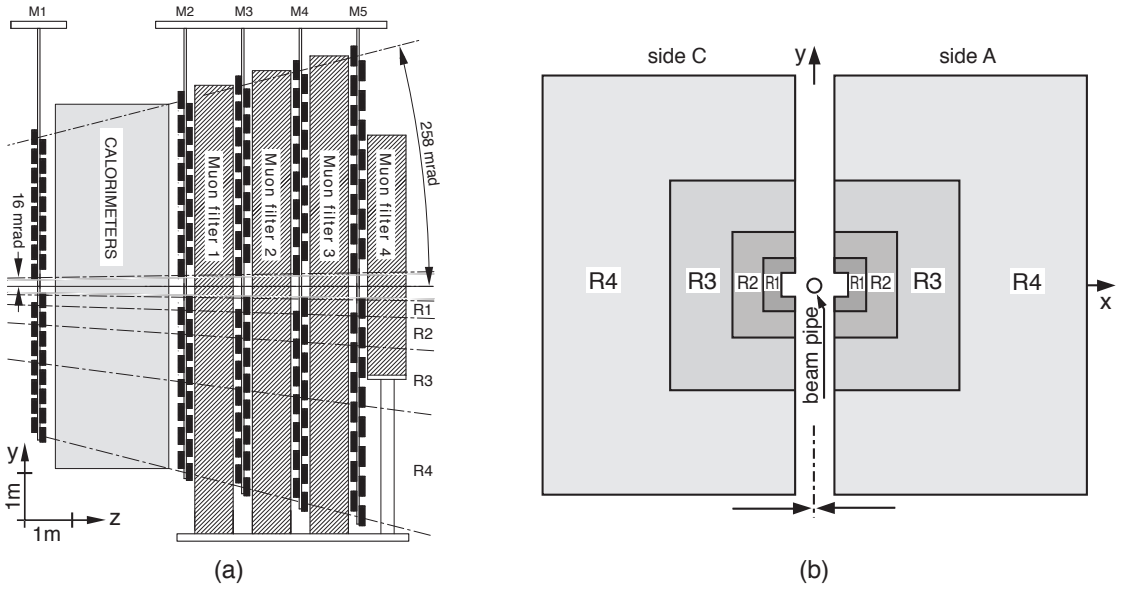

Figure 7.10: An overview of the LHCb muon system, obtained from Ref. [110].

the pads are smaller in the bending plane of the magnet, resulting in a more accurate transverse momentum measurement.

7.5 Hardware and software triggers

One of the most important components of the LHCb detector is its sophisticated trigger. The trigger ensures that the rate of collision at the LHC, 40 MHz, can be reduced by several orders of magnitude to a rate that is manageable to write to storage for later analysis. There are three trigger levels, starting with a hardware trigger known as Level 0 (L0) and two software triggers, also referred to as High Level Trigger 1 and 2 (HLT1 and HLT2).

Figure 7.11 shows a diagram of the hardware and software triggers used during Run 1 and 2, which are on the left and right, respectively. The maximum rate at which the LHCb subdetectors can read out data is restricted by the front-end electronics to around 1 MHz. Therefore, in both runs, the role of L0 is to reduce the LHC bunch-crossing rate to approximately 1 MHz.

As indicated by Fig. 7.11, in Run 1, the data pass through each trigger level sequentially. Events passing the hardware trigger proceed to HLT1, where a partial

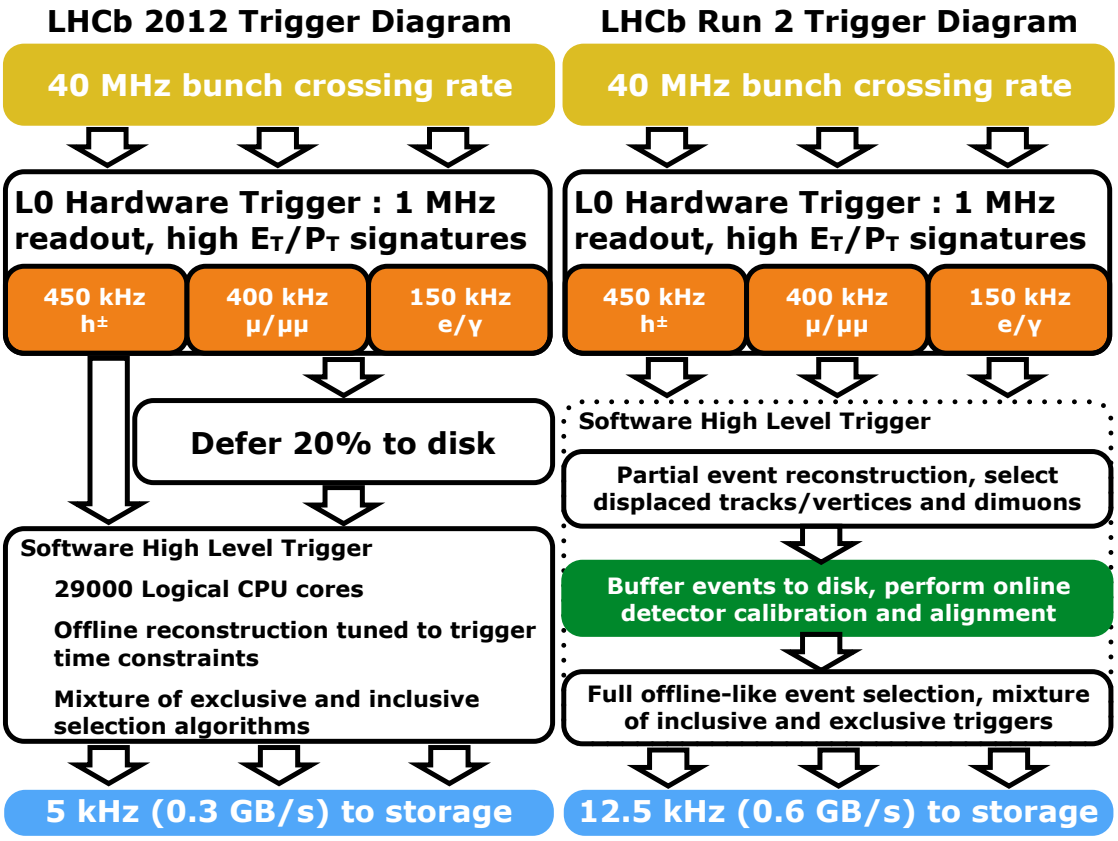

Figure 7.11: Trigger diagrams showing the dataflow during the (left) Run 1 data taking and (right) Run 2. The diagrams are taken from Ref. [111].

event reconstruction is performed. In HLT2, a full event reconstruction is executed. Each of the HLT stages reduces the rate by over an order of magnitude.

A small disk buffer is used to temporarily store 20% of all events accepted by L0. During periods without collisions, for instance during injection and acceleration, the computing resources can be tasked with processing these events, which maximises the use of available computing power.

Between Run 1 and 2, the software triggers were redesigned to become more flexible and enhance the trigger efficiency, allowing for more physics events to be selected. A key part of this upgrade was the installation of a large disk buffer, with sufficient storage space to save events accepted by HLT1 for up to two consecutive weeks of data taking. This provides the detector with the flexibility to perform real-time calibration and alignment directly in the software trigger, after the partial reconstruction in HLT1. When the events subsequently pass through HLT2, the

full event reconstruction can take advantage of this calibration and alignment.

Effectively, the full offline selection for dedicated analyses can be run directly in the software trigger. Thus, only information directly related to the signal candidate needs to be recorded, while the rest of the event may be discarded. As this reduces the size of each event that is written to disk by over an order of magnitude, this allows for a much higher selection rate. Moreover, with a full event reconstruction directly within the trigger, more efficient selection requirements may be imposed, using all the available information from all subdetectors.

7.5.1 The L0 hardware trigger

The L0 hardware trigger uses information from the calorimeters and the muon stations to provide a decision with a maximum latency of 4 µs. In particular, interesting physics events usually have particles in the final state with a large transverse momentum p_{T} or transverse energy E_{T}. Therefore, the calorimeter identifies events with large E_{T} based on the energy deposited in clusters of 2×2 cells in the ECAL and HCAL. The transverse energy is calculated using the expression

$$E_{\mathrm{T}} = \sum_{i=1}^{4} E_i \sin(\theta_i),$$

where E_i is the energy deposited in cell i and θ_i is the angle between the beam axis and the cell position, as measured from the pp interaction point. In addition, information from the SPD and PS can help determine if a hadron, photon or electron was responsible for the energy deposit. Events with E_{T} above a pre-defined threshold, which varies between data-taking years, will be selected by the hardware trigger.

For the L0 trigger to select muon events, a straight track is identified by the muon stations. A crude estimate of the p_{T}, precise to around 25%, is obtained by assuming the particle originated from the pp interaction point, and that it received a single "kick" from the magnetic field. The trigger decision requires either one or two muons to have p_{T} above a pre-defined threshold.

Finally, there is an upper limit to the number of hits in the SPD in order for an event to trigger the L0. This is to reduce the complexity of triggered events and speed up subsequent reconstruction, by rejecting unreasonably high-multiplicity events.

7.5.2 The High Level Trigger

In the first stage of the software trigger, a partial reconstruction is performed. The events of interest in this thesis are selected by an inclusive trigger in HLT1, which only looks for a single track with high p_{T} that is displaced from the primary vertex. To do so, hits in the VELO are used to reconstruct straight tracks and thence their primary vertices. Then these tracks are matched with hits in the TT and downstream tracking stations to determine their p_{T}. If a track is successfully matched with a high p_{T}, the different hits in the tracking stations are combined into a long track, which must satisfy a set of requirements [112].

In Run 1, the above inclusive trigger is denoted "Hlt1TrackAllL0Decision" and it is designed to select B decays. In Run 2 it was reoptimised and assigned the name "Hlt1TrackMVADecision". Additionally, a new HLT1 trigger was also added in Run 2 with the name "Hlt1TwoTrackMVADecision". This also looks for tracks that are displaced from the primary vertex, but it selects events with a displaced two-track vertex with high p_{T}.

Similar to HLT1, the analysis described in this thesis also relies solely on inclusive triggers in HLT2. Instead of relying only on tracks with high p_{T}, with a full event reconstruction in HLT2 these "topological" triggers look for two-, three- or four-track vertices with a large p_{T} and significant displacement from a primary vertex. The distance of closest approach between the tracks is required to be less than 0.2 mm. Furthermore, a discrete multi-variate algorithm is applied [113]. In Run 1, these topological lines are named "Hlt2Topo{2,3,4}BodyBBDTDecision", and they were reoptimised in Run 2, where they are known as "Hlt2Topo{2,3,4}BodyDecision".

In the $D \to K^+K^-\pi^+\pi^-$ decay, one of the most prominent resonances is the ϕ meson. It is therefore advantageous to also include an inclusive ϕ trigger line, which is labelled "Hlt2IncPhiDecision", for this decay mode. In simulation, it is found to improve the signal yield by a few per cent.

7.6 Stripping

When events have passed all three stages of trigger, they are written to disk with the full detector calibration and alignment. Furthermore, a "stripping" stage is performed where dedicated selections are applied to filter events into specific decay channels interesting for physics. In total there are hundreds of user-specific stripping lines. For instance, the decay $B^{\pm} \to DK^{\pm}$, where the D meson decays to $D \to \pi^+\pi^-\pi^+\pi^-$, $K^-\pi^+\pi^-\pi^+$, $K^+\pi^-\pi^+\pi^-$ or $K^+K^-\pi^+\pi^-$, is selected by a single stripping line. This selection starts by forming charged tracks, which are combined to form a D and a $B^{\pm}$ vertex.

The advantage of such dedicated stripping lines is that analysts are not required to process the whole data set. Instead, the stripping is processed centrally by the Worldwide LHC Computing Grid [114], and analysts who wish to perform a particular physics analysis only need to request events that pass a few specific stripping lines.

7.7 Simulation of LHCb

Simulation is required to model the effects of the detector acceptance, and for the study of possible background processes. In the simulation, pp collisions are generated using Pythia [115, 116] with a specific LHCb configuration [117]. Decays of unstable particles are described by EvtGen [80], in which final-state radiation is generated using Photos [118]. The $D^0 \to K^+K^-\pi^+\pi^-$ decay is simulated using the amplitude model from Ref. [38]. The interaction of the generated particles with the detector, and its response, is implemented using the Geant4 toolkit [78, 119] as described in Ref. [120]. The underlying pp interaction is reused multiple times, with an independently-generated signal decay for each event [121].

8

Selection of $B^{\pm} \to [K^+K^-\pi^+\pi^-]_D h^{\pm}$ and $[\pi^+\pi^-\pi^+\pi^-]_D h^{\pm}$ events

Contents

The analysis of $B^{\pm} \to Dh^{\pm}$, where $D \to K^+K^-\pi^+\pi^-$ and $D \to \pi^+\pi^-\pi^+\pi^-$, is performed using proton-proton collision data collected by the LHCb detector in 2011 and 2012 during Run 1 at centre-of-mass energies $\sqrt{s} = 7$ and 8 TeV, respectively, and in 2015–2018 during Run 2 at $\sqrt{s} = 13$ TeV. This sample corresponds to

pp collisions with an integrated luminosity of $9\,\text{fb}^{-1}$. The selection procedure described in this section was developed for the analysis of the $D \to K^+K^-\pi^+\pi^-$ channel, and it was adapted for the $D \to \pi^+\pi^-\pi^+\pi^-$ channel at a later stage with minimal modifications.

8.1 $B^{\pm} \to [K^+K^-\pi^+\pi^-]_D h^{\pm}$ candidate reconstruction

Charged $B^{\pm}$ mesons are produced in pp collisions, where a pair of $b\bar{b}$ quarks are produced at the interaction point with a very large cross section in the forward and backward directions, as demonstrated by Fig. 8.1. The angular acceptance of the LHCb detector is indicated by a red histogram in Fig. 8.1, and at $\sqrt{s} = 14\,\text{TeV}$, 27% of all b or $\bar{b}$ quarks are within this acceptance. These quarks subsequently hadronize into mesons or baryons, such as the $B^{\pm}$ meson.

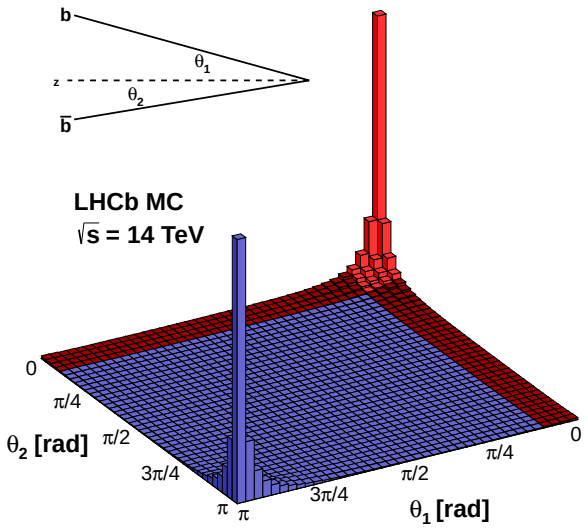

Figure 8.1: Cross section of $b\bar{b}$-production in a pp collider at a centre-of-mass energy of 14 TeV, as a function of the angle of the b and $\bar{b}$ quarks relative to the beam axis, θ_1 and θ_2, respectively. The figure is taken from Ref. [122].

The topology of the $B^{\pm}$ decays of interest to this analysis is shown in 8.2, which shows a final state with five charged tracks in total, four of which originate from

the D meson. From the primary vertex (PV), the $B^{\pm}$ meson flies about 1 cm before it decays. The charge of the $K^{\pm}$ (or $\pi^{\pm}$) meson of the $B^{\pm} \to Dh^{\pm}$ decay, which is referred to as the companion particle, determines the charge of the $B^{\pm}$ hadron. Furthermore, the D-decay vertex is also expected to be separated from the $B^{\pm}$-decay vertex by a few millimetres, before it decays into four charged particles.

It should be noted that the final state consists entirely of charged particles, making it a suitable decay for the LHCb detector. Quantitatively, the combined branching fraction of the $B^{\pm} \to [K^+K^-\pi^+\pi^-]_D K^{\pm}$ process is $(8.9 \pm 0.4) \times 10^{-6}$ [21]. The measurement presented in this thesis therefore requires a large sample of $B^{\pm}$ decays to be feasible. Given the $9\,\text{fb}^{-1}$ data set that has been collected, with a high trigger and reconstruction efficiency of the LHCb detector, this condition has been satisfied.

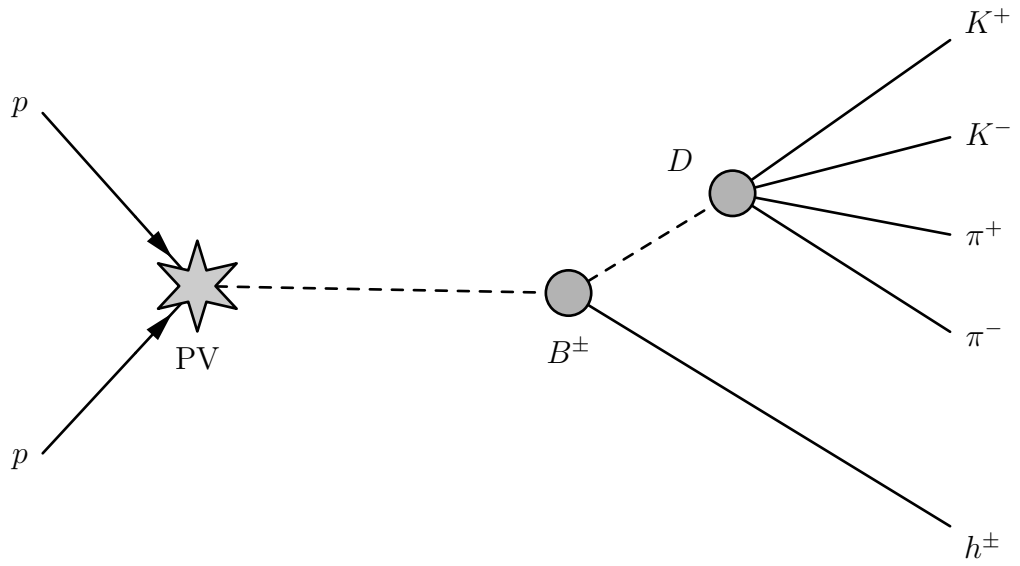

Figure 8.2: Decay topology of a $B^- \to [K^+K^-\pi^+\pi^-]_D h^{\pm}$ event in a pp-collider.

8.2 Preselection

In the initial preselection stage, decay candidates are reconstructed centrally in the stripping process, described in Section 7.6. The LHCb experiment has several hundreds of stripping lines that perform a reconstruction of tracks and vertices. Each stripping line, which has its own set of selection criteria to suppress

background events, identifies well reconstructed signal candidates from a particular physics process.

The stripping process starts with the identification of potential detector signatures from particles. The particles considered in this analysis are either charged pions or kaons, and additionally, there are different requirements for hadrons that decay from a D meson or a $B^{\pm}$ meson. The preselection requirements for these hadrons are listed in Table 8.1.

Table 8.1: Selection criteria applied to charged tracks during stripping. The values indicated inside parentheses are the criteria used in Run 1, but in Run 2 they were loosened to improve the signal efficiency.

	From D		From $B^{\pm}$	
Variable	$\pi^{\pm}$	$K^{\pm}$	$\pi^{\pm}$	$K^{\pm}$
p [MeV/c]	> 1000		> 5000	
p_T [MeV/c]	> 100		> 500	
χ^2_{track}/d.o.f	< 4.0 (3.0)		< 4.0 (2.5)	
χ^2_{IP}(BPV)	> 4.0		> 4.0	
P_{ghost}	< 0.4		< 0.4	
$\mathcal{L}_{\text{PID}}(K)$	< 20	> -10	—	

The variables p and p_T are the reconstructed momenta and transverse momenta of the hadron, respectively, and they are determined using the dipole magnet and the tracking system, as described in Section 7.1. The decay products of the $B^{\pm}$ meson generally have higher momenta, which is reflected in the tighter requirements imposed on these particles.

A fit is performed to determine the track parameters, and the resulting fit quality is described by the χ^2_{track} per degree of freedom. A track with a poor fit quality, which has a large χ^2_{track} value, is likely to be a ghost. These are reconstructed tracks that do not correspond to the trajectory of a true particle. Instead, it is likely to be from detector noise or from hits of separate particles.

The impact parameter (IP) of a particle is the distance of closest approach between a track and a given vertex, and it is determined by performing a fit. If a track has a large IP with respect to a PV, the track may have originated from a secondary vertex, for instance from the decay of a $B^{\pm}$ meson. For long-lived

particles, such as $B^{\pm}$ mesons, the IP of its decay products is therefore a powerful discriminator between real $B^{\pm}$ decays and background coming from random tracks. The quantity $\chi^2_{\text{IP}}(\text{PV})$ is called the significance of the IP, and it is defined as the χ^2 difference from a fit of the vertex with and without the track under consideration. A large $\chi^2_{\text{IP}}(\text{PV})$ value is therefore an indicator of a track that does not originate from the PV, which makes this variable a very useful discriminator as well.

The variable P_{ghost} is a used for identifying ghost tracks and it is known as the ghost probability. It is determined from a fast neural net that combines information from 22 input variables, including χ^2_{track}, as well as the individual χ^2 values from separate fits of downstream (IT and OT) and upstream (VELO and TT) tracking detectors [123]. The output of the neural net is mapped to the range $P_{\text{ghost}} \in [0, 1]$. This is therefore interpreted as a probability, with 0 (1) corresponding to a real (fake) track.

The final variable in Table 8.1 is the only variable that can discriminate between charged pions and kaons. It combines information from the two RICH subdetectors, described in Section 7.2. From the photon hits in the RICH subdetectors, the log-likelihood difference $\mathcal{L}_{\text{PID}}(K)$ between a kaon and a pion hypothesis is constructed. It allows for a very powerful discrimination between signal and background decays with misidentified particles, but it is also found that the loose requirements in Table 8.1 are highly efficient at rejecting combinatorial background. These are fake $B^{\pm}$-decay candidates formed from a set of random tracks, and it is one of the most prominent sources of background at hadron colliders due to the large number of tracks originating from the pp interaction.

It must be emphasised that all variables in Table 8.1, with the exception of $\mathcal{L}_{\text{PID}}(K)$, are properties that describe particle tracks. Thus, for particles with momenta much greater than their rest masses, these track variables possess no information that can distinguish between different mass hypotheses associated with the track.

More importantly, a selection requirement that is imposed on a variable describing the track of a pion is kinematically equivalent to applying the same

requirement on a kaon track. For this reason, a crucial aspect of the requirements in Table 8.1 is that the selection criteria are identical for the kaon and pion companion particles, and no information from the RICH subdetector is used at this stage. Since it is assumed that the $B^{\pm} \to DK^{\pm}$ and $B^{\pm} \to D\pi^{\pm}$ decays are kinematically identical, this preselection strategy ensures that the decay kinematics of the two $B^{\pm}$ decays remain identical.

Table 8.2: Selection criteria applied to composite particles during stripping.

Variable	D	$B^{\pm}$
m [MeV/c^2]	$[1764.84, 1964.84]$	$[4750, 7000]$
$\sum p_T$ [MeV/c]	> 1800	> 5000
χ^2_{DV}/d.o.f	< 10.0	< 10.0
DOCA [mm]	< 0.5	—
χ^2_{FD}	> 36	—
χ^2_{IP}(BPV)	—	< 25
DIRA(BPV)	—	> 0.999
τ(BPV) [ps]	—	> 0.2

After the selection of charged tracks, the composite D-meson candidate is formed, and the stripping requirements are listed in the middle column in Table 8.2. The first row is a selection window imposed on the reconstructed invariant-mass m of this composite particle. The sum $\sum p_T$ on the second row runs over the individual transverse momenta of its decay products. In the third row there is a requirement on the quality of the decay-vertex (DV) fit of the D meson. A true D-meson decay usually has a low value of the χ^2_{DV} per degree of freedom, which is equivalent to a good fit quality.

Two tracks that originate from the same vertex have a small distance of closest approach (DOCA), and the fourth requirement listed in Table 8.2 is applied to all combinations to decay products. Finally, the flight distance (FD) significance of the D meson, χ^2_{FD}, is defined analogously to χ^2_{IP}(PV).

From the reconstructed D meson, which is combined with the companion hadron, a composite $B^{\pm}$ meson is reconstructed using a similar set of requirements, listed in the final column of Table 8.2. The variable χ^2_{IP}(BPV) is required to be small, since

the $B^{\pm}$ meson must originate from the PV. The variable DIRA is the cosine of the angle between the momentum direction of a particle and the direction between a pair of vertices in the lab frame. For perfectly reconstructed vertices, DIRA should be equal to unity. Furthermore, similar to the FD requirements of the D meson, a minimum $B^{\pm}$-meson lifetime is imposed to suppress background contributions from random tracks near the PV.

8.3 Rectangular cuts before BDT

The offline selection that is performed after the stripping process, which is specific to this analysis, consists of a set of simple selection requirements, known as rectangular cuts. These should be distinguished from the Boosted Decision Tree described in Section 8.4, which is a multi-variate algorithm that targets combinatorial background. It is important to note that all selection requirements prior to the BDT are identical between the $B^{\pm} \to DK^{\pm}$ and $D\pi^{\pm}$ channels, in order to ensure that the BDT algorithm does not induce different phase-space acceptance effects in the two channels.

In general, the acquisition of a decay candidate selected by a stripping line is not necessarily prompted by the relevant triggers. Therefore, after the stripping process, the candidates are required to pass a well-defined set of trigger selections, which are described in Section 7.5. In each L0, HLT1 and HLT2 trigger stage, an event is required to pass at least one of the listed trigger lines listed in Table 8.3.

At the hardware trigger, L0, it is required that a particle associated with the signal decay triggered the hadron L0 trigger, and this is classified as a Trigger On Signal (TOS) event. It is also possible for an event to be triggered by a particle that is not associated with the signal decay, which is a Trigger Independent of Signal (TIS) event. The inclusion of TIS events increases the data set by roughly a factor two.

In the software trigger, all events are required to be TOS events, and the trigger lines listed in Table 8.3 are discussed in Section 7.5.

All candidates that pass the stripping selection must also undergo a Kalman kinematic fit, using the DecayTreeFitter framework [124], and this allows for a

Table 8.3: List of L0, HLT1 and HLT2 trigger requirements.

Trigger level	Trigger requirements
L0	L0HadronDecision_TOS L0Global_TIS
HLT1 Run 1	Hlt1TrackAllL0Decision_TOS
HLT1 Run 2	Hlt1TrackMVADecision_TOS Hlt1TwoTrackMVADecision_TOS
HLT2 Run 1	Hlt2Topo{2,3,4}BodyBBDTDecision_TOS Hlt2IncPhiDecision_TOS (only $K^+K^-\pi^+\pi^-$)
HLT2 Run 2	Hlt2Topo{2,3,4}BodyDecision_TOS Hlt2IncPhiDecision_TOS (only $K^+K^-\pi^+\pi^-$)

number of constraints to be applied. In particular, the D-meson invariant mass is constrained to its known value [21], and the momentum of the $B^{\pm}$ candidate is required to originate from its associated PV. In the subsequent analysis, the constrained variables, such as the four-momenta of the D-decay products, are used. The effect of using constrained kinematic variables is that the reconstructed phase-space coordinates have improved resolution, which ensures that all D decays are within the kinematically allowed region and bin-migration effects are reduced.

Table 8.4 lists a set of simple rectangular cuts, which are applied directly after stripping and trigger requirements. These are requirements on several common variables to remove obvious background candidates. Specifically, the invariant-mass windows are tighter than those in the stripping requirements. For the invariant-mass window of the $B^{\pm}$ meson, the value from DecayTreeFitter is used for the rectangular cut, which has a better resolution.

Table 8.4: Rectangular cuts applied before the BDT.

Particle	Variable [Unit]	Requirement
$B^{\pm}$	m_B [MeV/c^2]	$[5080, 5700]$
D	m_D [MeV/c^2]	$[1839.84, 1889.84]$
Companion	p [GeV/c]	< 100
Companion	Has RICH information	True
$B^{\pm}$	DecayTreeFitter	Converged

The third requirement in Table 8.4 is added because the RICH system has limited PID separation power at high momenta. Furthermore, to ensure that the companion hadron is assigned the correct mass hypothesis, any $B^{\pm}$ candidates where the companion hadron does not have information from the RICH systems is discarded from the analysis. Similarly, any decays where the Kalman fit fails are discarded from the analysis, as they are unlikely to originate from true D decays.

8.4 Boosted Decision Tree

A Boosted Decision Tree [125] (BDT) is a Multi-Variate Algorithm (MVA) with a wide range of applications, such as classification, regression and reweighting problems. The latter has already been encountered in Section 5.7, and in this analysis a BDT is used to classify reconstructed $B^{\pm}$ decays as either signal or background candidates. The advantage of an MVA algorithm is its ability to discriminate using a large set of variables with non-trivial correlations. This makes it a suitable strategy for the suppression of combinatorial background, which cannot be effectively discriminated with simple rectangular requirements, such as those described in Section 8.3.

8.4.1 Working principles of a BDT

A BDT classifier is an ensemble of simple classifiers. Each classifier may perform relatively poorly, perhaps only marginally better than random guessing, and hence they are referred to as weak learners. The core is idea is, by combining a large number of weak learners, the combined classifier has a very high accuracy. The ensemble of decision trees are constructed in a process called training, which requires large data samples that are representative of signal and background decays found in the LHCb data set. Thus, a BDT is a Machine Learning (ML) technique.

The weak learners in a BDT are binary decision trees. Figure 8.3 shows an illustration of such a tree, and it is the first tree of the BDT described in Section 8.4.2. The tree consists of nodes, which are the rectangular boxes, and leaves, which are shown as ellipses.

The working principles of a binary decision tree, by design, are relatively simple. At each node, a single rectangular selection requirement is imposed, and any candidate that satisfy this requirement move down to the right, otherwise it moves to the left. The variables in the BDT nodes in Fig. 8.3 are explained in Tables 8.5 and 8.6. The tree terminates at a leaf, and the number inside each leaf is the purity, defined as the number of signal candidates divided by the sum of signal and background candidates that reach the leaf.

During training, the top node in Fig. 8.3 starts with a purity of 0.5 since the training data set is reweighted to have an equal weight of signal and background candidates. As expected, the single decision tree in Fig. 8.3 has limited classification power and most leaves only show a small improvement in the purity. Due to its simplicity, each tree only has a maximum depth of three, and a node is replaced with a leaf if fewer than 2.5% of the training data set reaches the node.

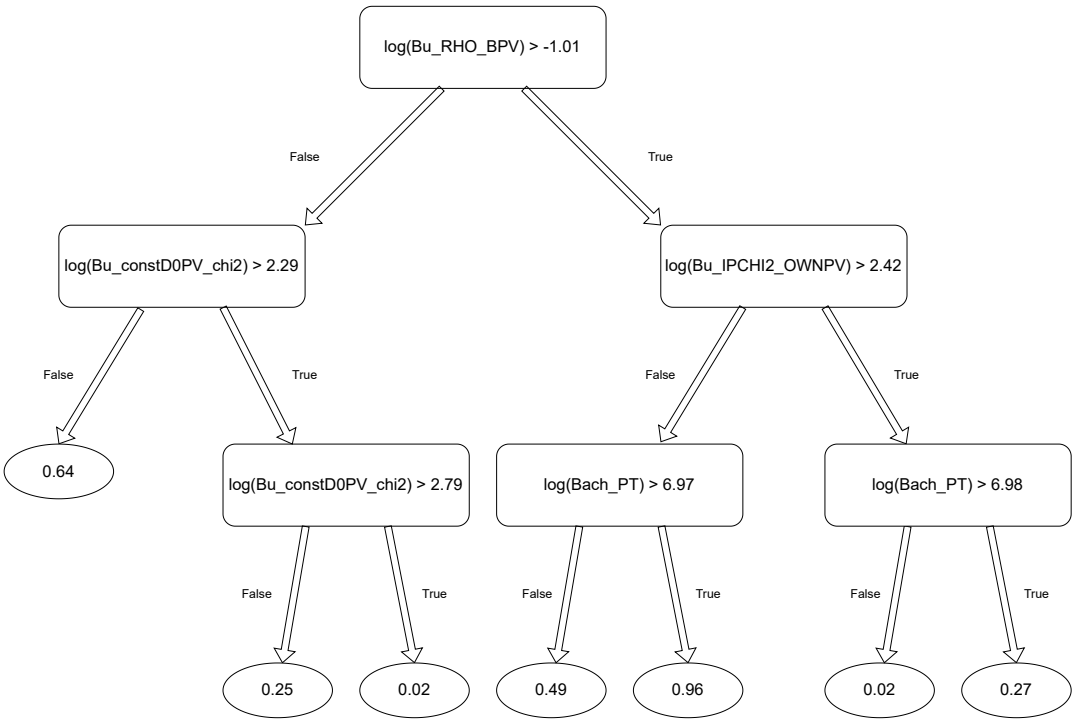

Figure 8.3: The first decision tree in the BDT algorithm developed for the suppression of combinatorial background. The rectangles are nodes that contain a single selection requirement, and the variables are explained in Tables 8.5 and 8.6. The ellipses are leaves, and the number inside indicate their purity.

During training, the variable and threshold value at each node in which the selection requirement is imposed, must be determined. Before the data are passed through a node, it is a mixture of signal and background decays that has a high level of disorder. The variable and threshold value are therefore chosen to achieve the best possible reduction of the disorder. A possible measure of disorder with close analogies to physics is Shannon entropy [126], but the Gini index [127] is more commonly used in ML applications.

At the leaves are the output values of the tree, which are directly related to its purity, but transformed into the range $[-1, +1]$. An output of $+1$ (-1) indicates a sample consisting solely of signal (background) candidates.

The special feature of a BDT is how the weak learners are combined into a strong learner, in a process called boosting. In the BDT chosen for this analysis, a gradient boosting technique [128] is selected, as it has been found effective in several similar analyses, such as Ref. [39]. The method constructs a weighted sum of all decision trees in a sequential manner by minimising a loss function. Specifically, since this BDT aims to perform a binary classification, the loss function is a (negative) log-likelihood function of the binomial distribution.

In the training process, the first tree will, by construction, attempt to assign signal (background) candidates an output of $+1$ (-1), and any discrepancies, also referred to as residuals, will increase the loss function. The second tree is not constructed to discriminate signal from background candidates, but instead tries to discriminate the residuals returned by the first tree. As implied by its name, this is achieved using knowledge of the gradient of the loss function.

Effectively, the second tree attempts to correct the errors of the first tree by assigning a larger weight to candidates from the first tree with large residuals. The weight is obtained directly from the gradient. With a large number of trees, where each tree corrects the errors of the previous tree, the weighted sum of all trees can achieve an accurate classification.

A common problem in ML models is overfitting, where the MVA algorithm adapts to fluctuations and noise in the training data set. To prevent this, the gradients are

scaled by a factor 0.1, known as the learning rate, which in practice reduces the error corrections of each tree. Therefore the number of trees must be increased accordingly, and the BDT described in Section 8.4.2 uses a sequence of 1000 decision trees.

8.4.2 Setup of BDT

The gradient BDT used in this analysis uses the implementation in TMVA [129]. Simulated $B^{\pm} \to [K^+K^-\pi^+\pi^-]_D h^{\pm}$ decays that undergo the selection requirements listed in Sections 8.2 and 8.3 are used as a proxy for signal decays. Similarly, the $B^{\pm}$ candidates from data in the upper sideband of the $B^{\pm}$ invariant-mass distribution, $m_B \in [5800, 7000]\,\mathrm{MeV}/c^2$, form a proxy for the combinatorial background decays. In total, the signal and background proxy samples contain approximately 5.4×10^6 and 4.4×10^6 candidates, respectively, and these are evenly split into a sample for training the BDT, and a sample for testing purposes. After training, the importance of each variable in the BDT can be determined by counting how often it occurs in the decision tree nodes.

The variables that are found to be useful in the BDT are variables describing vertex positions and their vertex χ^2_{DV}, the IP and flight distance significances χ^2_{IP} and χ^2_{FD}, DOCA, DIRA, and the momentum of the $B^{\pm}$, D and D-decay products. Additionally, a useful variable for suppression of combinatorial background is an isolation variable,

$$A_{p_T} = \frac{p_T(B^{\pm}) - \sum p_T}{p_T(B^{\pm}) + \sum p_T},$$

where the sum runs over all other tracks in a cone around the $B^{\pm}$ candidate. In the (η, ϕ) plane, which are the pseudo-rapidity and azimuthal angle, the cone is a circle with a radius of 1.5. A $B^{\pm}$-meson candidate with a large A_{p_T} value is, by definition, well isolated from other tracks in the event, making it less likely to be combinatorial background.

Finally, the BDT also uses knowledge of the χ^2 from the Kalman fit in DecayTreeFitter, which is denoted by χ^2_{DTF}. This variable is highly efficient at identifying

events containing a real D meson. There were also attempts to include other variables in the BDT, but variables of negligible importance were removed from the final BDT.

In summary, the BDT uses information from 28 variables. The distributions of these parameters are shown in Figs. 8.8 and 8.9. A detailed list of each variable, with explanation, is shown in Tables 8.5 and 8.6. The variables are ranked according to their importance.

Some variables in Figs. 8.8 and 8.9 show bimodal distributions, such as $\chi^2_{\rm IP}$ of the companion hadron. Such distributions are likely to be composed of combinatorial-background decays of different origins. For instance, events where a track from the PV is identified as a companion hadron usually has a lower $\chi^2_{\rm IP}$ than that of a track left behind by a decay product of a real b-hadron decay.

8.4.3 BDT performance

After training the BDT algorithm, its performance is illustrated by plotting its response when applied to the test samples. This is shown in solid colours in Fig. 8.4, where blue labels the signal candidates and red labels the background candidates. The data points show the BDT performance on the training sample, and the good agreement between training and test samples indicates there is no overfitting. The vertical scale is linear on the left, where an almost perfect separation is found, and on the right the vertical scale is logarithmic.

To verify that the BDT is agnostic to the particle species of the companion hadron, the ratio between the signal yields of $B^{\pm} \to DK^{\pm}$ and $B^{\pm} \to D\pi^{\pm}$ decays, denoted $R_{DK/D\pi}$, is determined for different BDT working points in the range $[0, 1]$. The yields are determined in a simultaneous fit of both $D \to K^+K^-\pi^+\pi^-$ and $D \to \pi^+\pi^-\pi^+\pi^-$ modes, using the setup described in Section 9.2.1. The resulting values of $R_{DK/D\pi}$ are shown in Fig. 8.5. The ratio $R_{DK/D\pi}$ is found to be very stable across the range of BDT working points, which suggests that the BDT acts identically on both $B^{\pm}$ decays.

Table 8.5: List of the first 14 variables used to train the BDT algorithm, ordered by importance. Variables with `constD0PV` in the name are the results of a refit with DecayTreeFitter.

Variable name in code	Importance (10^{-2})	Description
`log(Bu_RHO_BPV)`	7.092	Radial distance between the $B^{\pm}$-decay vertex and the best PV
`log(Bach_PT)`	6.890	Companion transverse momentum
`log(D0_PT)`	5.946	D-meson transverse momentum
`log(1-Bu_DIRA_BPV)`	5.655	DIRA of $B^{\pm}$
`log(Bu_PT)`	5.569	$B^{\pm}$ transverse momentum
`log(D0_RHO_BPV)`	4.859	Radial distance between the D-decay vertex and the best PV
`log(Bu_FDCHI2_OWNPV)`	4.726	$B^{\pm}$ FD significance, or χ^2
`log(Bu_constD0PV_chi2)`	4.675	DecayTreeFitter χ^2_{DTF}
`log(Bach_P)`	4.448	Companion momentum
`log(Bu_IPCHI2_OWNPV)`	4.375	$B^{\pm}$ IP significance, or χ^2
`Bu_PTASY_1.5`	4.071	Isolation variable
`log(D0_IPCHI2_OWNPV)`	3.508	D IP significance, or χ^2
`Bu_MAXDOCA`	3.481	$B^{\pm}$-vertex distance of closest approach
`log(Bu_constD0PV_D0_P)`	3.364	D momentum

Table 8.6: List of the last 14 variables used to train the BDT algorithm, ordered by importance. Variables with `constDOPV` in the name are the results of a refit with DecayTreeFitter.

Variable name in code	Importance (10^{-2})	Description
`log(Bach_IPCHI2_OWNPV)`	3.354	Companion IP significance, or χ^2
`log(1-D0_DIRA_BPV)`	3.295	DIRA of D
`log(D0_VTXCHI2DOF)`	2.973	D vertex fit χ^2
`log(max(h1_PT,h2_PT))`	2.944	Transverse momentum of kaons from D decay
`log(max(h1_P,h2_P))`	2.310	Momentum of kaons from D decay
`log(max(h3_PT,h4_PT))`	2.297	Transverse momentum of pions from D decay
`log(Bu_constDOPV_P)`	2.246	$B^{\pm}$-meson momentum
`log(Bu_VTXCHI2DOF)`	2.108	$B^{\pm}$ vertex fit χ^2
`log(max(h3_IPCHI2_OWNPV,h4_IPCHI2_OWNPV))`	1.922	IP significance, or χ^2, of pions from D decay
`log(min(h3_IPCHI2_OWNPV,h4_IPCHI2_OWNPV))`	1.790	IP significance, or χ^2, of pions from D decay
`D0_MAXDOCA`	1.745	D-vertex distance of closest approach
`log(min(h1_IPCHI2_OWNPV,h2_IPCHI2_OWNPV))`	1.602	IP significance, or χ^2, of kaons from D decay
`log(max(h1_IPCHI2_OWNPV,h2_IPCHI2_OWNPV))`	1.459	IP significance, or χ^2, of kaons from D decay
`log(max(h3_P,h4_P))`	1.295	Momentum of pions from D decay

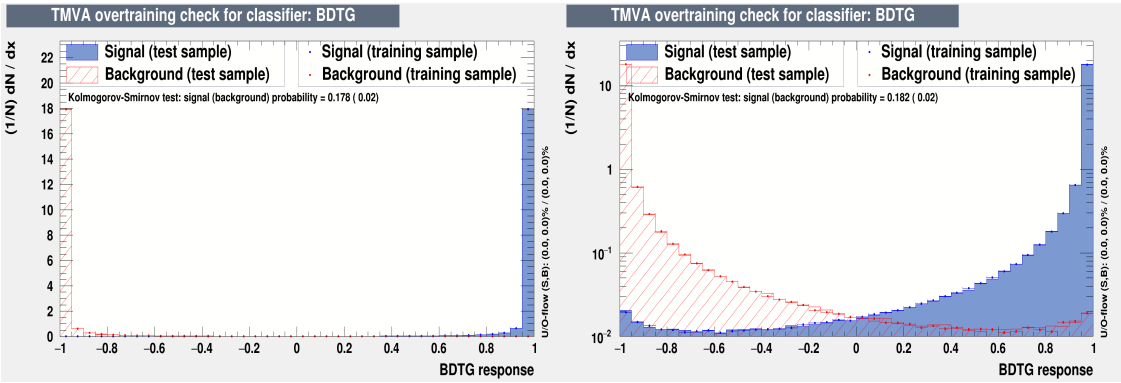

Figure 8.4: A comparison of the BDT output when applied to the test and training samples of (blue) signal and (red) background. The signal sample consists of simulated $B^{\pm} \to [K^+K^-\pi^+\pi^-]_D h^{\pm}$ decays, while the background sample uses the upper sideband of the $B^{\pm}$ invariant-mass distribution. The vertical axis is linear on the left and logarithmic on the right.

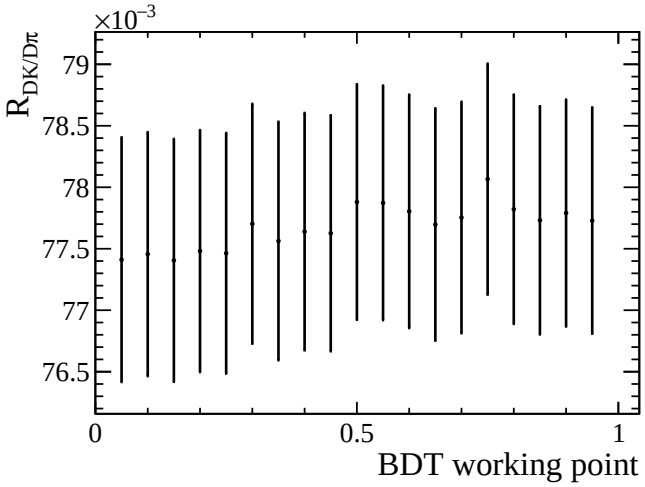

Figure 8.5: The ratio of signal yields $R_{DK/D\pi}$ between $B^{\pm} \to DK^{\pm}$ and $B^{\pm} \to D\pi^{\pm}$ decay modes as a function of the BDT working point. Both the $D \to K^+K^-\pi^+\pi^-$ and $D \to \pi^+\pi^-\pi^+\pi^-$ modes are fitted simultaneously with a common $R_{DK/D\pi}$ parameter.

8.4.4 Optimisation of BDT working point

As seen in Fig. 8.4, the BDT assigns a score in the range $[-1, +1]$ to all $B^{\pm}$ candidates, where candidates that are likely to be from a real $B^{\pm}$ decay obtain a larger score. It should be noted that when applying the BDT to data, a clear discrimination between signal and background, as seen in Fig. 8.4, is not expected. This is because candidates from the upper sideband do not form a perfect proxy for the combinatorial background. Therefore, the BDT working point, which is the threshold for classifying a candidate as signal or background, must be optimised.

Only candidates classified as signal are retained in the analysis.

In the optimisation, the yield of signal and background are first determined using the global invariant-mass fit described in Section 9.2.1. This fit is performed at BDT working points between 0 and +1, in increments of 0.05. Then for each working point, a set of 5000 pseudo-experiments are generated, according to the invariant-mass model described in Section 9.1. Each pseudo-experiment is fitted to obtain γ, and the average precision is obtained from the distribution of fitted values of γ. Due to different background levels, the optimisation is performed separately for Run 1 and 2.

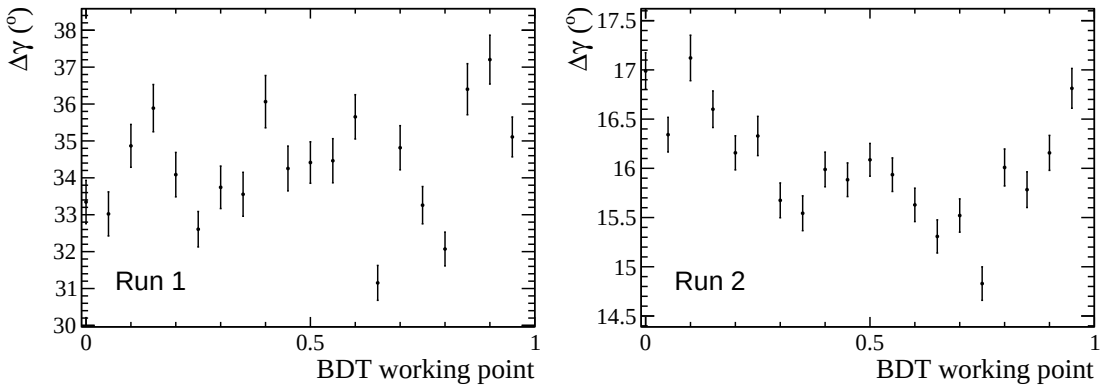

Figure 8.6: A study showing the precision of γ as a function of the BDT working point, with Run 1 on the right and Run 2 on the right.

The resulting precisions on γ are shown in Fig. 8.6. On the left, which shows the study with Run 1 yields, no clear minimum is found due to poor sensitivity, but the global minimum at 0.65 is chosen as the working point. On the right, a clear minimum is found at 0.75, which is the chosen working point for Run 2. The same working points are used for the $B^{\pm} \to [K^+K^-\pi^+\pi^-]_D h^{\pm}$ and $B^{\pm} \to [\pi^+\pi^-\pi^+\pi^-]_D h^{\pm}$ selections.

As a cross check, the signal significance, defined as $S/\sqrt{S+B}$ where S (B) is the yield of signal (background) candidates, is plotted in Fig. 8.7. The solid line shows the significance calculated from the yields found in data. The dotted line is an extrapolation where the signal yield is taken from simulation samples and the background yield is from the upper sideband in data, in the region $m_B \in [5400, 5600]\,\mathrm{MeV}/c^2$. The dotted lines are normalised to equal the solid line at a

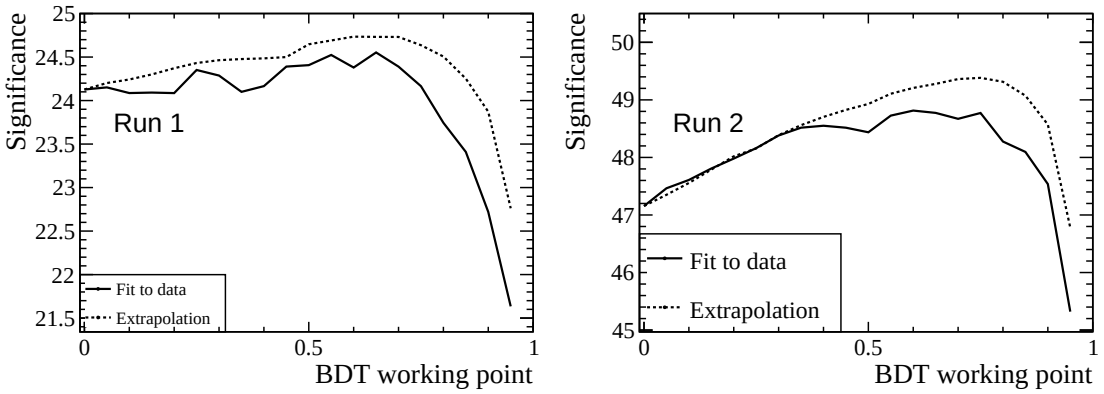

Figure 8.7: Signal significance as a function of the BDT working point, with Run 1 on the right and Run 2 on the right. The solid line shows that observed in data, while the dashed line is the extrapolation from the signal retention found in simulation and the yield of $B^{\pm}$ candidates in the upper sideband.

working point of 0.00. Although a perfect agreement is not found, the general behaviour agrees well. Furthermore, the significance is found to plateau in the region between 0.4 and 0.7 for Run 1, which would explain why no clear minimum is found in the optimisation study. The Run 2 significance in Fig. 8.7 has a maximum that agrees with the minimum of Fig. 8.6.

A comparison of the $B^{\pm}$ invariant-mass distributions is shown in Fig. 8.10, where the selection before the BDT is shown in red, and the blue histogram shows the selection after a BDT is applied. The BDT is found to have a high signal efficiency, and it successfully removes the majority of combinatorial background candidates.

8.5 Particle-identification requirements

The selection procedure described in this thesis so far, including the BDT, has not distinguished between the $B^{\pm} \to DK^{\pm}$ and $B^{\pm} \to D\pi^{\pm}$ modes, and their distinction is solely based on the mass hypothesis assigned to the companion particle. It also means that a candidate can appear in both selections. In order to separate two decays into two mutually exclusive selections, the samples are split using the log-likelihood difference $\mathcal{L}(K)$, which is described in Section 8.2. A candidate with $\mathcal{L}(K) = 0$ has an equal probability of being a kaon or a pion, while larger (smaller) values of $\mathcal{L}(K)$ favour a kaon (pion) mass hypothesis.

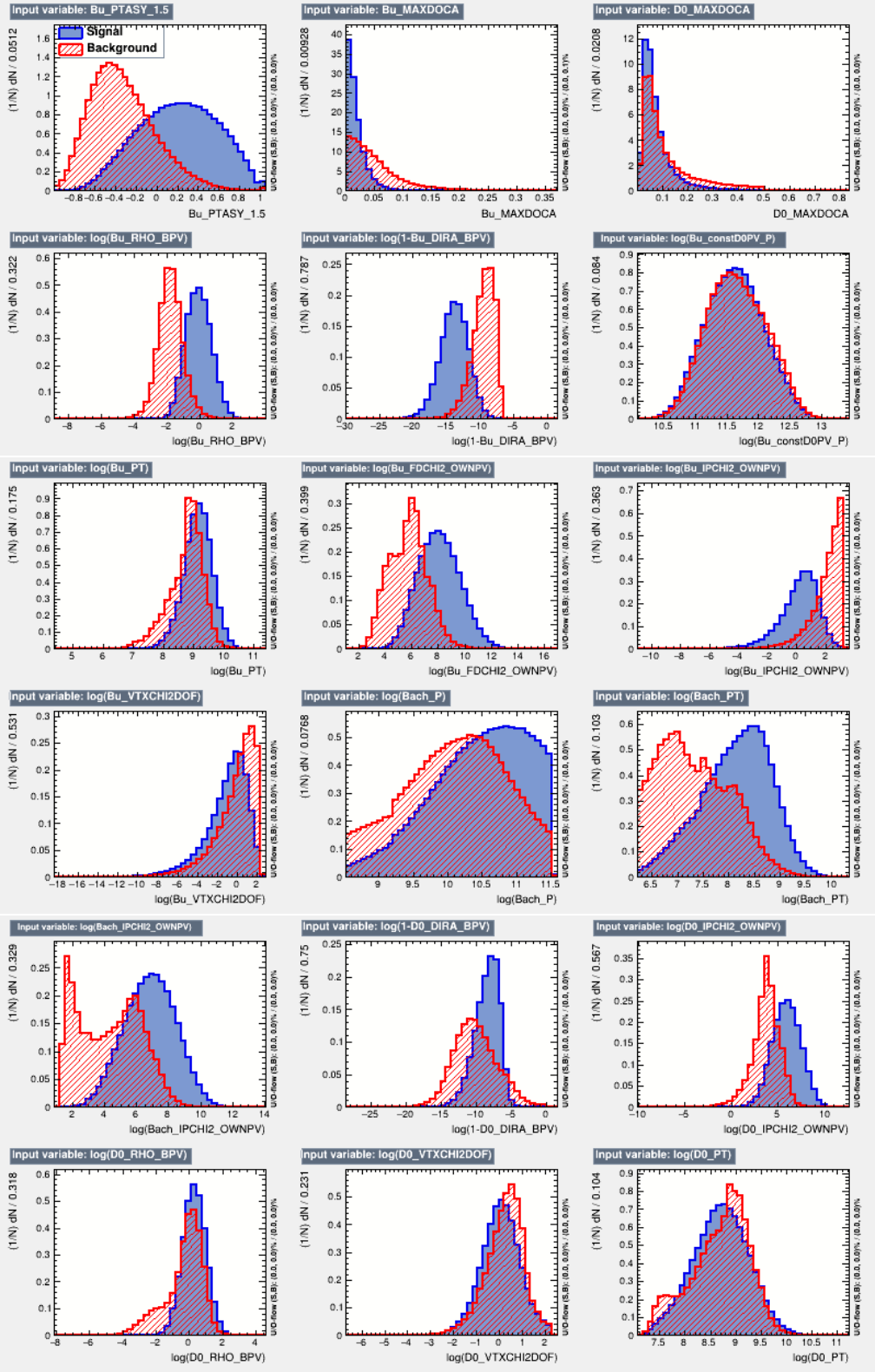

Figure 8.8: Distributions of variables used in the BDT, with the proxy of signal candidates in blue and background candidates in red.

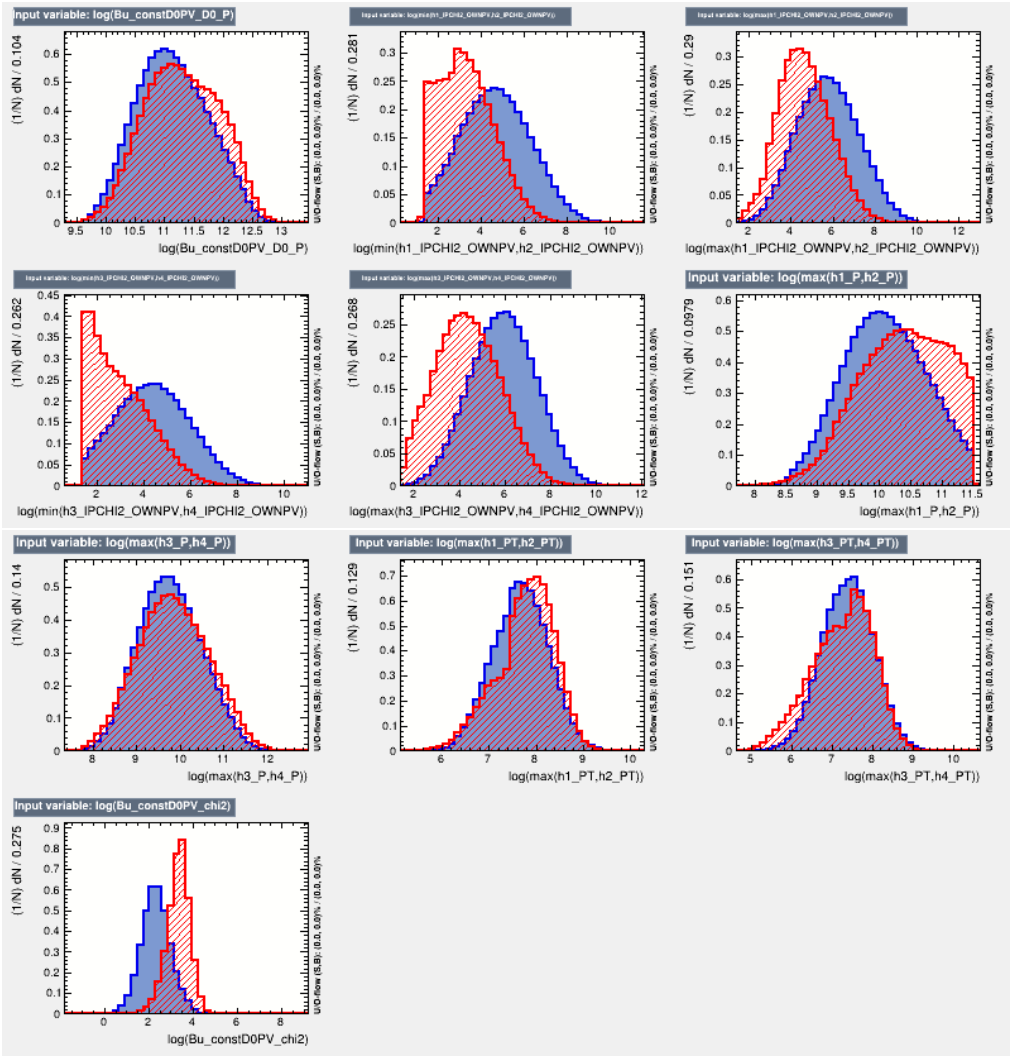

Figure 8.9: Distributions of variables used in the BDT, with the proxy of signal candidates in blue and background candidates in red.

In the analysis of $B^{\pm} \to Dh^{\pm}$ from Ref. [39], with the subsequent three-body $D \to K^0_S h^+ h^-$ decays, a threshold at $\mathcal{L}(K) = 4$ was used. The threshold must necessarily be greater than zero, since the branching fraction of the $B^{\pm} \to D\pi^{\pm}$ decay is 13 times larger than that of $B^{\pm} \to DK^{\pm}$. Furthermore, since the $B^{\pm} \to DK^{\pm}$ mode contains the *CP*-violating effects of interest, it is important to reduce the cross-feed contamination from the more abundant pion mode.

In Ref. [39], the $\mathcal{L}(K)$ working point was chosen such that the sensitivity to γ was maximised. The optimisation study was determined by fitting an ensemble of pseudo-experiments. In principle, the change from three-body $D \to K^0_S h^+ h^-$

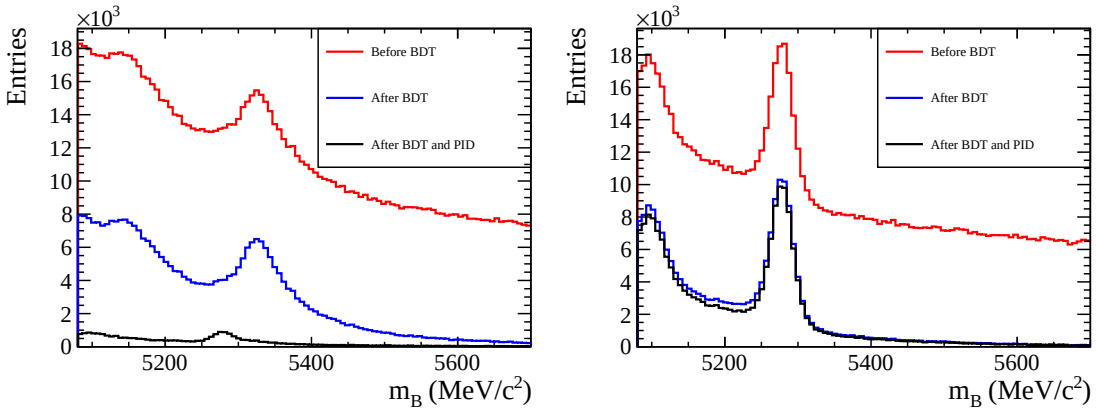

Figure 8.10: A comparison of the $B^{\pm}$ invariant-mass distributions (red) before and (blue) after a BDT is applied. In addition, the distribution after PID requirements have been applied to the companion hadron is shown in black. The left plot shows the $B^{\pm} \to DK^{\pm}$ selection, while the right plot shows the $B^{\pm} \to D\pi^{\pm}$ candidates.

decays in Ref. [39] to four-body $D \to K^+K^-\pi^+\pi^-$ and $D \to \pi^+\pi^-\pi^+\pi^-$ decays in this thesis requires an analogous optimisation study to be performed. However, since both analyses consider $B^{\pm}$ decays that are kinematically similar, with a large set of common background components, it may be assumed that the optimal $\mathcal{L}(K)$ will also be very similar. Hence, in this thesis the threshold $\mathcal{L}(K) = 4$ has been adopted from Ref. [39].

The effect of the PID requirement is clearly seen in Fig. 8.10, where the distribution before and after this requirement is shown in blue and black, respectively. In the $B^{\pm} \to DK^{\pm}$ selection on the left, the blue distribution is clearly dominated by misidentification from $B^{\pm} \to D\pi^{\pm}$, which has a peaking structure that sits in the upper sideband of the $B^{\pm} \to DK^{\pm}$ signal peak. The PID information is found to be crucial for suppressing this cross-feed background. The selection of $B^{\pm} \to D\pi^{\pm}$ candidates are affected by misidentification background to a lesser extent, and the PID requirement is found to mostly suppress combinatorial background.

When different PID selections are applied to the $B^{\pm} \to DK^{\pm}$ and $D\pi^{\pm}$ selections, the relative difference in selection efficiency must be accounted for. Unfortunately, as the $\mathcal{L}(K)$ response is poorly modelled in simulation, the efficiencies must be determined using data-driven methods. The strategy for studying the PID response of charged pions and kaons is to use large calibration samples of $D^{*+} \to D^0\pi^+$

decays, with the subsequent $D^0 \to K^-\pi^+$ decay. The soft pion produced in the strong decay of D^{*+} tags the flavour of the neutral D^0 meson, which allows for an unambiguous identification of the charged kaon and pion from the D^0 decay. Background components are removed using the sPlot method [130].

The PID response of the LHCb detector has a non-trivial dependence on several kinematic variables and track multiplicity, and therefore the calibration samples are partitioned into a three-dimensional binning scheme in momentum p, pseudo-rapidity η and number of tracks N_{track}. The bin boundaries are defined by:

- Three p bins with boundaries at $(3.0, 9.3, 15.6)\,\text{GeV}/c$ and then 15 uniformly separated bins in the range 15.6-100 GeV/c;
- Four uniformly separated η bins in the range 1.5-5.0;
- Five bins in N_{track} with boundaries at $(0, 50, 200, 300, 500)$.

The first three bin boundaries in p are the kinematic thresholds for Cherenkov radiation of pions in RICH1, kaons in RICH1 and kaons in RICH2, respectively.

In each bin, the PID efficiency of the selection requirements $\mathcal{L}(K) > 4$ and $\mathcal{L}(K) < 4$ on the calibration sample are calculated, and three-dimensional lookup tables of PID efficiencies are constructed. To convert this set of numbers into a combined PID efficiency, the large sample of $B^\pm \to D\pi^\pm$ decays in a region within $25\,\text{MeV}/c^2$ of the $B^\pm$ mass, which is referred to as the reference sample, is used as a proxy for both the $B^\pm \to D\pi^\pm$ and $B^\pm \to DK^\pm$ modes. In simulation, it is found that the p, η and N_{track} distributions are highly consistent between $B^\pm \to D\pi^\pm$ and $B^\pm \to DK^\pm$ decays.

Each candidate in the reference sample is assigned a PID efficiency from the lookup table, such that the requirement on $\mathcal{L}(K)$ is effectively applied through per-event reweighting. The total PID efficiency is then obtained as the average efficiency of all candidates in the reference sample. The whole PID calibration procedure is done using the PIDCalib2 framework [131–133].

The statistical uncertainties are estimated by bootstrapping the efficiency calculation 500 times. Each time, the reference sample is resampled with replacement. The RMS of the resulting distribution is taken as the statistical uncertainty.

The calculation is also repeated using four alternative binning schemes with uniformly spaced bins, and the standard deviation of the results is taken as the systematic uncertainty due to the choice of binning scheme. Table 8.7 shows the PID efficiencies obtained with each binning scheme, together with the resulting binning scheme systematic uncertainty. The second column lists the total number of bins in $(p, \eta, N_{\text{track}})$ for each binning scheme.

In addition to the systematic uncertainties listed in Table 8.7, a systematic uncertainty of 0.1% is added in quadrature. This uncertainty represents the breakdown of the assumptions of the sPlot method [130]. In particular, in the invariant-mass fit of calibration samples, it is found that the mass resolution have a correlation with p and η. The size of this effect is discussed in Ref. [132]. The average PID efficiencies are given in Table 8.8, with combined statistical and systematic uncertainties.

Table 8.7: PID efficiencies estimated with difference binning schemes.

Decay mode	Binning	$K^{\pm}$ efficiency (10^{-2})	$\pi^{\pm}$ efficiency (10^{-2})
$B^{\pm} \to [K^+K^-\pi^+\pi^-]_D h^{\pm}$	Default	86.40 ± 0.08	97.102 ± 0.009
	(14, 2, 2)	86.68 ± 0.08	97.148 ± 0.008
	(16, 3, 3)	86.12 ± 0.09	96.991 ± 0.011
	(20, 5, 5)	86.22 ± 0.08	96.998 ± 0.011
	(22, 6, 6)	86.17 ± 0.09	97.030 ± 0.012
Systematic uncertainty		0.23	0.07
$B^{\pm} \to [\pi^+\pi^-\pi^+\pi^-]_D h^{\pm}$	Default	87.01 ± 0.04	97.137 ± 0.005
	(14, 2, 2)	87.19 ± 0.05	97.174 ± 0.005
	(16, 3, 3)	86.87 ± 0.05	97.065 ± 0.006
	(20, 5, 5)	86.94 ± 0.05	97.055 ± 0.006
	(22, 6, 6)	86.91 ± 0.05	97.090 ± 0.006
Systematic uncertainty		0.13	0.05

Table 8.8: PID efficiencies of the bachelor PID cut. The uncertainties are the combined statistical and systematic uncertainties.

Decay mode	$K^{\pm}$ efficiency (10^{-2})	$\pi^{\pm}$ efficiency (10^{-2})
$B^{\pm} \to [K^+K^-\pi^+\pi^-]_D h^{\pm}$	86.40 ± 0.26	97.10 ± 0.12
$B^{\pm} \to [\pi^+\pi^-\pi^+\pi^-]_D h^{\pm}$	87.01 ± 0.17	97.14 ± 0.11

8.6 Background studies

There are several background decays which contaminate the $B^{\pm} \to Dh^{\pm}$ selections, and they are not suppressed by the BDT since they are not combinatorial in origin. In this section, a brief summary of each type of background is described, and the requirements imposed to suppress these background decays.

8.6.1 Cloned tracks

A relatively common contamination are $B^{\pm}$ candidates where two of the reconstructed final-state tracks are in fact from a single particle that has been duplicated during reconstruction. The opening angle between such tracks is expected to be small, as shown on the left in Fig. 8.11, and these are easily removed by discarding any candidates where the opening angle $\theta_{ij} < 0.03^{\circ}$. On the right of Fig. 8.11, the invariant-mass distribution of these candidates is shown, and these are found to be mostly combinatorial-background events.

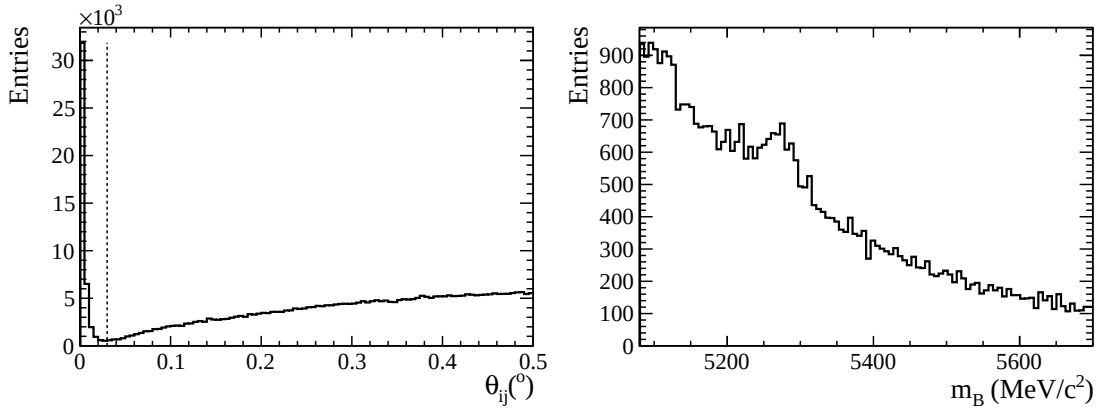

Figure 8.11: Left: Distribution of opening angles between all pairs of tracks from D-decay products, where cloned tracks correspond to the peak at $\theta_{ij} = 0^{\circ}$. The dotted line shows the requirement imposed to remove these candidates. Right: The $B^{\pm}$ invariant-mass distribution of candidates that are removed by the requirement $\theta_{ij} > 0.03^{\circ}$.

8.6.2 Removal of $K^0_S \to \pi^+\pi^-$ candidates

In Section 5.3.3 the decay $D \to K^0_S K^+K^-$ is discussed as a significant background contribution in the strong-phase measurement. In LHCb, this background is much smaller due to the larger boost of the $B^\pm$ mesons. However, since the measurement of c_i and s_i is performed without this region of phase space, it should also be removed from the analysis of $B^\pm$ candidates. Therefore, any $B^\pm \to [K^+K^-\pi^+\pi^-]_D h^\pm$ candidates with an invariant mass in the region $m(\pi^+\pi^-) \in [477, 507]\,\text{MeV}/c^2$ is rejected. Similarly, following the requirement in Ref. [40], any pair of pions that are in the region $m(\pi^+\pi^-) \in [480, 505]\,\text{MeV}/c^2$ in the $B^\pm \to [\pi^+\pi^-\pi^+\pi^-]_D h^\pm$ selection are also removed from the sample to reject $D \to K^0_S\pi^+\pi^-$ decays.

8.6.3 Semi-leptonic $B^\pm$ decays

It is possible that the companion hadron is a muon misidentified as a pion or kaon. This would lead to a contamination from a semi-leptonic $B^- \to D^0\mu^-\nu_\mu$ decay, where the neutrino is not reconstructed. In events where the companion hadron track has hits in the muon spectrometer associated with it, it is likely to be a muon misidentified as a pion or kaon. This semi-leptonic background can therefore be studied directly in data by looking at $B^\pm$ candidates where the companion hadron is identified as a muon, and this is shown in Fig. 8.12.

In the $B^\pm \to DK^\pm$ selection on the left, the $B^\pm$ invariant-mass distribution of candidates that are identified as muons, in blue, is almost consistent with those that are not muons, shown in black. For candidates where the companion hadron is identified as a muon, the peak at the $B^\pm$ mass is most likely from signal $B^\pm \to DK^\pm$ decays where the companion hadron decays in-flight. However, in the $B^\pm \to D\pi^\pm$ selection on the right, the distribution is not consistent with in-flight pion decays. A contribution from the $B^\pm$ semi-leptonic background is seen in the low-mass region. There is a rapidly falling slope, which has also been verified with RapidSim [134] simulation. Therefore it is necessary to remove these candidates from the selection.

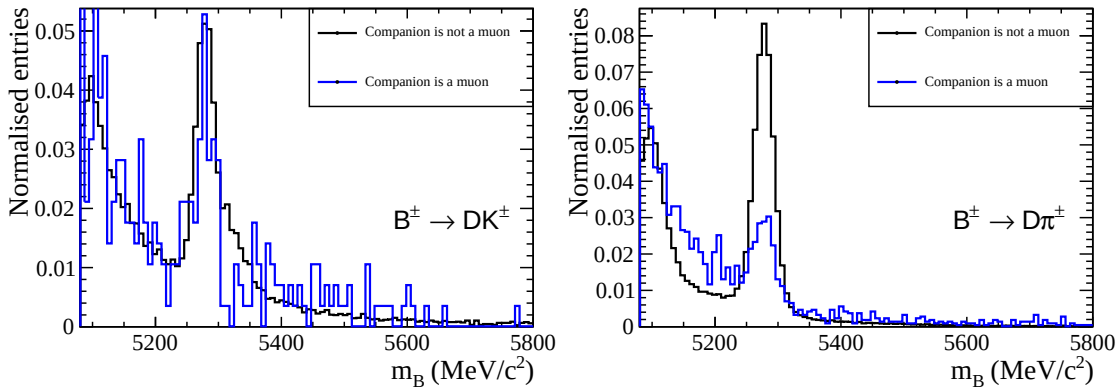

Figure 8.12: A comparison of $B^{\pm} \to DK^{\pm}$ ($D\pi^{\pm}$) candidates on the left (right) where the companion hadron is found to not be a muon, in black, and where it has been identified as a muon, in blue.

8.6.4 Flight-significance requirements

Direct decays of $B^{\pm}$ mesons to final states with five charged tracks, without an intermediate charm meson, are referred to as charmless decays. The tracks of such decays originate from the $B^{\pm}$-decay vertex, and this background is suppressed with a requirement on the flight significance $\Delta z^{D-B}_{\text{significance}}$, defined as the separation between the $B^{\pm}$ and D decay vertices along the z-direction. Due to the large number of these background events, a detailed study of these decays is described in Section 9.1.4.

In the selection after the BDT, the phase-space binned analysis uses a requirement at $\Delta z^{D-B}_{\text{significance}} > 2$, while the integrated analysis has a tighter requirement at $\Delta z^{D-B}_{\text{significance}} > 4$.

8.6.5 Background from Cabibbo-favoured decays

In Sections 9.1.4, 9.1.5 and 9.1.6, several CF decays that are present in the final selection are discussed. While many of these are suppressed by other selection criteria, an additional PID requirement is added to the $B^{\pm} \to [K^+K^-\pi^+\pi^-]_D h^{\pm}$ selection. In particular, a loose PID requirement, $\mathcal{L}(K) > 0$, is imposed on the kaon with opposite charge to the companion hadron, which removes a significant number of CF D decays while still retaining most of the $D \to K^+K^-\pi^+\pi^-$ decays.

8.7 Final selection of $B^{\pm}$ candidates

Figure 8.13 shows the invariant-mass distribution of the final sample of selected $B^{\pm}$ candidates, which will be analysed in Chapter 9.

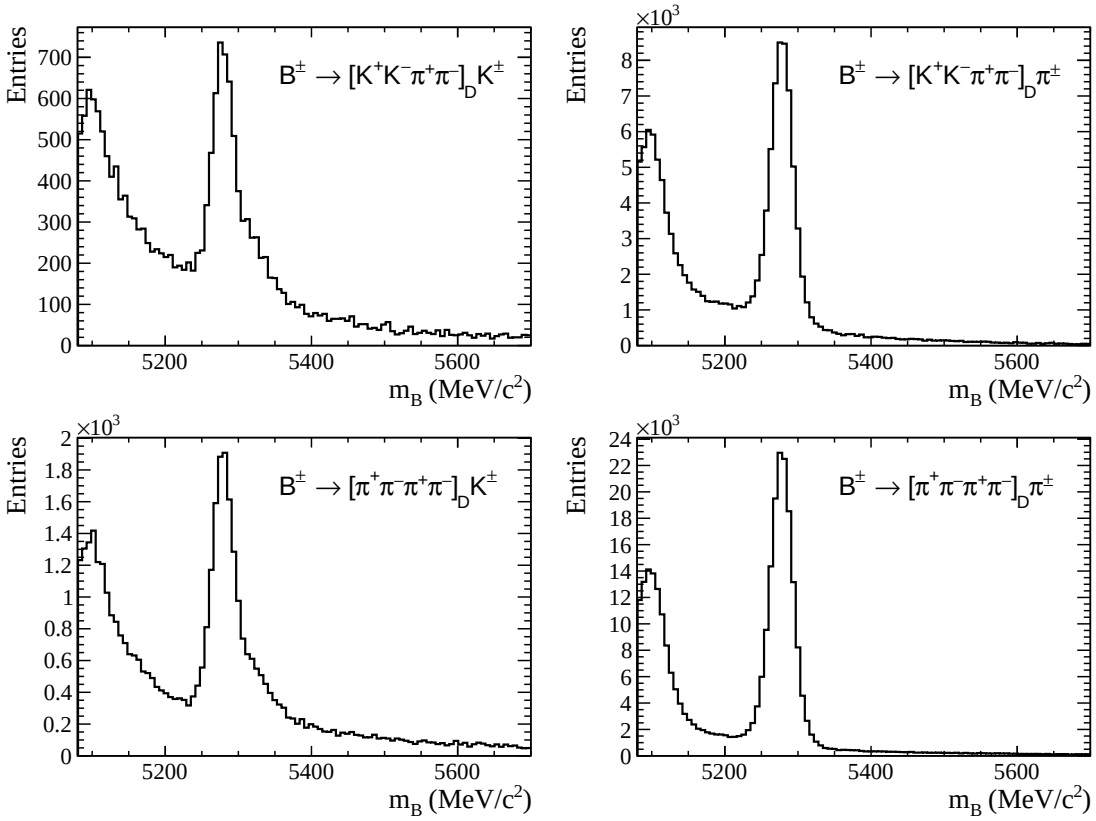

Figure 8.13: The $B^{\pm}$ invariant-mass distributions of the candidates in the final selection. The left (right) plot shows the $B^{\pm} \to DK^{\pm}$ ($D\pi^{\pm}$) selection and the top (bottom) plot shows the $D \to K^+K^-\pi^+\pi^-$ ($\pi^+\pi^-\pi^+\pi^-$) decay.

9

Model-independent measurement of γ

Contents

This chapter describes the complete analysis chain used to obtain γ from the sample of $B^{\pm} \to [h^+h^-\pi^+\pi^-]_D h'^{\pm}$ candidates. Important components in

the process include the modelling of signal and background decays, as well as phase-space binned and integrated *CP*-violation studies. The proper treatment of non-Gaussian uncertainties introduced by BESIII inputs is discussed, using the formalism discussed in Appendix A. The result of the binned analysis is one of the most precise measurements of γ to date. The combined result of phase-space binned and integrated measurements is finally presented, which will provide powerful constraints to the world average of γ.

9.1 Building an invariant-mass fit model

The determination of the CKM angle γ uses a series of unbinned maximum likelihood fits. The ultimate goal of these fits is to discriminate between signal and background contributions, and count the number of signal candidates. The discriminating variable is the $B^{\pm}$-invariant mass, which is reconstructed with the D-meson mass constrained to its PDG value [21].

To perform such a fit, a fit model is constructed where the shape and relative size of the different components are identified. The invariant-mass model described in this thesis builds on that used in Ref. [39]. The $D \to K^+K^-\pi^+\pi^-$ and $\pi^+\pi^-\pi^+\pi^-$ decay modes share the same invariant-mass shapes, with the exception of the background components that are studied in Section 9.1.4.

9.1.1 Signal shape

The main component of the invariant-mass fit is the shape of correctly reconstructed $B^{\pm} \to [K^+K^-\pi^+\pi^-]_D h^{\pm}$ and $B^{\pm} \to [\pi^+\pi^-\pi^+\pi^-]_D h^{\pm}$ decays. It is modelled as

$$\begin{aligned} f_{\text{signal}}(m|m_B,\sigma,\alpha_L,\alpha_R,\beta,k) =& k \times f_{\text{MG}}(m|m_B,\sigma,\alpha_L,\alpha_R,\beta) \\ &+(1-k)\times f_{\text{G}}(m|m_B,\sigma), \end{aligned} \tag{9.1}$$

where f_{G} is a Gaussian function and f_{MG} is a modified Gaussian function,

$$f_{\text{MG}}(m|m_B,\sigma,\alpha_L,\alpha_R,\beta) \propto \begin{cases} \exp\left(-\frac{\Delta m^2(1+\beta\Delta m^2)}{2\sigma^2+\alpha_L\Delta m^2}\right), & \Delta m = m - m_B < 0, \\ \exp\left(-\frac{\Delta m^2(1+\beta\Delta m^2)}{2\sigma^2+\alpha_R\Delta m^2}\right), & \Delta m = m - m_B > 0. \end{cases} \tag{9.2}$$

The function $f_{\rm MG}$ has approximately Gaussian behaviour when $\Delta m^2 \ll \sigma^2/\alpha_{L,R}$ or $\Delta m^2 \gg \beta^{-1}$, but it includes tails to better model the experimental resolution.

The parameters m_B and σ, which represent the mean position and the width of the signal shape, are free parameters determined in the fit to data. The mass m_B is common between the $B \to DK^{\pm}$ and $B \to D\pi^{\pm}$ channels, while the width σ is different for the two decays due to the lower energy release in the $B^{\pm} \to DK^{\pm}$ decay, which leads to a narrower width in this mode.

The tail parameters $\alpha_{L,R}$ and β, and the fraction k, are determined in a fit to a sample of simulated $B^{\pm} \to [K^+K^-\pi^+\pi^-]_D h^{\pm}$ events. The two $B^{\pm}$-decay channels are fitted simultaneously, with both sample sizes approximately three times larger than the number of $B^{\pm} \to D\pi^{\pm}$ candidates that are present in data. The simulated events undergo the same selection process as data, with the exception of the PID cut on the companion hadron. Instead, the effects of these cuts are applied by reweighting the simulated events, using the procedure described in Section 8.5. The fitted signal shape is plotted in blue in Fig. 9.1, and the black data points show the simulation samples. The vertical log scale emphasises the need for having a modified Gaussian function which can account for the longer tails.

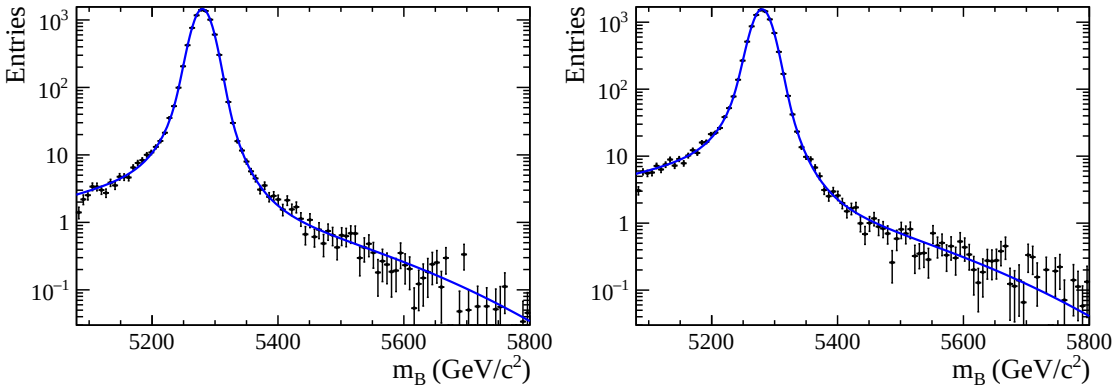

Figure 9.1: The PDF describing the invariant-mass distribution of (right) $B^{\pm} \to DK^{\pm}$ and (left) $B^{\pm} \to D\pi^{\pm}$ is shown in blue. The black data points are from the simulated sample used to fit the PDF.

9.1.2 Cross feed between $B^{\pm} \to DK^{\pm}$ and $B^{\pm} \to D\pi^{\pm}$

Near the peak of correctly reconstructed signal decays, there is a peaking structure due to the cross-feed contamination between the two $B^{\pm} \to Dh^{\pm}$ channels, but the peaks are displaced from the $B^{\pm}$ mass due to the particle misidentification. This background is most significant in the $B^{\pm} \to DK^{\pm}$ selection, since the $B^{\pm} \to D\pi^{\pm}$ decay has a much larger branching fraction. Nevertheless, it is accounted for in both decay modes, and its shape is determined using a data-driven approach.

In principle, the shape can be obtained by recalculating the invariant $B^{\pm}$-mass distribution, after swapping the mass hypothesis of the companion particle, and this will be referred to as the swapped $B^{\pm}$-mass distribution. However, there are two modifications that must be added in order to reproduce the correct misidentification shape.

First, in the data selection there are several other background components, which are well understood and described in Sections 9.1.3, 9.1.4 and 9.1.7. Assuming the misidentification of $B^{\pm} \to DK^{\pm}$ decays in the $B^{\pm} \to D\pi^{\pm}$ selection is negligible, a preliminary invariant-mass fit similar to that described in Section 9.2.1 is performed in order to use the sPlot method [130]. The resulting sWeights are applied to the swapped $B^{\pm}$-mass distribution.

Second, the different PID requirements on the companion particle in the selections of $B^{\pm} \to DK^{\pm}$ and $B^{\pm} \to D\pi^{\pm}$ decays are accounted for by using weights, as described in Section 8.5. Specifically, using the calibration samples, each event in the sWeighted $B^{\pm} \to D\pi^{\pm}$ data sample is assigned weights w according to the PIDK < 4 and PIDK > 4 requirements. To transform the PID requirement of the $B^{\pm} \to D\pi^{\pm}$ selection to that of the $B^{\pm} \to DK^{\pm}$ selection, the combined weight

$$w = \frac{w(\text{PIDK} > 4)}{w(\text{PIDK} < 4)}$$

is applied.

The resulting distribution is fitted with a sum of two Crystal Ball functions and it is shown in Fig. 9.2. The procedure is also cross checked by using a

simulated sample, instead of the sWeighted data sample, and the shapes are found to be consistent with each other.

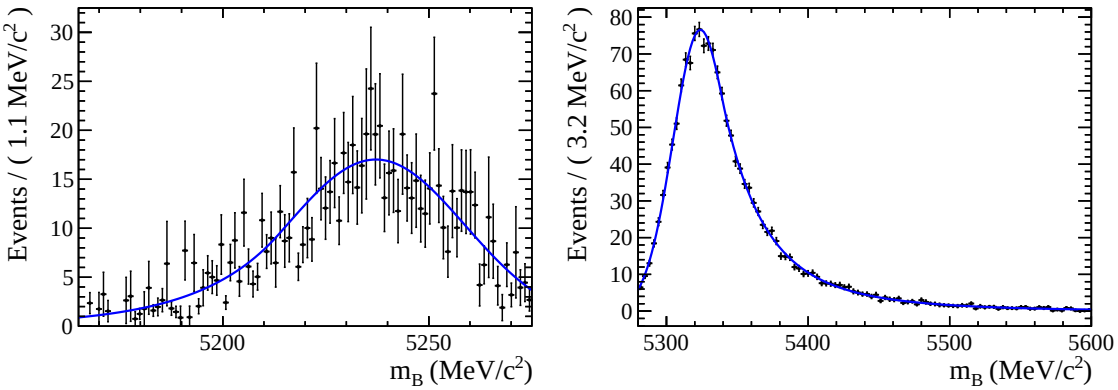

Figure 9.2: The PDF describing the misidentification shape of the (right) $B^\pm \to DK^\pm$ and (left) $B^\pm \to D\pi^\pm$ selections is shown in blue. The black data points show the swapped $B^\pm$ invariant-mass distributions after applying sWeights and PID weights.

Finally, the misidentification-background shape in the $B^\pm \to D\pi^\pm$ selection is obtained with an analogous procedure. To fit the swapped $B^\pm \to DK^\pm$-mass distribution, an additional component of misidentified $B^\pm \to D\pi^\pm$ decays is added, as this contribution cannot be neglected.

The shapes shown in Fig. 9.2 are fixed in all invariant-mass fits. The total yield of misidentified $B^\pm \to D\pi^\pm$ decays in the $B^\pm \to DK^\pm$ selection is fixed relative to the signal yield of the $B^\pm \to D\pi^\pm$ signal yield,

$$\frac{N(\text{Misidentification})}{N(\text{Signal})} = \frac{1-\epsilon_{\text{PID}}}{\epsilon_{\text{PID}}},$$

where ϵ_{PID} is the efficiency of the companion PID requirement, which is calculated in Section 8.5. The yield of misidentification background in the $B^\pm \to DK^\pm$ selection is also fixed, using a similar ratio of efficiencies.

9.1.3 Partially reconstructed B decays

In the selection of $B^\pm \to Dh^\pm$ decays, there is a low-mass background from decays of the type $B \to Dh^\pm X$, where X is either a pion or a photon that is either missed during reconstruction, or it is outside the angular acceptance of LHCb. These decays are therefore collectively referred to as partially reconstructed decays.

Kinematically, since these are decays from real B mesons, they leave a detector signature that is similar to that of $B^{\pm} \to Dh^{\pm}$ decays, but the reconstructed $B^{\pm}$-invariant mass is lower.

The majority of partially reconstructed decays are processes that involve an intermediate D^* vector meson with spin $J = 1$, which subsequently decays to DX. In the analysis described by Ref. [135], it was shown that the exact shape of the invariant-mass distribution can be derived analytically for such decays by considering the decay kinematics. In particular, the lower and upper end points of the invariant-mass distribution, a and b, can be calculated analytically using four-momentum conservation.

The invariant-mass shape in the range $m_B \in [a, b]$ is derived by considering the conservation of angular momentum. Since the combined $D^*h^{\pm}$ system has no net angular momentum, the D^* meson spin does not have a preferred direction. Thus, without loss of generality, one may consider a decay configuration where the D^*-meson spin component in the z-direction is zero.

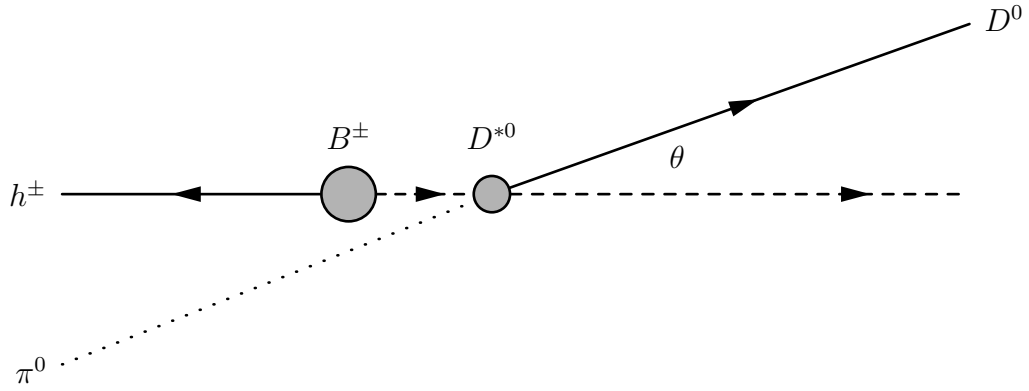

Figure 9.3: An illustration of the partially reconstructed $B^{\pm} \to D^{*0}h^{\pm}$ decay with $D^{*0} \to D^0\pi^0$. The helicity angle θ is defined as the angle between the D^{*0} and D^0 momentum directions in the D^{*0} rest frame. The arrows indicate the relative momentum directions, while the dashed lines show the direction of the D^{*0} momentum. The dotted line represents the missing π^0.

In the case where X is a spinless particle, the orbital angular momentum of the DX system must therefore be in a $(l, m) = (1, 0)$ state, which has an angular distribution given by the associated Legendre polynomial P_l^m with $l = 1$ and $m = 0$. This function takes the form $P_1^0 \propto \cos(\theta)$, where θ is defined as the angle between

the D^0 meson and the D^* meson in the D^* rest frame, as illustrated in Fig. 9.3. The Legendre polynomial P_1^0 has maxima at $\theta = 0$ and π, so when X is a spinless pion, the D meson prefers to either travel in a direction parallel or anti-parallel to the momentum direction of the D^* meson.

Qualitatively, when the D meson is emitted parallel to the D^* meson, corresponding to $\theta = 0$, it carries a larger fraction of the four-momentum, leading to a larger reconstructed $B^\pm$ invariant mass. Conversely, if it is emitted anti-parallel to the D^* meson, or $\theta = \pi$, the reconstructed $B^\pm$ invariant mass is lower. This one-to-one relationship between the helicity angle θ and the reconstructed $B^\pm$-invariant mass, which can be analytically calculated, is shown on the left in Fig. 9.4.

Using the decay $B^\pm \to D^{*0}h^\pm$ as an example, where $D^{*0} \to D\pi^0$, the missing π^0 results in a $|P_1^0|^2 = \cos^2(\theta)$ distribution for the helicity angle. Thus, a double-peak structure in the $B^\pm$ invariant mass is expected, and on the right in Fig. 9.4, in black, this distribution has been transformed into an invariant-mass distribution, using the relationship shown on the left.

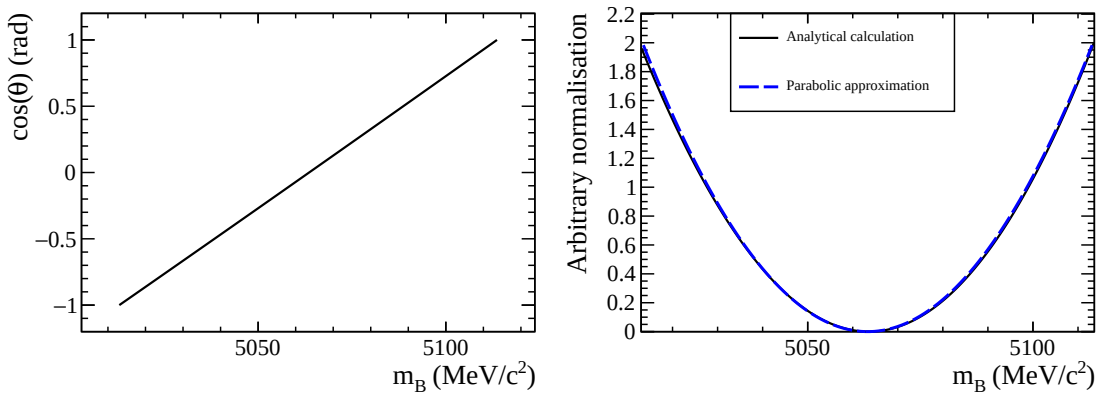

Figure 9.4: Left: Relationship between the reconstructed invariant mass m_B and the helicity angle θ. Right: Invariant $B^\pm$-mass distribution, assuming the helicity angle follows a $\cos^2(\theta)$ distribution.

The shape of the $B^\pm$ invariant-mass distribution can be, to leading order, be approximated as a parabolic function, with end points at $m_B = a$ and $m_B = b$. The analytical form of such a distribution is

$$p(m_B) = \begin{cases} \left(m_B - \frac{a+b}{2}\right)^2, & a < x < b \\ 0, & \text{otherwise,} \end{cases}$$

and it is shown as a dashed blue line in Fig. 9.4. There is a good agreement between this distribution and the analytical shape in black, which is a parabolic approximation. Therefore, in this analysis, partially reconstructed backgrounds are modelled using such a parabola.

To account for resolution effects, the parabolic shape is convolved with a double Gaussian function

$$p_{\mathrm{DG}}(x) = p_{\mathrm{G}}(x|\mu,\sigma) + f_{\mathrm{G}} p_{\mathrm{G}}(x|\mu, R_\sigma \sigma),$$

where σ is the width of the first Gaussian, f_{G} is the relative fraction between the two Gaussians and R_σ is their relative width.

Finally, differences in selection efficiencies can lead to one peak being higher than the other, and this possibility is accounted for with a linear polynomial with slope parameter ξ, such that ξ represents the height of the left peak, relative to the right peak. The resulting distribution, called the HORNSdini shape, is

$$p_{\mathrm{HORNSdini}}(m) = \int_a^b \mathrm{d}x \Big(x - \frac{a+b}{2}\Big)^2 p_{\mathrm{DG}}(m|x,\sigma,f_{\mathrm{G}},R_\sigma)\Big(\frac{1-\xi}{b-a}x + \frac{b\xi - a}{b-a}\Big).$$

An example of a fit of the HORNSdini shape to a simulation sample, which is taken from Ref. [39], is shown on the left in Fig. 9.5.

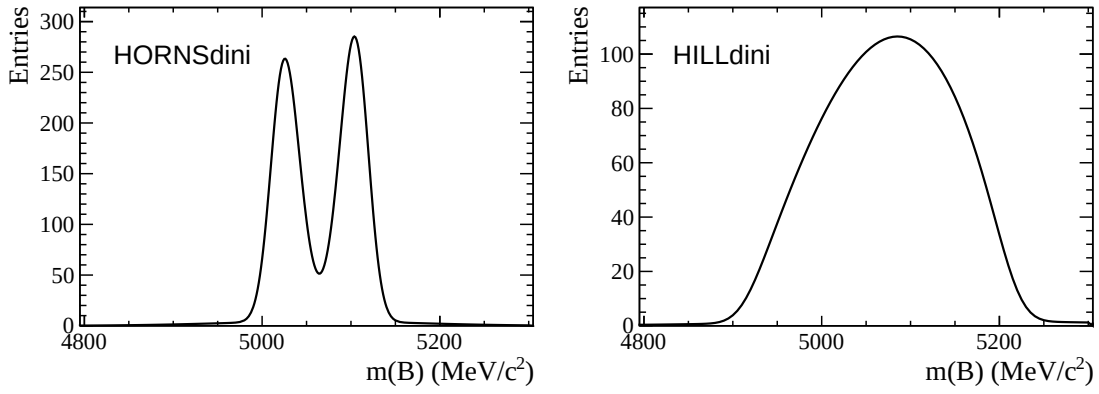

Figure 9.5: Examples of HORNSdini and HILLdini shapes taken from the analysis in Ref. [39]

It can be shown, with an analogous calculation, that if the missing particle is a photon, which is a massless spin $J = 1$ particle, the orbital angular momentum

must be in an $m = \pm 1$ state, such that the overall wavefunction has a $P_1^{\pm 1} \propto \sin(\theta)$ form. Therefore, qualitatively, for a decay such as $B^\pm \to D^{*0} h^\pm$, where $D^{*0} \to D\gamma$ and the photon γ is missed, the D meson prefers to travel perpendicular to the direction of the D^{*0} meson. This leads to a single-peak structure, shown on the right in Fig. 9.5, with the analytical expression

$$p(x) = \begin{cases} -(x-a)(x-b), & a < x < b \\ 0, & \text{otherwise.} \end{cases}$$

Resolution and selection efficiency effects are accounted for in an identical manner to the HORNSdini shape, resulting in a distribution named the HILLdini shape.

The process $B^\pm \to D h^\pm$, where the charm meson decays to a fully charged four-body final state, is kinematically very similar to the three-body decay $D \to K^0_S \pi^+ \pi^-$ with $K^0_S \to \pi^+ \pi^-$. In particular, since the missing particle in partially reconstructed decays is not a part of the D decay, the differences in partially reconstructed background shapes between different D decays are expected to be negligible. The $D \to K^0_S \pi^+ \pi^-$ decay was previously studied in detail [39], and in the current analysis, many of the parameters describing these background components are taken from Ref. [39]. A more detailed description of the treatment of these background contributions can also be found in Ref. [136].

The dominant component of the partially reconstructed backgrounds consists of real B mesons with a missing particle. In both the $B^\pm \to DK^\pm$ and $B^\pm \to D\pi^\pm$ channels, there are partially reconstructed backgrounds of the type $B \to D^* h^\pm$ and their PDFs are:

- $B^\pm \to D^{*0}(\to D[\pi^0])h^\pm$, described by HORNSdini;
- $\overline{(}B^0\overline{)} \to D^{*\mp}(\to D[\pi^\mp])h^\pm$, described by HORNSdini;
- $B^\pm \to D^{*0}(\to D[\gamma])h^\pm$, described by HILLdini.

For these three partially reconstructed backgrounds, the mass resolution σ^{low} is shared and varied in the fit to data, while all other shape parameters are taken from Ref. [39], and they were determined using simulation samples.

In the $B^\pm \to D\pi^\pm$ channel, there are also additional backgrounds from $B^\pm \to D\pi^\pm[\pi^0]$ and $\overline{(}B^0\overline{)} \to D\pi^\pm[\pi^\mp]$, which are described by samples of simulated $B^\pm \to D\rho^\pm$ and $\overline{(}B^0\overline{)} \to D\rho^0$ decays. The PDF shape used is HORNSdini and all shape parameters are fixed in the fit to data. Similarly, in the $B^\pm \to DK^\pm$ channel, the decays $B^\pm \to DK^\pm[\pi^0]$ and $\overline{(}B^0\overline{)} \to DK^\pm[\pi^\mp]$ contribute to the partially reconstructed background and are modelled with a HORNSdini PDF. The simulation samples use a Dalitz model [137] with smearing to account for resolution effects in the LHCb detector.

In addition to partially reconstructed background components where the companion hadron is correctly identified, in the $B^\pm \to DK^\pm$ selection there is also a contribution of partially reconstructed background from the $B^\pm \to D\pi^\pm$ mode where the companion pion is misidentified as a kaon. Such contributions can be studied using the same simulation samples as those used for partially reconstructed backgrounds with correctly reconstructed companion hadrons, but reconstructed under a kaon mass hypothesis for the companion hadron. The PID requirements are accounted for using the reweighting procedure described in Section 8.5. To model these components, empirical mass shapes known as Mis-ID HORNSdini and HILLdini PDFs, consisting of sums of HORNSdini and HILLdini PDFs, are fitted to the simulation samples.

Finally, in the $B^\pm \to DK^\pm$ channel, there is also a small contribution of $B^0_s \to D^0K^\pm[\pi^\mp]$ decays. Despite its small size, this component can have a relatively large impact in some phase-space bins since the flavour of the D meson is opposite to that of signal. Thus, in bins where F_i is small, this background has a yield proportional to F_{-i}, which can be large. Although the shape of this background is well known from Ref. [39], in this analysis the yield of this contribution, relative to that of the $B^\pm \to D\pi^\pm$ signal yield, has been updated with a data-driven estimate from Ref. [41]. After correcting for differences in selection and PID efficiencies, the ratio is found to be $(6.02 \pm 0.29) \times 10^{-3}$.

A complete summary of all partially reconstructed backgrounds is presented in Table 9.1. In the $B^\pm \to D\pi^\pm$ modes, the total yield of partially reconstructed

Table 9.1: List of all partially reconstructed backgrounds and their PDFs.

Number	Background	PDF
1	$B^{\pm} \to D^{*0}(\to D[\pi^0])\pi^{\pm}$	HORNSdini
2	$\overline{(B^0)} \to D^{*\mp}(\to D[\pi^{\mp}])\pi^{\pm}$	HORNSdini
3	$B^{\pm} \to D^{*0}(\to D[\gamma])\pi^{\pm}$	HILLdini
4	$B \to D\pi^{\pm}[\pi]$	HORNSdini
5	$B^{\pm} \to D^{*0}(\to D[\pi^0])K^{\pm}$	HORNSdini
6	$\overline{(B^0)} \to D^{*\mp}(\to D[\pi^{\mp}])K^{\pm}$	HORNSdini
7	$B^{\pm} \to D^{*0}(\to D[\gamma])K^{\pm}$	HILLdini
8	$B \to DK^{\pm}[\pi]$	HORNSdini
9	$B^0_s \to D^0K^{\pm}[\pi^{\mp}]$	HORNSdini
10	Cross feed from $B \to Dh^{\pm}[X]$	Mis-ID HORNSdini/HILLdini

backgrounds is a free parameter. The yield of component 2 is fixed relative to component 1 from branching ratios and selection efficiencies. The relative yield of component 3 relative to components 1 and 2 is denoted as $f^{D\pi}_{D^*\gamma}$, and it is varied in the fit. Similarly, the yield of component 4, relative to that of components 1, 2 and 3, is denoted as $f^{D\pi}_{D\pi\pi}$ and it is a also a free parameter in the fit.

In the $B^{\pm} \to DK^{\pm}$ channel, the total yield of partially reconstructed background, with the exception of B^0_s, is defined as

$$N_{DK,\text{low}} = R^{\text{low}}_{DK/D\pi} \times N_{D\pi,\text{low}} \times \frac{\epsilon_{K\to K}}{\epsilon_{\pi\to\pi}},$$

where $R^{\text{low}}_{DK/D\pi}$ is shared between all categories and floated. The PID efficiencies are assumed to be identical between signal and partially reconstructed background. The relative yields of components 5-10 are all fixed from selection and PID efficiencies.

9.1.4 Modelling of peaking backgrounds

There are two background components, specific to four-body D decays, which have non-trivial peaking structures directly under the signal peak. The first contribution, which only affects the $D \to K^+K^-\pi^+\pi^-$ channel, originates from CF $D^0 \to K^-\pi^+\pi^-\pi^+\pi^0$ decays that fake a $D \to K^+K^-\pi^+\pi^-$ signal when the π^0 meson is missed during the reconstruction and one of the charged pions is misidentified as

a kaon. Although events with missing particles or misidentified hadrons in the D decay are generally rejected by the D^0 invariant-mass range, in this particular charm decay the missing particle and the misidentified pion push the reconstructed D^0 invariant mass in different directions. The resulting invariant-mass distribution has a significant contribution inside the selected D^0 mass range, and must therefore be accounted for in the $B^\pm$ invariant-mass fit.

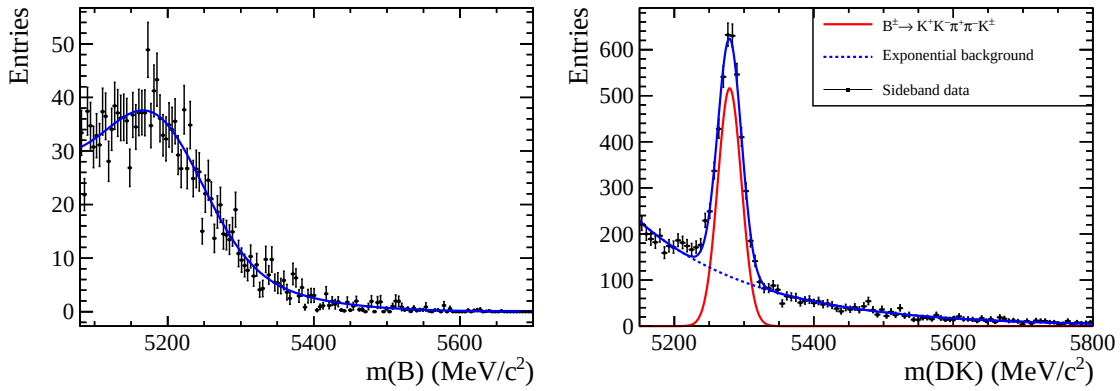

Figure 9.6: Fit of the invariant-mass shape of the $D \to K^-\pi^+\pi^-\pi^+\pi^0$ background on the left and the charmless background on the right in the $D \to K^+K^-\pi^+\pi^-$ channel.

This background is studied using LHCb simulation samples that undergo the same selection as that of data. The simulated decays are generated with a uniform phase-space distribution, since no amplitude analysis of this decay has been published. The PID cuts are accounted for through reweighting, analogous to that described in Section 9.1.2. Finally, the $B^\pm$ invariant-mass distribution is fitted with a sum of two Crystal Ball functions and the result is shown on the left in Fig. 9.6. As these candidates originate from real $B^\pm$ decays, they are found to have a peaking structure in the low-mass region, with a long tail inside the region under correctly reconstructed signal decays.

To ensure that the fit results are not biased due to having a uniform phase-space distribution, the same decay is generated in RapidSim [134], first using a uniform phase-space distribution and then with an intermediate $D \to K^{*0}\omega$ decay, where $K^{*0} \to K^-\pi^+$ and $\omega \to \pi^+\pi^-\pi^0$. The reconstructed $B^\pm$ invariant-mass distribution is found to be consistent between both samples, and therefore it is

assumed that the choice of phase-space model of the charm decay has a negligible effect on the invariant-mass shape. In the invariant-mass fit to data, the shape of this background is fixed, while the ratio between the yield of this background and that of the $B \to D^* h^\pm$ components, labelled $R_{K3\pi\pi^0}$, is a free parameter that is shared between the $B^\pm \to DK^\pm$ and $D\pi^\pm$ channels.

The second peaking background considered in these four-body decays arises from charmless decays, which are $B^\pm$ decays with the same final-state particles as that of signal, but without an intermediate D meson. Such decays therefore do not have a peak in the D invariant-mass distribution, and thus can be studied using the sideband region of this distribution. However, in the $D \to K^+K^-\pi^+\pi^-$ decay, the upper sideband is contaminated with CF $D^0 \to K^-\pi^+\pi^-\pi^+$ decays, and therefore the lower sideband region $m_B \in [1770, 1820]\,\text{MeV}/c^2$ is used for these studies. In the $D \to \pi^+\pi^-\pi^+\pi^-$ mode, this contamination is located in the lower sideband, and therefore the upper sideband region $m_B \in [1910, 1960]\,\text{MeV}/c^2$ is used. As mentioned in Section 8.6, a requirement on the D-meson flight significance suppresses this background.

Table 9.2: Yield of charmless background in the lower D mass sideband for all $B^\pm$ candidates, and also B^+ and B^- separately, in the $D \to K^+K^-\pi^+\pi^-$ mode. Both yields with and without a flight significance cut are shown.

B charge	No requirement	$\Delta z^{D-B}_{\text{significance}} > 2$	$\Delta z^{D-B}_{\text{significance}} > 4$
$B^\pm$	3387 ± 76	168 ± 26	3 ± 22
B^-	1682 ± 50	69 ± 18	3 ± 13
B^+	1705 ± 50	99 ± 19	0 ± 14

An effect of constraining the D invariant mass, as mentioned in Section 8.3, is that the χ^2 distribution of this Kalman-kinematic fit is highly correlated with the D invariant-mass distribution. This χ^2 variable is used in the BDT described in Section 8.4.2, and therefore the BDT has the effect of removing charmless decays in the sideband regions but not necessarily in the signal region. In order to obtain an unbiased estimate of charmless backgrounds, an alternative BDT is trained without the use of this variable. The overlap between the selections with these

BDTs, defined as $N_{\text{intersection}}/N_{\text{union}}$, is found to be 93.1%. Additionally, it is found that the level of combinatorial background is higher with the alternative BDT, so it may be concluded that both BDTs select the same signal candidates, while the nominal BDT is more efficient at rejecting combinatorial background. However, the alternative BDT, which does not rely on knowledge of the Kalman χ^2, does not remove charmless background decays from the sideband regions.

Table 9.3: Yield of charmless background in the lower D mass sideband for all $B^{\pm}$ candidates, and also B^+ and B^- separately, in the $D \to \pi^+\pi^-\pi^+\pi^-$ mode. Both yields with and without a flight significance cut are shown.

B charge	No requirement	$\Delta z^{D-B}_{\text{significance}} > 2$	$\Delta z^{D-B}_{\text{significance}} > 4$
$B^{\pm}$	11690 ± 145	689 ± 48	31 ± 32
B^-	5799 ± 94	344 ± 34	15 ± 23
B^+	5891 ± 95	345 ± 34	16 ± 23

On the right, Fig. 9.6 shows the $B^{\pm}$ invariant-mass distribution in the D sideband region of $D \to K^+K^-\pi^+\pi^-$, prior to the flight-significance requirement. The blue line is the result of a fit of this distribution, using an exponential distribution to describe the combinatorial background and a Gaussian function to describe the signal. The fitted Gaussian function is also shown in red. Table 9.2 shows the yield of charmless background of all $B^{\pm}$ candidates in the sideband region of $D \to K^+K^-\pi^+\pi^-$. Results of fits split by charge are also shown, and no *CP* asymmetry is found. Similarly, Table 9.3 shows the equivalent numbers for the $D \to \pi^+\pi^-\pi^+\pi^-$ mode.

It should be noted that the yield of charmless decays is similar to that of signal, but a flight significance requirement is highly efficient at rejecting this background. In Fig. 9.7, the results of fits with a flight significance of two and four are shown for the $D \to K^+K^-\pi^+\pi^-$ selection. The yields are shown in Tables 9.2-9.3. For the phase-space binned analysis the chosen requirement is $\Delta z^{D-B}_{\text{significance}} > 2$, while in the phase-space integrated analysis, which is more sensitive to backgrounds that affect the signal yield, the requirement is tightened to $\Delta z^{D-B}_{\text{significance}} > 4$, which reduces the charmless background yield to a very small level.

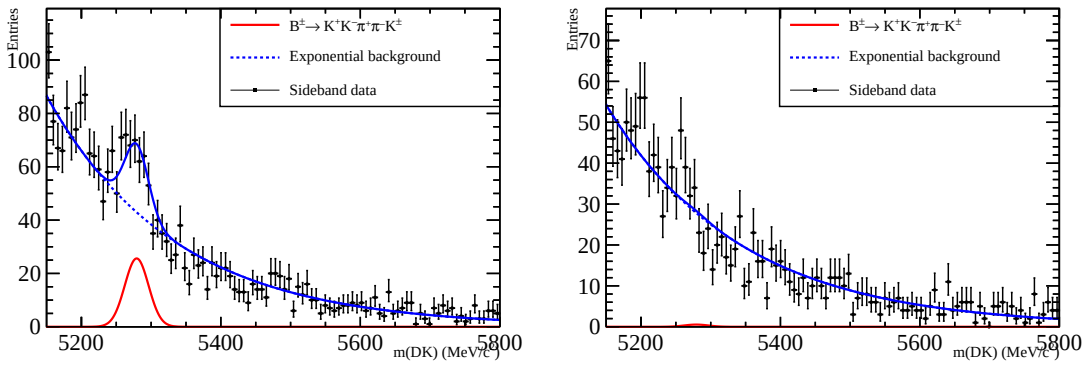

Figure 9.7: Fit of charmless-background yields in the data sideband, with a flight significance requirement at two on the left and a tighter requirement at four on the right.

In the fit to data, the shape of this background is fixed to that obtained from the fit without a flight significance requirement. In the binned fit of *CP*-violating observables, the fraction of charmless background in each bin is determined from fits similar to that shown on the left in Fig. 9.6, but split into phase-space bins, and it is assumed that these fractions are independent of any flight significance requirement.

The presence of charmless backgrounds in the $B^{\pm} \to D\pi^{\pm}$ selection is also investigated with an analogous procedure, but no evidence of such contributions is found.

9.1.5 Study of misidentified $D^0 \to K^-\pi^+\pi^-\pi^+$ decays

A potential source of background decays with a peaking structure in the signal region is the CF decay $D^0 \to K^-\pi^+\pi^-\pi^+$, which can be miscategorised as either $D \to K^+K^-\pi^+\pi^-$ or $D \to \pi^+\pi^-\pi^+\pi^-$ through a single misidentification. An LHCb simulation of $B^{\pm} \to [K^-\pi^+\pi^-\pi^+]_D h^{\pm}$ is used to study the impact of this background on the measurement. The sample undergoes the same selection as that of data, except for PID selections, which are accounted for through reweighting.

In particular, for a single misidentification of $K\pi\pi\pi \to KK\pi\pi$, where one of the pions is assigned a kaon hypothesis, has the effect of pushing the reconstructed D invariant-mass distribution into the sideband region above the mass window. This is illustrated on the left of Fig. 9.8, and it is found that a negligible number of candidates remain in the signal region, which is indicated by the blue lines. The effect in the $D \to \pi^+\pi^-\pi^+\pi^-$ mode is similar.

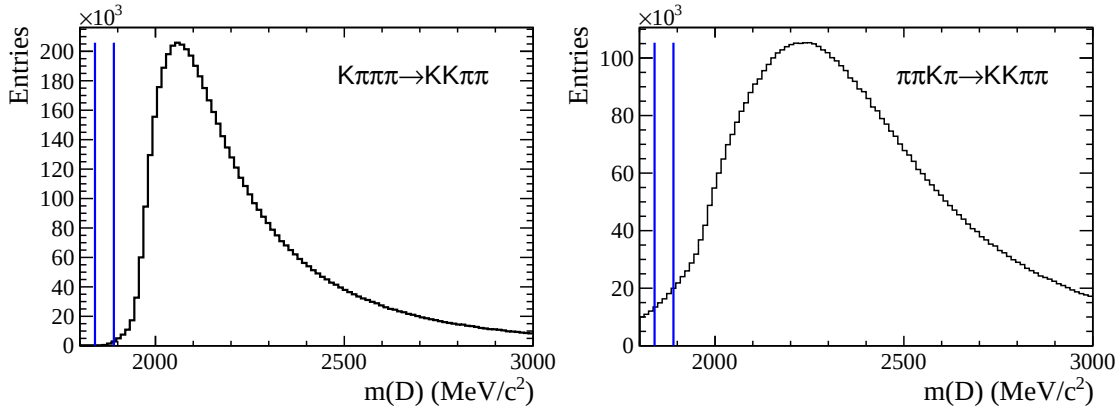

Figure 9.8: The D-mass distribution of $B^{\pm} \to [K^-\pi^+\pi^-\pi^+]_D\pi^{\pm}$ decays, misidentified as $B^{\pm} \to [K^+K^-\pi^+\pi^-]_D\pi^{\pm}$ decays. On the left is the single misidentification, on the right is the triple misidentification.

However, in the $D \to K^+K^-\pi^+\pi^-$ mode, there is also a second mechanism in which this CF decay can contaminate inside the signal region. This is shown on the right in Fig. 9.8, where a triple misidentification occurs, $\pi\pi K\pi \to KK\pi\pi$. Although three consecutive misidentifications is unlikely, the contribution from this mode, which has a large branching fraction, has a non-negligible number of background events inside the signal region.

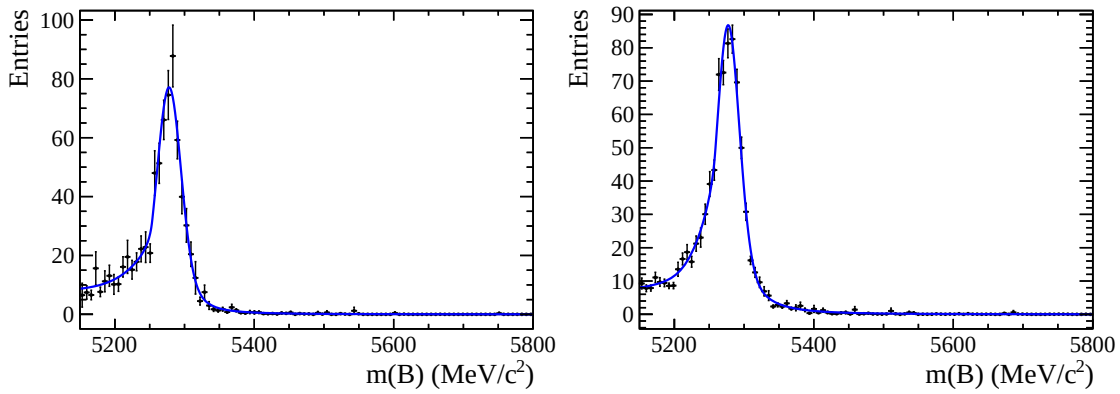

Figure 9.9: The $B^{\pm}$-mass distribution of $B^{\pm} \to [K^-\pi^+\pi^-\pi^+]_D h^{\pm}$ decays, triple misidentified as $B^{\pm} \to [K^+K^-\pi^+\pi^-]_D h^{\pm}$ decays. On the left is the $B^{\pm} \to DK^{\pm}$ mode, on the right is the $B^{\pm} \to D\pi^{\pm}$ mode.

The triple misidentification background is also important due to its invariant-mass shape, which is shown in Fig. 9.9 for both $B^{\pm} \to DK^{\pm}$ on the left and $B^{\pm} \to D\pi^{\pm}$ on the right. Since the shape has a sharp peaking structure near

the $B^{\pm}$ mass, these decays can easily fake a signal candidate, and the size of this background must therefore be understood.

After correcting for differences in branching fractions, selection efficiencies and PID efficiencies, it is found that this background is $(0.868 \pm 0.030)\%$ and $(0.89 \pm 0.03)\%$ of the signal yield, for $B^{\pm} \to D\pi^{\pm}$ and $B^{\pm} \to DK^{\pm}$ respectively. This is considered to be too small to model in the invariant-mass fit, but it is considered as a systematic uncertainty in Section 9.2.5.

9.1.6 Study of misidentified $D^0 \to K^{*-}\ell^+\nu_\ell$ decays

A different source of potential CF background decays is semi-leptonic decays of the form $D^0 \to K^{*-}\ell^+\nu_\ell$, where $K^{*-} \to K^-\pi^+\pi^-$ is some excited kaon state. The states considered in this analysis are the $K_1(1270)$, $K_1(1400)$, $K^*(1410)$, $K^*(1680)$, $K^*{}_2(1430)$ and $K^*(892)$ resonances. The lepton ℓ can either be a muon μ or an electron e.

The study of this background is first performed with the $D \to K^+K^-\pi^+\pi^-$ channel, where semi-leptonic decays can contribute in two ways. First, the lepton can be misidentified as a kaon, $K\ell\pi\pi \to KK\pi\pi$, or there can be a double misidentification $K\pi\pi\ell \to KK\pi\pi$. To determine the invariant-mass shape of this background and its size relative to the signal yield, large simulation samples are generated with RapidSim [134].

A simulation sample with the intermediate resonance $K_1(1270)$ is shown in Fig. 9.10. On the left is the D invariant-mass distribution after a single misidentification, and the blue lines indicate the signal region. On the left the $B^{\pm}$ invariant-mass distribution is shown for the candidates that pass the D invariant-mass requirement. The shape is found to contribute mostly in the low-mass region, but it also has a large tail present in the signal region.

To obtain a total background yield, relative to that of signal, a full study that accounts for differences in branching fractions, selection efficiencies and PID efficiencies is performed. Both the muon and electron modes are considered, and the contributions from single and double misidentifications are added together. Each

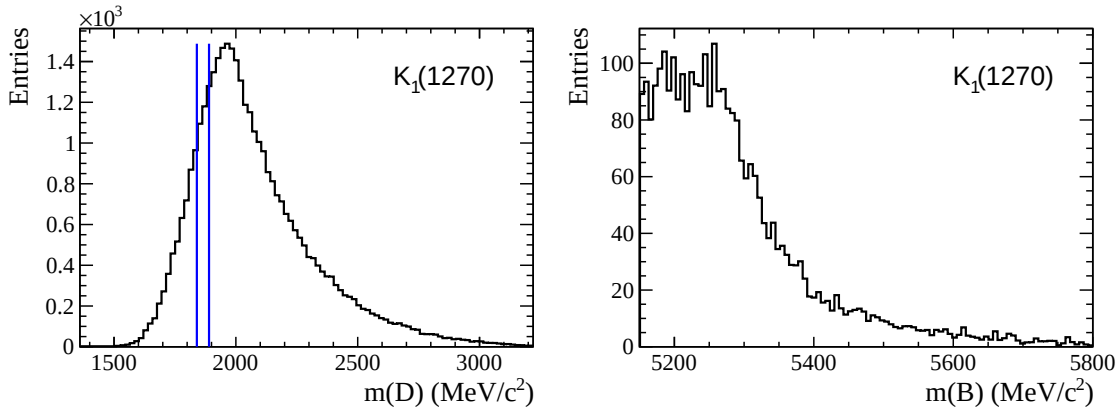

Figure 9.10: An example of a semi-leptonic D decay background, where $D^0 \to K_1(1270)^- \mu^+ \nu_\mu$. On the left is the invariant-mass distribution of the reconstructed D meson, with the selected candidates indicated by the vertical blue lines. On the right is the corresponding invariant $B^\pm$-mass distribution of the selected candidates.

kaon resonance is considered separately and their contributions are also added together. The resulting $B^\pm$ invariant-mass distribution is shown in Fig. 9.11 for $B^\pm \to DK^\pm$ on the left and $B^\pm \to D\pi^\pm$ on the right. The data points show the RapidSim simulation samples and the blue line is a sum of two Crystal Ball functions fitted to the simulation samples.

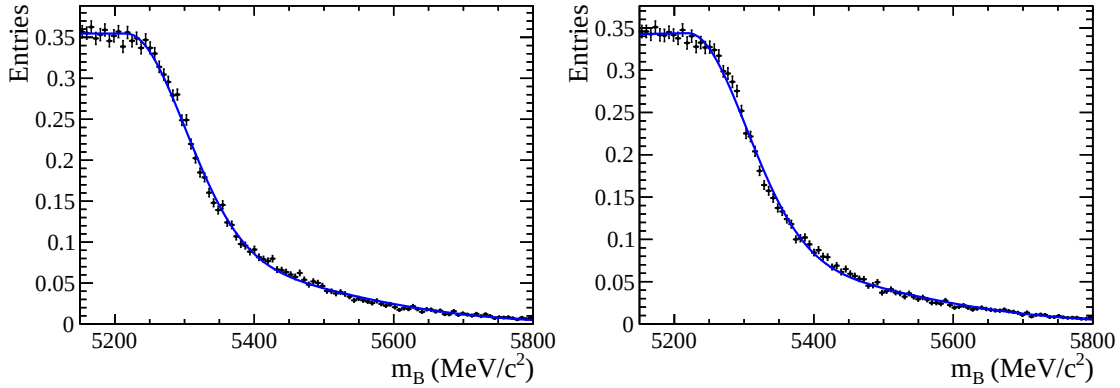

Figure 9.11: Fit of all semi-leptonic D-decay modes that contribute to the semileptonic D background contributions. On the left is the fit in the $B^\pm \to DK^\pm$ channel and on the right is the $B^\pm \to D\pi^\pm$ channel.

Both the shape and background yields relative to signal are found to be consistent between the two $B^\pm$ decays, and the final ratio between background and signal is found to be 0.8%. This small background level is considered to be negligible in the fit to data. In Section 9.2.5, it is considered a systematic uncertainty in the

$D \to K^+K^-\pi^+\pi^-$ channel. The $D \to \pi^+\pi^-\pi^+\pi^-$ decay has a branching fraction that is three times larger than that of $D \to K^+K^-\pi^+\pi^-$, and the semi-leptonic background can only contribute through double misidentification. Therefore, the relative size of this semi-leptonic background is almost an order of magnitude smaller in $D \to \pi^+\pi^-\pi^+\pi^-$, compared to $K^+K^-\pi^+\pi^-$. Thus, it is not considered as a systematic uncertainty in this channel.

9.1.7 Combinatorial background

The combinatorial background, which has no peaking structures in the $B^\pm$ invariant-mass spectrum, is modelled with an exponential function. The parameter describing the shape of this function is allowed to vary in the invariant-mass fits. In fits split by bins, the exponential shape is assumed to be the same in all phase-space bins, but the yield in each bin is varied independently.

9.2 Invariant-mass fits

9.2.1 Global invariant-mass fit

In the first stage of the analysis, an unbinned maximum likelihood fit is performed on the invariant-mass distribution of reconstructed $B^\pm$ mesons. The fit is, at this stage, performed integrated over all phase space and summed over both $B^\pm$ charges, and therefore it will be referred to as a global fit.

The two $B^\pm$ decays and two D decays, which make a total of four categories, are kept separate due to the different purities and background contributions, but the fit is performed simultaneously with several shared parameters. The purpose of such a fit, which is insensitive to any *CP*-violation effects, is to determine parameters that describe the PDF of the invariant-mass distribution, including contributions from both signal and background decays.

The fit is performed over the range $m_B \in [5080, 5700]\,\mathrm{MeV}/c^2$. The left limit is chosen such that a sufficient amount of the partially reconstructed background can be separated from the signal peak, while the upper limit ensures that the combinatorial background is correctly constrained.

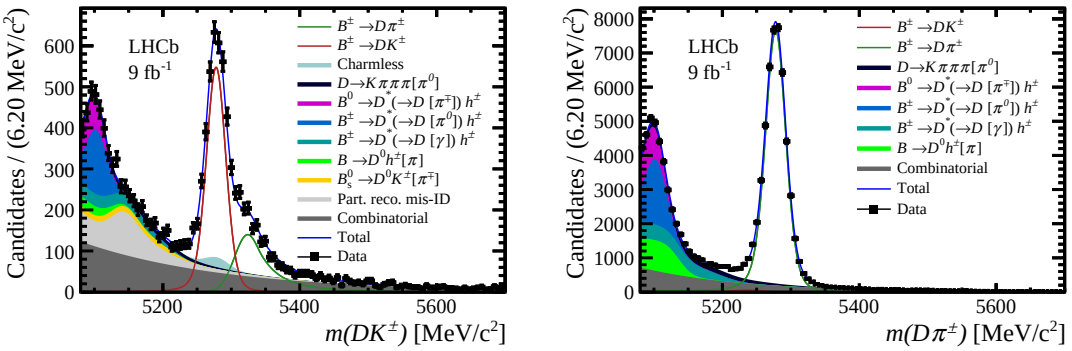

Figure 9.12: Invariant-mass distributions for the (left) $B^{\pm} \to DK^{\pm}$ and (right) $B^{\pm} \to D\pi^{\pm}$ selections, for the $D \to K^+K^-\pi^+\pi^-$ decay. The square brackets in the legend denote particles that are not reconstructed.

The projections of the global fit are shown in Fig. 9.12 and 9.13 for the $D \to K^+K^-\pi^+\pi^-$ and $\pi^+\pi^-\pi^+\pi^-$ modes, respectively. The fit model describes the data well, and there is good discrimination between signal and background.

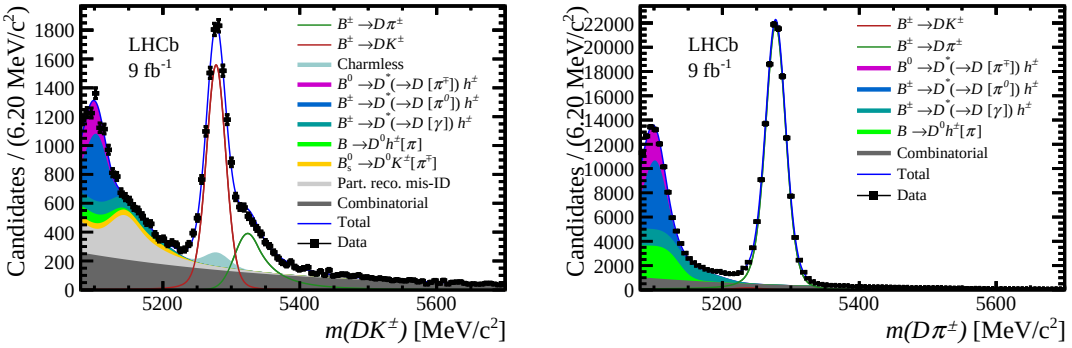

Figure 9.13: Invariant-mass distributions for the (left) $B^{\pm} \to DK^{\pm}$ and (right) $B^{\pm} \to D\pi^{\pm}$ selections, for the $D \to \pi^+\pi^-\pi^+\pi^-$ decay. The square brackets in the legend denote particles that are not reconstructed.

The numerical results of the free parameters that determine the invariant-mass shapes are shown in Table 9.4. The parameters μ and σ describe the mean and width of the signal shape, and the signal shape in $B^{\pm} \to D\pi^{\pm}$ is found to be wider than that of $B^{\pm} \to DK^{\pm}$ due to the larger energy released in the decay. The parameter $R_{DK/D\pi}$ is the ratio between the $B^{\pm} \to DK^{\pm}$ and $B^{\pm} \to D\pi^{\pm}$ yields, and it is consistent with the flavour-specific branching fractions of $B^- \to D^0K^-$ and $B^- \to D^0\pi^-$ from the PDG [21]. The ratio $R^{\text{low}}_{DK/D\pi}$ is defined analogously for

Table 9.4: Parameters describing the invariant-mass shape, determined by the global invariant-mass fit.

Signal shape parameters	
$\sigma_{D\pi}$ (MeV/c^2)	14.45 ± 0.04
σ_{DK} (MeV/c^2)	13.89 ± 0.17
μ (MeV/c^2)	5277.80 ± 0.04
$R_{DK/D\pi}$ (10^{-2})	7.76 ± 0.09
Combinatorial slopes	
Decay mode	Slope ($10^{-3}\,\mathrm{GeV}^{-1}c^2$)
$B^\pm \to [K^+K^-\pi^+\pi^-]_D\pi^\pm)$	-6.78 ± 0.26
$B^\pm \to [\pi^+\pi^-\pi^+\pi^-]_D\pi^\pm)$	-4.45 ± 0.09
$B^\pm \to [K^+K^-\pi^+\pi^-]_DK^\pm)$	-4.79 ± 0.19
$B^\pm \to [\pi^+\pi^-\pi^+\pi^-]_DK^\pm)$	-3.16 ± 0.09
Partially reconstructed background parameters	
$\sigma^{\mathrm{low}}_{D\pi}$ (MeV/c^2)	13.56 ± 0.30
$f^{D\pi}_{D\pi\pi}$	0.258 ± 0.015
$f^{D\pi}_{D^*\gamma}$	0.309 ± 0.007
$R_{K3\pi\pi^0}$	0.18 ± 0.04
$R^{\mathrm{low}}_{DK/D\pi}$ (10^{-2})	6.95 ± 0.16

the partially reconstructed background, but it is not necessarily equal to $R_{DK/D\pi}$ due to the different partially reconstructed decay components in the two selections.

In addition to the parameters listed in Table 9.4, the total yield of signal and partially reconstructed background are also free parameters in the $B^\pm \to D\pi^\pm$ categories, and the same parameters in the $B^\pm \to DK^\pm$ categories are related through the $R_{DK/D\pi}$ and $R^{\mathrm{low}}_{DK/D\pi}$ ratios, respectively. The combinatorial background is allowed to vary freely in each category. The total yield of signal candidates, as well as the total yield of each class of background contributions, are listed in Table 9.5.

9.2.2 Invariant-mass fit split by charge

In the second stage of the analysis, the phase-space integrated *CP*-violating observables are determined. The fit uses an identical setup to the global fit described in Section 9.2.1, but the candidates are separated by their $B^\pm$ charge, which makes a total of eight categories.

Table 9.5: Yields of signal, companion misidentification background, partially reconstructed background, background from $D \to K^-\pi^+\pi^-\pi^+\pi^0$ decays and combinatorial background, obtained from the global invariant-mass fit.

D decay	Component	Reconstructed as: $B^\pm \to DK^\pm$	Reconstructed as: $B^\pm \to D\pi^\pm$
$D \to K^+K^-\pi^+\pi^-$	$B^\pm \to DK^\pm$	3037 ± 38	143 ± 2
	$B^\pm \to D\pi^\pm$	239 ± 1	44186 ± 216
	Partially reconstructed bkg	87 ± 1	27 ± 1
	$D \to K^-\pi^+\pi^-\pi^+\pi^0$	43 ± 10	572 ± 132
	Combinatorial bkg	451 ± 20	1782 ± 153
	Charmless bkg	155	N/A
$D \to \pi^+\pi^-\pi^+\pi^-$	$B^\pm \to DK^\pm$	8452 ± 101	377 ± 4
	$B^\pm \to D\pi^\pm$	654 ± 2	122161 ± 368
	Partially reconstructed bkg	248 ± 1	78 ± 3
	Combinatorial bkg	897 ± 24	2211 ± 68
	Charmless bkg	629	N/A

Instead of having the yield of each category as free parameters, the yields are parameterised in terms of the *CP*-violating observables, $\mathcal{A}_h$ and $\mathcal{R}_{CP}$, defined by Eqs. (2.18) and (2.19). This makes a total of six parameters, while the remaining two parameters are the total yields of $B^\pm \to D\pi^\pm$ decays, where $D \to K^+K^-\pi^+\pi^-$ and $\pi^+\pi^-\pi^+\pi^-$.

In order to interpret the measured charge asymmetries in terms of a *CP* asymmetry, they must be corrected for the asymmetry in the production of B^+ and B^- mesons A_{B^+}, as well as the $K^\pm$ and $\pi^\pm$ detection asymmetries. By definition, charge asymmetries are defined as

$$A = \frac{N_- - N_+}{N_- + N_+},$$

where $N_\pm$ are the yields split by charge. To apply the asymmetry corrections to the measured yields, it is more convenient to express the asymmetries as a ratio

$$a \equiv \frac{1 + A}{1 - A},$$

such that the yield of positive and negative charges are related by $N_- = aN_+$. The advantage of this parameterisation is that each individual source of asymmetry can

be factorised into $a = a_{CP} a_{\rm det} a_{B^+}$, where a_{CP} is the CP asymmetry of interest, $a_{\rm det}$ is the detector asymmetry and a_{B^+} is the $B^\pm$ production asymmetry.

The asymmetry corrections are

$$A_{B^+} = (2.8 \pm 6.8) \times 10^{-4},$$
$$A_\pi = (-6.4 \pm 1.8) \times 10^{-4},$$
$$A_{K\pi} = (-9.6 \pm 1.3) \times 10^{-3},$$
$$A_{\rm L0} = (-1.7 \pm 0.8) \times 10^{-3},$$

which are taken from the analysis described in Ref. [41]. The pion detection asymmetry A_π is applied to each pion in the final state. The asymmetry $A_{K\pi}$ is the combined detection asymmetry of a $K^-\pi^+$ pair, and it is combined with A_π to obtain the detection asymmetry for each kaon. The parameter $A_{\rm L0}$ is an asymmetry in the L0 hardware trigger, and in the subsequent analysis it is combined with $A_{K\pi}$.

Table 9.6: Results of the phase-space integrated measurements. The first uncertainty is statistical and the second systematic.

CP-violating observable	Fit results
$A_K^{KK\pi\pi}$	$0.095 \pm 0.023 \pm 0.002$
$A_\pi^{KK\pi\pi}$	$-0.009 \pm 0.006 \pm 0.001$
$A_K^{\pi\pi\pi\pi}$	$0.061 \pm 0.013 \pm 0.002$
$A_\pi^{\pi\pi\pi\pi}$	$-0.0082 \pm 0.0031 \pm 0.0007$
$R_{CP}^{KK\pi\pi}$	$0.974 \pm 0.024 \pm 0.015$
$R_{CP}^{\pi\pi\pi\pi}$	$0.978 \pm 0.014 \pm 0.010$

The projections from the phase-space integrated fit are shown in Fig. 9.14 and 9.15. In the $B^\pm \to DK^\pm$ mode, shown on the top, a surplus of B^- decays is visible for both D-decay modes, while the $B^\pm \to D\pi^\pm$ mode at the bottom shows a much smaller asymmetry, but with more B^+ decays.

The final phase-space integrated CP-violating observables are listed in Table 9.6, where the first uncertainty is statistical. The second uncertainty is systematic in origin and will be discussed in Section 9.2.5. Non-zero values of A_K are seen, which is consistent with Figs. 9.14 and 9.15. Furthermore, both values of R_{CP} are smaller than unity. This indicates that relative to the $B^\pm \to D\pi^\pm$ decay, the

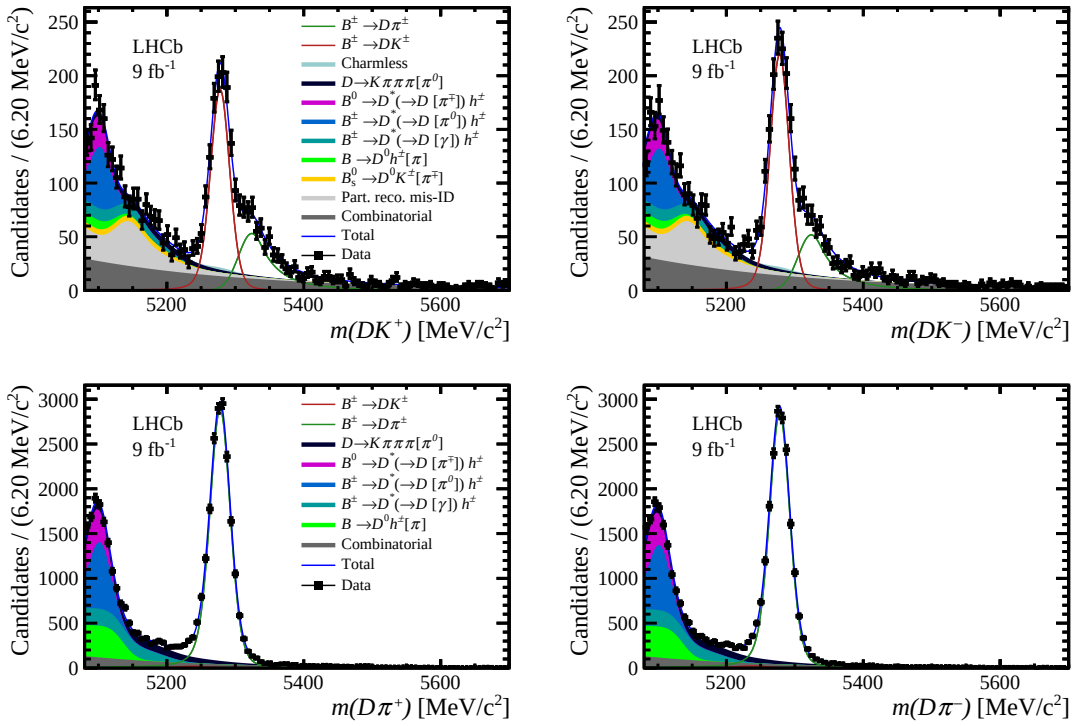

Figure 9.14: Invariant-mass distributions and fit projections of (top) $B^{\pm} \to [K^+K^-\pi^+\pi^-]_D K^{\pm}$ and (bottom) $B^{\pm} \to [K^+K^-\pi^+\pi^-]_D \pi^{\pm}$ candidates, for (left) B^+ and (right) B^- decays.

$B^{\pm} \to DK^{\pm}$ mode is more suppressed than the equivalent process where the charm decay is flavour specific, due to interference effects.

9.2.3 Strategy for determination of phase-space binned *CP*-violating observables

The binned *CP*-violating observables are determined with an unbinned maximum likelihood fit, similar to that described in Sections 9.2.1 and 9.2.2, where the $B^{\pm}$ candidates are also sorted into phase-space bins. This fit is conventionally referred to as a *CP* fit, since it relates the signal yields to the *CP*-violating observables using Eq.(2.15),

$$N_i^{\mp} = h_{DK}^{\mp}\left[F_i + \left(\left(x_{\mp}^{DK}\right)^2 + \left(y_{\mp}^{DK}\right)^2\right)F_{-i} + 2\sqrt{F_i F_{-i}}\left(x_{\mp}^{DK}c_i + y_{\mp}^{DK}s_i\right)\right]. \quad (2.15)$$

To improve the fit stability, the invariant-mass shape is fixed according to the parameters in Table 9.4. In addition, with the invariant-mass shape fixed,

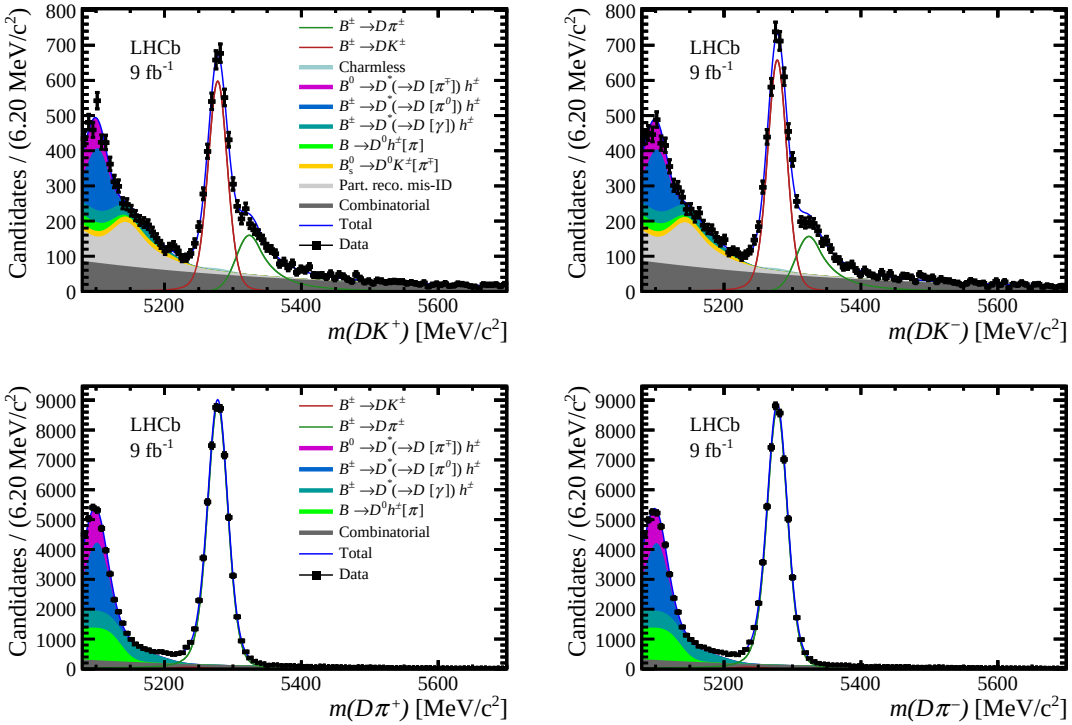

Figure 9.15: Invariant-mass distributions and fit projections of (top) $B^\pm \to [\pi^+\pi^-\pi^+\pi^-]_D K^\pm$ and (bottom) $B^\pm \to [\pi^+\pi^-\pi^+\pi^-]_D \pi^\pm$ candidates, for (left) B^+ and (right) B^- decays.

the fit range is reduced to $m_B \in [5150, 5700]\,\text{MeV}/c^2$ to minimise the impact of *CP*-violation effects in the partially reconstructed background.

Examples of *CP* violation in local phase-space regions are shown in Figs. 9.16 and 9.17 for $B^\pm \to DK^\pm$, where the B^- and B^+ yields in two conjugate bins are compared. In Fig. 9.16, which shows the $D \to K^+K^-\pi^+\pi^-$ decay, there are visibly more B^- decays in bin $+3$ compared to B^+ decays in bin -3. Similarly, in Fig. 9.17, an opposite asymmetry is seen. Although these asymmetries may seem small, the simultaneous fit of all phase-space bins can place significant constraints on γ.

For the $D \to K^+K^-\pi^+\pi^-$ channel, which has 2×4 phase-space bins, the two $B^\pm$ decays and two charges make a total of $2\times2\times2\times4 = 32$ categories. Similarly, in the $D \to \pi^+\pi^-\pi^+\pi^-$ channel there are 40 fit categories. In each category, the signal yield is parameterised in terms of the *CP*-violating observables using Eq. (2.15). Each $B^\pm$ decay has four *CP*-violating observables, but with the parameterisation in Eq. (2.16), the total number of *CP*-violating observables is six.

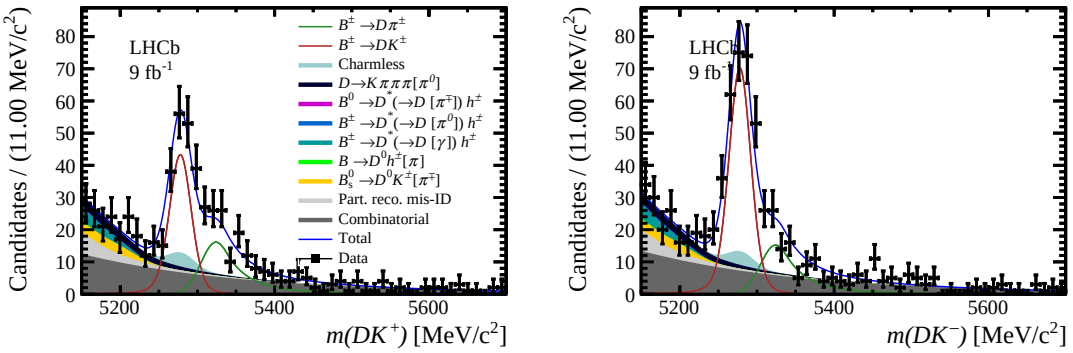

Figure 9.16: A comparison of the invariant-mass distributions and fit projections of $B^{\pm} \to [K^+K^-\pi^+\pi^-]_D K^{\pm}$ in (left) bin -3 for B^+ and bin $+3$ for B^-.

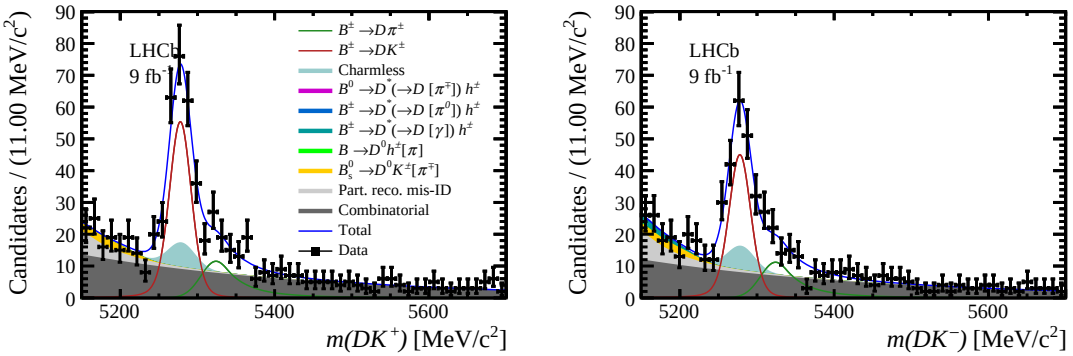

Figure 9.17: A comparison of the invariant-mass distributions and fit projections of $B^{\pm} \to [\pi^+\pi^-\pi^+\pi^-]_D K^{\pm}$ in (left) bin -5 for B^+ and bin $+5$ for B^-.

The yield of cross-feed background, where the companion hadron is misidentified, is parameterised in terms of the signal yield using ratios of PID efficiencies, analogous to what is described in Section 9.1.2, and using Eq. (2.15) to determine the yield in each phase-space bin. Additionally, in the $D \to K^+K^-\pi^+\pi^-$ selection, there is also the partially reconstructed misidentification background contribution from $D \to K^-\pi^+\pi^-\pi^+\pi^0$ decays. The total yield of this background is determined in the global fit through the parameter $R_{K3\pi\pi^0}$. In the binned fit it is empirically found that setting the bin yields proportional to the bin volumes gives a good description of this background component.

The combinatorial background in each category is allowed to vary independently, but the exponential slopes are fixed to the values in Table 9.4. Studies of the region $m_B \in [5400, 5700]\,\mathrm{MeV}/c^2$ show that the variation in the exponential slope

between bins is negligible. For the $D \to K^+K^-\pi^+\pi^-$ and $\pi^+\pi^-\pi^+\pi^-$ decays the combinatorial background yields adds 32 and 40 free parameters, respectively.

Finally, the total yield of partially reconstructed background is varied independently in each category, while the relative sizes of the different partially reconstructed components are fixed to the values determined from the global fit. This adds 32 and 40 free parameters to the fit for the $D \to K^+K^-\pi^+\pi^-$ and $\pi^+\pi^-\pi^+\pi^-$ modes, respectively.

In the $B^\pm \to DK^\pm$ selection, there are also three additional background components. First, the yield of charmless background is fixed, as discussed in Section 9.1.4. Second, there is a component of partially reconstructed background with a misidentified companion hadron, which is fixed with the same parameterisation as in the global fit. Third, the partially reconstructed decay $B_s^0 \to D^0K^\pm[\pi^\mp]$ is treated separately due to the different charm-meson flavour. For instance, in the $B^- \to DK^-$ selection, where the D^0 flavour dominates the amplitude of signal decays, the yield of the B_s^0 background in bin i is proportional to F_{-i}.

In Eq. (2.15), the fractional bin yields F_i and the normalisation constants $h_{DK}^\mp$ are also free parameters in the fit. There are separate normalisation constants for each $B^\pm$ charge and $B^\pm$ decay, resulting in four normalisation parameters. The parameterisation of F_i is identical to that used in the analysis of c_i and s_i described in Section 6.2.2. This makes seven parameters for the $D \to K^+K^-\pi^+\pi^-$ mode and nine parameters for the $D \to \pi^+\pi^-\pi^+\pi^-$ decay.

A key difference between the strategy described in this thesis, and that of the three-body analysis in Ref. [39], is the treatment of the strong-phase inputs. For the $D \to K^+K^-\pi^+\pi^-$ mode, these are taken from Table 6.11, while those for $D \to \pi^+\pi^-\pi^+\pi^-$ are obtained from Ref. [138]. This analysis treats the eight (ten) c_i and s_i parameters in $D \to K^+K^-\pi^+\pi^-$ ($\pi^+\pi^-\pi^+\pi^-$) as fit parameters that are Gaussian constrained by their covariance matrix. The motivation for this strategy and the impact of this constraint is discussed in Section 9.2.4.

In total, the fit of the $D \to K^+K^-\pi^+\pi^-$ decay has 89 parameters, while that of $D \to \pi^+\pi^-\pi^+\pi^-$ has 109 parameters. In a fit where both these decays are

fitted simultaneously, the *CP*-violating observables are shared, resulting in a total of $89 + 109 - 6 = 192$ free parameters.

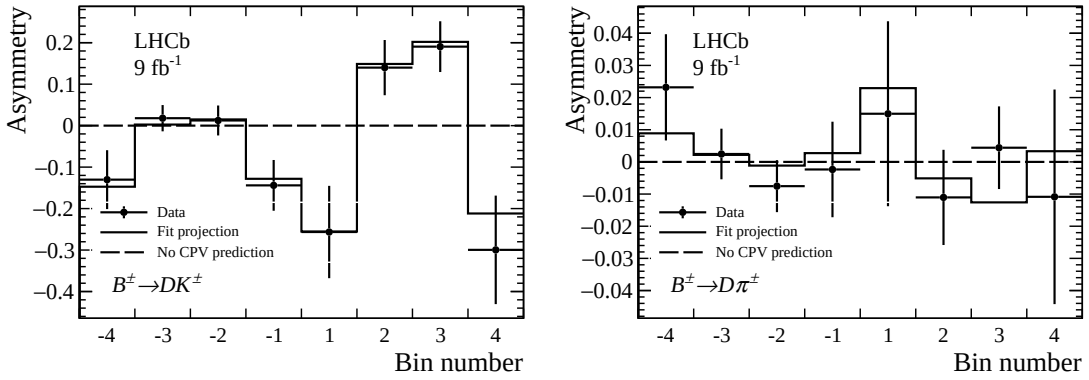

Figure 9.18: Fractional bin asymmetries for $B^{\pm} \to [K^+K^-\pi^+\pi^-]_D h^{\pm}$, with DK on the left and $D\pi$ on the right.

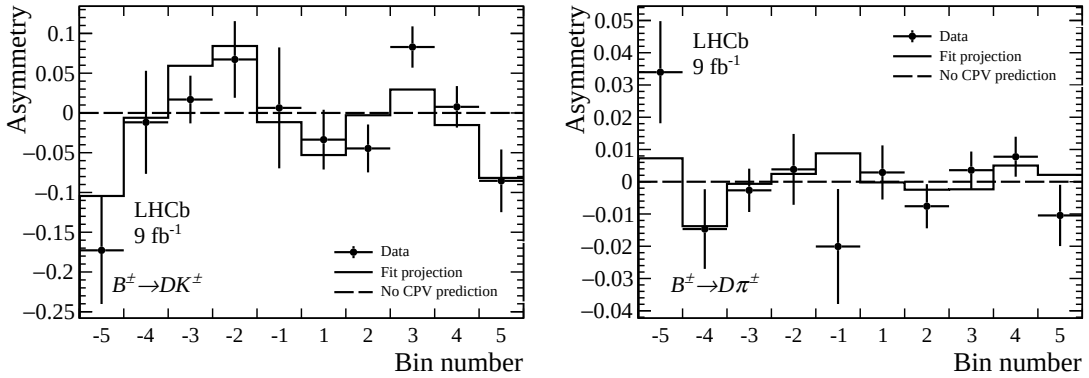

Figure 9.19: Fractional bin asymmetries for $B^{\pm} \to [\pi^+\pi^-\pi^+\pi^-]_D h^{\pm}$, with DK on the left and $D\pi$ on the right.

A nice visualisation is to plot the fractional bin asymmetries of each phase-space bin, defined as the difference between the fractional B^- yield in bin $+i$ and that of B^+ in bin $-i$, divided by their sum. The fractional bin yields are obtained from an alternative *CP* fit where instead of having the *CP*-violating observables as free parameters, the individual bin yields are varied independently in each bin.

The asymmetries are shown as data points in Figs. 9.18 and 9.19. In several phase-space bins, non-zero asymmetries are seen in the $B^{\pm} \to DK^{\pm}$ mode, and the difference in asymmetries between bins is driven by the variation of the D^0-$\overline{D}^0$ strong-phase differences. The asymmetries in the $B^{\pm} \to D\pi^{\pm}$ mode are much

smaller and not statistically significant. It should be noted that although the interpretation of these bin asymmetries in terms of γ and other physics parameters requires external strong-phase inputs, the *CP* violation illustrated in Figs. 9.18 and 9.19 do not rely on these inputs.

The solid line in Figs. 9.18 and 9.19 is the fit projection, or the predicted bin asymmetry, and it is obtained from Eq. (2.15) using the values of *CP*-violating observables obtained in a fit to data. The good agreement between the prediction and the individual bin asymmetries serves as a useful cross check of the quality of the *CP* fit.

9.2.4 Statistical properties of measured *CP*-violating observables

In previous measurements of the CKM angle γ at LHCb, the analyses have mainly been dominated by the statistical uncertainties due to the limited size of the data set. For instance, despite being the leading systematic uncertainty in the three-body analysis described by Ref. [39], the statistical uncertainties on the *CP*-violating observables are about 3-4 times larger than the systematic uncertainties. It is therefore possible to fix the c_i and s_i parameters in the fit, and then propagate the systematic uncertainties to the *CP*-violating observables by repeating the *CP* fit. In each iteration, the values of c_i and s_i are varied randomly according to their covariance matrix.

Such a procedure is preferred since the correlation between analyses that use the same c_i and s_i inputs can be evaluated without performing a simultaneous fit of all analyses. Furthermore, it allows the statistical and systematic uncertainties to be evaluated independently.

However, in the phase-space binned analysis of the four-body decay $B^\pm \to [K^\mp\pi^\pm\pi^\mp\pi^\pm]_D h^\pm$ [47], the magnitude of the systematic uncertainties due to BESIII charm strong-phase inputs were in fact found to be similar in size to the statistical uncertainties. In the analysis of $B^\pm \to [K^+K^-\pi^+\pi^-]_D h^\pm$ and $B^\pm \to [\pi^+\pi^-\pi^+\pi^-]_D h^\pm$ described by this thesis, a similar behaviour is seen. Unfortunately, if the c_i and s_i

parameters are fixed in the *CP* fit, it could bias both the central value of *CP*-violating observables and their uncertainties. Hence, it is necessary to Gaussian constrain the c_i and s_i parameters, at the expense of mixing the statistical uncertainty due to the LHCb data set with the systematic uncertainties due to the c_i and s_i uncertainties.

The statistical properties of the *CP* fit, with the c_i and s_i parameters Gaussian constrained, are studied with a series of pseudo-experiments in order to establish potential biases or non-Gaussian distributed uncertainties. Using the fit model described in Section 9.1, the data sets are generated with values of γ, δ_B^{DK}, r_B^{DK}, $\delta_B^{D\pi}$ and $r_B^{D\pi}$ taken from Ref. [48]. The rest of the free parameters are set to those obtained in a fit to data. Each data set is fitted using the strategy described in Section 9.2.3. These pseudo-experiments are exclusively performed on the $D \to K^+K^-\pi^+\pi^-$ mode, which is less well behaved than the $D \to \pi^+\pi^-\pi^+\pi^-$ mode due to the smaller data sample and the larger uncertainties in c_i and s_i.

Table 9.7: Mean and standard deviation of the pull distributions of the *CP*-violating observables.

Parameter	Pull mean (10^{-2})	Pull standard deviation
x_-^{DK}	-0.10 ± 0.03	0.974 ± 0.026
x_+^{DK}	-0.08 ± 0.03	0.949 ± 0.025
y_-^{DK}	0.29 ± 0.04	0.914 ± 0.032
y_+^{DK}	-0.05 ± 0.03	1.007 ± 0.025
$x_\xi^{D\pi}$	0.16 ± 0.03	0.877 ± 0.022
$y_\xi^{D\pi}$	-0.04 ± 0.03	0.907 ± 0.021

The resulting pull distributions of *CP*-violating observables from 1000 pseudo-experiments are shown in Fig. 9.20, and the fitted values for the mean and standard deviation are shown in Table 9.7. All parameters are found to have small biases in the central value, and some parameters have standard deviations that are lower than unity, which indicates so-called over-coverage in the uncertainty estimation.

This behaviour is particularly significant in the $x_\xi^{D\pi}$ and $y_\xi^{D\pi}$ observables, and it has also been seen in the analysis described in Ref. [39]. The origin of this effect is the poor sensitivity to these observables due to the small value of $r_B^{D\pi}$, and the

effect is found to reduce when fitting pseudo-experiments with larger sample sizes. Thus, it is a well-understood effect that is easily corrected for.

The small over-coverage in the $y_{\pm}^{DK}$ observables is not an artefact of poor sensitivity, but it is an effect of the large uncertainties in s_i. In fits where the external inputs c_i and s_i are fixed, the pull distributions of $x_{\pm}^{DK}$ and $y_{\pm}^{DK}$ are in fact consistent with a normal Gaussian distribution. By eye, the impact of the large uncertainties in s_i is seen to be much more severe in Fig. 9.20. While the pull distributions of $x_{\pm}^{DK}$ are symmetric and close to a normal Gaussian distribution, that of y_{-}^{DK} is asymmetric and not well behaved.

It is therefore unlikely that symmetric uncertainties can accurately describe the non-Gaussian distribution of all *CP*-violating observables, and doing so can potentially bias both the central value and the uncertainty of γ. To study the size of this effect, a profile-likelihood function is obtained for each DK observable, and they are plotted in blue in Fig. 9.21.

The black curve illustrates what is known as the "Hesse" approximation, which is a parabolic shape, from which symmetric uncertainties are determined in the fit. For an observable that is Gaussian distributed, its profile-likelihood function will coincide with the Hesse approximation, which is largely the case for the $x_{\pm}^{DK}$ parameters. While the Hesse approximation works well for the $y_{\pm}^{DK}$ parameters near the profile-likelihood minimum, it generally gives a poor description of the true profile-likelihood function. In particular, its asymmetric shape makes it inappropriate to assign symmetric uncertainties to $y_{\pm}^{DK}$.

It should be noted that in Eq. (2.15), the parameters $x_{\pm}^{DK}$ are multiplied with c_i, so generally an uncertainty in c_i will be propagated into an uncertainty in $x_{\pm}^{DK}$. Similarly, if the uncertainties of s_i are large, there will be a corresponding impact on $y_{\pm}^{DK}$. It is therefore interesting to study the effect of fixing the values of c_i and s_i, instead of Gaussian constraining them. In Fig. 9.21 these profile-likelihood functions are shown in red.

In the plots of the $x_{\pm}^{DK}$ parameters, the red curves are found to mostly coincide with both the full profile-likelihood function in blue and the Hesse approximation

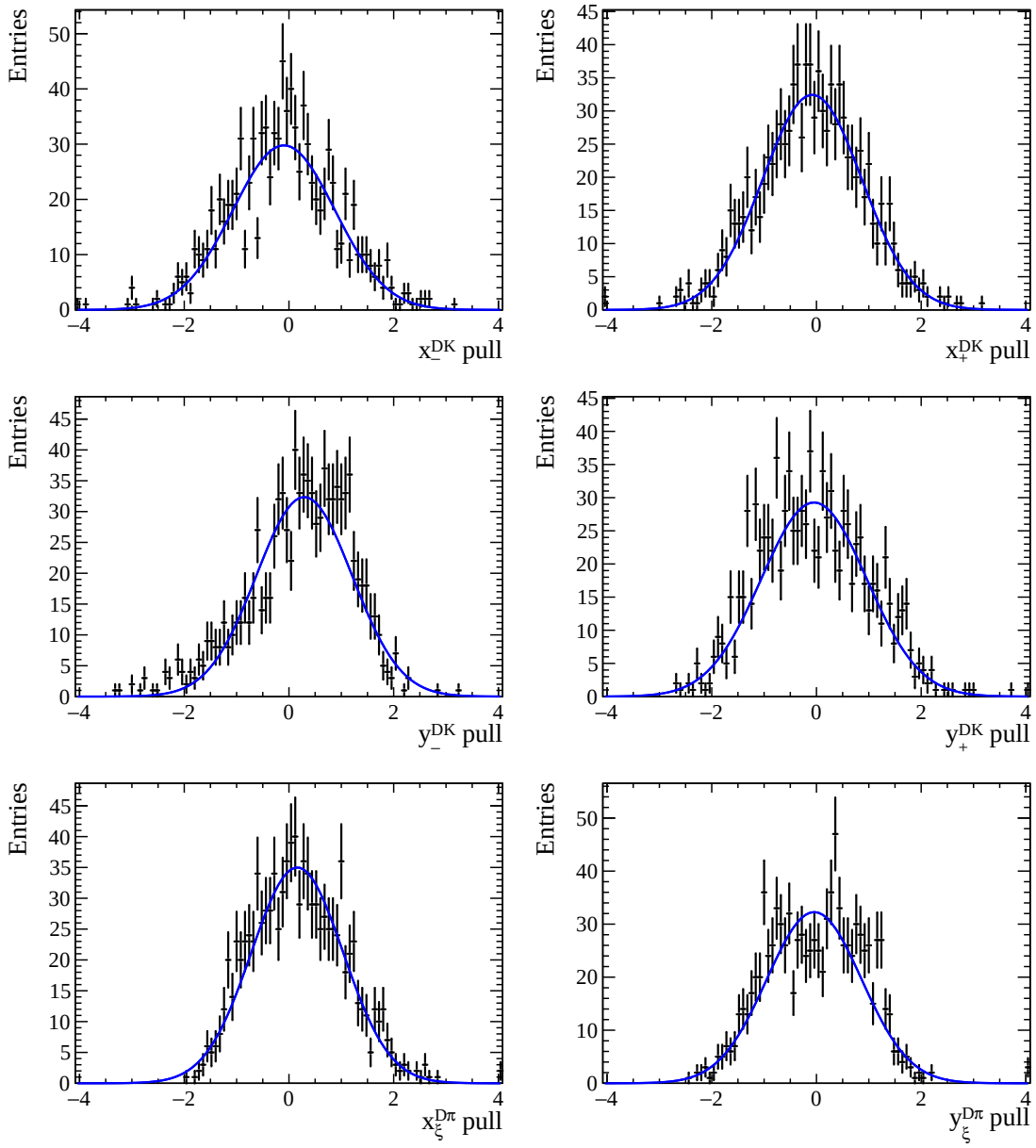

Figure 9.20: Pull distributions of *CP*-violating observables, for the $D \to K^+K^-\pi^+\pi^-$ channel, obtained from a fit of pseudo-experiments that are generated using the *CP*-fit model. The blue curve is a Gaussian function fitted to these distributions.

in black. This behaviour agrees with the numbers presented in Table 6.11, where the uncertainties of c_i are found to be much smaller than those of s_i. Therefore, the uncertainties of the c_i parameters have a very small impact on the *CP*-violating observables, in comparison to the statistical uncertainties of $x_\pm^{DK}$.

Similarly, in the plots of the $y_\pm^{DK}$ parameters, the red curves are symmetric and similar to the Hesse approximation in black, with a well-behaved parabolic

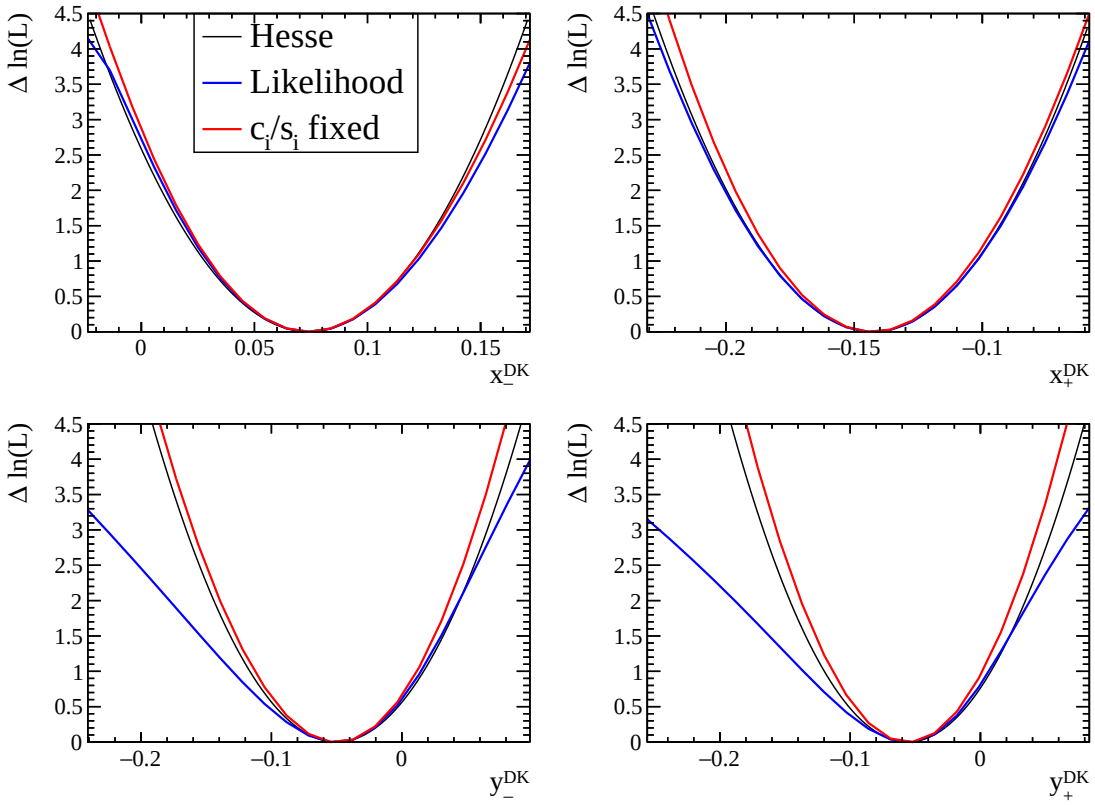

Figure 9.21: A scan of the profile-likelihood functions of the *CP*-violating observables in the $B^{\pm} \to [K^+K^-\pi^+\pi^-]DK^{\pm}$ channel. The blue curve shows the nominal likelihood function, while the red shows the same likelihood scan with c_i and s_i fixed. In black, labelled Hesse, is the parabolic approximation, which models uncertainties that are Gaussian distributed.

shape, and both the red and black curves differ significantly from the full profile-likelihood in blue. It can therefore be concluded that the non-Gaussian behaviour of the $y_{\pm}^{DK}$ uncertainties is entirely driven by the large uncertainties in s_i, and not by the limited sample size of $B^{\pm}$ decays. The proper treatment of this unusual behaviour is discussed in Section 9.3.

9.2.5 Systematic uncertainties of *CP*-violating observables

Although the systematic uncertainties due to the strong-phase inputs are currently absorbed into the statistical uncertainties due to the Gaussian-constraint strategy, as discussed in Section 9.2.4, there are several other sources of systematic uncertainty due to LHCb detector effects or due to the analysis procedure. In this section,

systematic uncertainties refer to these internal LHCb systematic uncertainties, and not those from c_i and s_i uncertainties.

The systematic uncertainties are not evaluated directly in terms of γ and other physics parameters. As discussed in Section 2.7.2, the statistical behaviour of these physics parameters is difficult to interpret due to complex trigonometric relations, and this was the motivation for using the Cartesian *CP*-violating observables. Although the uncertainties of s_i do introduce non-Gaussian behaviour in the *CP*-violating observables, the systematic uncertainties are sufficiently small that they can be considered independent of the c_i and s_i uncertainties. Therefore, in the evaluation of these systematic uncertainties, the values of c_i and s_i are fixed, which result in statistically well-behaved uncertainties on the *CP*-violating observables.

The systematic uncertainties associated with the fixed invariant-mass shape in the *CP* fit are propagated to the *CP*-violating observables by repeating the global and *CP* fits with different choices of shape. Each shape is determined by repeating the procedure in Section 9.1, after resampling the data and simulation samples with replacement. In order to correctly propagate these uncertainties, in each iteration the data set is resampled before the global fit is rerun. Then, with the new invariant-mass shape, the *CP* fit is run without resampling. The standard deviations of the resulting distributions of *CP*-violating observables are assigned as the systematic uncertainty.

To assess any bin-dependence on the invariant-mass shapes, the shapes of signal and that of companion misidentification are fitted separately in each phase-space bin. Using this alternative model, pseudo-experiments are generated, which are subsequently fitted using the baseline model, where the same shape is used in all bins. The shifts in the central values are taken as the corresponding systematic uncertainty.

In the *CP* fit, the PID efficiencies determined in Section 8.5 are fixed, and to propagate these to the *CP*-violating observables, the *CP* fit is repeated, each time varying these efficiencies according to their uncertainties. The standard deviation of the resulting distributions are taken as the systematic uncertainty. The same procedure is used to assign systematic uncertainties associated with the low-mass

background model, where the fractions of different background components are fixed. The charmless background is also treated analogously, using the uncertainties determined in Section 9.1.4.

The partially reconstructed background described in Section 9.1.3, which is from real B decays, is subject to similar *CP*-violating effects as that of signal decays. Although the invariant-mass range $m_B \in [5150, 5700]\,\mathrm{MeV}/c^2$ is chosen specifically to remove these backgrounds components, the residual contributions could potentially fake *CP*-violation effects in the signal region. The impact is studied by constructing an alternative invariant-mass model which includes *CP* violation in the partially reconstructed background. This model is used to generate pseudo-experiments, which are fitted with the baseline model. The shift in the central values is taken as the systematic uncertainty due to *CP* violation in the low-mass background.

Similarly, there are four small background contributions that are not modelled in the baseline model that could bias the fit. Two of these contributions have been studied in this thesis: the CF $D \to K^-\pi^+\pi^-\pi^+$ decay in Section 9.1.5, and the semi-leptonic charm decays in Section 9.1.6. Furthermore, there is a semi-leptonic $B^- \to D^0\mu^-\overline{\nu}_\mu$ decay and a baryonic decay $\Lambda_b^0 \to pD^0\pi^-$, which were studied in Ref. [39]. Each of these background decays are studied separately by generating pseudo-experiments that contain these background decays, and running the *CP* fit with the baseline model.

Finally, in Section 9.1.4 the partially reconstructed misidentification background $D \to K^-\pi^+\pi^-\pi^+\pi^0$ is studied. In the fit, it is assumed, from empirical observations, that the distribution of this background in phase-space bins is proportional to the bin volume. Due to the lack of amplitude model of this decay, the strategy is to assign a conservative systematic uncertainty. Instead of distributing these decays according to the bin volumes, the bin distribution is changed to be proportional to the F_i parameters of the $D^0 \to K^+K^-\pi^+\pi^-$ decay. Pseudo-experiments are generated with this alternative background model and fitted using the baseline model. The shifts in the central values are assigned as the systematic uncertainties.

A summary of all systematic uncertainties in the phase-space binned analysis is shown in Table 9.8. The statistical uncertainties of the *CP*-violating observables are also listed, and these are obtained in a fit to data where the c_i and s_i parameters are fixed. The total systematic uncertainty at the bottom is obtained by adding the individual covariance matrices, and it is almost an order of magnitude smaller than the statistical uncertainties. Similar systematic uncertainties are also evaluated for the setup where the $D \to K^+K^-\pi^+\pi^-$ and $\pi^+\pi^-\pi^+\pi^-$ modes are fitted separately.

Table 9.8: Summary of all systematic uncertainties of CP observables from the combined fit of $D \to K^+K^-\pi^+\pi^-$ and $D \to \pi^+\pi^-\pi^+\pi^-$, multiplied by 10^2. The first row has the statistical uncertainty in a fit to data where the c_i and s_i parameters are fixed.

Source	x_-^{DK}	y_-^{DK}	x_+^{DK}	y_+^{DK}	$x_\xi^{D\pi}$	$y_\xi^{D\pi}$
Statistical	1.80	1.72	1.68	1.61	3.82	3.58
Invariant-mass shape	0.02	0.02	0.03	0.02	0.01	0.01
Bin-dependent mass shape	0.10	0.26	0.06	0.01	0.17	0.09
PID efficiency	0.02	0.02	0.03	0.02	0.01	0.01
Background fractions	0.01	0.01	0.02	0.01	0.02	0.01
Charmless background	0.09	0.08	0.08	0.09	0.01	0.01
CP violation in low-mass background	0.14	0.04	0.03	0.01	0.06	0.07
Semi-leptonic charm decays	0.09	0.11	0.01	0.00	0.28	0.02
$D \to K^-\pi^+\pi^-\pi^+$ background	0.12	0.04	0.03	0.03	0.28	0.13
Semi-leptonic b-hadron decays	0.10	0.00	0.02	0.03	0.12	0.15
$\Lambda_b^0 \to pD\pi^-$ background	0.16	0.01	0.14	0.03	0.19	0.06
$D \to K^-\pi^+\pi^-\pi^+\pi^0$	0.06	0.05	0.18	0.03	0.10	0.12
Total systematic	0.32	0.30	0.26	0.11	0.50	0.26

There are also two other potentially important systematic effects that are studied, but found to be too small to include in Table 9.8. First, it is checked whether or not a non-uniform phase-space acceptance could affect the effective values of c_i and s_i. This is evaluated by calculating the model-predicted values of c_i and s_i, as described in Section 3.3. However, instead of non-resonant decays, the reweighting procedure used in Section 5.7 is applied to obtain an MC integration sample that contains phase-space acceptance effects. The difference between these efficiency-corrected values of c_i and s_i and the nominal values are all one or two orders of magnitude smaller than their statistical uncertainties, and therefore this effect is neglected.

Table 9.9: Uncertainties on the results of the phase-space integrated analysis.

	Uncertainty ($\times 10^3$)					
Source	$A_K^{KK\pi\pi}$	$A_\pi^{KK\pi\pi}$	$A_K^{\pi\pi\pi\pi}$	$A_\pi^{\pi\pi\pi\pi}$	$R_{CP}^{KK\pi\pi}$	$R_{CP}^{\pi\pi\pi\pi}$
Statistical	23.5	5.5	13.3	3.1	24.2	14.3
Invariant-mass shape	0.3	< 0.1	0.2	< 0.1	3.1	3.1
PID efficiency	0.1	< 0.1	0.1	< 0.1	2.5	1.6
Background fractions	0.1	< 0.1	0.1	< 0.1	1.3	1.4
Charmless background	1.2	< 0.1	0.4	< 0.1	13.9	8.5
External parameters	1.5	0.7	1.5	0.7	4.0	4.0
Total systematic	2.0	0.7	1.6	0.7	15.1	10.1

The second effect is the impact of charm mixing, which can be studied analytically using charm mixing equations from Ref. [21]. Using the amplitude from Ref. [38], the yield of $B^\pm \to Dh^\pm$ candidates in each phase-space bin is predicted, taking D^0-$\overline{D}^0$ mixing into account, with mixing parameters from Ref. [25]. These bin yields are fitted to obtain the *CP*-violating observables, and the shift in these observables is found to be negligible. This is consistent with the discussion in Section 2.7.2, where it is mentioned that to first order, mixing effects can be absorbed into the F_i parameters. To validate this claim, the fit is repeated with the F_i parameters fixed, and a shift of around 10^{-2} in each observable is observed, which is of similar size to the other systematic uncertainties.

In Table 9.9, the systematic uncertainties on the phase-space integrated *CP*-observables determined in Section 9.2.2 are listed. They are evaluated in an identical manner to those in the binned analysis, but the contributions specific to the *CP* fit are not included. In addition, the contribution labelled "External parameters" are the uncertainties of the production and detection asymmetries, which have been propagated to the *CP*-violating observables by repeating the fit, each time varying these inputs. The systematic uncertainties are generally much smaller than the corresponding statistical uncertainties.

9.3 Interpretation in terms of γ

In the final stage of the analysis, the *CP*-violating observables must be combined in a maximum likelihood fit to obtain the physics parameters γ, δ_B^{DK}, r_B^{DK}, $\delta_B^{D\pi}$ and $r_B^{D\pi}$. This fit is referred to as the interpretation.

9.3.1 Parameterisation of γ for interpretation

Following the discussion of Section 9.2.4, it is clear that constructing a likelihood function using the formalism from Appendix A, in particular Eq. (A.3), is inappropriate for this analysis since the *CP*-violating observables have uncertainties that do not follow a Gaussian distribution.

Instead, the strategy is to obtain the likelihood function of the *CP* fit from Section 9.2.3 and perform the interpretation directly. The advantage of such a fit is that the interpretation makes use of all the available information, while the disadvantage is that the interpretation also needs to include all nuisance parameters.

To be specific, let α_i denote the *CP*-violating observables, while n_k denotes the set of nuisance parameters in the *CP* fit. This includes all the background yields, F_i parameters, c_i and s_i parameters, and the normalisation parameters. The interpretation is effectively performed by doing a change of variables from α_i to β_j, which is the set of physics parameters γ, δ_B^{DK}, r_B^{DK}, $\delta_B^{D\pi}$ and $r_B^{D\pi}$. This relationship can be written as

$$\alpha_i = f_i(\beta_j) + G_i, \tag{9.3}$$

where f_i are the transformations given by Eq. (2.10). Note that although there are six *CP*-violating observables, only five physics parameters exist. The consequence is that when the likelihood function is minimised with respect to the new parameterisation (β_j, n_k), the transformation in Eq. (9.3) will constrain $(x_+^{DK})^2 + (y_+^{DK})^2 = (x_-^{DK})^2 + (y_-^{DK})^2$.

The term G_i is a multi-dimensional Gaussian distribution with zero mean and a covariance matrix that represent the systematic uncertainties on the *CP*-violating

observables, determined in Section 9.2.5. Thus, this conveniently merges the internal LHCb-specific systematic uncertainties into the interpretation.

9.3.2 Bias corrections in the interpretation

To check for biases in the central value of γ and other physics parameters, pseudo-experiments are generated, with an analogous procedure to those described in Section 9.2.4. The input values are those obtained in a fit to data. After the interpretation is performed, the pull distributions, which are shown as black data points in Fig. 9.22, are fitted with a Gaussian function, shown in blue. The mean and standard deviation of this Gaussian are shown in Table 9.10.

Table 9.10: Mean and standard deviation of the pulls of each floating variable in the combined interpretation of $D \to K^+K^-\pi^+\pi^-$ and $D \to \pi^+\pi^-\pi^+\pi^-$.

Parameter	Pull mean (10^{-2})	Pull standard deviation
γ	-33 ± 4	1.077 ± 0.028
δ_B^{DK}	19 ± 3	1.022 ± 0.026
r_B^{DK}	56 ± 3	0.990 ± 0.029
$\delta_B^{D\pi}$	1 ± 5	1.39 ± 0.04
$r_B^{D\pi}$	59.1 ± 2.4	0.737 ± 0.016

There is a small, but non-negligible bias in γ and δ_B^{DK}, which depends on the central values of the physics parameters. The origin of this bias is understood to be due to the large uncertainties of s_i. In similar bias studies of a fit with only the $D \to K^+K^-\pi^+\pi^-$ mode, the bias in γ is $(42 \pm 4) \times 10^{-2}$, while that of $D \to \pi^+\pi^-\pi^+\pi^-$ is $(-19 \pm 3) \times 10^{-2}$. The different biases are driven by both the different uncertainties on c_i and s_i between the two decays, and also by the different input parameters used to generate the pseudo-experiments.

The two r_B parameters have pull distributions which are not consistent with a normal Gaussian function. However, they are consistent with the behaviour observed in the signal-only pseudo-experiments in Fig. 3.7. This effect is expected, and it is due to the physical requirement that $r_B > 0$.

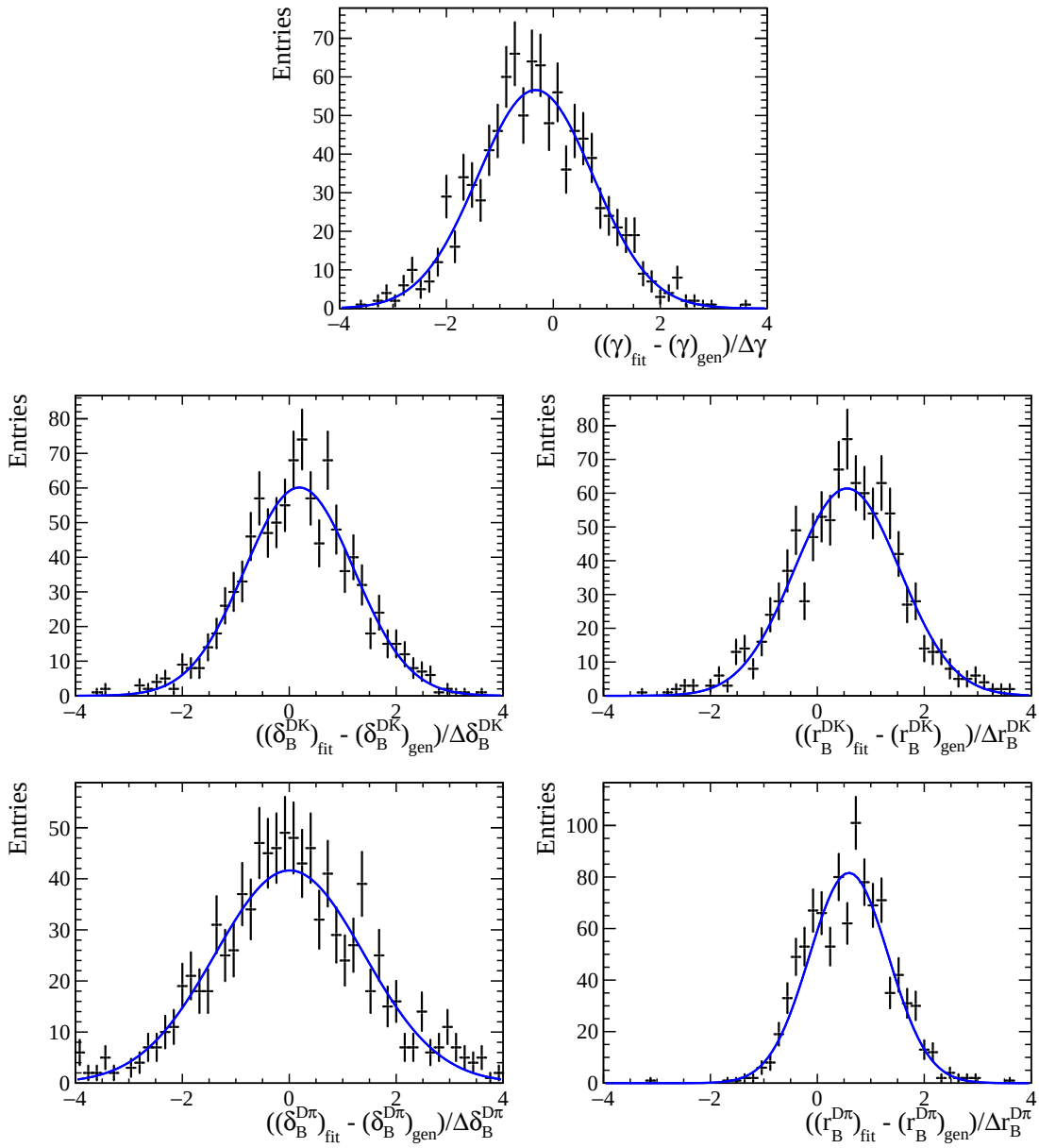

Figure 9.22: Pull distributions of physics parameters in a combined fit of the $D \to K^+K^-\pi^+\pi^-$ and $D \to \pi^+\pi^-\pi^+\pi^-$ channels, obtained from an interpretation of pseudo-experiments that are generated using the *CP*-fit model. The blue curve is a Gaussian function fitted to these distributions.

Although the phase $\delta_B^{D\pi}$ has a bias consistent with zero, its uncertainties are highly underestimated. This is a consequence of the low sensitivity to this phase, and it is expected to improve with a larger sample size.

In the interpretation results presented in this chapter, the central values of physics parameters are corrected for using the mean of the pull distributions from

Table 9.10. Their uncertainties are corrected for using the more in-depth study presented in Section 9.3.4. The size of these bias corrections for γ are approximately 6° and 2° for the $D \to K^+K^-\pi^+\pi^-$ and $\pi^+\pi^-\pi^+\pi^-$ modes, respectively, and for the combined fit the correction is 3°.

The biases in the pull distributions presented in Table 9.10 are in principle subject to the same assumptions and limitations discussed in Section 6.2.4. To a certain degree, the discussion at the end of Section 6.2.4 is more relevant in the analysis of LHCb data, as there are a larger number of nuisance parameters and background components.

Despite this, the fit described in Section 9.2.3 has been, to a large extent, tested for robustness and stability during the analysis. It is well understood that the *CP*-violating observables are only sensitive to differences in the fractional bin yields between that of B^- and B^+ decays, which makes them fairly insensitive to background decays. Hence, at the current precision, it is assumed that the choice of nuisance parameters does not significantly impact the bias corrections in Table 9.10. Nevertheless, in future studies it will be beneficial to study this dependence. A brute-force strategy is to sample the nuisance parameters based on their fitted values and covariance matrix, and examine the impact this has on the bias corrections.

9.3.3 Interpretation results with symmetric uncertainties

The fit results, with symmetric uncertainties, are shown in Tables 9.11 and 9.12 for the $D \to K^+K^-\pi^+\pi^-$ and $D \to \pi^+\pi^-\pi^+\pi^-$ modes, respectively.

Table 9.11: Fitted physics parameters with $D \to K^+K^-\pi^+\pi^-$. Fit biases have been corrected for.

Physics parameter	Fit result
γ (°)	117 ± 14
δ_B^{DK} (°)	80 ± 13
r_B^{DK}	$(11.7 \pm 2.7) \times 10^{-2}$
$\delta_B^{D\pi}$ (°)	297 ± 77
$r_B^{D\pi}$	$(-0 \pm 7) \times 10^{-3}$

Table 9.12: Fitted physics parameters with $D \to \pi^+\pi^-\pi^+\pi^-$. Fit biases have been corrected for.

Physics parameter	Fit result
γ (°)	41 ± 11
δ_B^{DK} (°)	120 ± 10
r_B^{DK}	$(8.5 \pm 1.9) \times 10^{-2}$
$\delta_B^{D\pi}$ (°)	210 ± 46
$r_B^{D\pi}$	$(4 \pm 6) \times 10^{-3}$

A striking detail of Tables 9.11 and 9.12 is the discrepancy of γ and δ_B^{DK} between the two decay channels. Furthermore, in the latest combination of γ measurements by the LHCb experiment, these parameters have been measured to be $\gamma = (63.8^{+3.5}_{-3.7})^\circ$ and $\delta_B^{DK} = (127.3^{+3.4}_{-3.5})^\circ$. While the results of the $D \to \pi^+\pi^-\pi^+\pi^-$ channel is in agreement with these numbers, the results of the $D \to K^+K^-\pi^+\pi^-$ decay differ by around $3\,\sigma$. However, these estimates are based on symmetric uncertainties, which assume that their uncertainties are Gaussian distributed.

A more informative visualisation of the results are shown in Fig. 9.23, where the contours from the profile-likelihood function of γ and δ_B^{DK} are shown on the left, and those of r_B^{DK} and δ_B^{DK} are shown on the right. The contours correspond to $\Delta\mathcal{L} = 2.30$ and $\Delta\mathcal{L} = 6.18$, which for a χ^2 distribution with two degrees of freedom results in a coverage probability of 68.27% and 95.45%. The contours for the $D \to K^+K^-\pi^+\pi^-$ ($\pi^+\pi^-\pi^+\pi^-$) mode is shown in red (blue). For comparison, the LHCb average [48] from other measurements is shown in black.

Table 9.13: Fitted physics parameters with the combination of $D \to K^+K^-\pi^+\pi^-$ and $D \to \pi^+\pi^-\pi^+\pi^-$. Fit biases have been corrected for.

Physics parameter	Fit result
γ (°)	54 ± 9
δ_B^{DK} (°)	113 ± 9
r_B^{DK}	$(9.4 \pm 1.6) \times 10^{-2}$
$\delta_B^{D\pi}$ (°)	233 ± 53
$r_B^{D\pi}$	$(2 \pm 4) \times 10^{-3}$

The $2\,\sigma$ contour of the $D \to K^+K^-\pi^+\pi^-$ mode in Fig. 9.23, in particular, is slightly larger than expected from a two-dimensional Gaussian distribution. This

confirms the findings discussed in Section 9.2.4, where the large uncertainties of s_i are shown to affect the profile-likelihood function in regions far from the minimum. Hence, by correctly accounting for all correlations and non-Gaussian uncertainties, the red and blue $2\,\sigma$ contours in Fig. 9.23 do in fact overlap. This allows for a combination of these measurements, and this is shown in green. A good agreement with the LHCb average in black is found. The numerical results of this combined fit of both modes is shown in Table 9.13.

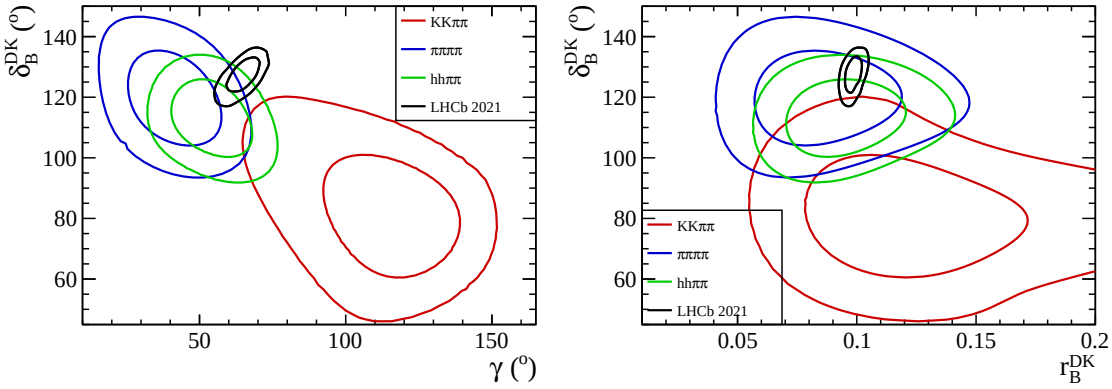

Figure 9.23: Two-dimensional scans of the profiled-likelihood functions of the interpretation. The 1σ and 2σ contours are shown, which correspond to $\Delta\mathcal{L} = 2.30$ and $\Delta\mathcal{L} = 6.18$, respectively. The red contour is from of fit of the $D \to K^+K^-\pi^+\pi^-$ channel, while in blue is the same fit to the $D \to \pi^+\pi^-\pi^+\pi^-$ mode. The simultaneous fit of both decays is shown in green. Also shown, in black, is the LHCb combination from 2021 [48].

9.3.4 The PROB and PLUGIN methods

An assumption in the interpretation of Fig. 9.23 is the fact that the profile-likelihood function is χ^2 distributed near the minimum. This method is known as the PROB method in previous literature on the CKM angle γ [48] and it makes use of Wilks' theorem, which is described in Appendix A.3. The PROB method is known to underestimate uncertainties, in particular in fits with low statistical sensitivity or fits with parameters near physical boundaries.

In order to validate the results presented in Section 9.3.3, a method known as the PLUGIN method, described in Appendix A.4, is performed on the parameter γ. The method determines the p-value, or the confidence interval CL, at each value of γ, using a set of pseudo-experiments at each scan point.

The result of PLUGIN scans of γ for the fit of the $D \to K^+K^-\pi^+\pi^-$ is shown in red in Fig. 9.24. The solid shape is that obtained using the PROB method, while the PLUGIN results are shown as data points. The intersection between the PROB or PLUGIN results with the two horizontal dotted lines denote the 68.27% and 95.45% confidence regions. In general, for the $D \to K^+K^-\pi^+\pi^-$ decay, the PROB method is seen to underestimate the uncertainties significantly, and there is also a long tail on the left hand side. Both these effects reduces the tension with the $D \to \pi^+\pi^-\pi^+\pi^-$ result shown in blue, which has a better agreement between the PROB and PLUGIN method.

Thus, from Fig. 9.24, it can be concluded that the size of the red contours in Fig. 9.23 are underestimated, and indeed there is a good consistency between the two decay modes. The PLUGIN scan of a fit with these modes combined is shown in black in Fig. 9.24, where the PROB method is found to underestimate the γ uncertainty slightly.

9.3.5 Binned result for γ

The true uncertainties on γ are determined by interpolating the PLUGIN points in Fig. 9.24 by a cubic spline. From the intersection of this line with the horizontal line corresponding to a 68.27% confidence interval, the final value of γ obtained from the $D \to K^+K^-\pi^+\pi^-$ mode is $\gamma = (116.9^{+17.2}_{-18.4})^\circ$, although the region outside $1\,\sigma$ does have long tails that do not follow a Gaussian distribution. For the $D \to \pi^+\pi^-\pi^+\pi^-$ decay, the result is determined to be $\gamma = (41.2^{+10.4}_{-10.4})^\circ$, while the combination of both decays results in

$$\gamma = (54.0^{+10.2}_{-9.5})^\circ.$$

9.3.6 Combined model-independent measurement of γ

The final measurement of the CKM angle γ from the four-body decays $B^\pm \to [K^+K^-\pi^+\pi^-]_D h^\pm$ and $B^\pm \to [\pi^+\pi^-\pi^+\pi^-]_D h^\pm$, using all available information, is achieved by combining the results of the phase-space binned measurement in

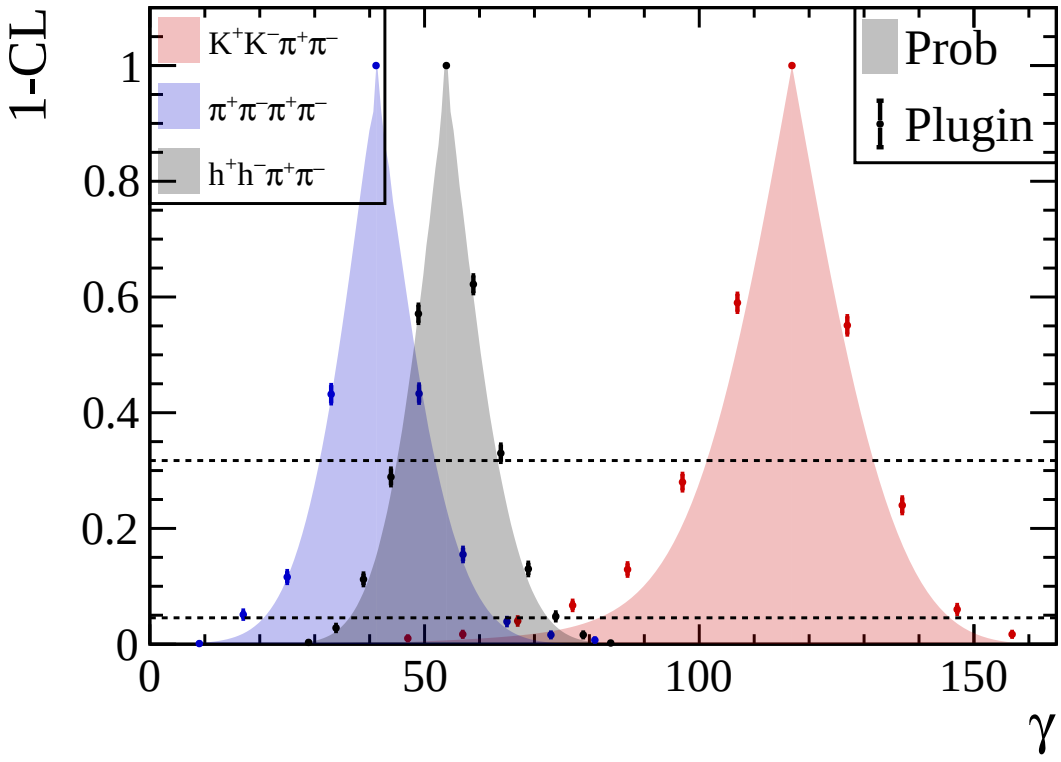

Figure 9.24: A comparison between the Prob and Plugin methods to determine the correct uncertainties of γ. In red is the scan of γ in $D \to K^+K^-\pi^+\pi^-$, while in blue is the $D \to \pi^+\pi^-\pi^+\pi^-$ decay. In black is the simultaneous fit of both decays.

Section 9.3.5 with the phase-space integrated *CP*-violating observables from Section 9.2.2.

To do so, the interpretation is rerun with a Gaussian constraint term, using Eq. (A.3), corresponding to the *CP*-violating observables. The formalism described in Section 2.7.3 is used to relate the phase-space integrated observables to the physics parameters, and corrections due to charm mixing are also included. The *CP*-even fractions of $D \to K^+K^-\pi^+\pi^-$ and $\pi^+\pi^-\pi^+\pi^-$ used in the constraint term are $F_+ = 0.730 \pm 0.037 \pm 0.021$ [43] and $F_+ = 0.735 \pm 0.015 \pm 0.005$ [44], respectively, and they are Gaussian constrained in the fit.

Although the phase-space binned results presented in Section 9.3.5 are obtained from the same data set that is used to measure the phase-space integrated results presented in Section 9.2.2, they are assumed to be statistically independent measurements in the combination. This is explicitly verified by performing both

measurements on a set of pseudo-experiments, and it is found that most correlation coefficients are around 1% or less. This statistical independence is understood to be a consequence of using different normalisation parameters $h^{\pm}_{Dh}$ for the B^- and B^+ decays in the phase-space binned measurement, which makes it insensitive to global asymmetry effects.

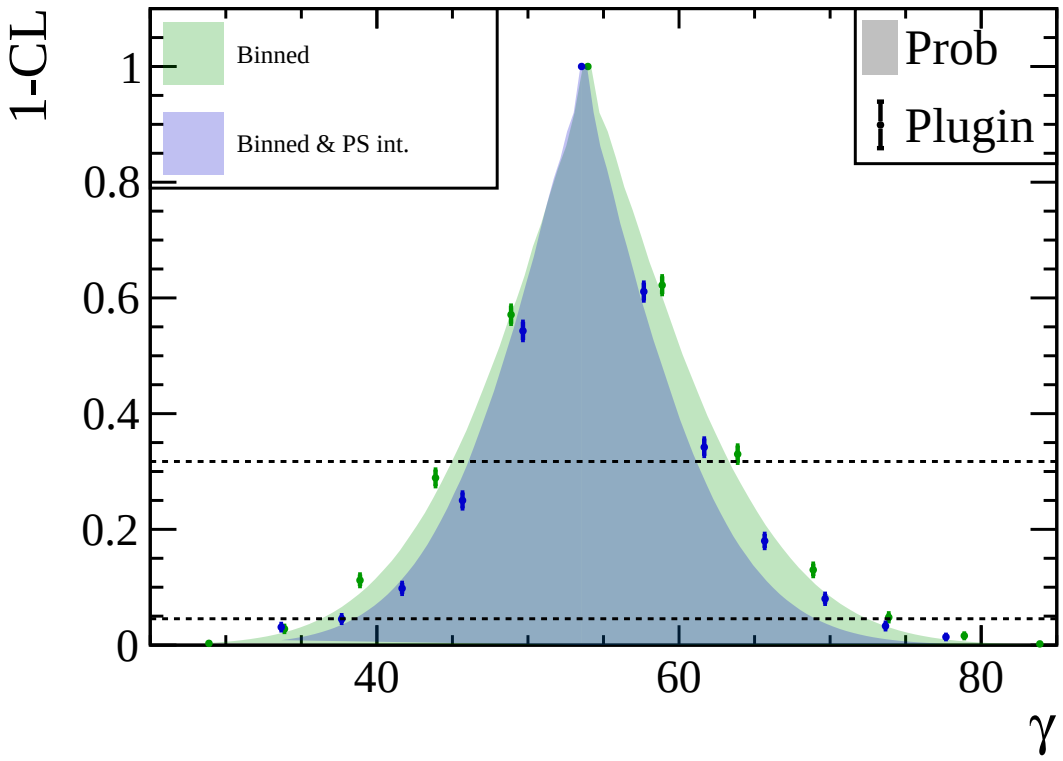

Figure 9.25: A comparison between the Prob and Plugin methods to determine the correct uncertainties of γ. In green is the scan of γ in the combined fit of $D \to K^+K^-\pi^+\pi^-$ and $D \to \pi^+\pi^-\pi^+\pi^-$ decays. In blue is the same fit including constraints from phase-space integrated *CP*-violating observables.

Another PLUGIN scan is performed where the phase-space integrated results are included in the interpretation, and this is shown in blue in Fig. 9.25. For comparison, the PLUGIN scan in green, which is identical to the black PLUGIN scan in Fig. 9.24, shows the interpretation without these constraints. A clear improvement in the precision of γ is seen, and the value of γ is determined to be

$$\gamma = (53.6^{+8.6}_{-6.7})^\circ.$$

Equivalent scans can be conducted for the other physics parameters, δ_B^{DK}, r_B^{DK}, $\delta_B^{D\pi}$ and $r_B^{D\pi}$. However, these scans are computationally very expensive, and since the parameters r_B^{DK} and $r_B^{D\pi}$ are close to the physical boundary at $r_B = 0$, their uncertainties are not expected to be well behaved. Instead, the strategy is to determine a different parameterisation, such as that used in Ref. [47], which is not limited by any physical boundaries. While this choice of parameterisation will not affect this measurement of γ, it will be advantageous for combinations with other measurements of γ.

10
Summary and outlook

A first model-independent measurement of the CKM angle γ has been performed with the $B^{\pm} \to Dh^{\pm}$ channels, with the subsequent four-body $D \to h^+h^-\pi^+\pi^-$ decays, where $h = K$ or π. To interpret the observed *CP*-violation effects in terms of γ, the complex resonance structure of these decays must be understood. Although amplitude models describe these decays well, reliable model uncertainties are difficult to evaluate. Specifically, the prediction of the D^0-$\overline{D}^0$ strong-phase difference can potentially generate a systematic bias in the determination of γ.

It is therefore desirable to obtain strong-phase information independently from a charm factory. However, this approach had never been pursued previously with the $D \to K^+K^-\pi^+\pi^-$ decay. To conduct this study, a binning scheme of phase space that achieves the optimal sensitivity to γ was developed in Chapter 3.

Once the optimised binning scheme had been acquired, data from BESIII at the $D\overline{D}$ threshold, corresponding to $16\,\text{fb}^{-1}$, was analysed to measure the amplitude-averaged strong-phase difference of the $D \to K^+K^-\pi^+\pi^-$ decay. Chapter 6 describes this binned analysis, which builds on that of other similar decays, but benefits from an improved fit strategy. In particular, a new parameterisation allowed for the determination of two auxiliary parameters. First, a world-leading measurement of the $D^0 \to K^+K^-\pi^+\pi^-$ branching fraction has been achieved. Second, this

analysis demonstrated that multi-body decays have interesting sensitivity to the phase $\delta_D^{K\pi}$. Finally, the results of interest are

$$\begin{aligned} c_1 &= -0.28 \pm 0.09 \pm 0.01, \quad & s_1 &= -0.68 \pm 0.24 \pm 0.04, \\ c_2 &= 0.83 \pm 0.04 \pm 0.01, \quad & s_2 &= -0.18 \pm 0.19 \pm 0.03, \\ c_3 &= 0.83 \pm 0.03 \pm 0.01, \quad & s_3 &= 0.27 \pm 0.17 \pm 0.03, \\ c_4 &= -0.28 \pm 0.10 \pm 0.01, \quad & s_4 &= 0.54 \pm 0.28 \pm 0.04. \end{aligned}$$

In all bins, the values of $c_i^2 + s_i^2$ were found to be close to unity, which suggests a minimal degradation in the statistical sensitivity to γ, compared to the optimal case. However, the s_i parameters are significantly less precise than the c_i parameters because of the limited sample size of data sets with the $D \to K^0_{S,L}\pi^+\pi^-$ tag modes.

In Chapter 9, a sample of $B^\pm \to [h^+h^-\pi^+\pi^-]_D h'^\pm$ decays collected by the LHCb detector, corresponding to $9\,\text{fb}^{-1}$, was analysed using two strategies. First, phase-space integrated *CP*-violating observables were determined from a study of global $B^\pm$ yields. Second, *CP*-violation effects in phase-space bins were analysed and interpreted in terms of γ using the model-independent measurements of c_i and s_i. It was discovered that the larger uncertainties of the s_i parameters resulted in a non-trivial statistical behaviour in the *CP*-violating observables. The analysis therefore proved to be challenging, as special care was required in order to interpret these observables in terms of γ with the non-Gaussian uncertainties and correlations accounted for.

Nevertheless, the phase-space binned result for γ was found to be

$$\gamma = (54.0^{+10.2}_{-9.5})^\circ,$$

where the uncertainty is the combined statistical uncertainty of the LHCb data set, the propagated uncertainties of c_i and s_i, and the internal LHCb systematic uncertainties. The uncertainties are determined using an ensemble of pseudo-experiments, and they are constructed to correctly represent a 68.27% confidence region.

When the binned results are combined with the phase-space integrated observables, the final result is

$$\gamma = (53.6^{+8.6}_{-6.7})^\circ.$$

This is one of the most precise stand-alone determinations of γ to date, and it brings important constraints to global CKM fits.

The measurement is currently statistically dominated and will benefit from the larger data set expected with LHCb Upgrade I. In particular, the removal of the L0 trigger will greatly boost the trigger efficiency of interesting physics events, allowing LHCb to fully benefit from the large production cross section of b-hadrons.

Currently the inputs of c_i and s_i dominate the systematic uncertainties, and with their current uncertainties it will be challenging to improve the γ precision during Upgrade I. Fortunately, the current BESIII analysis of the $D \to \pi^+\pi^-\pi^+\pi^-$ decay, which is based on a $3\,\text{fb}^{-1}$ data set, will be updated with the full $20\,\text{fb}^{-1}$ data set in the near future. This will ensure that systematic uncertainties will be sub-dominant in this mode.

However, in the measurement of c_i and s_i in the $D \to K^+K^-\pi^+\pi^-$ channel, which is analysed with a $16\,\text{fb}^{-1}$ data set, only minimal improvements are expected from the full $20\,\text{fb}^{-1}$ data set. The strong-phase uncertainties would therefore limit future precision measurements with this decay, and particularly the uncertainty of s_i will become the limiting systematic uncertainty.

There are several strategies that could improve the knowledge of s_i. First, the analysis described in Chapter 6 could be extended to measure c_i and s_i of additional multi-body final states, such as $D \to \pi^+\pi^-\pi^+\pi^-$, $K^0_{S,L}\pi^+\pi^-$, and $K^0_S\pi^+\pi^-\pi^0$. A simultaneous fit can extract more precise information from the data, and the multi-body decays are particularly sensitive to s_i.

Second, the complementarity between γ measurements and D^0-$\overline{D}^0$ mixing studies could be exploited. The behaviour of charm oscillations in each phase-space bin is driven by the strong-phase difference, analogous to the different CP-violation effects seen in different bins. By combining the measurements of γ and that of

mixing, both of which require external c_i and s_i inputs, the overall precision on γ, strong phases and mixing parameters could be significantly improved.

In summary, this thesis has explored the uncharted territory of four-body self-conjugate charm decays in an effort to determine the CKM angle γ. The result, which is one of the most precise measurements of its kind, is expected to improve further with the large data set anticipated from LHCb. Although challenges due to systematic uncertainties from strong-phase inputs are expected, there are several possible avenues of improvement that will be interesting to pursue in the future.

Appendices

A

The method of maximum likelihood

Contents

A.1 The likelihood function

Maximum likelihood is a method for estimating parameters of a Probability Distribution Function (PDF). If a set of N independent measurements $\vec{x} = (x_1, x_2, ..., x_N)$ is described by the PDFs $\vec{f} = (f_1(x), f_2(x), ..., f_N(x)$, the likelihood function L is defined as the joint probability density of observing these data,

$$L = \prod_i f_i(x_i).$$

In practice, it is more convenient to use the logarithm of L, which turns the product into a sum,

$$\mathcal{L} \equiv -2\ln(L) = -2\sum_i \ln\Big(f_i(x_i)\Big), \tag{A.1}$$

where the factor -2 is by convention. Henceforth, the "likelihood function" will always refer to $\mathcal{L}$.

The PDFs $f_i(x)$ are usually derived from a model described by M parameters $\vec{y} = (y_1, y_2, ..., y_M)$, and L should be considered a function of these free parameters, $L = L(\vec{y})$. To determine the model that best describe the data, the joint probability density should be maximised, or equivalently, $\mathcal{L}$ must be minimised with respect to $\vec{y}$.

The values $\hat{\vec{y}} = (\hat{y_1}, \hat{y_2}, ..., \hat{y_M})$ that minimise the value of $\mathcal{L}$ are referred to as Maximum Likelihood Estimators (MLE). The process of determining the value of these parameters through numerical minimisation is referred to as a "maximum likelihood fit".

A.2 Likelihood function of the Gaussian and Poisson distributions

In most cases of interest, the measurements can be assumed to be Gaussian distributed,

$$f_i(x; \mu_i, \sigma_i) = \frac{1}{\sqrt{2\pi}\sigma} \exp\Big(- \frac{(x-\mu_i)^2}{2\sigma_i^2}\Big),$$

where μ_i and σ_i are the mean and width parameters of the Gaussian distribution. The likelihood function of a Gaussian distribution is

$$\mathcal{L}(\{\mu_i, \sigma_i\}) = \sum_i \left(\frac{(x_i - \mu_i)^2}{\sigma_i^2} + \ln(\sigma_i^2) \right) + N \ln(2\pi). \tag{A.2}$$

It should be noted that the conventional factor of -2 transforms the first term into a weighted sum of squared differences, and in cases where the σ_i parameters are known, the minimisation of $\mathcal{L}$ is equivalent to a least-squares optimisation.

If the measurements $\vec{x}$ are correlated, with a covariance matrix V_{ij}, Eq. (A.2) can be generalised to

$$\mathcal{L}(\{\mu_i\}, V) = \sum_i \sum_j \Big((x_i - \mu_i)(x_j - \mu_j)(V^{-1})_{ij} \Big) + \ln\Big(\det(V)\Big) + N \ln(2\pi). \tag{A.3}$$

Equation (A.3) reduces to Eq. (A.2) in the case where V is a diagonal matrix.

In cases where the data are binned, the number of entries n_i in each bin i can be considered as measurements which follow a Poisson distribution,

$$f_i(n_i;\lambda_i) = \frac{\lambda_i^{n_i} e^{-\lambda_i}}{n_i!},$$

where λ_i is the expected number of events. The likelihood function in this case is

$$\mathcal{L} = -2\sum_i \Big(n_i \ln(\lambda_i) - \lambda_i - \ln(n_i!)\Big). \tag{A.4}$$

A maximum likelihood fit where the likelihood function is a sum over bins is known as a binned fit. For large data sets, it is computationally less expensive since the sum in Eq. (A.4) runs over the number of bins, and not the number of measurements. In maximum likelihood fits which are not binned, the likelihood contains a sum over all measurements and is referred to as unbinned fits.

A.3 Wilks' theorem

The method of maximum likelihood is useful for estimating parameters, and additionally, it is particularly powerful because of its statistical properties. These properties are derived from Wilks' theorem [139], which states that for a null hypothesis H_0 with likelihood $\mathcal{L}(H_0)$ and an alternative hypothesis H_1 and likelihood $\mathcal{L}(H_1)$, the test statistic

$$\Delta\mathcal{L} \equiv \mathcal{L}(H_0) - \mathcal{L}(H_1) \tag{A.5}$$

will asymptotically approach a χ^2_M distribution in the limit where the sample size is large. The number of degrees of freedom, M, is given by the difference in the number of free parameters between H_1 and H_0. By definition, the alternative hypothesis H_1 has more parameters than the null hypothesis H_0, so it will always describe the measurements better. Furthermore, in order for Wilks' theorem to be valid, it is also a requirement that H_0 is a subset of H_1. Hence, $\Delta\mathcal{L} \geq 0$, and in the special case where $\Delta\mathcal{L} = 0$, the alternative hypothesis H_1 reduces to the null hypothesis H_0.

For a model that has a set of M free parameters $\vec{y}$, these parameters may be fixed to some values $\vec{y} = (y_1, y_2, ..., y_M)$ under the null hypothesis. On the other

hand, under an alternative hypothesis H_1, these parameters may be free to take on any parameter values, and the best description of the observed measurements is when the parameters $\vec{y}$ are equal to their MLEs $\hat{\vec{y}}$. The likelihood difference

$$\Delta\mathcal{L}(\vec{y}) = \mathcal{L}(\vec{y}) - \mathcal{L}(\hat{\vec{y}}), \tag{A.6}$$

which should be considered a function of $\vec{y}$, is χ^2_M distributed, according to Wilks' theorem. Its statistical properties therefore provide an unambiguous determination of the confidence intervals of $\vec{y}$. Some of these statistical properties are provided in Table A.1, which show the values of χ^2_M that cover a probability of 68.27%, 95.45% and 99.73%. They are commonly referred to as 1, 2 and 3 σ confidence levels, respectively.

Table A.1: Values of $\Delta\mathcal{L}$ corresponding to a coverage probability corresponding to 1, 2 and 3 σ.

Number of σ	Coverage probability (%)	$M = 1$	$M = 2$	$M = 3$
1	68.27	1.00	2.30	3.53
2	95.45	4.00	6.18	8.03
3	99.73	9.00	11.83	14.16

The cases where $M = 1$ or $M = 2$ are most straightforward to visualise and interpret. In the first case, the confidence level of a single parameter y is determined by solving the equation $\Delta\mathcal{L}(y) = 1.00$. In many cases, $\mathcal{L}$ is symmetric around the minimum and the assigned uncertainty represents a symmetric 68.27% confidence interval. However, in general $\mathcal{L}$ can have any arbitrary shape and the resulting confidence interval may be asymmetric. Similarly, in the second case, the contour that covers a 68.27% confidence region is found by solving $\Delta\mathcal{L}(y_1, y_2) = 2.30$. Under ideal circumstances these confidence regions are ellipses, but generally they can take any arbitrary shape. Nevertheless, under the conditions for which Wilks' theorem is valid, the coverage probability will be given by Table A.1 for all M.

In practice, not all parameters $\vec{y}$ in Eq. (A.6) are of interest. It is sometimes useful to consider two sets of parameters $\vec{y}$ and $\vec{n}$, where $\vec{y}$ are the parameters of interest and $\vec{n}$ are "nuisance parameters". Under the null hypothesis, the parameters

$\vec{y}$ are fixed, but since the value of the nuisance parameters are irrelevant, they take the value of their MLEs, under the condition that the parameters of interest are fixed to $\vec{y}$. The alternative hypothesis remains the same, where $\vec{y}$ and $\vec{n}$ are equal to their MLEs $\hat{\vec{y}}$ and $\hat{\vec{n}}$. Equation (A.6) is modified into

$$\Delta\mathcal{L}(\vec{y}) = \mathcal{L}(\vec{y}, \hat{\vec{n}}(\vec{y})) - \mathcal{L}(\hat{\vec{y}}, \hat{\vec{n}}), \tag{A.7}$$

where the MLE notation $\hat{\vec{n}}(\vec{y})$ means that the likelihood has been minimised with respect to $\vec{n}$ while keeping the parameters of interest fixed to $\vec{y}$. By comparing Eq. (A.7) to Eq. (A.5), it can be concluded that $\Delta\mathcal{L}(\vec{y})$ in Eq. (A.7) is χ^2_M distributed, where M is the number of parameters in $\vec{y}$. Equation (A.7) is known as the profiled likelihood difference.

A.4 Confidence intervals without Wilks' theorem

Wilks' theorem loses its validity when the parameters of the likelihood function are near a boundary, or when the size of the data set is too small to provide sufficient sensitivity to one or more parameters. In such cases, the coverage probabilities provided in Table A.1 may no longer be applicable.

An example from the GammaCombo software framework [140] is shown in Fig. A.1, where a maximum likelihood fit is performed to determine a parameter a near a boundary $a > 0.4$. The vertical axis shows $1 - \mathrm{CL}$, with CL denotes the coverage probability. The filled graph shows the result of Wilks' theorem, and is also known as the Prob method. Since a cannot take any values below the $a = 0.4$ boundary, $1 - \mathrm{CL}$ is, by definition, zero for $a < 0.4$. Thus, the Prob method predicts that $1 - \mathrm{CL}$ abruptly drops to zero. This unphysical behaviour nicely illustrates the limitations of Wilks' theorem.

A strategy for assigning a confidence interval with the correct coverage probability is the Plugin method [141], which generalises the method by Feldman and Cousins [142] for constructing confidence intervals in the presence of nuisance parameters. For any arbitrary point $\vec{y}$ in the parameter space, the Plugin method can numerically determine the coverage probability at this point using the value of

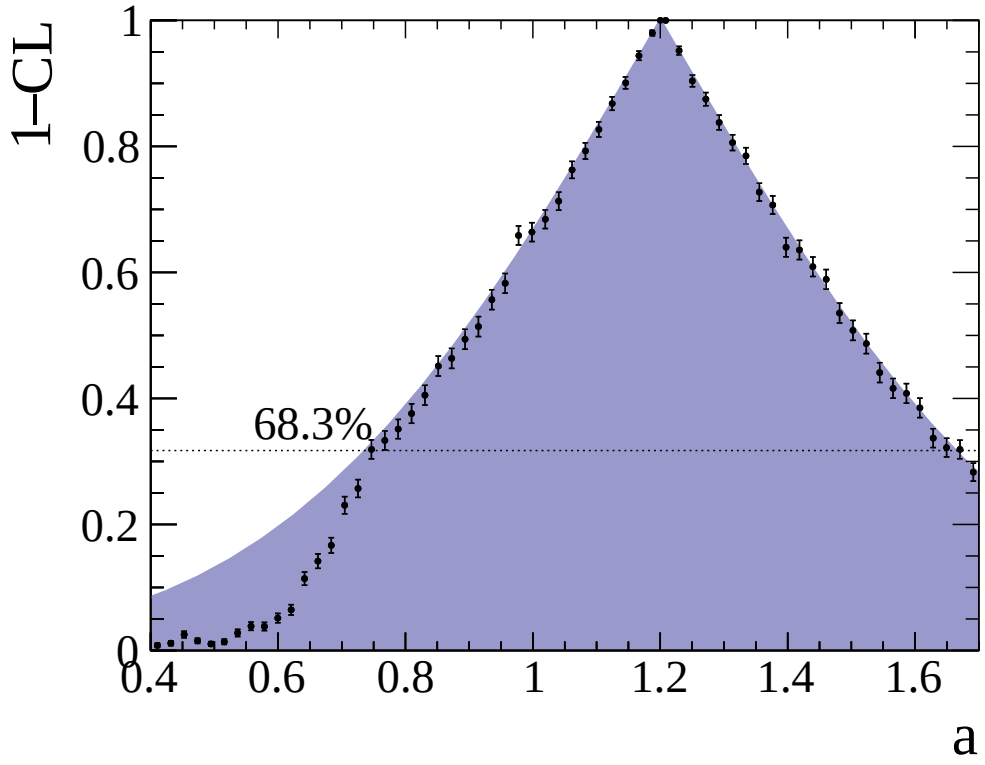

Figure A.1: A comparison of the (solid colour) Prob and (data points) Plugin methods near a boundary of some example fit of a parameter a.

$\Delta\mathcal{L}(\vec{y})$ in Eq. (A.7). By scanning over a range of points $\vec{y}$, the region with a coverage probability of 68.27% (or any other confidence level of interest) is determined.

At each scan point $\vec{y}$, a set of pseudo-experiments are generated using the parameters $\vec{y}$ and $\hat{\vec{n}}(\vec{y})$. The pseudo-experiments are generated by drawing random numbers from the PDF used to construct the likelihood $\mathcal{L}$. From each pseudo-experiment, the profile likelihood difference in Eq. (A.7) is constructed, and it is denoted $\Delta\mathcal{L}_{\text{pseudo}}(\vec{y})$ to distinguish it from the profile likelihood difference constructed from the data set $\Delta\mathcal{L}_{\text{data}}(\vec{y})$. From the full set of pseudo-experiments, the fraction of pseudo-experiments p where $\Delta\mathcal{L}_{\text{data}}(\vec{y}) < \Delta\mathcal{L}_{\text{pseudo}}(\vec{y})$ is determined. By construction, the value of $1 - p$ is therefore the coverage probability at point $\vec{y}$. In the special case where $M = 1$, the confidence interval $[y_-, y_+]$ of the parameter y are such that $p = 100\% - 68.27\% = 31.73\%$. This trivially generalises to higher dimensions.

In Fig. A.1, the result of the Plugin method are shown as black data points. Near the boundary, the behaviour of the Prob and Plugin method diverge, and the Plugin method shows a much more physical coverage probability. Although the Prob method predicts the correct 68.27% CL, to provide the correct coverage probability outside this region, the Plugin method offers a much more accurate description near the boundary.

References

[1] S. L. Glashow, J. Iliopoulos, and L. Maiani. "Weak Interactions with Lepton-Hadron Symmetry". In: *Phys. Rev. D* 2 (1970), pp. 1285–1292.

[2] S. Matsumoto. "Constraints on the electroweak universal parameters and the top and Higgs masses from updated LEP / SLC data". In: *Mod. Phys. Lett. A* 10 (1995), pp. 2553–2570. arXiv: `hep-ph/9411388`.

[3] H. Albrecht et al. "A New determination of the B^0 - $\bar{B}^0$ oscillation strength". In: *Z. Phys. C* 55 (1992), pp. 357–364.

[4] N. Barik et al. "$B_d^0 \bar{B}_d^0$ mixing and the prediction of the top quark mass in an independent particle potential model". In: *Phys. Rev. D* 48 (1993), pp. 3271–3276.

[5] N. Cabibbo. "Unitary Symmetry and Leptonic Decays". In: *Phys. Rev. Lett.* 10 (1963), pp. 531–533.

[6] M. Kobayashi and T. Maskawa. "*CP*-violation in the renormalizable theory of weak interaction". In: *Prog. Theor. Phys.* 49 (1973), pp. 652–657.

[7] X. Fan et al. "Measurement of the Electron Magnetic Moment". In: *Phys. Rev. Lett.* 130.7 (2023), p. 071801. arXiv: `2209.13084 [physics.atom-ph]`.

[8] *Standard Model*. Apr. 2024. URL: `https://en.wikipedia.org/wiki/Standard_Model`.

[9] E. Noether. "Invariant Variation Problems". In: *Gott. Nachr.* 1918 (1918), pp. 235–257. arXiv: `physics/0503066`.

[10] J. S. Schwinger. "The Theory of quantized fields. 1." In: *Phys. Rev.* 82 (1951). Ed. by K. A. Milton, pp. 914–927.

[11] T. D. Lee and C. N. Yang. "Question of Parity Conservation in Weak Interactions". In: *Phys. Rev.* 104 (1956), pp. 254–258.

[12] C. S. Wu et al. "Experimental Test of Parity Conservation in β Decay". In: *Phys. Rev.* 105 (1957), pp. 1413–1414.

[13] J. H. Christenson et al. "Evidence for the 2π Decay of the K_2^0 Meson". In: *Phys. Rev. Lett.* 13 (1964), pp. 138–140.

[14] E. Gabathuler and P. Pavlopoulos. "The CPLEAR experiment". In: *Phys. Rept.* 403-404 (2004), pp. 303–321.

[15] A. D. Sakharov. "Violation of CP Invariance, C asymmetry, and baryon asymmetry of the universe". In: *Pisma Zh. Eksp. Teor. Fiz.* 5 (1967), pp. 32–35.

[16] Patrick Huet and Eric Sather. "Electroweak baryogenesis and standard model CP violation". In: *Phys. Rev. D* 51 (1995), pp. 379–394. arXiv: `hep-ph/9404302`.

[17] M. Kobayashi and T. Maskawa. "CP Violation in the Renormalizable Theory of Weak Interaction". In: *Prog. Theor. Phys.* 49 (1973), pp. 652–657.

[18] L. L. Chau and W. Y. Keung. "Comments on the Parametrization of the Kobayashi-Maskawa Matrix". In: *Phys. Rev. Lett.* 53 (1984), p. 1802.

[19] L. Wolfenstein. "Parametrization of the Kobayashi-Maskawa Matrix". In: *Phys. Rev. Lett.* 51 (1983), p. 1945.

[20] C. Jarlskog. "Commutator of the Quark Mass Matrices in the Standard Electroweak Model and a Measure of Maximal CP Nonconservation". In: *Phys. Rev. Lett.* 55 (1985), p. 1039.

[21] R. L. Workman et al. "Review of Particle Physics". In: *PTEP* 2022 (2022), p. 083C01.

[22] J. Brod and J. Zupan. "The ultimate theoretical error on γ from $B \to DK$ decays". In: *JHEP* 01 (2014), p. 051. arXiv: 1308.5663 [hep-ph].

[23] J. Charles et al. "CP violation and the CKM matrix: Assessing the impact of the asymmetric B factories". In: *Eur. Phys. J. C* 41.1 (2005), pp. 1–131. arXiv: hep-ph/0406184.

[24] R. Aaij et al. "Measurement of CP Violation in $B^0 \to \psi(\to \ell^+\ell^-)K^0_S(\to \pi^+\pi^-)$ Decays". In: *Phys. Rev. Lett.* 132.2 (2024), p. 021801. arXiv: 2309.09728 [hep-ex].

[25] Y. S. Amhis et al. "Averages of b-hadron, c-hadron, and τ-lepton properties as of 2021". In: *Phys. Rev. D* 107.5 (2023), p. 052008. arXiv: 2206.07501 [hep-ex].

[26] R. Aaij et al. "A precise measurement of the B^0 meson oscillation frequency". In: *Eur. Phys. J. C* 76.7 (2016), p. 412. arXiv: 1604.03475 [hep-ex].

[27] R. Aaij et al. "Precise determination of the B^0_s–$\overline{B}^0_s$ oscillation frequency". In: *Nature Phys.* 18.1 (2022), pp. 1–5. arXiv: 2104.04421 [hep-ex].

[28] M. Gronau and D. London. "How to determine all the angles of the unitarity triangle from B(d)0 —> D K(s) and B(s)0 —> D0". In: *Phys. Lett. B* 253 (1991), pp. 483–488.

[29] M. Gronau and D. Wyler. "On determining a weak phase from CP asymmetries in charged B decays". In: *Phys. Lett. B* 265 (1991), pp. 172–176.

[30] D. Atwood, I. Dunietz, and A. Soni. "Enhanced CP violation with B —> K D0 (anti-D0) modes and extraction of the CKM angle gamma". In: *Phys. Rev. Lett.* 78 (1997), pp. 3257–3260. arXiv: hep-ph/9612433.

[31] A. Bondar. "Proceedings of BINP special analysis meeting on Dalitz analysis, 24-26 Sep. 2002". In: *unpublished* (2002).

[32] A. Bondar and A. Poluektov. "Feasibility study of model-independent approach to φ_3 measurement using Dalitz plot analysis". In: *The European Physical Journal C* 47.2 (June 2006), pp. 347–353. URL: http://dx.doi.org/10.1140/epjc/s2006-02590-x.

[33] A. Bondar and A. Poluektov. "The use of quantum-correlated D^0 decays for φ_3 measurement". In: *The European Physical Journal C* 55.1 (Apr. 2008), pp. 51–56. URL: http://dx.doi.org/10.1140/epjc/s10052-008-0600-z.

[34] A. Giri et al. "Determining γ using $B^\pm \to DK^\pm$ with multibody D decays". In: *Phys. Rev. D* 68 (5 Sept. 2003), p. 054018. URL: https://link.aps.org/doi/10.1103/PhysRevD.68.054018.

[35] I. Adachi et al. "Measurement of $\cos 2\beta$ in $B^0 \to D^{(*)}h^0$ with $D \to K^0_S\pi^+\pi^-$ decays by a combined time-dependent Dalitz plot analysis of BaBar and Belle data". In: *Phys. Rev. D* 98.11 (2018), p. 112012. arXiv: 1804.06153 [hep-ex].

[36] A. Bondar et al. "Effect of direct CP violation in charm on γ extraction from $B \to DK^\pm, D \to K^0_S\pi^+\pi^-$ Dalitz plot analysis". In: *Eur. Phys. J. C* 73.6 (2013), p. 2476. arXiv: 1303.6305 [hep-ph].

[37] T. Aaltonen et al. "Measurement of CP-violation asymmetries in $D^0 \to K_S\pi^+\pi^-$". In: *Phys. Rev. D* 86 (2012), p. 032007. arXiv: 1207.0825 [hep-ex].

[38] R. Aaij et al. "Search for CP violation through an amplitude analysis of $D^0 \to K^+K^-\pi^+\pi^-$ decays". In: *JHEP* 02 (2019), p. 126. arXiv: 1811.08304 [hep-ex].

[39] R. Aaij et al. "Measurement of the CKM angle γ in $B^\pm \to DK^\pm$ and $B^\pm \to D\pi^\pm$ decays with $D \to K^0_S h^+h^-$". In: *JHEP* 02 (2021), p. 169. arXiv: 2010.08483 [hep-ex].

[40] S. Harnew et al. "Model-independent determination of the strong phase difference between D^0 and $\bar{D}^0 \to \pi^+\pi^-\pi^+\pi^-$ amplitudes". In: *JHEP* 01 (2018), p. 144. arXiv: 1709.03467 [hep-ex].

[41] R. Aaij et al. "Measurement of CP observables in $B^\pm \to D^{(*)}K^\pm$ and $B^\pm \to D^{(*)}\pi^\pm$ decays using two-body D final states". In: *JHEP* 04 (2021), p. 081. arXiv: 2012.09903 [hep-ex].

[42] E. Norrbin and T. Sjostrand. "Production and hadronization of heavy quarks". In: *Eur. Phys. J. C* 17 (2000), pp. 137–161. arXiv: hep-ph/0005110.

[43] M. Ablikim et al. "Measurement of the CP-even fraction of $D^0 \to K^+K^-\pi^+\pi^-$". In: *Phys. Rev. D* 107.3 (2023), p. 032009. arXiv: 2212.06489 [hep-ex].

[44] M. Ablikim et al. "Measurement of the CP-even fraction of $D^0 \to \pi^+\pi^-\pi^+\pi^-$". In: *Phys. Rev. D* 106.9 (2022), p. 092004. arXiv: 2208.10098 [hep-ex].

[45] M. Nayak et al. "First determination of the CP content of $D \to \pi^+\pi^-\pi^0$ and $D \to K^+K^-\pi^0$". In: *Phys. Lett. B* 740 (2015), pp. 1–7. arXiv: 1410.3964 [hep-ex].

[46] S. Malde et al. "First determination of the CP content of $D \to \pi^+\pi^-\pi^+\pi^-$ and updated determination of the CP contents of $D \to \pi^+\pi^-\pi^0$ and $D \to K^+K^-\pi^0$". In: *Phys. Lett. B* 747 (2015), pp. 9–17. arXiv: 1504.05878 [hep-ex].

[47] R. Aaij et al. "Measurement of the CKM angle γ with $B^\pm \to D[K^\mp\pi^\pm\pi^\pm\pi^\mp]h^\pm$ decays using a binned phase-space approach". In: *JHEP* 07 (2023), p. 138. arXiv: 2209.03692 [hep-ex].

[48] R. Aaij et al. "Simultaneous determination of CKM angle γ and charm mixing parameters". In: *JHEP* 12 (2021), p. 141. arXiv: 2110.02350 [hep-ex].

[49] M. Ablikim et al. "Improved measurement of the strong-phase difference $\delta_D^{K\pi}$ in quantum-correlated $D\bar{D}$ decays". In: *Eur. Phys. J. C* 82.11 (2022), p. 1009. arXiv: 2208.09402 [hep-ex].

[50] M. Ablikim et al. "Measurement of the $D \to K^-\pi^+\pi^+\pi^-$ and $D \to K^-\pi^+\pi^0$ coherence factors and average strong-phase differences in quantum-correlated $D\bar{D}$ decays". In: *JHEP* 05 (2021), p. 164. arXiv: 2103.05988 [hep-ex].

[51] S. U. Chung et al. “Partial wave analysis in K matrix formalism”. In: *Annalen Phys.* 4 (1995), pp. 404–430.

[52] T. Evans. *AmpGen*. `https://github.com/GooFit/AmpGen`. 2021.

[53] M. Tat. *D0->KKpipi binning scheme*. Version 1.0. July 2022. URL: `https://doi.org/10.5281/zenodo.6940031`.

[54] J. Libby et al. “Model-independent determination of the strong-phase difference between D^0 and $\bar{D}^0 \to K^0_{S,L}h^+h^-$ ($h = \pi, K$) and its impact on the measurement of the CKM angle γ/ϕ_3”. In: *Phys. Rev. D* 82 (2010), p. 112006. arXiv: `1010.2817 [hep-ex]`.

[55] M. Ablikim et al. “Determination of Strong-Phase Parameters in $D \to K^0_{S,L}\pi^+\pi^-$”. In: *Phys. Rev. Lett.* 124.24 (2020), p. 241802. arXiv: `2002.12791 [hep-ex]`.

[56] M. Ablikim et al. “Model-independent determination of the relative strong-phase difference between D^0 and $\bar{D}^0 \to K^0_{S,L}\pi^+\pi^-$ and its impact on the measurement of the CKM angle γ/ϕ_3”. In: *Phys. Rev. D* 101.11 (2020), p. 112002. arXiv: `2003.00091 [hep-ex]`.

[57] M. Ablikim et al. “Improved model-independent determination of the strong-phase difference between D^0 and $\bar{D}^0 \to K^0_{\mathrm{S,L}}K^+K^-$ decays”. In: *Phys. Rev. D* 102.5 (2020), p. 052008. arXiv: `2007.07959 [hep-ex]`.

[58] P. K. Resmi et al. “Quantum-correlated measurements of $D \to K^0_{\mathrm{S}}\pi^+\pi^-\pi^0$ decays and consequences for the determination of the CKM angle γ”. In: *JHEP* 01 (2018), p. 082. arXiv: `1710.10086 [hep-ex]`.

[59] T. Evans et al. “Improved sensitivity to the CKM phase γ through binning phase space in $B^- \to DK^-$, $D \to K^+\pi^-\pi^-\pi^+$ decays”. In: *Phys. Lett. B* 802 (2020), p. 135188. arXiv: `1909.10196 [hep-ex]`.

[60] A. Bondar and A. Poluektov. “The use of quantum-correlated D^0 decays for φ_3 measurement”. In: *Eur. Phys. J. C* 55 (2008), pp. 51–56. arXiv: `0801.0840 [hep-ex]`.

[61] J. Rademacker and G. Wilkinson. “Determining the unitarity triangle gamma with a four-body amplitude analysis of B+- —> (K+ K- pi+ pi-)(D)K+- decays”. In: *Phys. Lett. B* 647 (2007), pp. 400–404. arXiv: `hep-ph/0611272`.

[62] J. M. Link et al. “Study of the D0 —> K+ K- pi+ pi-”. In: *Phys. Lett. B* 610 (2005), pp. 225–234. arXiv: `hep-ex/0411031`.

[63] M. Artuso et al. “Amplitude analysis of $D^0 \to K^+K^-\pi^+\pi^-$”. In: *Phys. Rev. D* 85 (2012), p. 122002. arXiv: `1201.5716 [hep-ex]`.

[64] Morris H. DeGroot and Mark J. Schervish. *Probability and Statistics*. 3rd. Addison Wesley, 2002.

[65] F. E. James. *Monte Carlo phase space*. CERN Academic Training Lecture. CERN, Geneva, 1 May 1968. Geneva: CERN, 1968. URL: `https://cds.cern.ch/record/275743`.

[66] M. Ablikim et al. “Design and Construction of the BESIII Detector”. In: *Nucl. Instrum. Meth. A* 614 (2010), pp. 345–399. arXiv: `0911.4960 [physics.ins-det]`.

[67] C. Yu et al. "BEPCII Performance and Beam Dynamics Studies on Luminosity". In: *7th International Particle Accelerator Conference*. 2016, TUYA01.

[68] K. X. Huang et al. "Method for detector description transformation to Unity and application in BESIII". In: *Nucl. Sci. Tech.* 33.11 (2022), p. 142. arXiv: 2206.10117 [physics.ins-det].

[69] M. Ablikim et al. "Measurement of the integrated luminosities of the data taken by BESIII at $\sqrt{s}$ =3.650 and 3.773 GeV". In: *Chin. Phys. C* 37 (2013), p. 123001. arXiv: 1307.2022 [hep-ex].

[70] M. Ablikim et al. "Measurement of the $e^+e^- \to \pi^+\pi^-$ cross section between 600 and 900 MeV using initial state radiation". In: *Phys. Lett. B* 753 (2016). [Erratum: Phys.Lett.B 812, 135982 (2021)], pp. 629–638. arXiv: 1507.08188 [hep-ex].

[71] D. M. Asner et al. "Physics at BES-III". In: *Int. J. Mod. Phys. A* 24 (2009), S1–794. arXiv: 0809.1869 [hep-ex].

[72] S. Sun. "Time calibration for barrel TOF system of BESIII". In: *J. Phys. Conf. Ser.* 396 (2012). Ed. by Michael Ernst et al., p. 022051.

[73] X. Li et al. "Study of MRPC technology for BESIII endcap-TOF upgrade". In: *Radiat. Detect. Technol. Methods* 1.2 (July 2017), p. 13.

[74] Y. X. Guo et al. "The study of time calibration for upgraded end cap TOF of BESIII". In: *Radiat. Detect. Technol. Methods* 1.2 (July 2017), p. 15.

[75] P. Cao et al. "Design and construction of the new BESIII endcap Time-of-Flight system with MRPC Technology". In: *Nucl. Instrum. Meth. A* 953 (2020), p. 163053.

[76] M. He. "Simulation and reconstruction of the BESIII EMC". In: *Journal of Physics: Conference Series* 293.1 (Apr. 2011), p. 012025. URL: https://dx.doi.org/10.1088/1742-6596/293/1/012025.

[77] M. Ablikim et al. "Study of BESIII trigger efficiencies with the 2018 J/ψ data". In: *Chin. Phys. C* 45.2 (2021), p. 023002. arXiv: 2009.11566 [hep-ex].

[78] S. Agostinelli et al. "GEANT4 – a simulation toolkit". In: *Nucl. Instrum. Meth. A* 506 (2003), p. 250.

[79] S. Jadach, B.F.L. Ward, and Z. Was. "The precision Monte Carlo event generator KK for two fermion final states in e^+e^- collisions". In: *Comput. Phys. Commun.* 130 (2000), p. 260.

[80] D. J. Lange. "The EvtGen particle decay simulation package". In: *Nucl. Instrum. Meth. A* 462 (2001). Ed. by S. Erhan, P. Schlein, and Y. Rozen, p. 152.

[81] R. G. Ping. "Event generators at BESIII". In: *Chin. Phys. C* 32 (2008), p. 599.

[82] R. L. Yang, R. G. Ping, and H. Chen. "Tuning and Validation of the Lundcharm Model with J/ψ Decays". In: *Chin. Phys. Lett.* 31 (2014), p. 061301.

[83] J. C. Chen et al. "Event generator for J/ψ and $\psi(2S)$ decay". In: *Phys. Rev. D* 62 (2000), p. 034003.

[84] E. Richter-Was. "QED bremsstrahlung in semileptonic B and leptonic tau decays". In: *Phys. Lett. B* 303 (1993), p. 163.

[85] C. Rosner et al. "Determination of the CP-even fraction of D0→KS0π+π-π0". In: *Phys. Rev. D* 108.3 (2023), p. 032003. arXiv: 2305.03975 [hep-ex].

[86] Q. G. Liu et al. "Track reconstruction using the TSF method for the BESIII main drift chamber*". In: *Chinese Physics C* 32.7 (July 2008), p. 565. URL: https://dx.doi.org/10.1088/1674-1137/32/7/011.

[87] M. Ablikim et al. "Study of Dynamics of $D^0 \to K^- e^+ \nu_e$ and $D^0 \to \pi^- e^+ \nu_e$ Decays". In: *Phys. Rev. D* 92.7 (2015), p. 072012. arXiv: 1508.07560 [hep-ex].

[88] M. He et al. "Energy loss correction for a crystal calorimeter*". In: *Chinese Physics C* 32.4 (Apr. 2008), p. 269. URL: https://dx.doi.org/10.1088/1674-1137/32/4/006.

[89] M. Ablikim et al. "Measurement of the $D \to K^-\pi^+\pi^+\pi^-$ and $D \to K^-\pi^+\pi^0$ coherence factors and average strong-phase differences in quantum-correlated $D\bar{D}$ decays". In: *JHEP* 05 (2021), p. 164. arXiv: 2103.05988 [hep-ex].

[90] W. D. Hulsbergen. "Decay chain fitting with a Kalman filter". In: *Nucl. Instrum. Meth. A* 552 (2005), pp. 566–575. arXiv: physics/0503191.

[91] A. Rogozhnikov. "Reweighting with Boosted Decision Trees". In: *J. Phys. Conf. Ser.* 762.1 (2016). Ed. by Luis Salinas and Claudio Torres, p. 012036. arXiv: 1608.05806 [physics.data-an].

[92] A. Rogozhnikov. *hep_ml*. https://github.com/arogozhnikov/hep_ml. 2023.

[93] K. S. Cranmer. "Kernel estimation in high-energy physics". In: *Comput. Phys. Commun.* 136 (2001), pp. 198–207. arXiv: hep-ex/0011057.

[94] H. Albrecht et al. "Search for Hadronic $b \to u$ Decays". In: *Phys. Lett. B* 241 (1990), p. 278.

[95] X. Zhou et al. "TopoAna: A generic tool for the event type analysis of inclusive Monte-Carlo samples in high energy physics experiments". In: *Computer Physics Communications* 258 (2021), p. 107540. URL: https://www.sciencedirect.com/science/article/pii/S0010465520302575.

[96] J. Insler et al. "Studies of the decays $D^0 \to K^0_S K^-\pi^+$ and $D^0 \to K^0_S K^+\pi^-$". In: *Phys. Rev. D* 85 (2012). [Erratum: Phys.Rev.D 94, 099905 (2016)], p. 092016. arXiv: 1203.3804 [hep-ex].

[97] M. Ablikim et al. "Measurement of $e^+e^- \to D\bar{D}$ cross sections at the $\psi(3770)$ resonance". In: *Chin. Phys. C* 42.8 (2018), p. 083001. arXiv: 1803.06293 [hep-ex].

[98] M. Ablikim et al. "Measurement of the $e^+e^- \to \pi^+\pi^-$ cross section between 600 and 900 MeV using initial state radiation". In: *Phys. Lett. B* 753 (2016). [Erratum: Phys.Lett.B 812, 135982 (2021)], pp. 629–638. arXiv: 1507.08188 [hep-ex].

[99] M. Ablikim et al. "Measurement of the integrated luminosity of the data collected at 3.773 GeV by BESIII from 2021 to 2023". In: *Chin. Phys. C, in preparation* ().

[100] R. Barlow. "Asymmetric statistical errors". In: *PHYSTAT (2005): Statistical Problems in Particle Physics, Astrophysics and Cosmology*. June 2004, pp. 56–59. arXiv: physics/0406120.

[101] Kaikai He, Hailong Ma, and Xinping Xi. *Studies of $K^\pm/\pi^\pm$ tracking and PID efficiencies for $\psi(3770)$ data*. DocDB-1283. 2023.

[102] A. A. Alves et al. "The LHCb Detector at the LHC". In: *JINST* 3 (2008). Also published by CERN Geneva in 2010, S08005. URL: https://cds.cern.ch/record/1129809.

[103] R. Aaij et al. "LHCb Detector Performance". In: *Int. J. Mod. Phys. A* 30.07 (2015), p. 1530022. arXiv: 1412.6352 [hep-ex].

[104] R. Aaij et al. "Design and performance of the LHCb trigger and full real-time reconstruction in Run 2 of the LHC". In: *JINST* 14.04 (2019), P04013. arXiv: 1812.10790 [hep-ex].

[105] R. Aaij et al. "Performance of the LHCb Vertex Locator". In: *JINST* 9 (2014), P09007. arXiv: 1405.7808 [physics.ins-det].

[106] R. W. Forty and O. Schneider. *RICH pattern recognition*. Tech. rep. Geneva: CERN, 1998. URL: https://cds.cern.ch/record/684714.

[107] R. Calabrese et al. "Performance of the LHCb RICH detectors during LHC Run 2". In: *JINST* 17.07 (2022), P07013. arXiv: 2205.13400 [physics.ins-det].

[108] M. Adinolfi et al. "Performance of the LHCb RICH detector at the LHC". In: *Eur. Phys. J. C* 73 (2013), p. 2431. arXiv: 1211.6759 [physics.ins-det].

[109] C. Abellán Beteta et al. "Calibration and performance of the LHCb calorimeters in Run 1 and 2 at the LHC". In: (Aug. 2020). arXiv: 2008.11556 [physics.ins-det].

[110] A. A. Alves Jr. et al. "Performance of the LHCb muon system". In: *JINST* 8 (2013), P02022. arXiv: 1211.1346 [physics.ins-det].

[111] "RTA and DPA dataflow diagrams for Run 1, Run 2, and the upgraded LHCb detector ". In: (2020). URL: https://cds.cern.ch/record/2730181.

[112] V. V. Gligorov, C. Thomas, and M. Williams. *The HLT inclusive B triggers*. Tech. rep. LHCb-INT-2011-030. Geneva: CERN, 2011. URL: https://cds.cern.ch/record/1384380.

[113] V. V. Gligorov and M. Williams. "Efficient, reliable and fast high-level triggering using a bonsai boosted decision tree". In: *JINST* 8 (2013), P02013. arXiv: 1210.6861 [physics.ins-det].

[114] I. Bird. "Computing for the Large Hadron Collider". In: *Ann. Rev. Nucl. Part. Sci.* 61 (2011), pp. 99–118.

[115] Torbjörn Sjöstrand, Stephen Mrenna, and Peter" Skands. "PYTHIA 6.4 physics and manual". In: *JHEP* 05 (2006), p. 026. arXiv: hep-ph/0603175 [hep-ph].

[116] Torbjörn Sjöstrand, Stephen Mrenna, and Peter" Skands. "A brief introduction to PYTHIA 8.1". In: *Comput. Phys. Commun.* 178 (2008), pp. 852–867. arXiv: 0710.3820 [hep-ph].

[117] I. Belyaev et al. "Handling of the generation of primary events in Gauss, the LHCb simulation framework". In: *J. Phys. Conf. Ser.* 331 (2011), p. 032047.

[118] N. Davidson, T. Przedzinski, and Z. Was. "PHOTOS interface in C++: Technical and physics documentation". In: *Comp. Phys. Comm.* 199 (2016), p. 86. arXiv: 1011.0937 [hep-ph].

[119] J. Allison et al. “Geant4 developments and applications”. In: *IEEE Trans.Nucl.Sci.* 53 (2006), p. 270.

[120] M Clemencic et al. “The LHCb simulation application, Gauss: Design, evolution and experience”. In: *J. Phys. Conf. Ser.* 331 (2011), p. 032023.

[121] D. Müller et al. “ReDecay: A novel approach to speed up the simulation at LHCb”. In: *Eur. Phys. J.* C78 (2018), p. 1009. arXiv: 1810.10362 [hep-ex].

[122] C. Elsasser. *$\bar{b}b$ production angle plots*. URL: https://lhcb.web.cern.ch/speakersbureau/html/bb_productionangles.html.

[123] M. De Cian et al. “Fast neural-net based fake track rejection in the LHCb reconstruction”. In: (2017).

[124] W. D. Hulsbergen. “Decay chain fitting with a Kalman filter”. In: *Nucl. Instrum. Meth. A* 552 (2005), pp. 566–575. arXiv: physics/0503191.

[125] L. Breiman et al. *Classification and regression trees*. Belmont, California, USA: Wadsworth international group, 1984.

[126] C. E. Shannon. “A Mathematical Theory of Communication”. In: *The Bell System Technical Journal* 27 (1948), pp. 379–423. URL: http://plan9.bell-labs.com/cm/ms/what/shannonday/shannon1948.pdf (visited on 04/22/2003).

[127] E. H. Simpson. “Measurement of Diversity”. In: *Nature* 163 (1949), pp. 688–688. URL: https://api.semanticscholar.org/CorpusID:204990535.

[128] J. H. Friedman. “Greedy Function Approximation: A Gradient Boosting Machine”. In: *The Annals of Statistics* 29.5 (2001), pp. 1189–1232. URL: http://www.jstor.org/stable/2699986 (visited on 07/18/2024).

[129] A. Hocker et al. “TMVA - Toolkit for Multivariate Data Analysis”. In: (Mar. 2007). arXiv: physics/0703039.

[130] M. Pivk and F. R. Le Diberder. “SPlot: A Statistical tool to unfold data distributions”. In: *Nucl. Instrum. Meth. A* 555 (2005), pp. 356–369. arXiv: physics/0402083.

[131] L. Anderlini et al. “The PIDCalib package”. In: (2016).

[132] R. Aaij et al. “Selection and processing of calibration samples to measure the particle identification performance of the LHCb experiment in Run 2”. In: *Eur. Phys. J. Tech. Instr.* 6 (2019), p. 1. arXiv: 1803.00824 [hep-ex].

[133] D. Cervenkov. *PIDCalib2*. https://gitlab.cern.ch/lhcb-rta/pidcalib2. 2021.

[134] G. A. Cowan, D. C. Craik, and M. D. Needham. “RapidSim: an application for the fast simulation of heavy-quark hadron decays”. In: *Comput. Phys. Commun.* 214 (2017), pp. 239–246. arXiv: 1612.07489 [hep-ex].

[135] R. Aaij et al. “Measurement of *CP* observables in $B^\pm \to DK^\pm$ and $B^\pm \to D\pi^\pm$ with two- and four-body D decays”. In: *Phys. Lett. B* 760 (2016), pp. 117–131. arXiv: 1603.08993 [hep-ex].

[136] M. Bjorn. “CP Violation in $B^\pm \to Dh^\pm$ Decays where $D \to K^0_S h'^+ h'^-$”. Presented 08 Oct 2020. Oxford U., 2020. URL: https://cds.cern.ch/record/2753911.

[137] R. Aaij et al. "Constraints on the unitarity triangle angle γ from Dalitz plot analysis of $B^0 \to DK^+\pi^-$ decays". In: *Phys. Rev. D* 93.11 (2016). [Erratum: Phys.Rev.D 94, 079902 (2016)], p. 112018. arXiv: `1602.03455 [hep-ex]`.

[138] M. Ablikim et al. "Model-independent determination of the strong-phase difference between D^0 and $\bar{D}^0 \to \pi^+\pi^-\pi^+\pi^-$ decays at BESIII". In: *Phys. Rev. D, to be published* (2024).

[139] S. S. Wilks. "The Large-Sample Distribution of the Likelihood Ratio for Testing Composite Hypotheses". In: *Annals Math. Statist.* 9.1 (1938), pp. 60–62.

[140] M. W. Kenzie et al. *GammaCombo*. `https://github.com/gammacombo/gammacombo`. 2019.

[141] S. Bodhisattva, M. Walker, and M. Woodroofe. "On the Unified Method with Nuisance Parameters". In: *Statist. Sinica* 19 (2009), pp. 301–314.

[142] G. J. Feldman and R. D. Cousins. "A Unified approach to the classical statistical analysis of small signals". In: *Phys. Rev. D* 57 (1998), pp. 3873–3889. arXiv: `physics/9711021`.